

ALMA MATER STUDIORUM
UNIVERSITÀ DEGLI STUDI DI BOLOGNA

DOTTORATO DI RICERCA IN ASTROFISICA
Ciclo XXXI

**NEW DETECTIONS AND
STATISTICS OF DIFFUSE RADIO
SOURCES IN GALAXY CLUSTERS**

Presentata da:

Massimo Cau

Supervisore:
Chiar.mo Prof.

Gabriele Giovannini

Coordinatore Dottorato:
Chiar.mo Prof.

Francesco R. Ferraro

Esame Finale anno 2019

Settore concorsuale: 02/C1–Astronomia, Astrofisica, Fisica della Terra e dei Pianeti
Settore scientifico–disciplinare: FIS/05–Astronomia e Astrofisica

Contents

List of acronyms	5
Abstract	7
1 Cluster of galaxies	11
1.1 Introduction: galaxy clusters overview	11
1.2 The intra-cluster medium (ICM)	13
1.2.1 The thermal component of ICM	13
1.2.2 The non-thermal component of ICM	15
1.2.3 Halos	16
1.2.4 Relics	21
1.2.5 Mini-halos	23
2 Diffuse emission I	25
2.1 Introduction	25
2.2 2011 halos statistical study	25
2.2.1 Radio Halos and redshift	26
2.2.2 Radio halos power and largest linear size	27
2.2.3 Radio halos power and X-ray properties	28
2.2.4 X-ray luminosity from MCXC catalog	30
2.3 2011 relics statistical study	33
2.3.1 Different structures, redshift and projected distance distribution of 2011 radio relics	33
2.3.2 Radio Power of relics vs linear largest size (LLS)	35
2.3.3 Radio and X-ray connection for radio relics	35
2.3.4 Comparison between halos and relics	36
2.4 Statistical study of mini-halos population	37
3 Diffuse emission II	41
3.1 Introduction	41

3.2	2018 Halo collection: scaling relations	42
3.2.1	Redshift distribution	42
3.2.2	Radio power at 1.4 GHz and LLS	43
3.2.3	Radio power at 1.4 GHz and $L_{X,500}$	45
3.3	2018 Relic collection: scaling relations	46
3.3.1	Redshift and projected distance distribution	48
3.3.2	Radio power of relics vs linear largest size (LLS)	50
3.3.3	Radio and X-ray connection	51
3.4	Minihalos: a 2017 updated overview	56
3.5	Redshift limits of the current knowledge	58
3.5.1	Updated redshift distribution of halos and relics	58
3.5.2	z evolution of the $P_{1.4GHz} - L_{X,500}$ correlation for halos	59
3.5.3	A possible correlation with z of the $P_{1.4GHz} - L_{X,500}$ scaling relation for relics	61
3.5.4	z evolution of the $P_{1.4GHz} - LLS$ correlations for halos and relics	63
4	Dynamical state and diffuse emission	67
4.1	Estimators of cluster dynamical state	67
4.1.1	Power ratios	68
4.1.2	Centroid shift	68
4.1.3	Concentration parameter	69
4.1.4	X-ray peak–BCG offset	69
4.2	D_{X-BCG} and diffuse radio emission	70
4.3	D_{X-BCG} vs other morphological estimators	73
4.4	Correlations with D_{X-BCG}	75
4.4.1	c vs. D_{X-BCG}	76
4.4.2	w vs. D_{X-BCG}	77
4.4.3	P_3/P_0 vs. D_{X-BCG}	78
5	Topics and aims of the present thesis	83
5.1	Overview	83
5.2	Scarce sampling at $z \geq 0.3$ of known halos and relics	84
5.3	Selection of a high redshift cluster sample	85
6	JVLA observation	87
6.1	The Jansky Very Large Array Radio Telescope	87
6.2	Observing proposal	88
6.3	Obs ID: 17A-025	90

6.3.1	D array observations	90
6.3.2	C array observations	91
6.3.3	the VLA calibration pipeline	92
6.3.4	imaging	93
6.4	Data reduction and imaging: halos and relics	94
6.4.1	MACSJ0018.5+1626	94
6.4.2	MACSJ0025.4–1222	96
6.4.3	MACSJ0152.5–2852	98
6.4.4	MACSJ0257.6–2209	100
6.4.5	MACSJ0308.9+2645	100
6.4.6	MACSJ0451.9+0006	104
6.4.7	MACSJ0454.1–0300	106
6.4.8	MACSJ0520.7–1328	108
6.4.9	MACSJ0553.4–3342	110
6.4.10	MACSJ0744.9+3927	113
6.4.11	MACSJ2211.7–0349	116
6.4.12	MACSJ2228.5+2036	118
6.5	Data reduction and imaging: mini halos	120
6.5.1	MACSJ0159.8–0849	120
6.5.2	MACSJ0947.2+7623 (RBS0797)	122
6.5.3	MACSJ1532.8+3021	124
6.5.4	MACSJ1931.8–2634	125
7	Notes on individual clusters	129
7.1	Clusters without diffuse emission	129
7.1.1	Clusters without diffuse emission	129
7.1.2	Plots of clusters without diffuse radio emission	134
7.2	Clusters with uncertain diffuse emission	139
8	Summary and conclusions	147
8.1	Results of the Project 17A-025 radio observations	148
8.2	Discovery of new diffuse emission at $z \geq 0.3$	149
8.3	Statistical analysis	150
8.4	Redshift evolution of radio halos	151
8.5	Redshift evolution of radio relics	154
8.6	Redshift evolution of radio minihalos	157
8.7	Dynamical state indicators and redshift	158
8.8	Future perspectives	158

References

153

List of acronyms

AGN	Active Galactic Nuclei
AIPS	Astronomical Image Processing System
BCES	Bivariate Correlate Errors and Scatters
BCG	Brightest Cluster Galaxy
CASA	Common Astronomy Software Applications
CDM	Cold Dark Matter
CMB	Cosmic Microwave Background
DSS2	Digitized Sky Survey 2 (Northern Sky Objects)
FWHM	Full Width at Half Maximum
GHRS	GMRT Radio Halo Survey
GMRT	Giant Metrewave Radio Telescope
JVLA	Jansky Very Large Array
ICM	Intra Cluster Medium
LLS	Largest Linear Size
LOFAR	LOW Frequency ARray Telescope
LoTSS	LOFAR Two-meter Sky Survey
MACS	MAssive Cluster Survey
MCXC	Meta-Catalog of X-ray Clusters
NRAO	National Radio Astronomy Observatory

NVSS	NRAO VLA Sky Survey
OLS	Ordinary Least Squares
RFI	Radio Frequency Interference
SMBH	Super Massive Black Hole
VLSS	VLA Low-Frequency Sky Survey
WENSS	Westerbork Northern Sky Survey
WSRT	Westerbork Synthesis Radio Telescope

Abstract

Galaxy clusters are the largest gravitationally bound structures of the Universe, formed from density fluctuations and grown hierarchically through the extreme process of merging and mass accretion. They represent very interesting tools to study the cosmology and the evolution of large scale structures. In the last years most of the detailed knowledge of galaxy clusters has been obtained from the study of thermal X-ray and non-thermal diffuse radio emission of the intra-cluster medium (ICM). Observational evidences showed the presence of a strong correlation between total radio power and X-ray luminosity, suggesting a strict interconnection between non-thermal properties and cluster mass. Synchrotron non-thermal emission detected in the forms of radio halos, relics and minihalos according to their morphology, size and location is linked to the different dynamical state of the hosting clusters. Halos and relics are detected in clusters characterized by a strong merger activity and a dynamical disturbed state (although few relics have been discovered in clusters with no strong evidence of ongoing merger activity), while minihalos are present only in relaxed cool-core clusters. This dichotomy represents an important reference to test the dynamical state of a cluster usually carried out with indicators based on the morphology of the X-ray images (e.g. the concentration parameter c , the centroid shift w , the power ratios P_3/P_0 and the X-ray peak–BCG offset). In spite of many encouraging results obtained up to now, the occurrence and the luminosity function of diffuse radio sources with the redshift are still unknown: present data are strongly limited to nearby clusters ($z < 0.2 - 0.3$). The aim of this PhD thesis is mainly to investigate the evolutionary history of non-thermal properties of galaxy clusters and to determine whether the correlations observed at low redshift evolve with time.

To attempt this ambitious goal we selected an homogeneous sample of 44 massive and high X-ray luminous galaxy clusters in the redshift range $0.3 \leq z < 0.7$, extracted from the Ebeling MAssive Cluster Survey (MACS).

We have undertaken an observational campaign on this sample with the JVLA in L-band, C and D configurations. Our targets have been the following:

- establish in our sample the presence or absence of diffuse radio emission and increase the number of halos, relics and minihalos detected at $z \geq 0.3$;
- compare the statistical properties of non thermal emission of high redshift clusters ($z \geq 0.3$) to those of low redshift clusters ($z < 0.3$);
- verify from this comparison the existence of an evolution with the redshift of the scaling relations existing between radio power at 1.4 GHz, the R_{500} X-ray luminosity and the projected size of diffuse radio sources.

The morphological estimators adopted to assess the dynamical state of clusters are very useful to study the time evolution of these latter. Focusing on the offset between the BCG and the X-ray peak, its properties together with the other morphological parameters (c , w and P_3/P_0) could be an important instrument to strengthen the redshift correlations in clusters hosting diffuse radio emission. We present in this thesis a preliminary step that can be further investigated when the offset data for high redshift clusters will be available in the literature. The chapters in this thesis are organized as follows:

- in **Chapter 1** we introduce galaxy clusters, focusing the attention on the observational properties of non-thermal phenomena and in particular on diffuse synchrotron sources (radio halo, relics and minihalos);
- in **Chapter 2** we describe the properties and the scaling relations of the September 2011 updated collections of halos, relics and minihalos. For this purpose we converted all the radio data reported in the literature to the same cosmology and adopted the R_{500} X-ray luminosity when available.
- in **Chapter 3** we present the same properties and scaling relations of Chapter 2 referred to the diffuse emissions discovered between September 2011 and April 2018. At the end of this chapter we highlight the redshift limitations of the knowledge we possess about diffuse radio emission and introduce the possible correlations with z ;

- in **Chapter 4** we present a preliminary study of the correlations existing between the offset BCG–X-ray peak and the other morphological parameters (c , w and P_3/P_0) when considered in clusters hosting diffuse radio emission. These scaling relations when correlated with the redshift could be adopted as proxies to strengthen the correlations: $(P_{1.4GHz}, L_{X,500}, z)$ and $(P_{1.4GHz}, LLS, z)$;
- in **Chapter 5** we present topics and aims of this thesis;
- in **Chapter 6** we present the observing proposal submitted to the JVLA. We describe the 16 individual clusters where diffuse radio emission have been detected and in particular the discovery of 6 new radio halos and 2 radio relics;
- in **Chapter 7** we report the notes on individual clusters where our observations did not detect diffuse emission. We report also the individual clusters where the classification of the radio emission are quite uncertain and requires further investigations;
- **Chapter 8** we summarize our results and conclusions.

Chapter 1

Cluster of galaxies

1.1 Introduction: galaxy clusters overview

Optical observations of the large scale structures of the Universe show that matter, under 100 Mpc scale, is not uniformly distributed. Galaxies tend to clump together forming the largest gravitationally bound objects of the Universe, indicated in literature with the name of *galaxy clusters*.

The tendency of galaxies to form groups and clusters was noticed a long time ago (e.g. Charles Messier in 1754 observing nebular objects in the Virgo constellation), but their systematic study only started in the second half of XX century with the publication of the first *Catalogue of Galaxies and Clusters of Galaxies* by Herzog et al. in 1957, followed a year later by the Abell's famous paper *The distribution of rich clusters* (1958).

Galaxy clusters contain a number of galaxies that ranges between few tens and thousand spread over volumes of about 100 Mpc^3 , trapped in a dark matter potential and embedded in a hot low density intra-cluster medium (ICM) that makes clusters among the most powerful X-ray sources in the sky. Cluster mass is dominated by dark matter ($\sim 80\%$) and only a tiny fraction of it assumes the form of stars in galaxies ($\sim 3 - 5\%$) while the rest ($\sim 15 - 17\%$) is made of diffuse hot gas of ICM. Denser regions form a filamentary structure in the Universe and galaxy clusters form the intersection of these filaments. According to the hierarchical scenario of structure formation, galaxy clusters are assembled from the merger of smaller units (galaxy, groups, and small clusters) under gravitational pull in the course of time. Major cluster mergers are among the most energetic events in the Universe since the Big Bang (e.g. Sarazin 2002).

From observational evidences, merger activities appear to be continuing at

the present time. Mergers drive shocks into the ICM with the subsequent generation of turbulence and explain the relative abundance of substructures and temperature gradients detected in cluster of galaxies by optical and X-ray observations. In particular, new unprecedented insights into merging processes in galaxy clusters are offered by X-ray satellites Chandra and XMM-Newton (e.g. Markevitch & Vikhlinin 2007). X-ray studies are useful to discriminate between pre and post collision phases and give useful information about the features of the intra-cluster medium, in particular in the case of detection of a shock.

Optical data are a powerful way to investigate the presence and the dynamics of cluster mergers too (e.g. Girardi & Biviano 2002). The spatial and kinematical analysis of member galaxies permit to detect and measure the amount of substructures, to identify and investigate possible pre-merging clumps or merger remnants. The optical information is really complementary to X-ray information since galaxies and intra-cluster medium react on different time-scales during a merge.

Galaxy clusters are spectacular systems also in the radio band. Obvious radio sources are the individual galaxies, whose emission has been observed in recent decades with sensitive radio telescopes. On the other end, while baryonic content of galaxy clusters is dominated by the hot intra-cluster gas whose thermal emission is observed in X-rays, in recent years there has been growing evidences for the existence of cluster large-scale diffuse radio sources, of synchrotron origin, which have no optical counterpart and no obvious connection to the cluster galaxies and are therefore associated with the intra-cluster medium (e.g., Ferrari et al. 2008; Feretti et al. 2012). This radio emission represents a striking feature of clusters, since it demonstrates that the thermal ICM plasma is mixed with non thermal components. Diffuse sources are typically observationally grouped as **halos**, **relics** and **mini-halos** according to their size, location in the cluster (center or periphery), polarization properties and the dynamical state of the host cluster (merging or cool core). These systems all require the presence of large-scale magnetic fields and a population of relativistic electrons spread over hundreds of kpc to Mpc scales throughout the cluster volume.

Non-thermal components are important for a comprehensive physical description of the intra-cluster medium in galaxy clusters and play a major role in the evolution of large scale structures in the Universe. Moreover, the discovery of diffuse cluster radio emission represents an important step in the understanding of the physical processes in cluster of galaxies (e.g.

Feretti et al. 2012): diffuse synchrotron sources are sensitive to the turbulence and shock structures of large-scale environment and provide essential complements to studies at other wavebands as well as unique physics not probed by any other wavelength regime.

1.2 The intra-cluster medium (ICM)

When galaxy clusters were observed for the first time in the X-ray band during the *Uhuru* satellite mission (1970-1973), it appeared clear that the space among the galaxies is not empty but filled with a hot X-ray emitting gas. This gas is the main component of the intra-cluster medium, but radio observation demonstrated also the presence of another minority component related to the detection of diffuse radio sources. For this reason, it is useful to make a distinction between *thermal* and *non-thermal* components of ICM.

1.2.1 The thermal component of ICM

To explain the X-ray emission from galaxy clusters, Felten (1996) suggested the presence of a hot diffuse intergalactic gas in thermal equilibrium with the gravitational potential well. This gas is characterized by densities of about $10^{-2} - 10^{-3} \text{ cm}^{-3}$ in the central regions that decreases to 10^{-4} cm^{-3} in the outskirts. It is mainly composed by hydrogen and helium and traces of heavier elements, kept in a ionized state because of the extremely high temperature $T \approx 10^7 - 10^8 \text{ }^\circ\text{K}$ (1-10 keV). High temperature are related to the process of cluster formation when a big fraction of the released gravitational energy was converted into thermal energy by shocks, turbulence and bulk motions that heated the ICM. Under this conditions the gas particles emit in the X-ray band through the thermal bremsstrahlung mechanism. The X-ray luminosity is expressed by:

$$L_X = \int n_e(\mathbf{r})n_{ions}(\mathbf{r})\Lambda[T(\mathbf{r})]d^3\mathbf{r} \quad (1.1)$$

where n_e and n_{ions} are the electron and ion number densities in the ICM and $\Lambda(T)$ is the cooling function. For temperature $k_B T > 2 \text{ keV}$, the ICM is almost fully ionized and $\Lambda(T) \propto T^{-1/2}$. The bremsstrahlung emissivity (i.e. emitted energy per unit time, frequency and volume) at frequency ν

and temperature T of the ICM plasma is:

$$J(\nu, T) \propto Z^2 n_e n_{ions} T^{-1/2} e^{-h\nu/kT} g_{eff}(\nu, T) \quad (1.2)$$

where g_{eff} is the effective Gaunt factor, slowly varying function of temperature and energy, which corrects for quantum mechanical effects and whose value is ≈ 1 . By integrating eq. 1.2 over frequency, the total power per unit volume results:

$$J(T) \propto Z^2 n_e n_{ions} T^{1/2} g_{eff}(T) \quad (1.3)$$

This equation well describes the continuum X-ray emission of clusters with typical temperatures of 2-10 keV (soft X-ray band) but on the top of the spectra it is also possible to observe line emission, the most prominent being the ionized 7 keV iron line (e.g. Werner et al. 2008). The distribution of the intra-cluster gas has been described with a physically consistent isothermal hydrostatic model for the first time in 1976 by Cavaliere and Fusco-Fermiano. In this model, both the galaxies and the gas are assumed to be isothermal, bound to the cluster, and in equilibrium. Their velocity dispersions are not the same and galaxies are assumed to have an isotropic velocity dispersion. The square of the ratio of the galaxy-to-gas velocity dispersion is:

$$\beta \equiv \frac{\mu m_p \sigma}{k T_g} \quad (1.4)$$

where μ is the mean molecular weight, m_p is the mass of the proton, σ_r is the one-dimensional velocity dispersion, and T_g is the gas temperature. Then the gas and galaxy densities vary as:

$$\rho \propto \rho_{gal}^\beta \quad (1.5)$$

If the galaxy distribution is taken to follow a King analytical form, for the isothermal sphere, the gas density distribution results:

$$\rho_g(r) = \rho_0 \left[1 + \left(\frac{r}{r_c} \right)^2 \right]^{-\frac{3}{2}\beta} \quad (1.6)$$

where r is the distance from the cluster X-ray center, r_c is the cluster core radius that identifies the linear size of the central part of the cluster, and ρ_0 is the central thermal gas density. The X-ray surface brightness corresponding

to this thermal gas distribution is:

$$I_X(r) = I_0 \left[1 + \left(\frac{r}{r_c} \right)^2 \right]^{-3\beta + \frac{1}{2}} \quad (1.7)$$

The adoption of this single β model was demonstrated to be inaccurate and also not self-consistent in several cases. When a central excess emission, associated with a cooling flow, is present (i.e. in cool core clusters) and $\beta < 0.5$, the X-ray luminosity is divergent and an arbitrary cut-off radius should also be introduced (e.g. Henry & Henriksen 1986). This approximation leads to the so called β discrepancy (e.g. Bahcall & Lubin 1994). The slope of the gas radial profile described by a single β model is systematically smaller than the required by the equipartition between specific kinetic energy in galaxies and in that gas. Better fits are obtained when a double β model is introduced (e.g., Mohr et al. 1999; Xue & Wu 2000) especially in the description of strong cooling flow clusters. Assuming that the intra-cluster gas has two phases, an inner core phase and an outer core phase, the gas distribution becomes:

$$\rho_g(r) = \rho_{0,inn} \left[1 + \left(\frac{r}{r_{c,inn}} \right)^2 \right]^{-\frac{3}{2}\beta_{inn}} + \rho_{0,out} \left[1 + \left(\frac{r}{r_{c,out}} \right)^2 \right]^{-\frac{3}{2}\beta_{out}} \quad (1.8)$$

where $r_{c,inn}$ and $r_{c,out}$ are the internal and external cluster radii, while $\rho_{0,inn}$ and $\rho_{0,out}$ are the internal and external central gas density respectively.

Even if these parameterizations are widely used in the X-ray astronomy, high resolution observations of clusters with Chandra and XMM-Newton revealed that the ICM is not strictly isothermal. Typically, temperature decreases towards the cluster centers and toward the edges (e.g. Vikhlinin et al. 2006). Moreover, the assumption of hydrostatic equilibrium is not strictly applicable in the case of unrelaxed merging clusters.

1.2.2 The non-thermal component of ICM

When observed in the radio band, galaxy clusters exhibit synchrotron emission from individual radio emitting galaxies. But in some clusters it is also detected a diffuse radio emission not associated with a particular galaxy but related to the ICM. To explain this experimental evidence a suggested hypothesis is that the ICM does not only contain thermal gas but also magnetic fields and relativistic particles (electrons and protons), revealed through non-thermal mechanism and therefore referred to as non-thermal

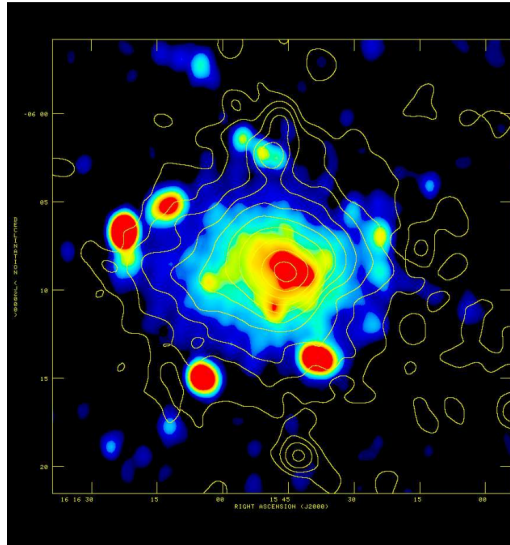


Figure 1.1: Abell 2163: example of halo. Radio contours (green) are overlaid onto the X-ray image.

components of the ICM. The existence of intra-cluster magnetic fields is also probed by Faraday Rotation Measure of radio sources located behind and inside galaxy clusters and enhanced if compared to the field sources (e.g., Clarke et al. 2001; Clarke 2004; Govoni et al. 2001a; Johnston-Hollitt & Ekers 2004) while it is more debated the origin of the relativistic electrons (excess of emission in the hard X-ray band, AGN, merger shocks, dark matter bow shocks, etc.). Thermal and non-thermal components are closely mixed in the ICM and this is supposed to drive physical processes still unknown. Strong correlations have been found between radio properties of diffuse emission and X-ray luminosity, related to the dynamical state of clusters. Diffuse radio sources have common properties such as nature of emission and steep radio spectra but they also show important differences in physical properties: size, position, polarization, morphology and association to other cluster properties (e.g. dynamical state, presence of a cooling flow). In the literature (see e.g. the review Feretti et al. (2012)) they are typically grouped in: *halos*, *relics* and *mini-halos*.

1.2.3 Halos

These diffuse, low surface brightness sources ($\sim 1\mu\text{Jy}/\text{arsec}^2$ at 1.4 GHz), permeate the central regions of galaxy clusters. Their morphology is quite regular, with a brightness distribution generally peaked in the X-ray cluster center and then decreasing towards the cluster outskirts. The linear size

of radio halos ranges from few hundreds of kpc up to 2 Mpc. Spectra are steep ($\alpha \geq 1$, with $S(\nu) \propto \nu^{-\alpha}$) and no polarized flux has been usually detected, if we exclude the discover just in two cases of polarized filaments in A2255 (Govoni et al. 2005; Pizzo et al. 2011) and in MACSJ0717.5+3475 (Bonafede et al. 2009a).

The morphology of radio halos and the X-ray emission of their hosting clusters show strong similarities ((e.g. Govoni et al. 2001b; Feretti et al. 2001). Most of radio halos have been discovered in clusters with high X-ray luminosity ($L_X \simeq 10^{44} - 10^{45}$ erg s $^{-1}$) and intense merger activity (e.g. Buote 2001; Cassano et al. 2011; Rossetti et al. 2011, 2016, 2017). However, not all merging clusters host a radio halo and indeed they are rare phenomena, found only in a fraction of X-ray luminous galaxy clusters. Evidences of the link between cluster merging and radio halos have been outlined in several works confirming the presence of radio halos only in luminous X-ray clusters with substructure, X-ray temperature gradients and weak or absent cooling flow. The first quantitative analysis of the cluster dynamical state was performed by Buote (2001), who obtained the cluster dipole ratio from X-ray images and found that the strongest radio halos appear only in these clusters experiencing the largest departures from a virialized state (see review Feretti et al. 2012). Cassano et al. (2010) confirmed the connection between radio halos and cluster mergers from a quantitative study on a large sample, using Chandra X-ray data and adopting three methods to characterize the cluster dynamical state, i.e. power ratio, the centroid shift and the X-ray brightness concentration parameter (see Chap. 4 for discussion). The link between radio halos and cluster merger is well supported by several findings obtained with improved statistics and confirm the idea that there is a clear separation between relaxed and non-relaxed clusters in the radio behavior. The bi-modality between halo e non-halo clusters (Brunetti et al. 2009) reflects the dichotomy existing in the evolutionary state of clusters between non-relaxed and relaxed clusters. But also the existence of dynamically disturbed clusters with any evidence of radio halo arises intriguing questions. The detection of merging clusters with halos and merging clusters without halos indicate that there is a dichotomy in merging clusters which is not currently understood.

To attempt an answer to this question it is necessary to deeply investigate the nature of the existing strong correlation between radio power at 1.4 GHz and X-ray temperature and luminosity. X-ray luminosity correlates with the mass of the cluster, suggesting a dependence of radio power on the

cluster mass (Govoni et al. 2001b; Feretti 2003). The cluster mass could be indeed a fundamental parameter concerning the formation of these diffuse structures. Giant radio halos are only present above a threshold of mass and temperature, even if radio halos have been observed also in the low X-ray luminosity galaxy clusters A1213 (Giovannini et al. 2009) and 0217+70 (Brown et al. 2011a). The question appears more complex and its answer needs a wider extension of the number of known radio halos (see Chap. 2, 3 and 5).

Halo emission processes

The existence of radio halos probes the presence, in the central regions of the hosting clusters, of magnetic fields and relativistic particles (electrons and protons) mixed with the thermal ICM. The extremely wide dimensions of these sources poses important questions about the origin and properties of these particles. The relativistic particles are injected in the ICM by different sources: shock fronts originated from supernova remnants and during cluster formation processes, radio galaxies, AGN, and galactic winds (Ensslin et al. 1997; Völk & Atoyan 2000; Vazza et al. 2009). After the injection, particles are subject to energy losses. Relativistic protons lose energy because of proton-proton inelastic scattering and Coulomb interaction while energy dissipation of electrons is due to synchrotron emission, inverse Compton scattering with the CMB photons, Coulomb interactions, and bremsstrahlung emission. The lifetime of protons is $\sim 10^{10}$ yr, comparable to the diffusion timescale over the cluster size (Völk et al. 1996; Berezhinsky et al. 1997), and therefore they can be accumulated in the cluster volume. The higher energy loss of the relativistic electrons makes their radiative lifetime shorter than the Hubble time. If the Lorentz factor is $\gamma < 10^8$ the radiative lifetime of a particle is given by (e.g. Longair 1981; Slee et al. 2001):

$$\tau \approx 2 \cdot 10^{12} \gamma_L^{-1} \left[(1+z)^4 + \left(\frac{B}{3.3 \mu G} \right)^2 \right]^{-1} \text{ yr} \quad (1.9)$$

For electrons with $\gamma_L = 10^4$ and emitting synchrotron radiation at 1.4 GHz, the lifetime is $\sim 10^8$ yr. During this timescale their diffusion speed is limited by the Alfvén speed ($\sim 1000 \text{ km s}^{-1}$) and so they can cover distances of about few tens of kpc which are very small if compared with the extended Mpc scale of radio halos (*slow diffusion problem*). In order to explain the

observed long life emission of relativistic electrons a mechanism of *in situ* generation or (re-)acceleration processes has to be considered. Two main classes of models have been proposed to explain the origin of the emitting particles (for review see Brunetti & Jones 2014):

- *Primary models*: ICM turbulence, generated during cluster mergers, stochastically re-accelerates electrons in situ through second-order Fermi mechanism (Petrosian 2001; Brunetti et al. 2004; Brunetti & Lazarian 2007, 2011a; Brunetti & Jones 2014). This models predict the presence of radio halos only in massive merging clusters and not in clusters with low X-ray luminosity. Moreover, a high frequency cut-off in the radio halo spectrum and a radial steepening of the spectral index are also expected;
- *Secondary models*: hadronic collisions between relativistic protons and thermal protons of ICM continuously produce pions (π^0 , π^\pm) whose decay generates secondary electrons, neutrinos and gamma rays (Dennison 1980; Blasi & Colafrancesco 1999; Pfrommer & Enßlin 2004; Enßlin et al. 2011). The decay for the injection of secondary particle is the following (Blasi & Colafrancesco 1999):

$$p + p \longrightarrow \pi^0 + \pi^+ + \pi^- \quad (1.10)$$

$$\pi^0 \longrightarrow \gamma\gamma \quad (1.11)$$

$$\pi^\pm \longrightarrow \mu^\pm + \nu_\mu(\bar{\nu}_\mu) \quad , \quad \mu^\pm \longrightarrow e^\pm + \bar{\nu}_\mu(\nu_\mu) + \nu_e(\bar{\nu}_e) \quad (1.12)$$

This scenario predicts that radio halos should be present in all galaxy clusters. A uniform distribution of radio halo spectral index due to continuous and uniform injection of electrons and a γ -ray and neutrinos emission from the decay of secondary π^0 are also expected.

The hadronic scenario is able to resolve the slow diffusion problem and to explain the morphological connection between radio and X-ray emission in galaxy clusters because the X-ray traces the thermal matter that provides the targets for the hadronic collisions (Brunetti & Jones 2014). But radio halos are rare phenomena and the experimental evidences of steep integrated spectra and the radial steepening of the spectral index of radio halos are not explainable with secondary models. With regard to γ -ray emission, only an upper limit has been derived in galaxy clusters (e.g. Reimer et al. 2003; Aleksić et al. 2010). The minimal flux predicted by hadronic models is under these values and would require high magnetic field strengths.

Nevertheless, more realistic magnetic fields would imply a γ -ray flux above the present upper limit (Brunetti 2009). The turbulence acceleration model assumes that turbulence is generated during cluster mergers and that a fraction of its energy is dissipated into (re-)acceleration of cosmic-ray electrons via Fermi II type mechanism. The in situ (re-)acceleration also solves the slow diffusion problem and explain the complex, spatially varying and very steep spectra of radio halos, providing a close connection between giant radio halos and cluster mergers. But we have to consider that also primary models are not able to give a complete description of the observational properties of radio halos. In fact, the turbulent (re-)acceleration mechanism is poorly efficient and intermittent. The generation of radio halo emission is allowed only just during the most recent ongoing mergers and it is difficult to account for the observed regular morphology of radio halos. The global scenario has become very complex and hybrid models have been recently considered (Brunetti & Blasi 2005; Brunetti & Lazarian 2011a). Since relativistic protons are accumulated in any case in galaxy clusters, it seems more reliable the coexistence of relativistic electrons continuously generated by hadronic collisions and present in all galaxy clusters with a population of relativistic electrons (re-)accelerated through MHD turbulence due to cluster mergers (Cassano 2009). In recent years the radio halo formation processes become even more complex after the discovery of radio halos in low X-ray luminosity clusters.

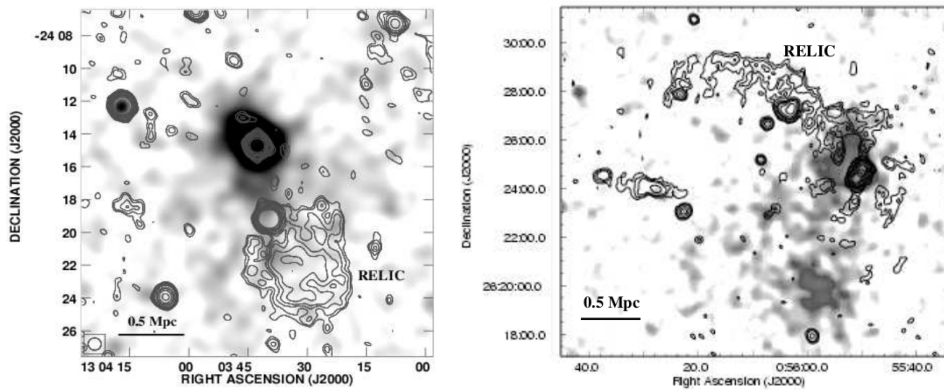


Figure 1.2: *Left panel:* the roundish relic of A1664. *Right panel:* the elongated relic of A115. Radio contours are superimposed to the grey-scale X-ray emissions detected from ROSAT.

1.2.4 Relics

Radio relics are diffuse extended radio sources associated with ICM and characterized by observational properties similar to radio halos but with important differences. Also relics are wide (≈ 1 Mpc) with low surface brightness and steep spectrum but their shape is generally elongated and the location is at the outskirts of the host clusters, usually at the boundary of the X-ray emission. Contrary to radio halos, the emission of radio relics is strongly polarized with typical degree of polarization at 1.4 GHz of 10-30% reaching up to 30-50% in some regions as in the case of A2256 (Clarke & Ensslin 2006a) and CIZA J2242.8+5301 (van Weeren et al. 2010a). A double radio relic system, extending on both sides of the X-ray emission, has been observed in some galaxy clusters as A3667 (Rottgering et al. 1997), A3376 (Bagchi et al. 2006), A2345 (Bonafede et al. 2009b), A1240 (Bonafede et al. 2009c), and MACSJ0025.4-1222 A1240 (Riseley et al. 2017). In about 23 galaxy clusters both a radio relic and a radio halo emission have been detected, connected sometimes by a bridge of diffuse radio emission as for example in A2744 (Govoni et al. 2001a). In 9 clusters a pair of radio relics is associated with a radio halo emission at the center (for an overview see Bonafede et al. (2017); Nuza et al. (2017)). In A2069 (Giovannini 1999) has been found a relic source located at a projected distance of 4.6 Mpc from the center, a huge distance that makes not straightforward its association with the host cluster. The formation of radio relics is still debated. Theoretical models consider different scenarios that can be divided in:

Diffusive shock acceleration

The radio emitting electrons are accelerated up to relativistic energies

directly from thermal ICM. The model identifies two main categories of cosmological shocks: *accretion shocks*, originated from accretion of cold gas, and *merging (or internal) shocks*, due to the merging of substructures. In a full ionized plasma as ICM the power spectrum of the electrons accelerated by the shocks is a power law in energy $N(E) \propto e^{-p}$, where p is related to the shock Mach number \mathcal{M} as follows:

$$p = 2 \frac{\mathcal{M}^2 + 1}{\mathcal{M}^2 - 1} + 1 \quad (1.13)$$

Radio emission spectral index α is a function of p , $\alpha = (p - 1)/2$, and thus also of the Mach number of the shock. Weak shocks during cluster mergers are expected to produce steep spectra which may be consistent with the steep integrated spectra observed in radio relics. In particular, it is expected that the spectral index distribution of radio emission in these sources exhibits a steepening going from the current shock location to the border edge (Enßlin et al. 1998) and that the shock may cause the magnetic field aligned with the shock plane and because of this it causes the high levels of polarization observed in radio relics.

Adiabatic compression

Following this model, radio relics originate from the adiabatic compression of fossil radio plasma as result of the passage of a merger shock (Enßlin & Gopal-Krishna 2001a). This mechanism requires therefore the presence of a radio galaxy in which the central engine of the AGN has ceased to inject fresh relativistic plasma. These sources are able to produce radio emission only at very low frequencies (tens of MHz), not detectable with the current instrumentation, and for this reason they are called *radio ghosts*. When a radio ghost is crossed by a merger shock wave, propagating with a typical velocity of 1000 km s⁻¹, it is adiabatically compressed and not shocked, because of the much higher sound speed within it. Such compression may increase the magnetic field strength and re-energize the electron population in such fossil radio plasma, thus leading a synchrotron emission observable at decimeter wavelengths (Enßlin & Gopal-Krishna 2001b). From this model it is expected that (re-)accelerated electrons produce diffuse radio emission in front of the bow shock and then rapidly lose their energy while moving away from the front, explaining in this way the observed steepening of the spectral index distribution. Moreover,

the compression rate of the shock wave is much higher in the low density peripheral region than in the cluster center and this would explain why radio relics are observed in the cluster outskirts.

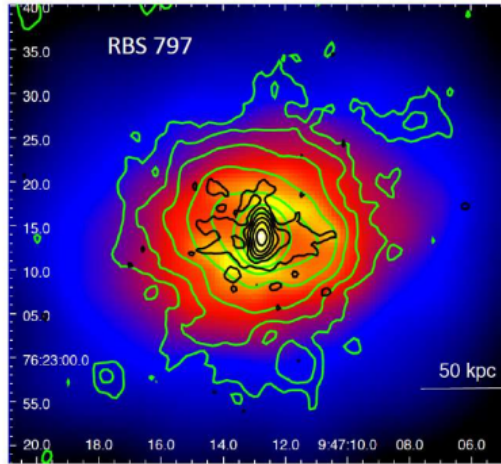


Figure 1.3: Mini-halo MACSJ0947.2+7623 (RBS797): total intensity radio contour overlaid on the CHANDRA X-ray color image.

1.2.5 Mini-halos

A number of relaxed cool-core clusters are known to host centrally located, diffuse radio emission. These sources, called *mini-halos*, have very low surface brightness, quite regular morphology, moderate sizes (few hundred of kpc) and are usually found around radio-loud brightest cluster galaxies (BCG). Because of their size, faint nature and association with a bright radio galaxy, mini-halos are very difficult to detect. The study of mini-halos has been in fact limited by their small number (Gitti et al. 2004; Cassano et al. 2008; Govoni et al. 2009; Giacintucci et al. 2014), with only 10 confirmed in 2011 (Feretti et al. (2012); see Chap. 2 for further discussion). In the last years this number has rapidly increased, with 22 confirmed detections and 6 candidates up to date (Giacintucci et al. 2014; van Weeren et al. 2014a; Kale et al. 2015a,b; Giacintucci et al. 2017).

The new detections confirm and support the association of mini-halos with the most massive and hottest relaxed cool-core clusters (Giacintucci et al. 2014). Anyway, the origin of these radio sources is still unclear. In fact, even if they have active galaxies in their centers, the time needed by the electrons to diffuse from the galaxy across the cooling regions is much longer than the radiative cooling timescale (e.g. Taylor et al. 2002). Thus, also for

explaining mini-halos in situ production and (re-)acceleration of relativistic electrons are required.

Among different possibilities one is inelastic collision between relativistic cosmic-ray protons and thermal protons, which can provide a continuous injection of relativistic electrons ("secondary" or "hadronic" models) (e.g. Pfrommer & Enßlin 2004; Keshet & Loeb 2010; Fujita & Ohira 2013). Alternatively, (re-)acceleration models (Gitti et al. 2002, 2004) consider that the radio synchrotron emission comes from preexisting, cooled relativistic electrons (re-)accelerated to ultra-relativistic energies, via sloshing-driven turbulence, detected using X-ray observations in the cool-core of most relaxed clusters (e.g. Markevitch et al. 2001; Mazzotta et al. 2001, 2003; Ghizzardi et al. 2010).

Throughout this work we adopted a Λ CDM cosmology with $H_0 = 70 \text{ km s}^{-1} \text{ Mpc}^{-1}$, $\Omega_m = 0.3$, and $\Omega_\Lambda = 0.7$ and the convention $S(\nu) \propto \nu^{-\alpha}$. Derived parameter in the literature have been scaled to this cosmology.

Chapter 2

Detections and statistics of diffuse radio emission in galaxy clusters I

2.1 Introduction

In this chapter we summarize the state of the art of the observational properties of the diffuse radio emissions discovered and confirmed up to 2011. This will be the starting point to introduce in the next chapters the contribution to the radio diffuse emission statistics of our observational campaign with the JVLA. The main physical parameters and their link to the X-ray properties of the host clusters are extracted from the review article by Feretti et al. published in 2012.

2.2 Statistical study of the 2011 radio halos population

The number of the discovered radio halos in September 2011 was 42 (Feretti et al. 2012). In Table 2.3 a complete list of these sources is given, inclusive of literature. The statistics is scanty, nevertheless the important features that have been pointed out still represent a very useful reference for the current studies on diffuse emission in clusters of galaxies. In the following sections we summarize some discussions about the statistics of radio halos vs redshift, the relation between their radio power and largest linear scale and the similarities between the X-ray and the radio properties at 1.4 GHz.

2.2.1 Radio Halos and redshift

The redshift distribution of the clusters hosting the September 2011 halo collection, shows an overall average redshift $\langle z \rangle = 0.20$. In particular, among 42 radio halos observed 22 are located at $z < 0.2$, 11 at $0.2 < z < 0.3$, 6 at $0.3 < z < 0.4$, and 3 at $z > 0.4$ (see Fig. 2.1). The most distant is MACSJ0717.5+3745 with $z = 0.545$ (Bonafede et al. 2009c; van Weeren et al. 2009b). The distribution is quite homogeneous up to $z = 0.35$ and it is unequivocally limited to the nearby clusters. Different reasons have been introduced to explain these evidences. At high redshift only the most luminous halos can be observed because of sensitivity limits, while nearby large halos could be missing due to baseline limitations of interferometric surveys (the angular size limit for VLA in 2011 was at 1.4 GHz of $7'$ for snapshot observations like NVSS). For these reasons, at low redshift just the smallest radio halos can be detected, while at high redshift just the brightest one (Giovannini et al. 2009). Anyway, a real lack of high redshift radio halos correlated with the cluster evolution or with strong inverse Compton losses with the CMB cannot be excluded (Feretti et al. 2012).

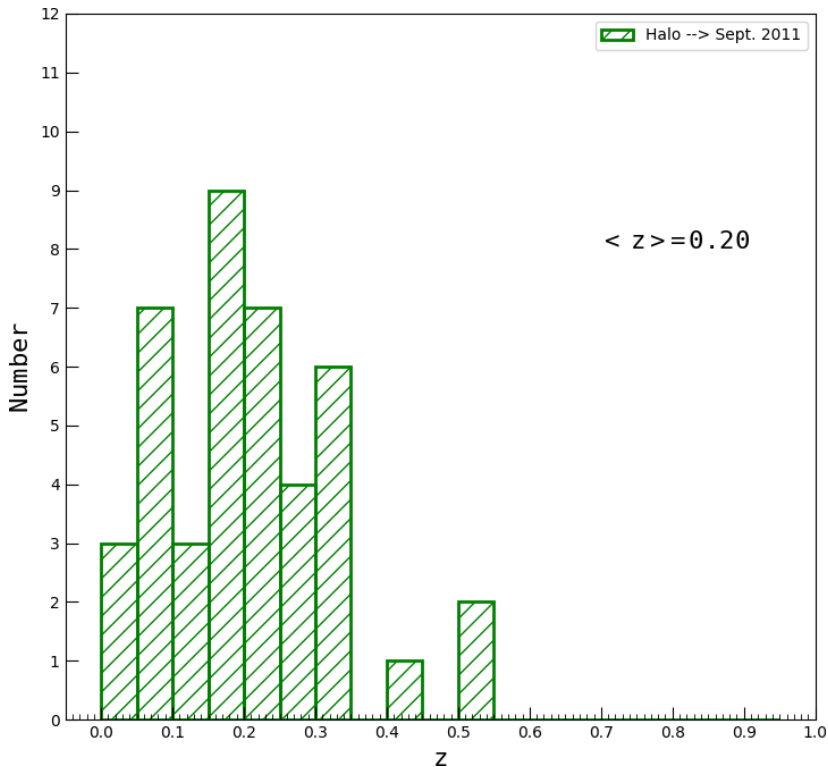


Figure 2.1: Histogram of the redshift distribution of the clusters containing the September 2011 halo collection. Clusters appear to have an average redshift of 0.20 and just three radio halos have been observed at redshift larger than 0.4.

2.2.2 Radio halos power and largest linear size

In the plot of the halo radio power at 1.4 GHz ($P_{1.4GHz}$) vs the largest linear size at 1.4 GHz (LLS) of the September 2011 halo collection, a correlation can be observed (see Fig. 2.2): the most powerful radio halos are, the most they are extended. On average, the radio halo power for the 2011 collection scales as the cube of LLS, as already found by Cassano et al. (2007) and Murgia et al. (2009) using only giant radio halos. In fact, they found a radio halo emissivity quite constant for all radio halos and because the radio power of the source is equal to the product of the radio halo emissivity and the volume, a consequent scaling of the radio power with the volume is expected. Furthermore, the correlation is continuous from small halos up to giant Mpc-scale radio halos and this suggests a common origin and physical mechanism for radio halos of different sizes (Giovannini et al. 2009). In the

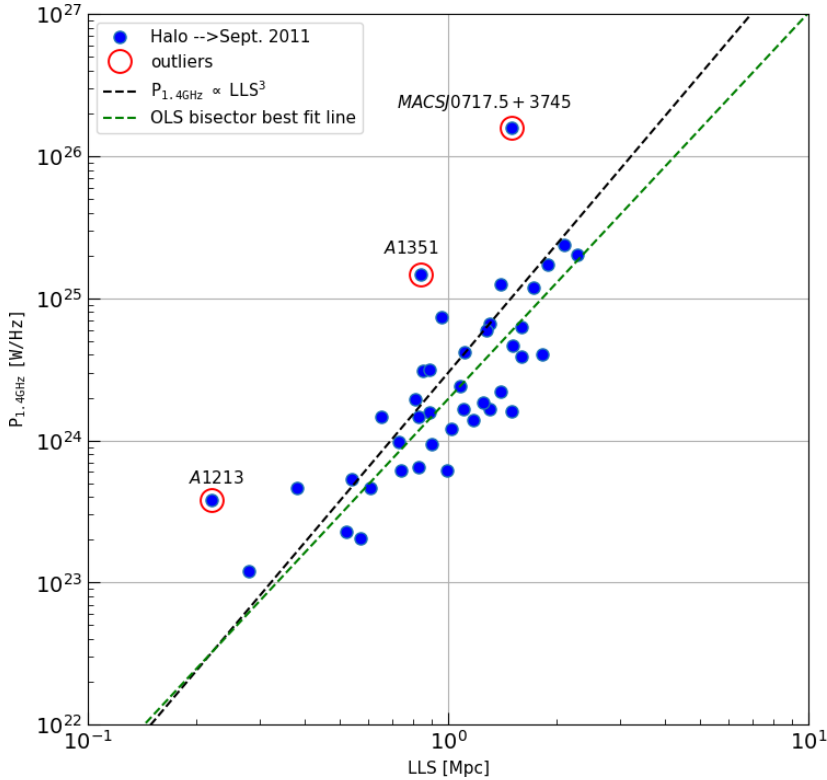


Figure 2.2: Radio Halo power $P_{1.4GHz}$ versus the largest linear size (LLS) at 1.4 GHz of the 2011 updated halo collection. The dashed black line is referred to a radio halo power that scales as LLS^3 . The green dashed line is the OLS best fit line. Outliers are excluded from the fit. Names of outliers are indicated ($H_0 = 70 \text{ km s}^{-1} \text{ Mpc}^{-1}$, $\Omega_m = 0.3$, and $\Omega_\Lambda = 0.7$).

plot there are three outliers, but in general the correlation of radio size vs radio power of this collection shows a small dispersion (Feretti et al. 2012). An interesting analysis of the correlation $P_{1.4GHz}$ vs LLS could be performed

by adopting as physical size of radio halos their e -folding radius r_e , i.e. the radius at which the brightness drops of a factor e^{-1} respect to the central value (Murgia et al. 2009). In this way it is possible to calculate the slope of the correlation using a parameter relatively independent on the sensitivity of the observations, even if detailed and deep observations are available only for a few of halos.

2.2.3 Radio halos power and X-ray properties

Radio and X-ray properties of the clusters hosting radio halos seem to be intimately connected (Liang 2000; Govoni et al. 2001a; Feretti 2003; Cassano et al. 2007, 2011; Giovannini et al. 2009; Venturi 2011). The plot of the logarithm of radio power at 1.4 GHz of the 2011 halo collection vs the logarithm of X-ray luminosity in the 0.1–2.4 keV band is reported in Figure 2.3.

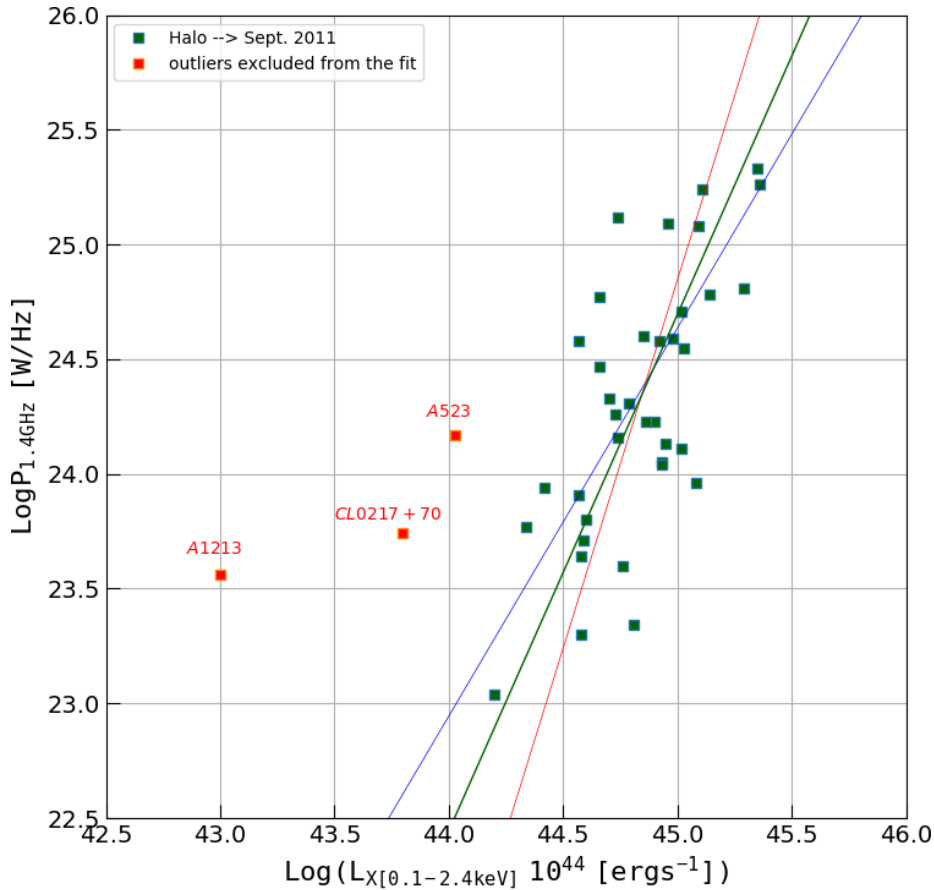


Figure 2.3: The 2011 halo collection in the $P_{1.4GHz}$ vs L_X log-log plane. The OLS best fitting lines are reported with different colours: OLS(Y/X): blue, OLS(X/Y): red, OLS(bisector): green. ($H_0 = 71 \text{ km s}^{-1} \text{ Mpc}^{-1}$, $\Omega_m = 0.27$, and $\Omega_\Lambda = 0.73$). Outliers, not included in the fits, are indicated with red dots.

It is expected to find that $P_{1.4GHz}$ scales as the square of L_X (Feretti et al. 2011). We performed a regression analysis based on OLS estimators, that in case of no measurement errors are simply moment estimators (Akritas & Bershadsky 1996). Because of the different origin of the radio and X-ray data reported in the 2011 updated collection we have not considered the errors of the measured values, using simply estimator moments only. Assuming a linear fit in the form:

$$\log(P_{1.4}) = A \times \log(L_X) + B \quad (2.1)$$

in Tab. 2.1 we report the values of the slope A and the intercept B and their respective variances, calculated applying three regression models: OLS(Y/X), OLS(X/Y), and OLS(bisector).

Table 2.1: Regressions for the correlations $P_{1.4GHz}$ versus L_X .

mode	A	$\sigma(A)$	B	$\sigma(B)$
OLS(Y/X)	1.691	0.251	-51.46	11.25
OLS(X/Y)	3.211	0.469	-119.65	21.05
OLS(bisector)	2.251	0.225	-76.60	10.10

Adopting the OLS(bisector) as the best fit we find $\log(P_{1.4}) = (2.25 \pm 0.23) \times \log(L_X) + (-76.60 \pm 10.10)$ which is in agreement with the expected correlation. The strong correlation (Pearsons $r = 0.726$, $p = 2.55 \times 10^{-6}$) confirms the close link between non-thermal and thermal galaxy clusters physics. It is possible to note that this correlation is not generally applicable to all clusters but is present only between radio halos and parent galaxy clusters: relaxed, cooling clusters should not to be considered for this correlation (Giovannini et al. 2009). This empirical relationship shows that the most powerful radio halos are expected to be detected in the most X-ray luminous clusters, though in the plot there are three clusters of the 2011 halo collection well outside the correlation: A1213 (Giovannini et al. 2009) and CL0217+70 (Brown et al. 2011a) have a lower X-ray luminosity than the expected from the radio power of their halos, while in A523 (Giovannini et al. 2011) is present a radio halo with a power higher than the predicted correlation. These few cases opened new questions about the origin of powerful radio halos associated with clusters characterized by low X-ray luminosity and therefore low density environments: they could be either young halos or related to clusters at a special time of the merger event, when particle processes have a higher efficiency (e.g. Brunetti & Lazarian 2011b).

2.2.4 X-ray luminosity from MCXC catalog

With the purpose to homogenize the X-ray data of cluster collections, in the following chapters we have considered the X-ray luminosity within a R_{500} radius extracted from the MCXC on-line catalog (Piffaretti et al. 2011). R_{500} , i.e. the radius within the mean overdensity of the cluster is 500 times the critical density at the cluster redshift, is chosen as a standard aperture radius since it encloses a substantial fraction of the total virialized mass of the system. The MCXC is a survey that comprises 1743 clusters whose 0.1–2.4 keV band luminosity L_{500} is homogeneously estimated. The bulk of the X-ray data used to construct the MCXC are based on publicly available ROSAT All Sky Survey (RASS)-based (NORAS, REFLEX, BCS, SGP, NEP, MACS, and CIZA) and ROSAT serendipitous (160SD, 400SD, SHARK, WARPS, and EMSS) cluster catalogs (Piffaretti et al. 2011). In Figure 2.4 we report the correlation $\log(P_{1.4GHz})$ vs $\log(L_X)$ (green square dots) and the correlation $\log(P_{1.4GHz})$ vs $\log(L_{X,500})$ (red square dots), the latter with the X-ray data taken from the MCXC catalog and both in the [0.1–2.4] keV band.

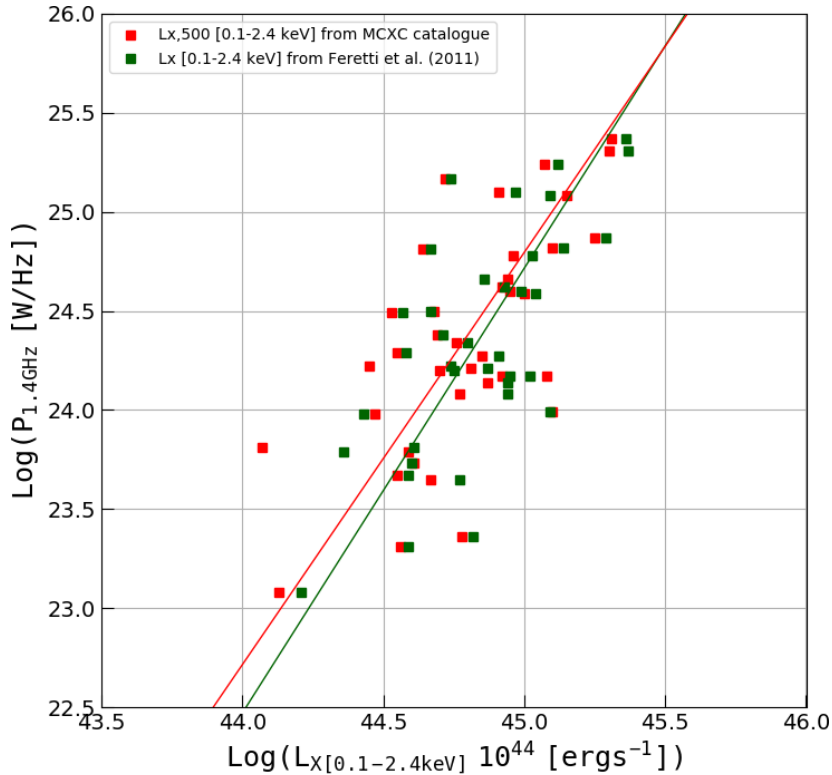


Figure 2.4: 2011 halo collection: $\log(P_{1.4GHz})$ vs $\log(L_X)$ and $\log(L_{X,500})$ in the 0.1 – 2.4 keV band. The OLS(bisector) best fitting lines $\log(P_{1.4}) = A \cdot \log(L_X) + B$ (green) and $\log(P_{1.4}) = A \cdot \log(L_{X,500}) + B$ (red) are shown (See tab. 2.2). Outliers, not reported in the plot, have been excluded from the fits.

The cosmology used in the MXCX catalogue ($H_0 = 70 \text{ km s}^{-1} \text{ Mpc}^{-1}$, $\Omega_m = 0.3$, and $\Omega_\Lambda = 0.7$) is different from the cosmology adopted by Feretti et al. in the 2011 cluster collection ($H_0 = 71 \text{ km s}^{-1} \text{ Mpc}^{-1}$, $\Omega_m = 0.27$, and $\Omega_\Lambda = 0.73$), and so before drawing the plot we needed to rescale both radio and X-ray data of the latter to the Universe of the first. Adopting $S \propto \nu^{-\alpha}$ we calculate the radio power at 1.4 GHz using:

$$P_{1.4GHz} = 4\pi D_L^2 \times S_{1.4GHz} \times (1+z)^{\alpha-1} \quad (2.2)$$

where:

$$D_L = \frac{c(1+z)}{H_0} \int_0^z \frac{dz'}{\sqrt{\Omega_m(1+z')^3 + \Omega_\Lambda}} \quad (2.3)$$

is the luminosity distance of a cluster at redshift z , $S_{1.4GHz}$ is the radio flux at 1.4 GHz, $(1+z)^{\alpha-1}$ is the k -correction as in (Cassano et al. 2013), and α is the spectral index of diffuse radio sources as reported by Feretti et al. (2011). When not present the spectral index is assumed to be 1.3.

To compare the two X-ray luminosity sets of data we performed a regression analysis based on OLS estimators (Akritas & Bershadsky 1996). For the same reason reported in par. 2.2.3, we have not considered the errors of the measured values, using simply estimator moments only. In Tab. 2.2 we report the values of the slope A and the intercept B and their respective variances, calculated applying the OLS(bisector) method. By assuming

Table 2.2: Regressions for the correlations $P_{1.4GHz}$ versus L_X and $L_{X,500}$ in the [0.1 – 2.4] keV band. Radio Power and L_X are rescaled to the same cosmology ($H_0 = 70 \text{ km s}^{-1} \text{ Mpc}^{-1}$, $\Omega_m = 0.3$, and $\Omega_\Lambda = 0.7$)

fit mode	L_X				$L_{X,500}$			
	A	$\sigma(A)$	B	$\sigma(B)$	A_{500}	$\sigma(A_{500})$	B_{500}	$\sigma(B_{500})$
OLS(bisector)	2.245	0.222	-76.31	9.97	2.081	0.248	-68.85	10.10

the bisector regressions whose slope values are the nearest to the expected square power, it is possible to evaluate if the use of $L_{X,500}$ luminosities instead of L_X luminosities introduces significant differences, verifying that:

$$|A^{bisec} - A_{500}^{bisec}| < |\sigma(A^{bisec}) + \sigma(A_{500}^{bisec})| \quad (2.4)$$

we found that the difference between the two slopes is less than the sum of their respective variances i.e. the two sets of data are equivalent.

Table 2.3: September 2011 Halo collection (radio and X-ray data rescaled with MCXC cosmology: $H_0 = 70 \text{ km s}^{-1} \text{ Mpc}^{-1}$, $\Omega_m = 0.3$, and $\Omega_\Lambda = 0.7$)

Cluster Name	z	$S_{1.4GHz}$ mJy	$\text{Log}P_{1.4GHz}$ [W/Hz]	LLS Mpc	$L_X(10^{44})$ erg/s	$L_X^{500}(10^{44})$ erg/s	Other sources	Ref.
A209	0.2060	16.9	24.34	1.40	6.29	5.70	+relic	1
A399	0.0718	16.0	23.31	0.57	3.90	3.59		2
A401	0.0737	17.0	23.36	0.52	6.64	6.09		3
A520	0.1990	34.4	24.62	1.11	8.46	8.31		4
A521	0.2533	5.9	24.14	1.17	8.62	7.45	+relic	1
A523	0.1036	59.0	24.22	1.30	1.10	–		5
A545	0.1540	23.0	24.20	0.89	5.67	5.01		3
A665	0.1819	43.1	24.60	1.82	9.85	8.90		6
A697	0.2820	5.2	24.17	0.65	10.57	11.9		7
A746	0.2320	18.0	24.49	0.85	3.75	3.38	+relic	7
A754	0.0542	86.0	23.79	0.99	2.27	3.85	+relic	3
A773	0.2170	12.7	24.27	1.25	8.10	7.11		4
A781	0.3004	20.5	24.81	1.60	4.67	4.34	+relic	8
A851	0.4069	3.7	24.38	1.08	5.09	4.91		1
A1213	0.0469	72.2	23.58	0.22	0.10	–		1
A1300	0.3072	20.0	24.82	1.30	13.94	12.5	+relic	9
A1351	0.3224	39.6	25.17	0.84	5.55	5.24		1
A1656	0.0231	530.0	23.81	0.83	4.10	1.17	+relic	10
A1689	0.1832	9.9	23.99	0.73	12.25	12.5		11
A1758a	0.2780	16.7	24.66	1.51	7.21	8.80		1
A1914	0.1712	64.0	24.78	1.28	10.64	9.18		3
A1995	0.3186	4.1	24.17	0.83	8.96	8.28		1
A2034	0.1130	13.6	23.67	0.61	3.90	3.51	+relic	1
A2136	0.2030	155.0	25.31	2.28	23.17	20.2	+relic	12
A2218	0.1756	4.7	23.65	0.38	5.89	4.67		6
A2219	0.2256	81.0	25.08	1.72	12.42	14.1		3
A2254	0.1780	33.7	24.50	0.89	4.64	4.79		4
A2255	0.0806	56.0	23.98	0.90	2.71	2.95	+relic	13
A2256	0.0581	103.4	24.29	0.81	3.84	3.54	+relic	14
A2294	0.1780	5.8	23.73	0.54	3.98	4.05		1
A2319	0.0557	153.0	24.08	1.02	8.68	5.94		15
A2744	0.3080	57.1	25.24	1.89	13.05	11.8	+relic	4
A3582	0.0490	20.0	23.08	0.28	1.61	1.35		16
RX J0107.7+5408	0.1066	55	24.22	1.10	5.55	2.80		7
CL0016+16	0.5456	5.5	24.87	0.96	19.71	17.9	+2relics	6
CL0217+70	0.0655	58.6	23.79	0.74	0.65	–		17
1E0657-56	0.2960	78.0	25.37	2.10	22.94	20.4		18
MACSJ0717.5+3745	0.5458	118.0	26.20	1.50	24.60	22.7	+relic	19
RXC J1314.4-2515	0.2439	20.3	24.59	1.60	10.94	9.89		20
RXC J1514.9-1523	0.22	10.0	24.21	1.50	7.34	6.43	+2relics	21
RXC J2003.5-2323	0.3171	35.0	25.10	1.40	9.25	8.16		22
CIZA J2242.8+5301	0.1921	–	–	3.10	6.94	–	+2relics	23

Col.1: Cluster Name; Col.2: Redshift; Col.3: Angular to linear conversion; Col.4: Flux at 20 cm; Col.5: Log of Power at 20 cm; Col.6: Radio largest linear size estimated at 3σ noise level; Col.7: X-ray luminosity from MCXC catalog in the 0.1-2.4 keV band; Col.8: other radio diffuse sources when present; Col.9: References for radio data.

1=Giovannini et al. (2009); 2=Murgia et al. (2010); 3=Bacchi et al. (2003); 4=Govoni et al. (2001a); 5=Giovannini et al. (2011); 6=Giovannini & Feretti (2000); 7=van Weeren et al. (2011d); 8=Govoni et al. (2011); 9=Reid et al. (1999); 10=Kim (1990); 11=Vacca et al. (2011); 12=Feretti et al. (2001); 13=Govoni et al. (2005); 14=Clarke & Ensslin (2006b); 15=Feretti et al. (1997); 16=Venturi et al. (2003); 17=Brown et al. (2011b); 18=Liang (2000); 19=Bonafede et al. (2009a); 20=Feretti et al. (2005); 21=Giacintucci et al. (2011a); 22=Giacintucci et al. (2009); 23=van Weeren et al. (2010b).

2.3 Statistical study of the 2011 radio relics population

As for radio halos, we report in the following sections the properties and the list of the radio relic collection updated to Sept. 2011 with the purpose to introduce also for this kind of diffuse radio objects the next comparison with the more recently updated collection (Chap. 3) and with our JVLA observed sample of galaxy clusters (Chap. 5, 6). Systematic searches for radio relics have been carried out in the last decades e.g. by investigating both X-ray bright Abell-type clusters (Giovannini 1999) in the NRAO VLA Sky Survey (NVSS) (Condon 1999) and Abell clusters accessible to the Westerbork Northern Sky Survey (WENSS) (Kempner & Sarazin 2001a); by searching for steep spectrum sources in the NVSS (van Weeren et al. 2011d) or in the Giant Metrewave Radio Telescope (GMRT) radio survey. In the 2011 updated collection are reported 50 relics hosted in 39 galaxy clusters (Feretti et al. 2012). This collection shows a lot of correlations between relics and cluster properties: some of them include the relation between radio emission and cluster X-ray luminosity or mass, between relic luminosity and largest linear size (LLS). In analogy with radio halos, we start the discussion of these correlations considering the different structures of relics and their distribution with redshift.

2.3.1 Different structures, redshift and projected distance distribution of 2011 radio relics

As discussed in Chap. 1, radio relics are a class of large scale diffuse radio sources generally associated with merging clusters. Observation data is broadly consistent with an interpretation of diffusive shock acceleration. Radio relics are indeed usually aligned perpendicularly to the merger axis towards the outskirts of the cluster. Relics show two types of morphology that are in very good agreement with models predicting that these sources are related to large-scale shocks generated during cluster merger events. Feretti et al. (2011) divided relics in *elongated* and *roundish* (see Fig. 1.2). The elongated relics are more extended, irregular in shape, show the highest level of polarization and are found at peripheral cluster regions. The roundish relics are less extended, more regular in shape and found nearer to the cluster central regions and also the periphery. The interpretation that roundish relics may be elongated relics seen face-on is excluded because of

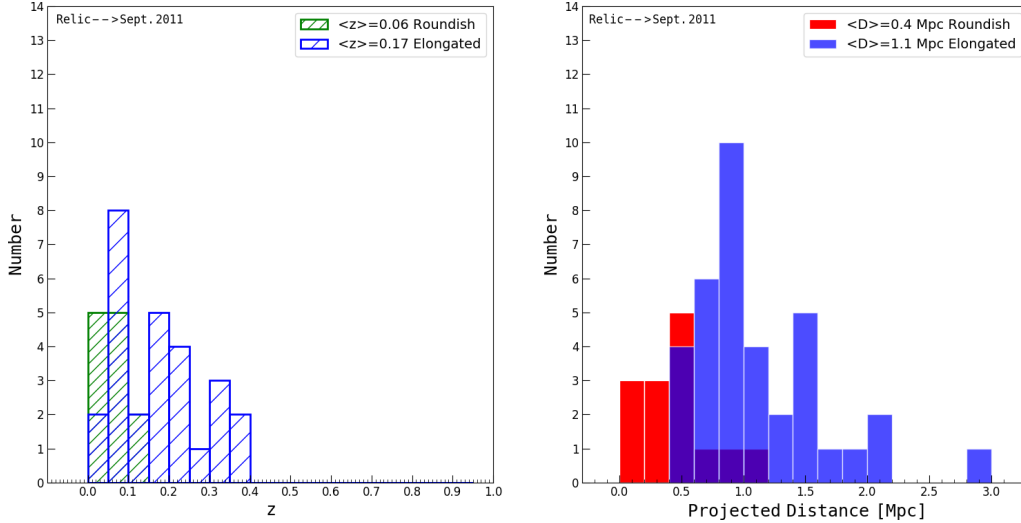


Figure 2.5: *Left panel:* Redshift distribution of the clusters containing the 2011 relic (roundish and elongated) collection. *Right panel:* Distribution of the roundish and elongated relics with their projected distances from the cluster center.

the too high number of relics with elongated shape, inconsistent with simple projection effects (Feretti et al. 2011). In Fig. 2.5 we report the redshift distribution of the clusters hosting the 2011 relic collection, split up in the previous two different morphologies. Among 39 clusters hosting radio relics, 27 host elongated type relics with an average redshift $\langle z \rangle = 0.17$, whereas 12 host roundish type relics and show a $\langle z \rangle = 0.06$. The most distant cluster is PLCKG287.0+32.9 at $z = 0.39$ where a system of double relics is present. In the 2011 updated collection relics have a redshift distribution similar to the redshift distribution of halos and, as well as halos, there is a low detection of high redshift relics due to selection effects and/or to the evolution of cluster mergers or to the inverse Compton losses which became more relevant at increasing redshift (see next chapters for further discussion). In the plot of fig. 2.5 it is possible to notice that roundish relics are peaked at lower redshifts with respect to the total redshift distribution and that no roundish relics at $z > 0.2$ are known. In Fig. 2.5 we reported also the distribution of 2011 relic collection vs. their projected distance from the cluster center. Roundish relics appear more concentrated towards the cluster center with an average distance of ~ 0.4 Mpc, while elongated sources are distributed in a range of distance from 0.5 and 1.5 Mpc, up to 3 Mpc and are located in the cluster outskirts. Vazza et al. (2012) suggested that high Mach number shocks, needed to supply energy to the emitting particles, are only present in cluster peripheral regions.

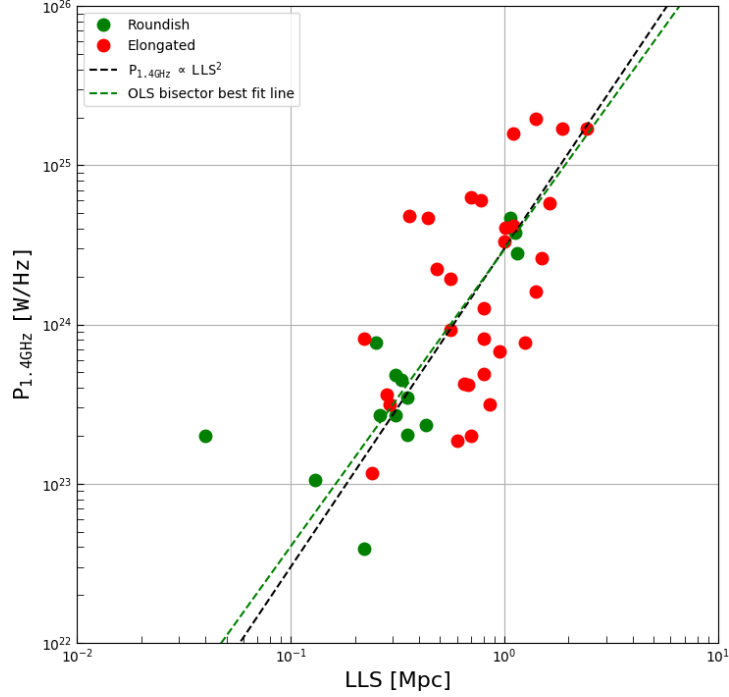


Figure 2.6: Radio power $P_{1.4GHz}$ versus the largest linear size (LLS) at 1.4 GHz of the 2011 updated relic collection. The dashed black line is referred to a radio power that scales as LLS^2 . The green dashed line is the OLS best fit line.

2.3.2 Radio Power of relics vs linear largest size (LLS)

In the plot of radio power at 1.4 GHz vs LLS (Fig. 2.6), elongated relics are on average more powerful and more extended than roundish relics. Relics with low radio power $< 10^{24} \text{ WHz}^{-1}$ are present in both the two kinds of shape but elongated relics have larger size. In analogy with radio halos, also relics the most powerful are the most they are large.

2.3.3 Radio and X-ray connection for radio relics

As with halos, the properties of radio relics are related to the properties of the host clusters. In fact, also for relics a correlation has been measured between the radio power at 1.4 GHz and the cluster X-ray luminosity. The same correlation is present for both the two classes of relics: roundish and elongated. Feretti et al. found for the 2011 relic collection that $P_{1.4GHz}$ scales as $L_X^{1.2}$. Adopting the MCXC catalog X-ray luminosities within R_{500} and introducing the necessary corrections to rescale the 2011 radio data at the MCXC cosmology (see par. 2.2.4) we verify also for radio relics the same scaling relation using $L_{X,500}$ respect to the L_X data reported in Feretti et al. (2012). We show our results in table 2.4 and in Fig. 2.7.

Table 2.4: 2011 Relic Collection. Regressions for the correlations $P_{1.4GHz}$ versus L_X and $L_{X,500}$ in the range 0.1 – 2.4 keV

fit mode	L_X				$L_{X,500}$			
	β	$\sigma(\beta)$	α	$\sigma(\alpha)$	β_{500}	$\sigma(\beta_{500})$	α_{500}	$\sigma(\alpha_{500})$
OLS(bisector)	1.267	0.145	-32.23	6.49	1.350	0.151	-35.87	6.74

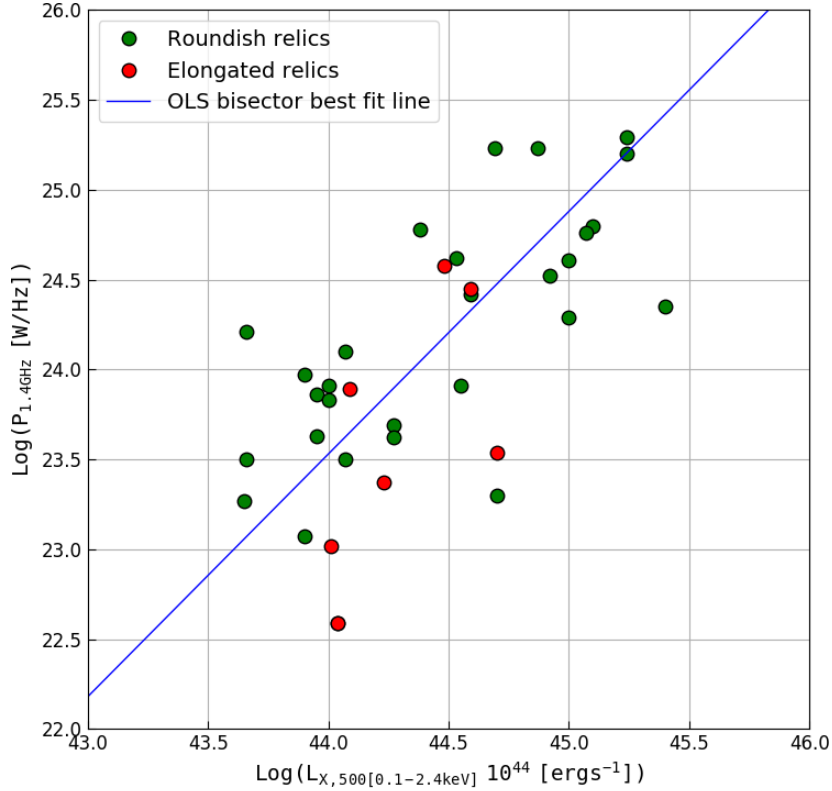


Figure 2.7: 2011 Relic Collection $P_{1.4GHz}$ vs $L_{X,500}$ log-log plane. The OLS(bisector) best fitting line (blue) $\log(P_{1.4}) = (1.35 \pm 0.15) \times \log(L_X) + (-35.87 \pm 6.74)$ is shown. ($H_0 = 70 \text{ km s}^{-1} \text{ Mpc}^{-1}$, $\Omega_m = 0.3$, and $\Omega_\Lambda = 0.7$).

2.3.4 Comparison between halos and relics

The similar behavior of halos and relics is shown in the plot of fig. 2.8: the most powerful sources have comparable values in radio power and cluster X-ray luminosity with similar dispersion. In the region of low X-ray luminosity instead, it is interesting to note that there are few radio halos whereas relics are present in a larger number especially in the region with $P_{1.4} < 10^{24} \text{ WHz}^{-1}$ and $L_X < 3 \times 10^{44} \text{ ergs}^{-1}$. This observational evidence is in agreement with the flatter correlation expected for relics in respect to halos.

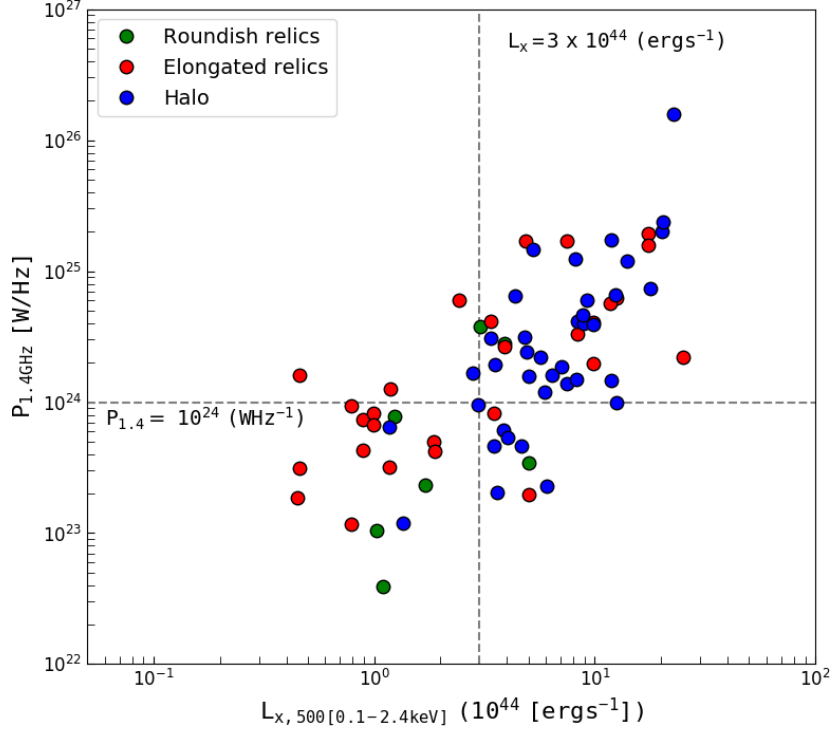


Figure 2.8: Monochromatic radio power of halos and relics (2011 collections) vs the cluster X-ray luminosity. Gray dotted lines divide the plane in four regions: in the bottom left there is the region of low radio power and low X-ray luminosity.

2.4 Statistical study of mini-halos population

The mini-halos classification and recognition is particularly troublesome due to the relatively small angular size in combination with a possibly strong emission of the eventually associated central radio galaxy (BCG). At the time of the review of Feretti et al. (2012) the knowledge of radio mini-halos in cluster cores was based on about only 11 detected objects, which was not sufficient to investigate their origin and answer the question why they are so rare. Anyway also from this scanty scenario it was clear that radio mini-halos are a kind of radio sources different from giant radio halos and also from other kind of steep spectrum radio sources detected in clusters, such as radio bubbles related to AGN activity and dying radio galaxies, sometimes found at the cluster centers. For a long time, clusters hosting mini-halos have been identified with relaxed clusters based on the presence of cool core at their center, even if in four clusters of the 2011 collection thanks to Chandra and XMM-Newton observations signs of minor mergers and/or accretion of small subclumps have been detected (Perseus: Churazov et al. (2004); A2626: Wong et al. (2008); RXJ1347.5-1145: Allen et al. (2002); Gitti et al. (2007); A2390*: Allen et al. (2001). In the previous sections

Table 2.5: September 2011 Relic collection (radio and X-ray data rescaled with MCXC cosmology: $H_0 = 70 \text{ km s}^{-1} \text{ Mpc}^{-1}$, $\Omega_m = 0.3$, and $\Omega_\Lambda = 0.7$)

Cluster Name	z	$S_{1.4GHz}$ mJy	$\text{Log}P_{1.4GHz}$ [W/Hz]	Rcc Mpc	LLS Mpc	$L_X(10^{44})$ erg/s	$L_X^{500}(10^{44})$ erg/s	Shape	Other sources	Ref.
A13	0.0943	31.0	23.89	0.21	0.26	1.21	1.23	rnd		1
A85	0.0551	43.0	23.54	0.46	0.37	4.21	5.01	rnd		1
A115	0.1971	147.0	25.23	1.38	2.54	9.09	7.41	elg		2
A521	0.2533	15.0	24.52	0.96	1.04	8.62	8.32	elg	+halo	3
A548b-NW	0.0424	61.0	23.43	0.44	0.27	0.15	–	rnd		4
A548b-N	0.0424	60.0	23.42	0.52	0.32	0.15	–	rnd		4
A610	0.0954	18.6	23.65	0.32	0.34	–	–	rnd		5
A746	0.232	24.5	24.62	1.62	1.11	3.75	3.39	eln	+halo	6
AS753	0.014	460.0	23.31	0.40	0.35	0.03	0.04	rnd		7
A754	0.0542	69.0	23.69	0.51	0.82	2.27	1.86	elg	+halo	8
A781	0.3004	15.5	24.67	0.67	0.44	4.67	–	elg	+halo	9
A1240-N	0.1590	6.0	23.63	0.72	0.67	1.02	0.89	elg		10
A1240-S	0.1590	10.1	23.86	1.14	1.29	1.02	0.89	elg		10
A1300	0.3072	20.0	24.80	0.81	0.72	13.94	12.59	elg	+halo	11
A1367	0.0220	35.0	22.59	0.61	0.22	0.66	1.10	rnd		12
A1612	0.179	62.8	24.78	0.90	0.79	2.46	2.40	elg		8
A1656	0.0231	260.0	23.50	2.18	0.84	4.10	1.17	elg	+halo	13
A1664	0.1283	107.0	24.67	1.06	1.10	3.16	–	rnd		3
A2034	0.1130	24.0	23.91	0.74	0.22	3.90	3.55	elg	+halo	8
A2048	0.0972	19.0	23.68	0.34	0.32	1.96	–	rnd		14
A2061	0.0784	27.6	23.62	1.58	0.69	4.05	1.86	elg		8
A2063	0.0349	67.0	23.30	0.04	0.04	1.01	–	rnd		15
A2163	0.2030	18.7	24.35	1.21	0.50	23.17	25.11	elg		16
A2255	0.0806	12.0	23.30	0.94	0.73	2.71	5.01	elg	+halo	17
A2256	0.0581	462	24.58	0.46	1.18	3.85	3.02	rnd	+halo	18
A2345-W	0.1765	30.0	24.45	1.04	1.20	6.02	3.89	rnd		19
A2345-E		29.0	24.42	0.93	1.57	6.02	3.89	elg		19
A2443	0.1080	6.5	23.37	0.24	0.45	1.95	1.70	rnd		20
A2744	0.3080	18.2	24.76	1.62	1.68	13.05	11.74	elg	+halo	3
A3365-E	0.0926	42.6	23.97	1.12	0.58	0.88	0.79	elg		6
A3365-W		5.3	23.07	0.52	0.25	0.88	0.79	elg		6
A3376-W	0.0456	166.0	23.91	1.47	0.82	1.11	1.00	elg		21
A3376-E		136.0	23.83	0.52	0.98	1.11	1.00	elg		21
A3667-NW	0.0556	2400.0	25.23	2.15	1.95	4.65	4.90	elg		22
A3667-SE		–	–	1.43	1.36	1.35	–	elg		22
A4038	0.0300	49.0	23.02	0.04	0.14	2.02	1.02	rnd		1
ZwCl0008.8+5215-W	0.1032	11.0	23.50	0.89	0.30	0.51	0.46	elg		23
ZwCl0008.8+5215-E		56.0	24.21	0.89	1.46	0.51	0.46	elg		23
S1081	0.2200	2.4	23.56	2.02	0.28	–	–	elg		24,25
CL0217+70-NW	0.0655	–	–	1.00	0.95	0.65	–	elg		26
CL0217+70-NW		–	–	1.00	0.38	0.65	–	elg		26
CIZA J0649.3+1801	0.064	125	24.10	0.81	0.81	3.45	1.17	elg		6
RXCJ1053.7+5452	0.0704	15.0	23.27	0.99	0.61	3.78	0.45	elg		6
RXCJ1314.4-2515-E	0.2474	10.1	24.29	0.93	0.58	10.94	10.0	elg	+halo	27
RXCJ1314.4-2515-W		20.2	24.61	0.57	1.04	10.94	10.0	elg	+halo	27
CL1446+26	0.3700	9.2	24.68	0.67	0.36	3.46	–	elg		28
CIZA J2242.8+5301-N	0.1921	–	–	1.63	1.77	6.94	–	elg	+halo	29
CIZA J2242.8+5301-S		–	–	1.10	1.51	6.94	–	elg	+halo	29
PLCK G287.0+32.9-N	0.39	33.0	25.29	1.59	1.41	17.40	17.38	elg		30
PLCK G287.0+32.9-S		25.0	25.20	3.02	1.11	17.40	17.38	elg		30

Col. 1: Cluster Name; Col. 2: Redshift; Col. 3: Flux at 20 cm; Col. 4: Log of Power at 20 cm at 1.4 GHz; Col. 5: Distance from the cluster center; Col. 6: Radio largest linear size estimated at 3σ noise level; Col. 7: total X-ray luminosity in the 0.1-2.4 keV band; Col. 8: X-ray luminosity from MCXC catalog; Col. 9: other radio diffuse sources when present; Col. 10: References for radio data.

1=Slee et al. (2001); 2=Govoni et al. (2001a); 3=Giacintucci et al. (2008); 4=Feretti et al. (2006); 5=Giovannini & Feretti (2000); 6=van Weeren et al. (2011a); 7=Subrahmanyam et al. (2003); 8=Bacchi et al. (2003); 9=Govoni et al. (2011); 10=Bonafede et al. (2009c); 11=Reid et al. (1999); 12=Gavazzi & Trinchieri (1983); 13=Giovannini et al. (1991); 14=van Weeren et al. (2011a); 15=Komisarov & Gubanov (1994); 16=Feretti et al. (2001); 17=Feretti et al. (1997); 18=Clarke & Ensslin (2006b); 19=Bonafede et al. (2009c); 20=Cohen & Clarke (2011); 21=Bagchi et al. (2006); 22=Rottgering et al. (1997); 23=van Weeren et al. (2011b); 24=Mao et al. (2010); 25=Middelberg & Bach (2008); 26=Brown et al. (2011a); 27=Feretti et al. (2005); 28=Giovannini et al. (2009); 29=van Weeren et al. (2011c); 30=Bagchi et al. (2011).

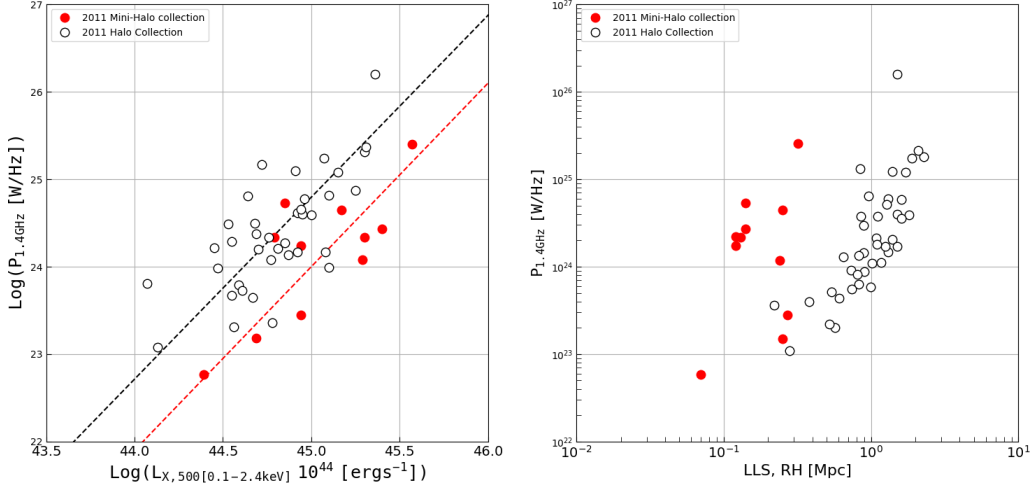


Figure 2.9: *Left panel:* Radio power at 1.4 GHz vs R_{500} X-ray luminosity in the $[0.1 - 2.4]$ keV band. The black dotted line is the best fit correlation for 2011-halo collection, the red dotted line is the best fit correlation for the 2011-mini-halo collection. *Right panel:* Monochromatic radio power at 1.4 GHz of halos and mini-halos vs the radio size (R_H for mini-halos, LLS for radio halos).

for radio halos and relics we have reported some observed correlations that relates thermal and non-thermal properties of the ICM such as radio power at 1.4 GHz, $P_{1.4}$, and X-ray luminosity L_X or $P_{1.4}$ and size (LLS), but the statistical properties of mini-halos were less explored and only a trend between $P_{1.4}$ and the maximum power of the cooling flow (estimated as $P_{CF} = \dot{M}kT/\mu m_p$, Gitti et al. (2004)) has been found for this class of sources. Cassano et al. (2008) showed the distribution of giant radio halos in the $(P_{1.4}, L_X)$ plane together with the mini-halos known at that time. They found that mini-halos share the same region of giant halos and that a possible $P_{1.4} - L_X$ correlation also exists for mini-halos and it is barely consistent with that of radio halos, although, as already underlined in par. 2.2.3, Giovannini et al. (2009) noted that this correlation is not generally applicable to all clusters but is present only between radio halos or relics and parent galaxy clusters: relaxed, cooling clusters should not be considered for this correlation. Applying to the radio data and the X-ray luminosity reported in tab. 2.6 a regression analysis based on the OLS estimators (Y/X, X/Y and bisector), we found $P_{1.4\text{GHz}} \propto L_{X,500}^{(2.10 \pm 0.21)}$ (Pearson correlation coefficient $r = 0.762$, $p = 6.44 \times 10^{-3}$). Cassano et al. (2008) also considered the distribution of mini-halos in the plane $(P_{1.4}, R_H)$ together with a sample of radio halos, finding a trend that is not consistent with what was found for radio halos. We report in fig. 2.9 for the 2011 mini-halo collection the plot of the planes $(P_{1.4}, L_X)$ and $(P_{1.4}, R_H)$ as starting point for further

discussion in the next chapters. The list of the 2011 mini-halo collection, with their main properties is reported in tab. 2.6.

Table 2.6: 2011 Mini-halo collection. Radio data from Giacintucci et al. 2014, $L_{X,500}$ from MXCX on line catalogue (Piffaretti et al. 2011)

Cluster Name	z	$S_{1.4GHz}$ mJy	$\text{Log}P_{1.4GHz}$ [W/Hz]	R_{MH} kpc	$L_X^{500}(10^{44})$ erg/s	Ref.
Perseus	0.0179	3020	24.34	130	6.21	1,2
A1835	0.2532	6.1	24.08	240	19.72	3,4
Ophiuchus	0.0280	83.4	23.18	250	4.94	2,3
A2029	0.0765	19.5	23.45	270	8.73	3,4
A2390*	0.2280	28.3	24.65	250	14.81	4,5
RBS797	0.3540	5.2	24.34	120	20.04	4,7
RXCJ1504.1-0248	0.2153	20.0	24.43	140	24.97	4,8
RXJ1347.5-1145	0.4510	34.1	25.40	320	37.30	5,9
RXJ1720.1+2638	0.1644	72.0	24.73	140	7.07	4
MS1455.0+2232	0.2578	8.5	24.24	120	8.63	4
2A0335+096	0.0363	21.1	22.77	70	2.45	6

Col.1: Cluster Name; Col.2: Redshift; Col.3: Flux at 20 cm; Col.4: Log of Power at 20 cm; Col.5: average radius defined as $R_{MH} = \sqrt{R_{max} \cdot R_{min}}$; Col.6: References to the radio flux density.

1=Sijbring (1993); 2=Ikebe et al. (2002); 3=Govoni et al. (2009); 4=Cavagnolo et al. (2008); 5=Bacchi et al. (2003); 6=Hudson et al. (2010); 7=Gitti et al. (2006); 8=Giacintucci et al. (2011b); 9=Gitti et al. (2007).

*Sommer et al. (2017) identified the diffuse radio emission of A2390 as a radio halo, previously classified by Bacchi et al. (2003) as a minihalo.

Chapter 3

Detections and statistics of diffuse radio emission in galaxy clusters II

3.1 Introduction

In chapter 2 we have seen that until September 2011 only a few dozens of halos, relics and even less mini-halos were discovered. A significant number of these sources have been found thanks to the available radio surveys, such as the NRAO VLA Sky Survey (NVSS) and the VLA Low-Frequency Sky Survey (VLSS) (Giovannini 1999; van Weeren et al. 2009a). However, further searches in a larger sample of galaxy clusters were needed to realize an objective study of the statistics and the occurrence of these diffuse radio sources.

The steep spectrum of radio halos and relics makes them suitable for a search with sensitive, low frequency aperture synthesis instruments such as the Giant Metrewave Radio Telescope (GMRT) and the LOw Frequency ARray Telescope (LOFAR; van Haarlem et al. 2013). They have indeed produced in these last years new surveys of radio sources with a significant increase of the detection of new diffuse radio sources such as the GMRT Radio Halo Survey (GHRS; Venturi et al. 2007, 2008) and its extension (EGRS; Kale et al. 2015a,b) or more recently the LOFAR Two-meter Sky Survey (LoTSS; Shimwell et al. 2017), thanks also to the Planck satellite's discovery of new galaxy clusters through the SZ effect (e.g. The Planck SZ Cluster Catalog - Planck Collaboration et al. 2015). Also the modernization of the VLA radio telescope, built in the 1970s and 1980s, at the end of 2012

with the Expanded VLA (EVLA) project gave and is giving its contribute to increase the statistics of halos, relics and mini-halos (see Chapt. 6 for a general review) as well as the Westerbork Synthesis Radio Telescope (WSRT) with the Deep APERTIF North-Sky Survey (WODAN). In the following sections we report the general properties of the objects (halos, relics and mini-halos) discovered and confirmed between September 2011 and April 2018 and their correlation with the cluster properties. We compare the resulting statistics with that of the 2011 diffuse radio emission collection.

3.2 2018 Halo collection: scaling relations

Using the SAO/NASA Astrophysics Data System (ADS) we searched in the literature by authors, object name, title and abstract words for the new radio halos discovered between September 2011 and April 2018. We found 30 new confirmed halos and 7 candidates (**A1443**: Bonafede et al. (2015); **A1682**: Venturi et al. (2008, 2013); **A2142**, **A2061**, **A2065**, **A2069**: Farnsworth et al. (2013); **A2252**: Kale et al. (2015b)). Their properties, compared with those of the 2011 updated collection, are reported in the next sections and summarized in tab. 3.2.

3.2.1 Redshift distribution

Thanks to the improved sensitivity of the largest high frequency radio telescopes (EVLA, WSRT) and to the radio observations extended also at lower frequencies (GMRT, LOFAR) it has been possible in these last years to increase the detection of radio halos in a larger number of high redshift clusters respect to the 2011 halo collection. In fig. 3.1 is reported the redshift distribution of the halos discovered until April 2018 superimposed to the z-distribution of the 2011 halo collection. We can observe an overall average redshift increased from $\langle z \rangle = 0.20$ to $\langle z \rangle = 0.25$, 11 new halos with $0.35 < z < 0.45$, 3 with $z > 0.5$ and the incredible radio halo of ACT-CLJ102-4915, also known as "El Gordo", detected at $z = 0.87$ (Lindner et al. 2014). Even if the increase of the detection of high redshift halos it's important to prove the existence of this class of radio sources at even high z (see par. 2.2.1 for discussion), nevertheless the statistics is not still sufficiently broad to shed light on their occurrence, on their intrinsic characteristics and in particular on the correlation between the non-thermal cluster properties and the cluster evolution (see sect. 3.5 for discussion).

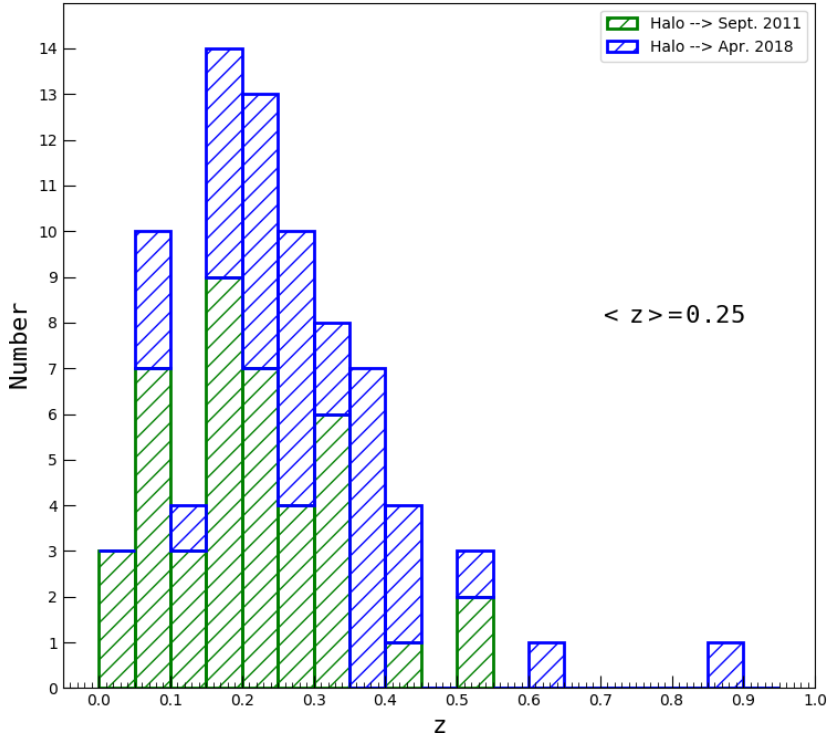


Figure 3.1: Histogram of the redshift distribution of the clusters containing the 2018 halo collection (blue) overlapped to the z distribution of the 2011 halo collection (green). The statistics is significantly increased in the redshift range $0.30 < z < 0.45$

3.2.2 Radio power at 1.4 GHz and LLS

As we discussed in Chap. 2, Cassano et al. (2007) studying the scaling relation between $P_{1.4GHz}$ and radio halo size R_H , defined as $R_H = \sqrt{R_{min} \times R_{max}}$, found $P_{1.4GHz} \propto R_H^{(4.18 \pm 0.68)}$. Ferretti et al. (2012) confirmed for the 2011 halo collection the slope of the correlation using the LLS instead of R_H , but without discussing the possible evolutionary effects with redshift, because of the poor statistics. In fig. 3.2 we report the plot of $P_{1.4GHz}$ vs LLS of 2011 (blue dots) and 2018 (cyan dots) updated collections. Most of the new halos follow the correlation with the oldest collection, even if we observe the presence of almost 3 outliers: A2061, A2069 and A2142 (filled red circles of Fig. 3.2). These three halos appear overly large for their radio luminosity if compared to the other halos. Farnsworth et al. (2013) discussed the complex origin of the diffuse emission of A2061, A2069 and A2142. Their sizes are somewhat dependent upon sensitivity of the 100 m GBT telescope (Green Bank Telescope), which detected them. If the e-folding radius, R_e , is considered, following Murgia et al. (2009) and Vacca et al. (2011), the single structures of these halos are at the high end for

halo size when compared to the sample of Murgia et al. (2009), but not anomalously so (Farnsworth et al. (2013)). It is important to remark that all these outliers radio sources have been classified as candidate radio halos and therefore further observations to fully understand their properties are required. Performing the OLS bisector best fit of the whole halo collection excluding the outliers we found a robust correlation (Pearson $r = 0.743$ and $p = 6.27 \times 10^{-11}$) and a scaling relation $P_{1.4GHz} \propto LLS^{2.82}$ which is in good agreement with Cassano et al. (2007) and Feretti et al. (2012), confirming also for the higher redshift halos that the more extended the more powerful they are.

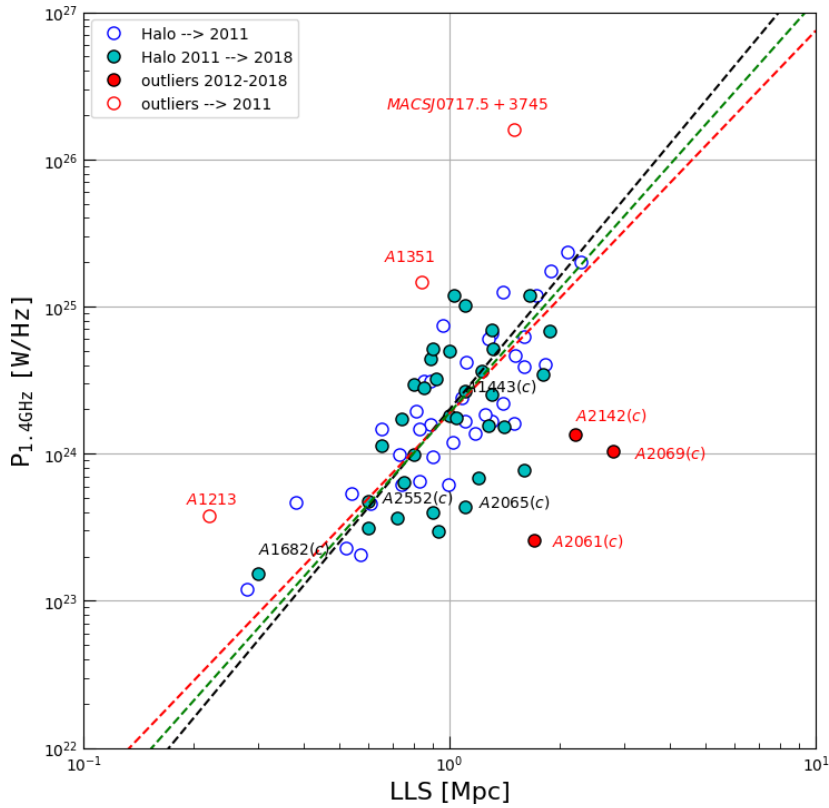


Figure 3.2: Radio Halo power $P_{1.4GHz}$ versus the largest linear size (LLS) of the 2011 halo collection (blue circles) and the 2018 halo collection (cyan dots). Labelled red circles are the outliers of the 2011 relic collection, red dots are the outliers of the 2011-2018 relic collection. The dashed black line is referred to a radio halo power that scales as LLS^3 , the dashed red line is the OLS bisector best fit of the whole halo collection, the dashed green line is the OLS bisector best fit excluding all the outliers (see text) ($H_0 = 70 \text{ km s}^{-1} \text{ Mpc}^{-1}$, $\Omega_m = 0.3$, and $\Omega_\Lambda = 0.7$).

3.2.3 Radio power at 1.4 GHz and $L_{X,500}$

Also the radio halos discovered between 2011 and 2018 confirm that these sources are not ubiquitous in clusters and that the probability to detect a radio halo is higher in the highest X-ray luminous galaxy clusters. Almost the whole objects of the 2011-2018 collection have been detected in clusters with X-ray luminosity above the threshold $L_X \geq 5 \times 10^{44}$ erg s $^{-1}$ in the (0.1 – 2.4) keV band, as in Cassano et al. (2013). Cassano et al. (2013) and more recently Kale et al. (2015a) reported the distribution in the $P_{1.4GHz} - L_{X,500}$ plane of a wide sample of radio halos contained in the GRHS and EGRHS surveys, designed to search for radio halos using GMRT 610/235 MHz observations. They performed a linear fit using the BCES method (Akritas & Bershady 1996):

$$\log(P_{1.4GHz}) = A \log(L_{X,500}) + B \quad (3.1)$$

finding (BCES-bisector) $A = 2.11 \pm 0.20$ (Cassano et al. 2013) and $A = 2.24 \pm 0.28$ (Kale et al. 2015a) respectively. Following the analysis performed in chapter II, we homogenized the radio and X-ray data of the 2018 halo collection scaling them to the same cosmology ($H_0 = 70$ km s $^{-1}$ Mpc $^{-1}$, $\Omega_m = 0.3$, and $\Omega_\Lambda = 0.7$) and considering, when available, the X-ray luminosity within R_{500} of the MCXC on line catalog (Piffaretti et al. 2011). The distribution of the 2011-2018 halo collection in the plane is reported in fig. 3.3. Applying the BCES-bisector method (Akritas & Bershady 1996), we calculated the linear regressions of the radio and X-ray data of the 2011-2018 and of the whole halo collections. The resulting regression parameters are listed in tab. 3.1. We measured also the linear correlation be-

Table 3.1: Halo Collections. Regressions for the correlations $P_{1.4GHz}$ versus $L_{X,500}$ 0.1 – 2.4 keV

fit mode	Halo 2011-2018				Full Collection			
	A	$\sigma(A)$	B	$\sigma(B)$	A_{Full}	$\sigma(A_{Full})$	B_{Full}	$\sigma(B_{Full})$
OLS(bisector)	1.634	0.193	-49.11	8.68	1.865	0.171	-59.33	7.67

tween the $\log P_{1.4}$ and the $\log L_{X,500}$ for both the collections by calculating the parametric Pearson coefficient (r). We found for the 2011-2018 collection: $r = 0.640$ ($p = 6.12 \times 10^{-5}$) and for the whole collection: $r = 0.650$ ($p = 8.26 \times 10^{-10}$). The best fit of the whole collection, consisting of 72 halos, are in agreement with Cassano et al. (2013) and Kale et al. (2015a)

which have performed the linear regressions on a sample of 25 and 33 halos respectively.

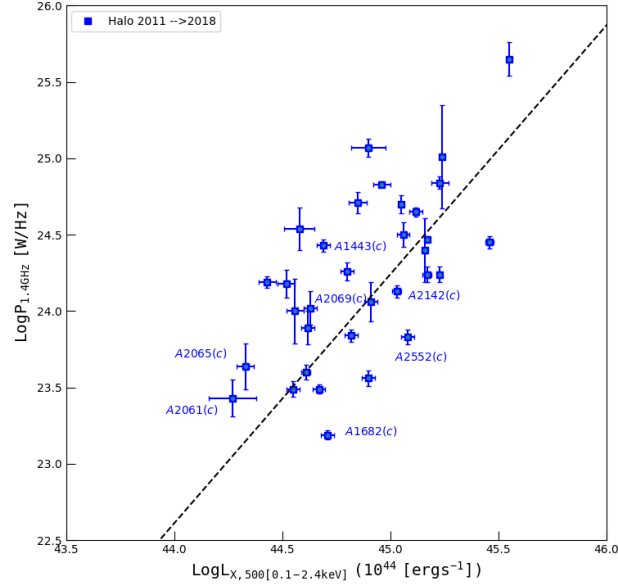


Figure 3.3: Distribution of radio halos discovered between Sept. 2011 and April 2018 in the $P_{1.4GHz} - L_{X,500}$ plane. The best fitting line (dashed) $\log(P_{1.4GHz}) = A \log(L_{X,500}) + B$ with $A=1.63 \pm 0.19$ and $B=-49.11 \pm 8.68$ is shown.

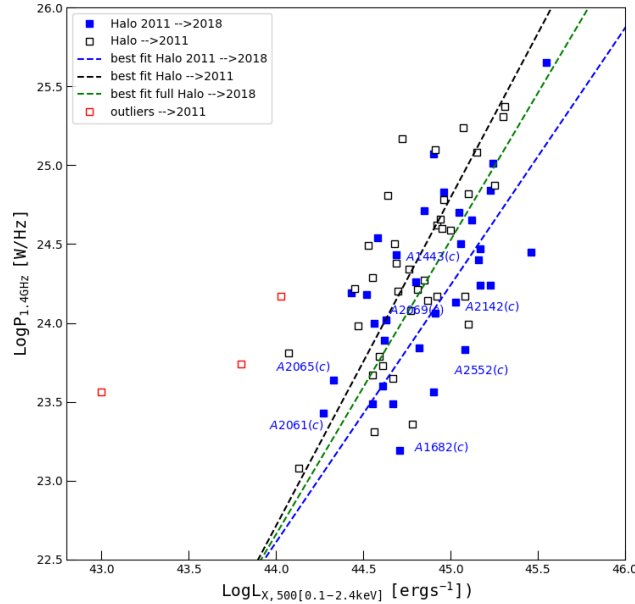


Figure 3.4: Distribution of radio halos discovered up to April 2018 in the $\log P_{1.4GHz} - \log L_{X,500}$ plane. The best fitting lines (dashed) $\log(P_{1.4GHz}) = A \log(L_{X,500}) + B$ are shown: $A=1.63 \pm 0.19$ and $B=-49.11 \pm 8.68$ for the 2011-2018 collection (blue). $A=2.08 \pm 0.25$ and $B=-68.85 \pm 11.10$ for the 2011 collection (black). $A=1.87 \pm 0.17$ and $B=-59.33 \pm 7.67$ for the full collection (green)

Table 3.2: Sept.2011–Apr.2018 Halo collection (radio and X-ray data rescaled with MCXC cosmology: $H_0 = 70 \text{ km s}^{-1} \text{ Mpc}^{-1}$, $\Omega_m = 0.3$, and $\Omega_\Lambda = 0.7$)

Cluster Name	z	$S_{1.4GHz}$ mJy	$\text{Log}P_{1.4GHz}$ [W/Hz]	LLS Mpc	$L_X^{500}(10^{44})$ erg/s	$\alpha_{\nu_1}^{\nu_2}$ [ν_i]=GHz	Other sources	Ref.
A800	0.2223	10.6±0.9	24.19±0.04	1.28	2.72±0.22			1
A1550	0.2540	7.7±1.60	24.18±0.09	1.41	3.32±0.27			1
CL1446+26N	0.370	7.7±2.60	24.56±0.15	1.22				1
A1443(c)	0.27	11±1	24.43±0.04	1.1	4.89±0.39		+relic	2
A1451	0.1994	5.4±0.5	23.81±0.04	0.75	6.61±0.53		+relic	3
A1682(c)	0.2260	0.9±0.3	23.19±0.03	0.3	5.13±0.41	$\alpha_{0.610}^{1.4}=1.6$	+relic	4,5
A1758S	0.2790	3.1±0.7	23.89±0.11	1.6	4.18±0.33	$\alpha_{0.144}^{1.4}=1.1$	+relic	6
A2061(c)	0.0784	16.9±4.2	23.43±0.12	1.70	1.88±0.33	$\alpha_{0.3}^{1.4}=1.8$	+relic	7
A2065(c)	0.0726	33±11	23.64±0.15	1.10	2.12±0.20			7
A2069(c)	0.1160	28.8±7.2	24.00±0.11	2.80	4.26±0.34	$\alpha_{0.3}^{1.4}<1.3$		7
A2142(c)	0.0909	64.0±6.1	24.11±0.04	2.20	10.69±0.50			7
A2552(c)	0.3050	1.5±0.4	23.68±0.11	0.6	10.42±0.83			8
A2261	0.224	4.4±0.35	23.84±0.03	1.2	11.89±0.56	$\alpha_{0.240}^{1.4}=1.2$		9
A2390	0.228	16.8±0.37	24.47±0.02	0.8	14.81±0.50	$\alpha_{1.0}^{2.0}=1.6$		9,17,29
A3411	0.1687	4.8±0.5	23.60±0.05	0.9	4.07±0.14		+relic	10
A3888	0.1510	27.6±0.24	24.26±0.06	0.99	6.38±0.51	$\alpha_{1.4}^{2.4}=1.48$		11
CL1821+643	0.299	14.3±0.7	25.65±0.03	0.89	13.18±1.00	$\alpha_{0.323}^{1.665}=1.0$		12,17
MACSJ0949.8+1708*	0.3826	3.1±0.3	24.24±0.05	1.04	14.90±0.83			13
MACSJ0416.1-2403	0.396	1.75±0.05	24.06±0.13	0.65	8.11±0.50	$\alpha_{0.340}^{1.5}=1.5$		14,31
MACSJ0417.5-1154	0.440	13.0±1.22	25.05±0.04	1.02	29.10±1.50	$\alpha_{0.610}^{1.575}=1.72$		15
MACSJ0553.4-3342*	0.431	9.2±0.7	24.84±0.04	1.3	17.0±1.4			16,17
MACSJ1149.5+2223	0.544	1.2±0.5	24.40±0.18	1.3	14.47±0.27		+2relics	16,17
MACSJ1752.0+4440	0.366	23.3±4.2	25.07±0.06	1.65	8.0±1.4	$\alpha_{0.323}^{1.7}=1.33$	+2relics	16
MACSJ2243.3-0935	0.447	3.1±0.6	24.50±0.08	0.92	11.56±0.67	$\alpha_{kT=8.24}^{1.4}=1.4$	+relic	18
Z5247	0.229	1.9±0.2	23.54±0.05	0.93	3.57±0.24	$\alpha_{0.610}^{1.4}=1.7$		8
Toothbrush	0.225	35.4±1.7	24.83±0.02	1.88	9.12±0.86	$\alpha_{0.074}^{4.9}=1.15$	+3relics	19,17
CIZAJ1938.3+5409	0.26	1.9±0.2	23.56±0.05	0.72	7.96±0.50			13
Sausage	0.192	42.4±9.9	24.54±0.14	1.8	3.77±0.65	$\alpha_{0.145}^{2.3}=1.03$	+4relics	20,17
El gordo	0.870	10.7±2.0	25.65±0.11	1.1	35.50±1.00	$\alpha_{0.610}^{2.1}=1.2$	+3relics	21,17
ACT-CLJ0256.5+0006	0.363	2.1±0.9	23.99±0.21	0.8	3.66±0.36			22
PLCKG147.3-16.6	0.645	2.5±0.4	24.71±0.07	0.9	7.16±0.66			23,32
PLCKG171.9-40.7	0.27	18±2	24.70±0.06	1.0	11.28±0.19			24,28
PLCKG285.0+23.7	0.39	2.94±0.36	24.24±0.05	0.74	16.91±0.27	$\alpha_{0.235}^{1.4}=1.84$		25,28
PLCKG287.0+32.9	0.39	8.8±6.4	25.00±0.34	1.32	17.20±0.11		+2relics	26,28
PSZ1G108.18-11.53	0.335	6.7±0.2	24.45±0.02	0.85		$\alpha_{0.147}^{1.38}=1.40$	+2relic	27
ZwCl0634.1+4750	0.174	3.6±0.2	23.49±0.03	0.60	4.72±0.38			3

Col.1: Cluster Name; Col.2: Redshift; Col.3: Flux at 20 cm; Col.4: Log of Power at 20 cm; Col.5: Radio largest linear size estimated at 3σ noise level; Col.6: X-ray luminosity within R_{500} from MCXC catalog or literature in the 0.1-2.4 keV band; Col. 7 spectral index; Col.8: other radio diffuse sources when present; Col.9: References for radio data and X-ray data when different from Piffaretti et al. 2011. 1=Govoni et al. (2012); 2=Bonafede et al. (2015); 3=Cuciti et al. (2018); 4=Venturi et al. (2011); 5=Venturi et al. (2018); 6=Botteon et al. (2018); 7=Farnsworth et al. (2013); 8=Kale et al. (2015a); 9=Sommer et al. (2017); 10=van Weeren et al. (2013); 11=Shakouri et al. (2016); 12=Bonafede et al. (2014b); 13=Bonafede et al. (2015); 14=Ogorean et al. (2015); 15=Parekh et al. (2017); 16=Bonafede et al. (2012); 17=Yuan et al. (2015); 18=Cantwell et al. (2016); 19=van Weeren et al. (2012); 20=Hoang et al. (2017a); 21=Lindner et al. (2014); 22=Knowles et al. (2016); 23=van Weeren et al. (2014b); 24=Giacintucci et al. (2013); 25=Martinez Aviles et al. (2016); 26=Bonafede et al. (2014a); 27=de Gasperin et al. (2015); 28=Planck Collaboration et al. (2011); 29=Mantz et al. (2010); 30=Cassano et al. (2013); 31=Sayers et al. (2013); 32=Planck Collaboration et al. (2015).

3.3 2018 Relic collection: scaling relations

Our search in the literature found 51 new radio relics (12 have been classified as candidate) discovered between 2011 and 2018 and hosted in 36 clusters: 8 clusters show the presence of a double relic system as MCSJ0025.4-1222 (Riseley et al. 2017), MACSJ1149.5+2223 (Bonafede et al. 2012),

MACSJ1752.0+4440 (Bonafede et al. 2012), CIZA J0107.7+5408 (Randall et al. 2016), PLCKG287.0+32.9 (Bonafede et al. 2014a), PSZ1G096.89+24.17 (de Gasperin et al. 2014), PSZ1G108.18-11.63 (de Gasperin et al. 2015) and ZwCl2341.1+0000 ((de Gasperin et al. 2014), while 3 clusters host a multiple relic system as the "toothbrush cluster" 1RXSJ0603.3+4214 (Van Weeren et al. 2014), the "sausage cluster" CIZA J2242.8+5301 (van Weeren et al. 2010b; Hoang et al. 2017b) and the "El gordo" cluster ACT-CLJ0102-4915 (Lindner et al. 2014). Among them 7 host also a radio halo (MACSJ1149.5+2223, MACSJ1752.0+4440, toothbrush, sausage, el gordo, PLCKG287.0+32.9 and PSZ1G108.18-11.63). In general 20 clusters of the 2011-2018 collection have the simultaneous presence of a halo and at least one relic. A comparison of single, double and multiple-relic plus halo systems allows a simultaneous estimate of the acceleration efficiency during shocks (to produce relics) and turbulence (to produce the halo) as shown by Bonafede et al. (2012). A complete list of the 2011-2018 collection of relics with their main properties is reported at the end of this section (Tab. 3.3)

3.3.1 Redshift and projected distance distribution

In Fig. 3.5 we report the redshift distribution of the clusters hosting the radio relics discovered between 2011 and 2018, divided into roundish (left histogram) and elongated (right histogram) and superimposed to the 2011 relic collection. A significant increase in the number of elongated relics observed at $z > 0.2$ is evident, confirming also for the relics the enhanced capacity of the biggest radio telescopes to detect these diffuse radio sources beyond the nearby clusters ($z < 0.2 - 0.3$). 11 relics have been discovered in 5 clusters with $z > 0.4$ (MCSJ0025.4-1222, MACSJ0717.5+3745, MACSJ1149.5+2223, MACSJ2243.3-0935, el gordo, PLCKG004.5-19.5). El Gordo is the highest redshift ($z = 0.870$) radio halo/relic cluster known, thereby providing important constraints on the non-thermal emission of a cluster merger at high redshift (Lindner et al. 2014).

In fig. 3.6 we report the distribution of the elongated and roundish relics of the 2011-2018 collection with their projected distance from the cluster centre. Compared to the 2011 relic collection, in the 2011-2018 collection the roundish relics show a greater average projected distance that seems to be related a to greater LLS (see Fig. 3.7) but not with redshift. These relics have an average LLS \sim 1.2 Mpc while the average LLS of the

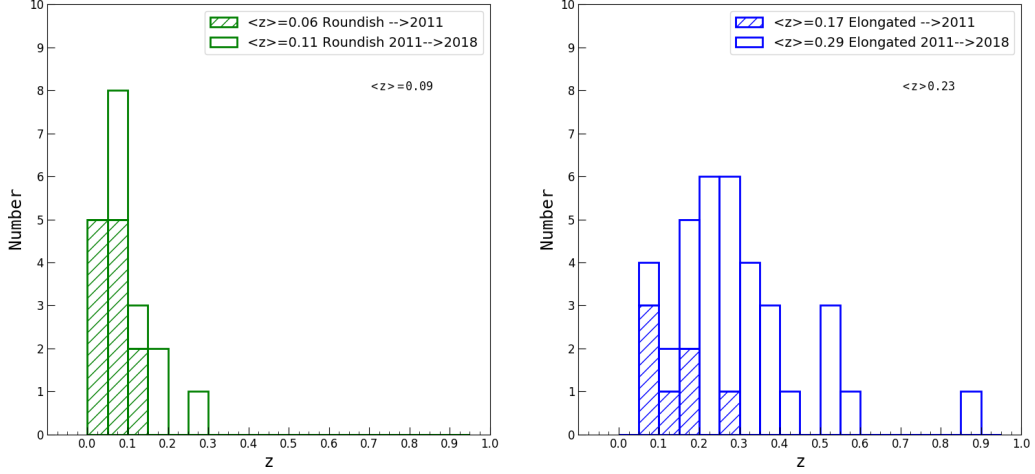


Figure 3.5: *Left panel:* Histogram of the redshift distribution of the clusters containing the roundish relics of the 2011–2018 and 2011 collections. *Right panel:* Histogram of the redshift distribution of the clusters containing the elongated relics of the 2011–2018 and 2011 collections.

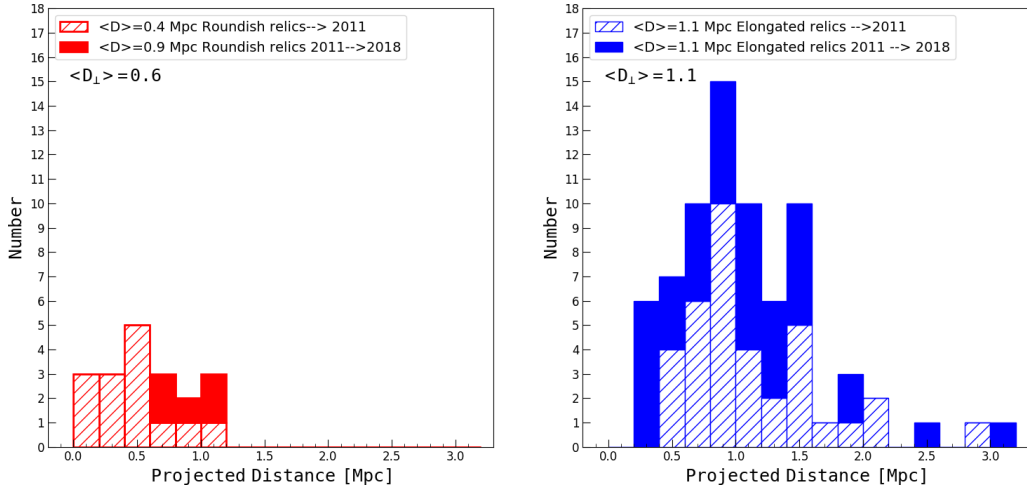


Figure 3.6: *Left panel:* Histogram of the projected distance distribution of roundish relics, both 2011 and 2011-2018 collections. *Right panel:* Histogram of the projected distance distribution of elongated relics, both 2011 and 2011-2018 collections.

14 roundish relics of the 2011 collection is ~ 0.45 . About the 2011-2018 elongated relics their average projected distance is equal to the average projected distance of the 2011 elongated relics. Among the 6 relics with D_{\perp} between 0.2 and 0.4 Mpc there are 2 relics with the smallest distances from the centre: MACSJ0025.4-1222 with $D_{\perp} = 0.192$ Mpc (Riseley et al. 2017) and MACSJ0717.5+3745 with $D_{\perp} = 0.260$ Mpc Bonafede et al. (2009a). The first relic shows the typical arc-like morphology and it's located at the NW periphery of the X-ray emission with a cluster core radius $r_c \sim 0.442$ Mpc while the second has a filamentary morphology, embedded by a complex

radio emission consisting in a giant radio halo and several radio galaxies, located at the cluster periphery but appearing closer to the cluster centre when viewed in projection. Bonafede et al. (2009a) argued that the bright radio emission previously classified as relic is more likely a bright, polarized filament connected with the radio halo. More recently Nuza et al. (2017) have introduced a new class of diffuse objects calling it "*radio gischlet*" to indicate radio sources not located at the cluster outskirts and without several aspects of the standard relic classification, including among them also MACSJ0717.5+3745. In our statistical analysis we decided to include also the gischlet so as to consider the widest variability of the diffuse radio sources different from the radio halos. In A1451 it has been recently discovered by Cuciti et al. (2018) a candidate radio relic with a projected distance of ~ 3 Mpc associated to an accretion/external shocks, that if confirmed, would be the most distant relic from the cluster centre ever detected.

3.3.2 Radio power of relics vs linear largest size (LLS)

When plotted in the ($P_{1.4GHz}$, LLS) plane the roundish and elongated relics of the 2011-2018 collection shows a similar correlation if compared to the 2011 relic collection (see Fig. 3.7). The roundish relics hosted in A2073 (Farnsworth et al. 2013) and in A3411 van Weeren et al. (2013) have the largest dimensions between the roundish objects of the two collections with LLS of 2.5 and 1.9 Mpc respectively. In particular the relic of A2073 seems to be under-luminous for its size, but it is reported as a candidate radio relics and further investigation and observation are therefore necessary. The structure of the relic in A3411 is quite complex with a morphology broken up into five fragments whose shape appears generally roundish but anyway in good agreement with the correlation $P_{1.4GHz}$ vs LLS.

About elongated relics we can see that in the 2011-2018 collection the number of diffuse sources with large dimensions and radio power has increased. We can note in particular that three relics have a greater radio power and lower LLS respect to the correlation: MACSJ0717.5+3745 (Bonafede et al. 2009a; Nuza et al. 2017), PLCKG004.5-19.5 (Sifón et al. 2014) and "El Gordo" ACT-CLJ0102-4915-NW (Lindner et al. 2014). As discussed in the previous subsection (3.3.1) MACSJ0717 is characterized by a highly complex radio emission with the relic-filament strictly connected to one of the most powerful radio halo ever detected, that could be justify its outlier position in the ($P_{1.4GHz}$, LLS) plane. The measure of the spectral index from

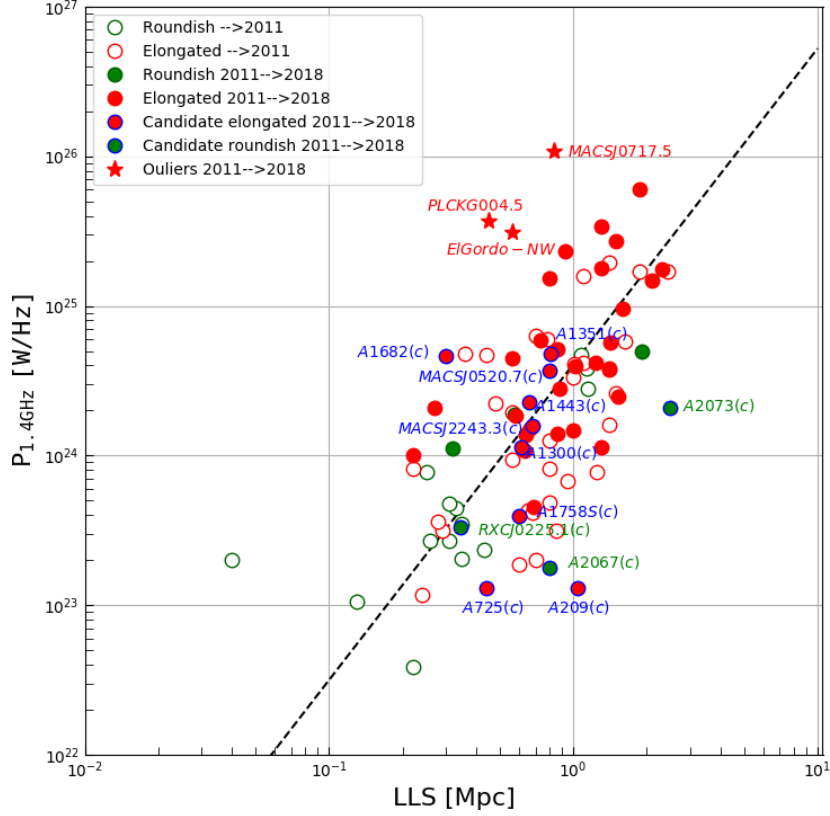


Figure 3.7: Radio power at 1.4 GHz vs the largest linear size (LLS) of the roundish and elongated relics of the 2011 and 2011-2018 collections. The dashed black lines is referred to a radio relic power that scales as $LLS^{2.11}$ (see text). Names of the candidate relics of the 2011-2018 collection are reported. Red labels are referred to particular objects (see text).

three frequencies (150 MHz, 843 MHz and 1.4 GHz) in PLCKG004.5-19.5, suggests that the radio emission at 843 MHz and/or 1.4 GHz may be contaminated by unresolved point sources, thus boosting the flux and lowering α (Sifón et al. 2014). This would explain a high radio power in a ~ 500 kpc dimension scale. Finally, the internal structure of the NW relic in "El Gordo", the highest redshift cluster ever known, is complex with unresolved structures that could explain together with the relatively flat spectral index the outer position respect to the correlation.

Performing the OLS bisector best fit regression on the whole relic collection we found $P_{1.4GHz} \propto LLS^{(2.11 \pm 0.21)}$ (Pearson $r = 0.579$; $p = 1.43 \times 10^{-9}$), in good agreement with the scaling relations reported in the literature.

3.3.3 Radio and X-ray connection

The scaling relation between radio power $P_{1.4}$ and the $L_{X,500}$ of galaxy clusters hosting the 2011-2018 relic collection appears consistent with the scaling

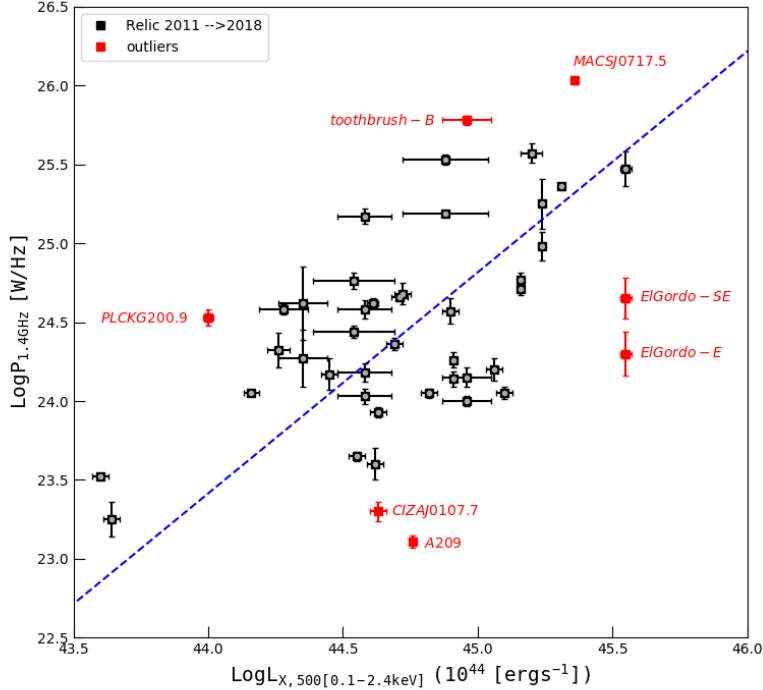


Figure 3.8: 2011-2018 relic collection: radio power at 1.4 GHz vs $L_{X,500}$. The BCES-bisector best fitting line (blue dashed) is shown. In red are reported the relics with the greatest dispersion from the fitting line.

relation of the 2011 relic collection, though the data of the first results more scattered around the fitted line. We checked the correlation of both these data sets by calculating the Spearman rank-order correlation coefficient ρ and the Pearson's correlation coefficient r . We found for the 2011 collection $\rho = 0.66$ and $r = 0.68$ and for the 2011–2018 collection $\rho = 0.45$ and $r = 0.52$. Yuan et al. (2015) estimated the scaling relations of a sample of 25 galaxy clusters with relic and found a ρ value of ~ 0.6 . The correlation results marginal and seems to be confirmed also with the relic collections considered in this thesis.

Performing a BCES-bisector regression analysis we found for the 2011-2018 collection the following best fit relation: $\log(P_{1.4}) = (1.39 \pm 0.16) \times \log(L_{X,500}) + (-38.18 \pm 7.16)$ which is in good agreement with the 2011 relic collection best fit (see section 2.3.3). In Fig. 3.8 we report the 2011-2018 relic collection in the log-log ($P_{1.4}$, $L_{X,500}$) plane and the best fit line. Finally, we report in Fig. 3.9 the $P_{1.4}$ vs $L_{X,500}$ correlations for both the collections and their respective best fitting lines, obtained following Akri-

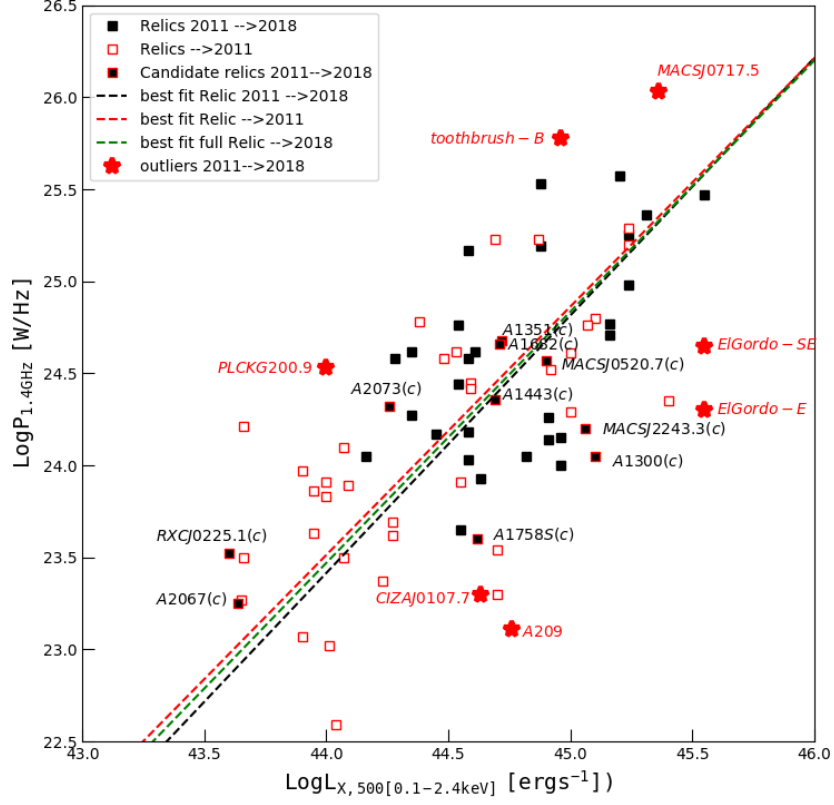


Figure 3.9: Distribution of radio relic discovered up to April 2018 in the $(P_{1.4}, L_{X,500})$ in the log-log plane. $\log(P_{1.4GHz}) = A \log(L_{X,500}) + B$ are shown. $A=1.39 \pm 0.17$ and $B=-38.18 \pm 7.16$ for the 2011-2018 collection (black). $A=1.35 \pm 0.15$ and $B=-35.87 \pm 6.38$ for the 2011 collection (red). $A=1.37 \pm 0.11$ and $B=-36.60 \pm 4.84$ for the full collection (green). ($H_0 = 70 \text{ km s}^{-1} \text{ Mpc}^{-1}$, $\Omega_m = 0.3$, and $\Omega_\Lambda = 0.7$)

tas & Bershadsky (1996). The names of the candidate relics discovered in the 2011-2018 collection are also reported. With the exception of A209, excluded from the fits, the other relic candidates follow the correlation.

Table 3.3: Sept.2011–Apr.2018 Relic collection (radio and X-ray data rescaled with MCXC cosmology: $H_0 = 70 \text{ km s}^{-1} \text{ Mpc}^{-1}$, $\Omega_m = 0.3$, and $\Omega_\Lambda = 0.7$)

Cluster Name	z	$S_{1.4GHz}$ mJy	$\text{Log}P_{1.4GHz}$ [W/Hz]	Rcc Mpc	LLS Mpc	$L_X^{500}(\times 10^{44})$ erg/s	Shape	$\alpha_{\nu_1}^{\nu_2}$ [ν_i]=GHz	Other sources	Ref.
A133	0.056	136.75±0.16	24.05±0.01		0.320	1.46±0.09	rnd	$\alpha_{0.330}^{1.4}=2.11$		1
A209(c)	0.206	1.0±0.1	23.11±0.04	1.1	1.04	5.70±0.13	el		Ha	2
A725(c)	0.0904	6.0±1.0	23.12±0.09	0.31	0.44		el	$\alpha_{0.327}^{1.4}=1.73$		1
A910	0.2055	12.1±2.9	24.17±0.10	0.45	1.0	2.81±0.22	el			4
CL1446+26S	0.370	5.3±1.2	24.40±0.10	1.0	1.53		el			4
A1300(c)	0.3075	3.4±0.3	24.05±0.04	0.5	0.61	12.46±0.99	el	$\alpha_{0.325}^{0.625}=1.17$	Ha+1Re	5
A1351(c)	0.322	13.0±2.2	24.68±0.07	0.71	0.81	5.24±0.34	el		Ha	2
A1443(c)	0.27	9.8±1.0	24.36±0.04	0.70	0.66	4.89±0.39	el		Ha	6
A1451	0.199	9.8±0.4	24.05±0.03	~3	1.3	6.61±0.53	el	$\alpha_{0.320}^{1.5}=1.1$	Ha	7
A1682(c)	0.226	26.9±1.3	24.66±0.02		0.3	5.13±0.41	el		Ha	8,9
A1758S(c)	0.297	1.5±0.3	23.60±0.10	1.2	0.60	4.18±0.33	el	$\alpha_{0.144}^{1.4}=1.3$	Ha	10
A2067(c)	0.0739	12.4±3.1	23.25±0.11	1.01	0.80	0.44±0.04	rnd			11
A2073(c)	0.1717	21.7±5.4	24.32±0.11	0.70	2.5	1.82±0.15	rnd			11
A3411	0.1687	53±3	24.61±0.03	1.3	1.9	4.07±0.15	rnd	$\alpha_{0.074}^{1.4}=1.0$	Ha	12
A3527bis	0.20	35±2	24.58±0.03	1.3	1.4	1.9±0.4	el	$\alpha_{0.323}^{1.4}=0.70$		13
RXCJ0225.1-2928(c)	0.0604	37.0±0.9	23.52±0.01	1.0	0.35	0.40±0.03	rnd			14
MACSJ0025.4-1222-NW*	0.5857	0.79±0.09	24.11±0.05	0.19	0.64	8.04±0.20	el			15
MACSJ0025.4-1222-SE*	0.5857	1.06±0.12	24.24±0.05	0.32	0.58	8.04±0.20	el			15
MACSJ0520.7-1328-D1*(c)	0.3360	9.0±1.6	24.56±0.08	~2	0.80	7.90±0.63	el			16
MACSJ0717.5+3745	0.5458	80±12	26.03±0.02	0.26	0.83	22.7±0.3	el	$\alpha_{1.365}^{4.885}=1.3$	Ha	17
MACSJ1149.5+2223-W	0.544	5.6±0.3	24.77±0.04	1.10	0.73	14.47±0.27	el	$\alpha_{0.323}^{1.4}=0.75$	Ha+1Re	18
MACSJ1149.5+2223-E	0.544	4.1±0.2	24.71±0.04	1.38	0.86	14.47±0.27	el	$\alpha_{0.323}^{1.4}=1.15$	Ha+1Re	18
MACSJ1752.0+4440-NE	0.366	69.6±3.0	25.53±0.03	1.13	1.30	7.6±2.8	el	$\alpha_{0.323}^{1.7}=1.21$	Ha+1Re	18,32
MACSJ1752.0+4440-SW	0.366	32.3±0.8	25.19±0.02	0.91	0.80	7.6±2.8	el	$\alpha_{0.323}^{1.7}=1.12$	Ha+1Re	18,32
MACSJ2243.3-0935-W(c)	0.447	2.1±0.3	24.20±0.07	2.13	0.68	11.56±0.67	el		Ha	19
Z5247	0.229	3.1±0.2	23.65±0.03	1.3	0.69	3.57±0.24	el	$\alpha_{0.610}^{1.4}=1.3$	Ha	20
Toothbrush-B	0.225	315.0±20.6	25.78±0.03		1.87	9.12±1.89	el	$\alpha_{0.074}^{4.9}=1.10$	Ha+2Re	21,32
Toothbrush-D	0.225	5.30±0.31	24.00±0.03		0.22	9.12±1.8	el	$\alpha_{0.074}^{4.9}=1.10$	Ha+2Re	21,32
Toothbrush-E	0.225	9.36±0.98	24.15±0.06		0.86	9.12±1.8	el	$\alpha_{0.074}^{4.9}=1.0$	Ha+2Re	21,32

Table 3.4: Sept.2011–Apr.2018 Relic collection (radio and X-ray data rescaled with MCXC cosmology: $H_0 = 70 \text{ km s}^{-1} \text{ Mpc}^{-1}$, $\Omega_m = 0.3$, and $\Omega_\Lambda = 0.7$)

Cluster Name	z	$S_{1.4GHz}$ mJy	$\text{Log}P_{1.4GHz}$ [W/Hz]	Rcc Mpc	LLS Mpc	$L_X^{500}(\times 10^{44})$ erg/s	Shape	$\alpha_{\nu_i}^{\nu_1^2}$ [ν_i]=GHz	Other sources	Ref.
CIZAJ0107.7+5408-NW	0.1066	29.0±1.9	23.93±0.03			4.24±0.34	el			22
CIZAJ0107.7+5408-SE	0.1066	6.8±0.9	23.30±0.06			4.24±0.34	rnd			22
Sausage-N	0.192	138±14	25.17±0.05	1.5	2.1	3.77±0.87	el	$\alpha_{0.145}^{2.3}=1.11$		23,32
Sausage-S	0.192	33±4	24.58±0.06	1.5	1.4	3.77±0.87	el	$\alpha_{0.145}^{2.3}=1.41$	Ha+3Re	23,32
Sausage-E1	0.192	9.8±1.0	24.03±0.05	1.5	0.63	3.77±0.87	el	$\alpha_{0.145}^{2.3}=1.18$	Ha+3Re	23,32
Sausage-E2	0.192	14.8±2.0	24.18±0.06	1.5	0.67	3.77±0.87	el	$\alpha_{0.145}^{2.3}=0.91$	Ha+3Re	23,32
El Gordo-NW	0.870	7.1±1.3	25.47±0.11	0.9	0.56	35.5±1.6	el	$\alpha_{0.610}^{2.1}=1.19$	Ha+3Re	24,32
El Gordo-E	0.870	0.6±0.1	24.30±0.14	0.5	0.27	35.5±1.6	el	$\alpha_{0.610}^{2.1}=0.9$	Ha+2Re	24,32
El Gordo-SE	0.870	0.9±0.2	24.65±0.13	0.8	0.19	35.5±1.6	el	$\alpha_{0.610}^{2.1}=1.4$	Ha+2Re	24,32
Bullet	0.296	56.4±2.3	25.36±0.02	0.75	0.93	20.43±0.47	el	$\alpha_{1.1}^{3.1}=1.37$	Ha+2Re	25
PLCKG004.5-19.5	0.516	37±2	25.57±0.06	0.25	0.45	16.0±1.3	el	$\alpha_{0.150}^{1.4}=0.9$	Ha	26,33
PLCKG200.9-28.2	0.22	22.9±2.4	24.53±0.05	0.96	1.02	0.99±0.04	el	$\alpha_{0.150}^{1.5}=1.21$		27,33
PLCKG287.0+32.9-NW	0.39	29.4±9.1	25.25±0.16	0.35	2.31	17.20±0.39	el	$\alpha_{0.150}^{3.0}=1.36$	Ha+1Re	28,33
PLCKG287.0+32.9-SE	0.39	16.2±2.6	24.98±0.09	2.8	1.60	17.20±0.39	el	$\alpha_{0.150}^{3.0}=1.33$	Ha+1Re	28,33
PSZ1G096.89+27.17-N	0.3	8.9±0.8	24.44±0.04	0.77	0.88	3.47±1.20	el			29,32
PSZ1G096.89+27.17-S	0.3	18.2±1.9	24.76±0.05	1.46	1.42	3.47±1.20	el			29,32
PSZ1G108.18-11.53-NE	0.335	67.5±2.3	25.43±0.02	1.75	1.50		el	$\alpha_{0.147}^{1.38}=1.25$	Ha+1Re	30
PSZ1G108.18-11.53-SW	0.335	44.2±1.9	25.25±0.02	1.28	1.30		el	$\alpha_{0.147}^{1.38}=1.28$	Ha+1Re	30
ZwCl2341.1+0000-N	0.27	9.3±3.4	24.27±0.18	0.74	0.57	2.24±0.46	rnd	$\alpha_{0.147}^{1.4}=0.49$		31,32
ZwCl2341.1+0000-S	0.27	19.4±9.5	24.61±0.23	1.19	1.23	2.24±0.46	el	$\alpha_{0.147}^{1.4}=0.78$		31,32

Col.1: Cluster Name; Col.2: Redshift; Col.3: Flux at 20 cm; Col.4: Log of Power at 20 cm; Col.5: Distance from the cluster center; Col.6: Radio largest linear size estimated at 3σ noise level; Col.7: X-ray luminosity within R_{500} from MCXC catalog or literature in the 0.1-2.4 keV band; Col.8 spectral index; Col.9: other radio diffuse sources when present; Col.10: References for radio data and X-ray data when different from Piffaretti et al. 2011.

1=Randall et al. (2010); 2=Nuza et al. (2017); 3=Kempner & Sarazin (2001b); 4=Govoni et al. (2012); 5=Venturi et al. (2013); 6=Bonafede et al. (2015); 7=Cuciti et al. (2018); 8=Venturi et al. (2008); 9=Venturi et al. (2013); 10=Botteon et al. (2018); 11=Farnsworth et al. (2013); 12=van Weeren et al. (2013); 13=de Gasperin et al. (2017); 14=Shakouri et al. (2016); 15=Riseley et al. (2017); 16=Macario et al. (2014); 17=Bonafede et al. (2009a); 18=Bonafede et al. (2012); 19=Cantwell et al. (2016); 20=Kale et al. (2015a); 21=van Weeren et al. (2012); 22=Randall et al. (2016); 23=Hoang et al. (2017a); 24=Lindner et al. (2014); 25=Shimwell et al. (2015); 26=Sifón et al. (2014); 27=Kale et al. (2017); 28=Bonafede et al. (2014a); 29=de Gasperin et al. (2014); 30=de Gasperin et al. (2015); 31=van Weeren et al. (2009a); 32=Yuan et al. (2015); 33=Planck Collaboration et al. (2011).

3.4 Minihalos: a 2017 updated overview

As discussed in Chap. 2, about mini-halos are reported few works in the literature because of the scanty number of detections and the difficulty in recognizing them. In recent years Giacintucci et al. (2014) have undertaken a systematic search for new radio minihalos in a large sample of X-ray luminous clusters with available high-quality VLA and/or GMRT radio data. They reported the detection of 9 new sources (including 3 candidates and 2 uncertain) and the significantly extension from 10 (excluding A2390 classified as a halo by Sommer et al. (2017) and A2626 classified as uncertain) to 20 of the number of this kind of objects. Giacintucci et al. (2017) investigated the occurrence of these diffuse radio sources in a statistical sample of 58 clusters drawn from the *Planck* Sunyaev-Zel'dovich cluster catalog with $M_{500} > 6 \times 10^{14} M_{\odot}$. They found that the 80% of the massive clusters with a cool core host a minihalo and the drop of the fraction of minihalos in cool cores with lower cluster total mass. They reported also the 2017 updated number of minihalos: 28 (including 6 candidates and 2 uncertain, Giacintucci et al. in prep.). We report in Tab. 3.5 the 2014-2017 updated minihalo collection and their main properties.

Table 3.5: Mini-halo 2017 updated collection.

Cluster Name	z	$S_{1.4GHz}$ mJy	$\text{Log}P_{1.4GHz}$ [W/Hz]	R_{MH} kpc	$L_X^{500}(10^{44})$ erg/s	Ref.
MACSJ0159.8–0849(c)	0.404	2.4 ± 0.2	24.15 ± 0.04	90	14.4	1,5
MACSJ0329.6–0211(c)	0.450	3.8 ± 0.4	24.45 ± 0.05	70	13.6	1,5
A478	0.088	16.6 ± 3.0	23.51 ± 0.08	160	7.2	1,5
ZwCl13146	0.290	5.2 ± 0.8^a	24.14 ± 0.07	90	12.8	1,3,5
A1795(c)	0.062	85.0 ± 4.9	23.90 ± 0.03	100	5.5	1,5
RXJ1532.9+3021	0.362	7.5 ± 0.4	24.53 ± 0.02	100	14.7	1,5
A2204	0.152	8.6 ± 0.9	23.73 ± 0.04	50	13.6	1,5
ZwCl1742.1+3306(u)	0.076	13.8 ± 0.8	23.30 ± 0.02	40	2.3	1,5
MACSJ1931.8–2634(u)	0.352	47.9 ± 2.8	25.30 ± 0.03	100	19.6	1,5
A3444	0.254	10.0 ± 0.2	24.32 ± 0.02	110	11.9	1,5
AS780	0.236	11.9 ± 0.5	24.33 ± 0.02	110	14.0	2,3,5
A1068(c)	0.138	3.4 ± 1.1	23.23 ± 0.30	100	3.7	4,5
A1413(c)	0.143	1.9 ± 0.7	23.00 ± 0.17	140	6.0	4,5
RXCJ2129.6+0005	0.235	2.4 ± 0.4^a	23.69 ± 0.08	157	10.0	2,5
RXCJ1115.8+0129(c)	0.350		< 23.45 UL		12.3	2,5,6

Col.1: Cluster Name; Col.2: Redshift; Col.3: Flux at 20 cm; Col.4: Log of Power at 20 cm; Col.5: average radius defined as $R_{MH} = \sqrt{R_{max} \cdot R_{min}}$; Col.6: References to the radio flux density.

1=Giacintucci et al. (2014); 2=Kale et al. (2015b); 3=Yuan et al. (2015); 4=Govoni et al. (2009).

5=Giacintucci et al. (2017); 6=Pandey-Pommier et al. (2016)

^a Uncertainty assumed to be 15% *

As for the 2011 minihalo collection, we tested the correlation $P_{1.4GHz}$ vs $L_{X,500}$ also for this collection performing an OLS regression analysis (Akritas & Bershady 1996). We found that the bisector best fit line is:

$$\log(P_{1.4GHz}) = (2.24 \pm 0.49 \log L_{X,500} + (-76.84 \pm 21.98)) \quad (3.2)$$

with a Pearson correlation coefficient $r = 0.788$ ($p = 8.18 \times 10^{-4}$). Despite the significant number of candidate and uncertain minihalos (see Fig. 3.10), the correlation is in agreement with that of the previous collection (see Fig. 3.11 *left panel*).

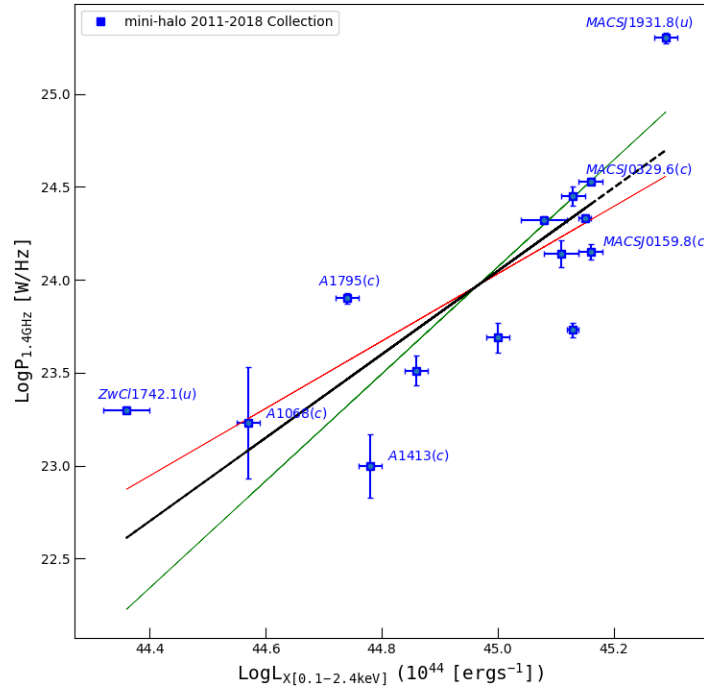


Figure 3.10: 2011-2017 minihalo collection: radio power at 1.4 GHz vs $L_{X,500}$. The OLS best fitting lines are reported with different colors: OLS(Y/X): red, OLS(X/Y): green, OLS(bisector): black. The bisector line is $\log(P_{1.4}) = (2.24 \pm 0.49) \times \log(L_{X,500}) + (-76.84 \pm 21.28)$. Labels of candidate (c) and uncertain (u) minihalos are shown.

The scaling relation for the whole collection of the 25 minihalos known up to 2017 results $P_{1.4} \propto L_{X,500}^{2.15 \pm 0.24}$ (Pearson $r = 0.773$; $p = 9.23 \times 10^{-5}$). In *left panel* of Fig. 3.11 we summarize the OLS bisector best fit lines above considered. The R_{MH} sizes of the new collection (green dots in *right panel* of Fig. 3.11) are somewhat smaller than those of the previously known minihalos, as already discussed in Giacintucci et al. (2014). It is also confirmed for a wider number of minihalos a trend $P_{1.4}/R_{MH}$ not consistent with the scaling relation found for radio halos (e.g. Cassano et al. 2008) and

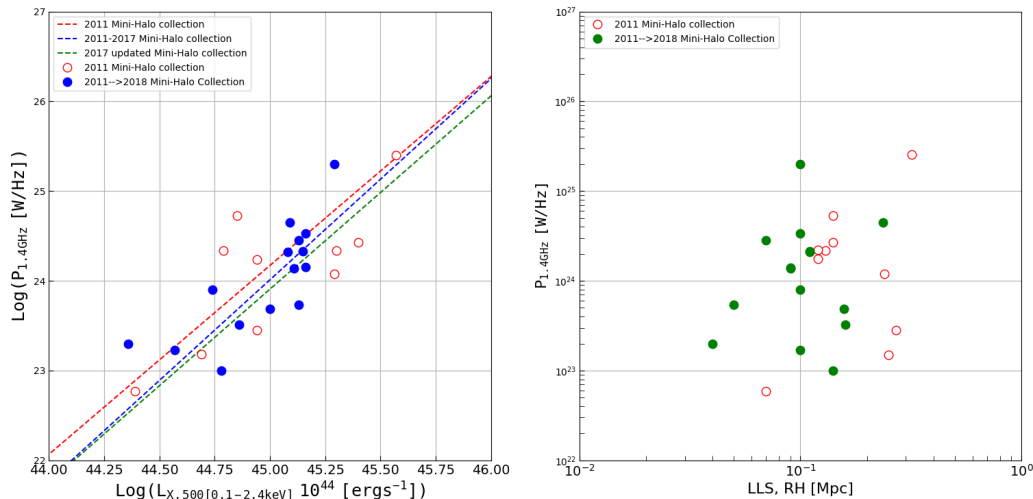


Figure 3.11: *Left panel:* radio power at 1.4 GHz vs $L_{X,500}$. Red circles: 2011 update collection, blue dots 2011-2017 updated collection. OLS bisector best fitting lines $\log(P_{1.4}) = A \times \log(L_{X,500}) + B$.

$A = (2.10 \pm 0.21)$; $B = (-70.50 \pm 9.28)$ red dotted line: 2011 updated minihalo collection;

$A = (2.24 \pm 0.49)$; $B = (-76.84 \pm 21.98)$ blue dotted line: 2011-2017 minihalo updated collection;

$A = (2.15 \pm 0.24)$; $B = (-72.91 \pm 10.86.28)$ green dotted line: whole minihalo 2017 updated collection Giacintucci et al. (2017).

Right panel: radio power at 1.4 GHz vs the radio size R_{MH} . Red circles: 2011 MH collection. Green dots: 2011-2017 MH collection.

the absence of a significant correlation due to the large dispersion of data.

3.5 Redshift limits of the current knowledge

3.5.1 Updated redshift distribution of halos and relics

In spite of the overall agreement described in the previous section, we do not know yet why not all bright X-ray clusters in a strong merger phase show a diffuse non-thermal emission. The crucial question remains namely how the collision of massive clusters gives rise to the wide range of observed non-thermal properties which run the gamut from radio quiet to the presence of a radio halo and/or one or more radio relics. The key to understanding the origin of the diffuse radio emission is likely to lie in the details of the complex interactions of the cluster constituents (dark matter, intra-cluster gas, galaxies) during a merger event, and how they relate to and effect the non-thermal components, i.e. relativistic particles and magnetic fields embedded in the ICM. Clusters are objects with a complex evolution effecting their main properties as mass, total energy, ICM temperature and dynamics: this evolution is related to merging events or to their absence.

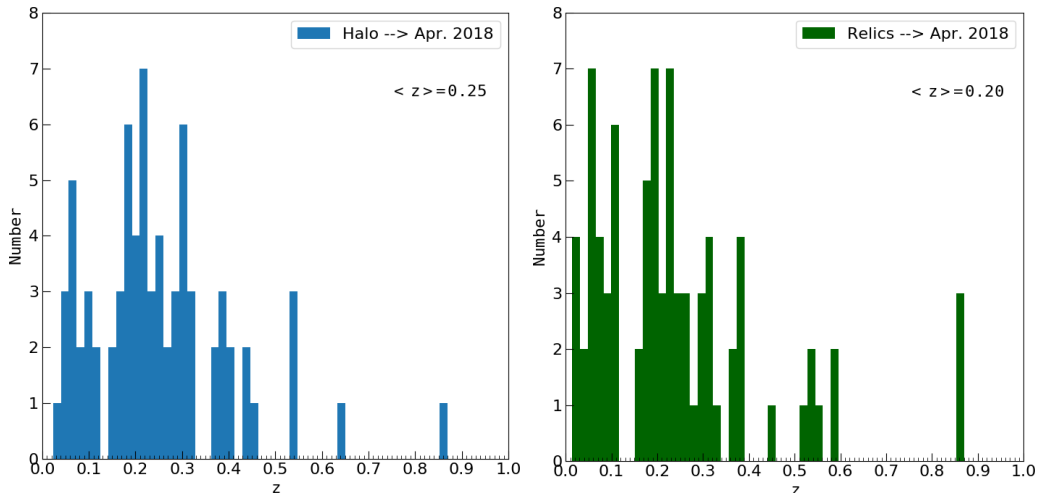


Figure 3.12: *Left panel:* Histogram of the redshift distribution of the Apr.2018 updated halo collection. *Right panel:* Histogram of the redshift distribution of the Apr.2018 updated relic collection.

For these reasons in order to shed light on the physical mechanisms governing the dynamics and the energetics of particle acceleration in cluster mergers, and magnetic field amplification, it is necessary to correlate the non-thermal cluster properties with cluster evolution. As already described in the previous chapters most of the clusters studied up to now are at redshift < 0.3 , even if in the last decade the number of diffuse radio sources with redshift beyond this value has significantly increased. To date, among 78 hosting a halo, we know 15 clusters with $0.3 \leq z < 0.4$, 4 cluster with $0.4 \leq z < 0.5$, 3 clusters with $0.5 \leq z < 0.6$. Exceptionally, in PLCKJ147.3-16.6 (van Weeren et al. 2014b) and in "El Gordo" (Lindner et al. 2014) has been found a halo at $z = 0.65$ and $z = 0.87$ respectively. Among 73, radio relics have been found in 10 clusters with $0.3 \leq z < 0.4$, in 1 cluster with $0.4 \leq z < 0.5$, in 3 clusters with $0.5 \leq z < 0.6$ and finally in the "El gordo" cluster at $z = 0.87$. Nevertheless, the overall average redshift is 0.25 for halos and 0.20 for relics (see Fig. 3.12).

3.5.2 z evolution of the $P_{1.4GHz} - L_{X,500}$ correlation for halos

Bonafede et al. (2012) reported the existence of a $P_{1.4GHz} - z$ correlation in a collection of 2012 published data on radio halos which would confirm, since the most powerful mergers are expected at $z > 0.3 - 0.4$, a link between the energy injected in the ICM and the particle acceleration efficiency and/or

magnetic field amplification. If we compare the dependence from the redshift of this distribution with that of the 2011-2018 updated halo collection, characterized by a higher mean value of the redshift, it is possible to confirm, excluding some outliers, the analysis of Bonafede et al. (2012). However, the possible presence of selection effects can not be ruled out. At larger distances only the intrinsically brightest objects will be included in the studied sample, which will skew the statistics (Malmquist bias)(Malmquist 1922).

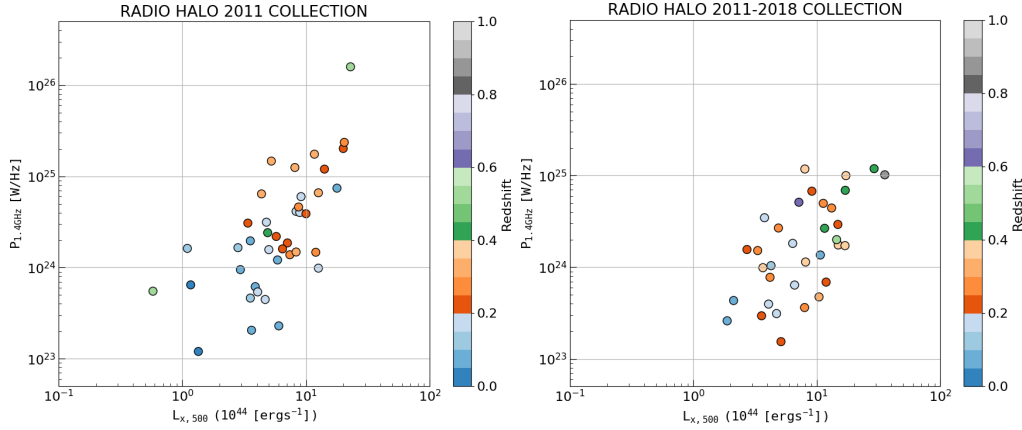


Figure 3.13: *Left panel:* z evolution of the $P_{1.4GHz} - L_{X,500}$ correlation in the 2011 halo collection as in Bonafede et al. 2011. *Right panel:* z evolution of the $P_{1.4GHz} - L_{X,500}$ correlation in the 2011-2018 halo collection.

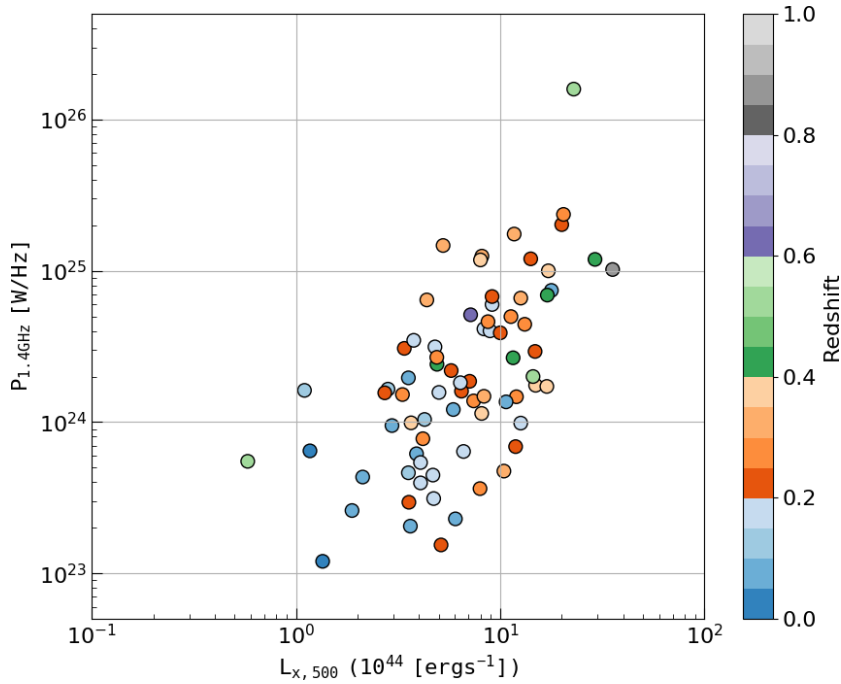


Figure 3.14: z evolution of the $P_{1.4GHz} - L_{X,500}$ correlation in the Apr. 2018 updated halo collection.

The scaling relation reported in Fig. 3.15 is relative to the halos detected in cluster with $z > 0.3$. The slope of the OLS bisector best fit line results lower than the regression line reported in the literature for halo collections with redshift $z < 0.3$ (e.g. Cassano et al. 2013). However, data are quite dispersed and the correlation is not so "robust" (Pearson $r = 0.442$; $p = 4.5 \times 10^{-2}$) as in the halo collections see in Chapt. 2 and 3. We hypothesize as possible explanations the inhomogeneities of the data and the adoption of average but not real spectral indices for the k -corrections.

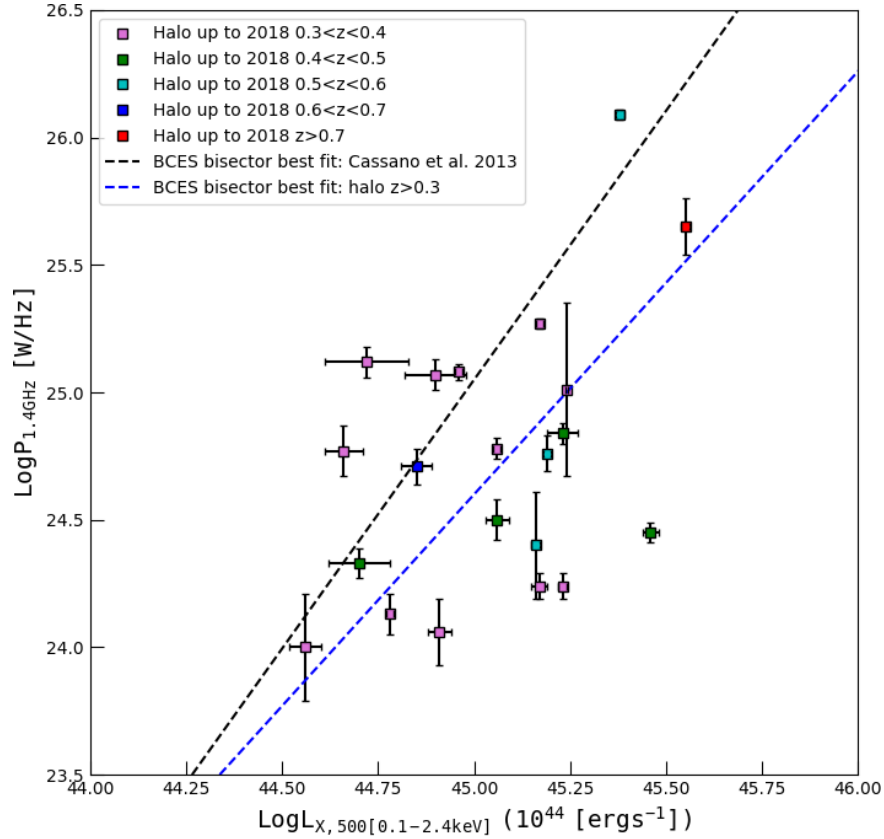


Figure 3.15: Scaling relation for radio halos at $z > 0.3$ discovered up to April 2018. Differently colored dots belong to different redshift ranges. The best fitting line (dashed blue line) $\log(P_{1.4GHz}) = (1.66 \pm 0.36) \log(L_{X,500}) + (-50.17 \pm 16.30)$ is shown. Dashed black line is the fit reported in Cassano et al. (2013).

3.5.3 A possible correlation with z of the $P_{1.4GHz} - L_{X,500}$ scaling relation for relics

When we consider the dependence of $P_{1.4GHz}$ from $L_{X,500}$ and z for the 2011 and 2011-2018 relic collections, the correlations appear statistically only marginal because of the large dispersion of data and the presence of a high number of outliers, especially in the 2011-2018 collection probably due

to data inhomogeneities and to not "true" values of the adopted spectral indices for the k -correction to calculate the radio powers.

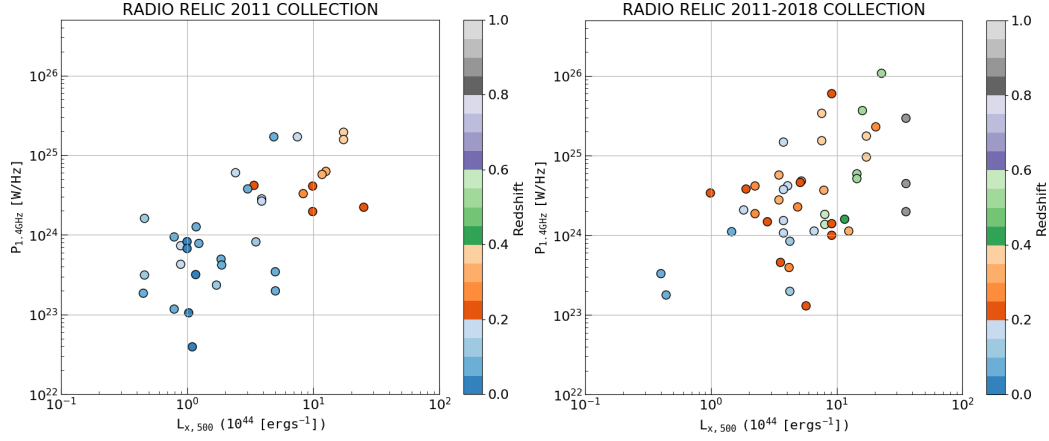


Figure 3.16: *Left panel:* z evolution of the $P_{1.4GHz} - L_{X,500}$ correlation in the 2011 relic collection as in Bonafede et al. 2011. *Right panel:* z evolution of the $P_{1.4GHz} - L_{X,500}$ correlation in the 2011-2018 relic collection.

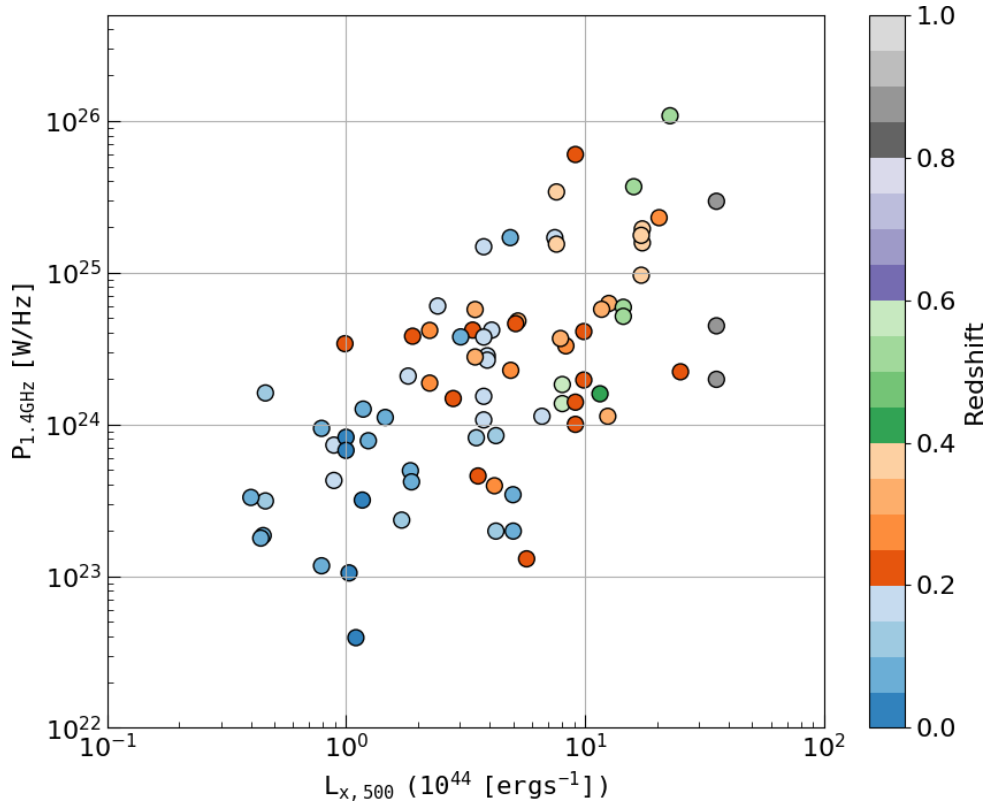


Figure 3.17: z evolution of the $P_{1.4GHz} - L_{X,500}$ correlation in the Apr. 2018 updated relic collection.

As expected, the scaling relation for the relics discovered in clusters at $z > 0.3$ results even more marginal than the 2011 and 2011-2018 collections. We argue as possibly explanation the scanty statistics and the wide dispersion of the data due specially to the poor homogeneity of the spectral indices, sometimes adopted and not measured. However, the slope of the scaling relation for relics at high redshift results slightly lower with that reported in the literature (e.g. de Gasperin et al. 2014; Yuan et al. 2015) as shown in Fig. 3.18.

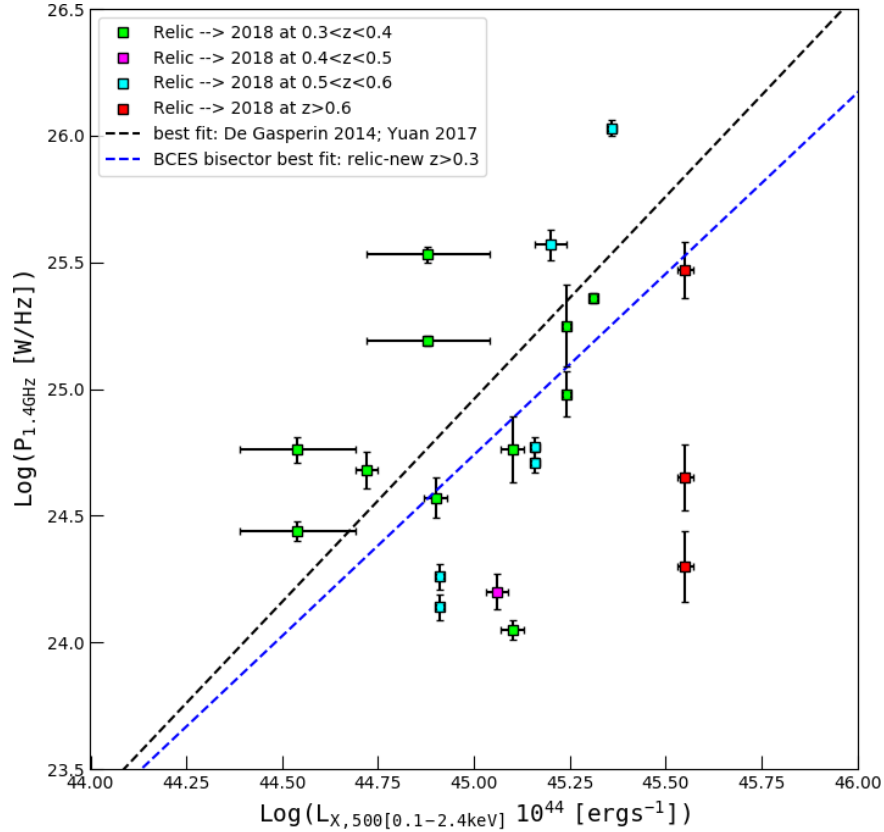


Figure 3.18: Scaling relation for radio relics at $z > 0.3$ discovered up to April 2018. The best fitting line (dashed blu line) $\log(P_{1.4GHz}) = (1.43 \pm 0.33) \log(L_{X,500}) + (-39.59 \pm 14.81)$ is shown. Dashed black line is the fit reported in de Gasperin et al. (2014).

3.5.4 z evolution of the $P_{1.4GHz} - LLS$ correlations for halos and relics

The possible existence of a correlation between the largest linear size (LLS) of a halo and the redshift of the host cluster is reported in Bonafede et al. (2012). However, it is not easily explained since ultrarelativistic particles lose more energy through the IC (Inverse Compton) mechanism as the red-

shift increases (Bonafede et al. 2012). Similar consideration can also be extended to radio relics. In Fig. 3.19, 3.20 and 3.21, 3.22 we report the $P_{1.4GHz} - LLS - z$ correlation for the different collections of halos and relics.

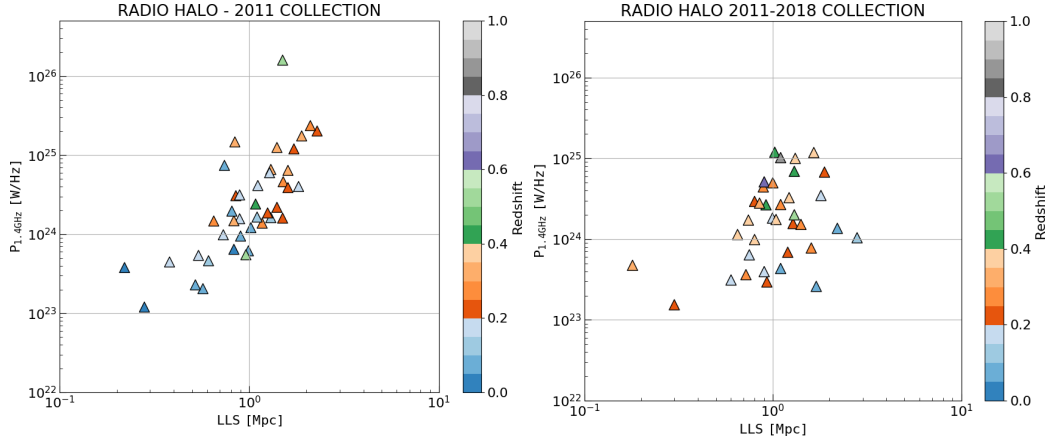


Figure 3.19: *Left panel:* z evolution of the $P_{1.4GHz} - LLS$ correlation in the 2011 halo collection (see Bonafede et al. 2012). *Right panel:* z evolution of the $P_{1.4GHz} - LLS$ correlation in the 2011-2018 halo collection.

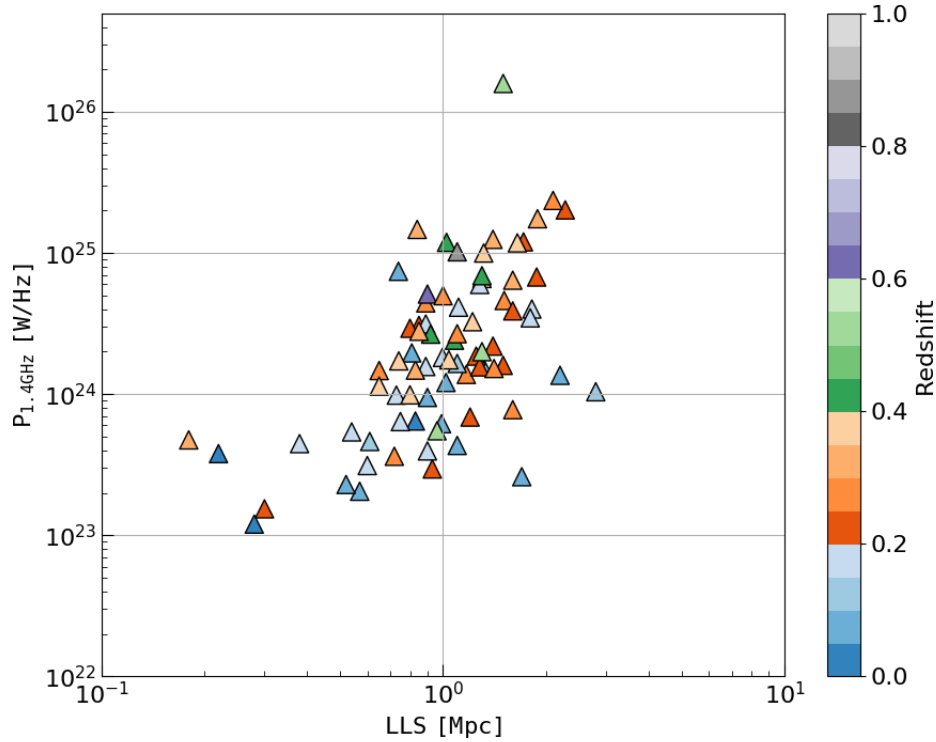


Figure 3.20: z evolution of the $P_{1.4GHz} - LLS$ correlation in the Apr. 2018 updated halo collection.

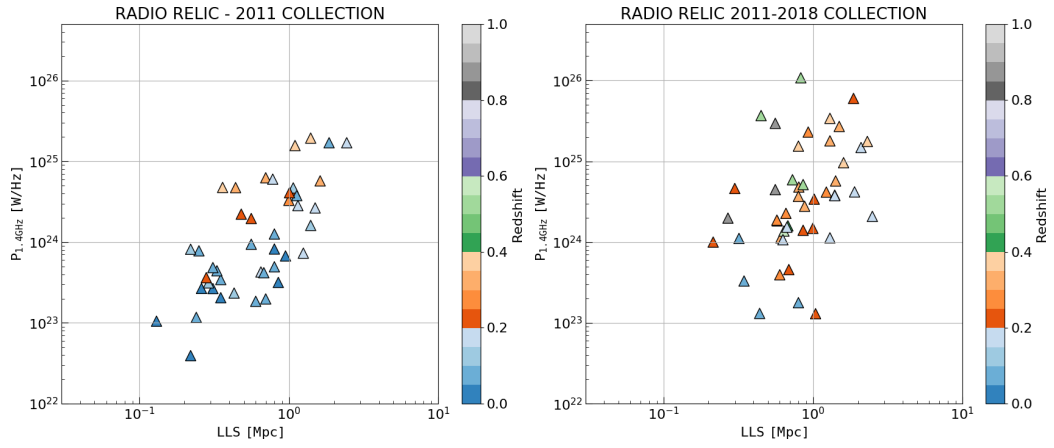


Figure 3.21: *Left panel:* z evolution of the $P_{1.4GHz} - LLS$ correlation in the 2011 relic collection. *Right panel:* z evolution of the $P_{1.4GHz} - LLS$ correlation in the 2011-2018 relic collection.

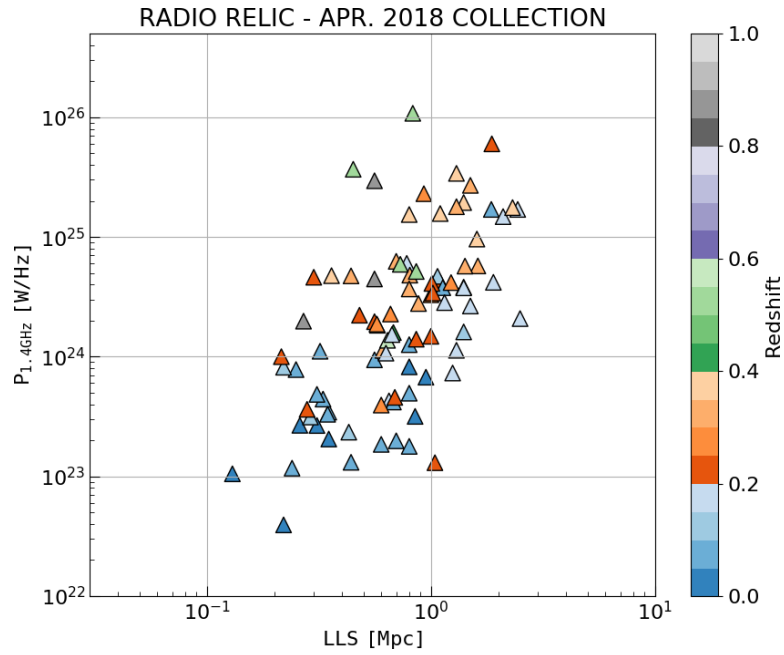


Figure 3.22: z evolution of the $P_{1.4GHz} - LLS$ correlation in the Apr. 2018 updated relic collection.

Chapter 4

Diffuse emission and dynamical state of galaxy clusters

If we want to establish the dynamical state of a galaxy cluster we have to tackle a very difficult task. The maximum amount of information on the dynamical evolution of a cluster can be derived by mapping the thermodynamic quantities, of metal abundance distribution associated to the galaxy population and the mass distribution through gravitational lensing. Moreover, the presence of diffuse radio emission (halos and/or relics) can be connected to the merger activity in non relaxed clusters. In this chapter we test the possible correlation between the properties of the diffuse radio emission and the indicators of the dynamical state of a cluster based on the morphology of the X-ray images (i.e. power ratio, centroid shift, the concentration parameter and the X-ray peak/BCG offset).

4.1 Morphological estimators of cluster dynamical state

X-ray observations of galaxy clusters reveal a large range of morphologies with various degrees of disturbance. It is important for the understanding of the dynamical state of clusters to detect and quantify substructures in the X-ray images. Substructures are the tracers of merging activity and indicate the deviation from the relaxed and virialized state. Over the years many methods to characterize and quantify substructures in galaxy clusters were proposed. Among them we will consider the methods described in the following subsection.

4.1.1 Power ratios

The power ratio method was introduced by Buote & Tsai (1995) and more recently studied by several authors (Jeltema et al. 2005; Ventimiglia et al. 2008; Böhringer et al. 2010) with the aim to parametrize the amount of substructures in the intracluster medium and to relate it to the dynamical state of a cluster. Power ratios are based on 2D multipole expansion of the cluster gravitational potential using the surface mass density distribution. In the X-rays, the surface brightness is used instead of the projected mass density assuming that the X-ray surface brightness distribution traces the gravitational potential. It is calculated within a certain aperture radius R_{ap} (e.g. r_{500}) centered on the mass centroid. The power ratios are usually defined as:

$$P_0 = [a_0 \ln(R_{ap})] \quad (4.1)$$

where a_0 is the total intensity inside the aperture radius $a_0 = S(< R_{ap})$; $S(x)$ is the X-ray surface brightness, and

$$P_m = \frac{1}{2m^2 R_{ap}^{2m}} (a_m^2 + b_m^2) \quad (4.2)$$

where the moments a_m and b_m are given by:

$$a_m(R) = \int_{R' \leq R_{ap}} S(x')(R') \cos(m\phi') d^2x' \quad (4.3)$$

and

$$b_m(R) = \int_{R' \leq R_{ap}} S(x')(R') \sin(m\phi') d^2x' \quad (4.4)$$

Here we will consider only the P_3/P_0 parameter that is related to the presence of multiple peaks in the X-ray distribution, providing a clear substructure measure (e.g. Böhringer et al. 2010).

4.1.2 Centroid shift

Numerical simulations of cluster mergers demonstrated that the centroid shift method is very sensitive to the dynamical state of the cluster (Poole et al. 2006). The centroid shift is computed in a series of circular apertures centered on the cluster X-ray peak. It is defined as the standard deviation of the projected separation between the peak and the centroid in unit of R_{ap} , as:

$$w = \left[\frac{1}{N-1} \sum (\Delta_i - \langle \Delta \rangle)^2 \right]^{1/2} \times \frac{1}{R_{ap}} \quad (4.5)$$

where Δ_i is the distance between the X-ray peak and the centroid of the i -th aperture.

4.1.3 Concentration parameter

The concentration parameter has been used in literature for a first identification of relaxed cool core clusters in those cases where a spatially resolved spectroscopic analysis was not possible (e.g. in the case of high redshift clusters). Santos et al. (2008) defined the concentration parameter c as the ratio of the peak over the ambient surface brightness, S :

$$c = \frac{S(r < 40 \text{ kpc})}{S(< 400 \text{ kpc})} \quad (4.6)$$

where $S(r < 40 \text{ kpc})$ is the flux within 40 kpc from the centre (representing the core region) and $S(< 400 \text{ kpc})$ is the flux within 400 kpc, representing the cluster emission. They tuned the choice of the radii of the two regions (40 and 400 kpc) to separate more efficiently CC from NCC and to compute c with *Chandra* data.

It is important to note that among these methods, the power ratio and the centroid shift are less sensitive to the presence of substructures (and thus mergers) along the line of sight, while the concentration parameter is in principle not affected by these projection effects (Cassano et al. 2010).

4.1.4 X-ray peak–BCG offset

Another approach to quantify the dynamical state of a cluster is based on the correlation between the brightest cluster galaxies (BCGs) and some global cluster properties such as X-ray temperature or luminosity (e.g. Edge 1991; Edge & Stewart 1991; Brough et al. 2005, 2008), indicating that their origin is closely connected to that of the host cluster. When a cluster is dynamically relaxed, it is expected the BCG to be at rest at the center of the gravitational potential well van den Bosch et al. (2005). On the other hand it exists also a class of cluster for which the BCGs are not close to the X-ray center of the host cluster. Observational studies (Katayama et al. 2003; Patel et al. 2006) and simulations (e.g. Skibba & Macciò 2011)

established the connection between the presence of offsets and the disturbed dynamical state of the cluster due to a merger activity. Thanks to the modern and powerful X-ray satellites as *Chandra* and *XMM-Newton* the correlation between the X-ray Peak–BCG offset, D_{X-BCG} , and disturbed X-ray morphology has become a simply but robust diagnostic of an active dynamical state. Sometimes it is used the X-ray centroid rather than the peak, but the results are basically the same. In the literature Mann & Ebeling (2012) classify objects with an offset > 42 kpc as extreme mergers. Sanderson et al. (2009) defined the offset threshold in terms of R_{500} and divided the objects into two classes: "small offset" ($< 0.02R_{500}$) systems, which can be considered as relaxed, and "large offset" ($> 0.02R_{500}$) systems which are likely disturbed.

4.2 D_{X-BCG} and diffuse radio emission

Rossetti et al. (2016) analyzed a subsample of the *Planck* SZ catalogue to characterize the dynamical state of 132 clusters by using the BCG/X-ray peak offset as dynamical indicator. From the cluster collection reported in this paper, we selected those clusters where a diffuse radio emission (halo, relic and minihalo) has been detected. These clusters with the hosted diffuse emission are listed in Tab. 4.1 at the end of the section. The offset distributions divided by types of diffuse emission are reported in Fig. 4.2.

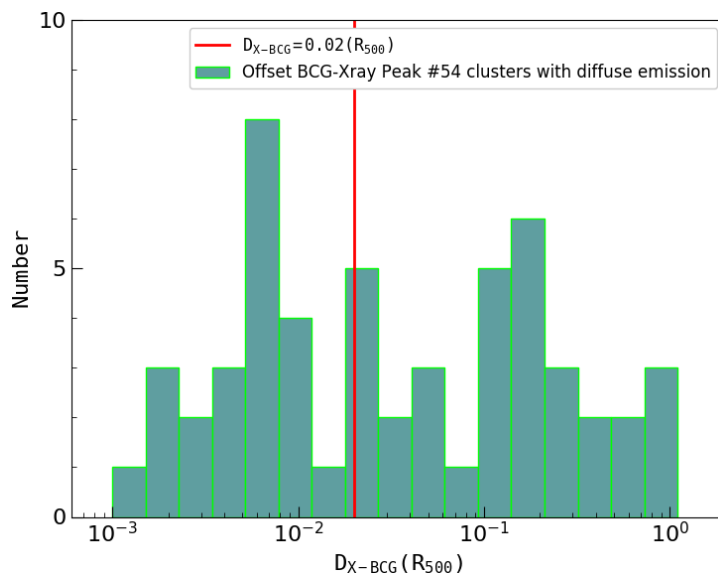


Figure 4.1: Offset distribution between the X-ray peak and the BCG position in units of R_{500} of a sample of clusters with diffuse radio emission. The red line indicates the separation between small offset (relaxed) and large offset (disturbed) clusters.

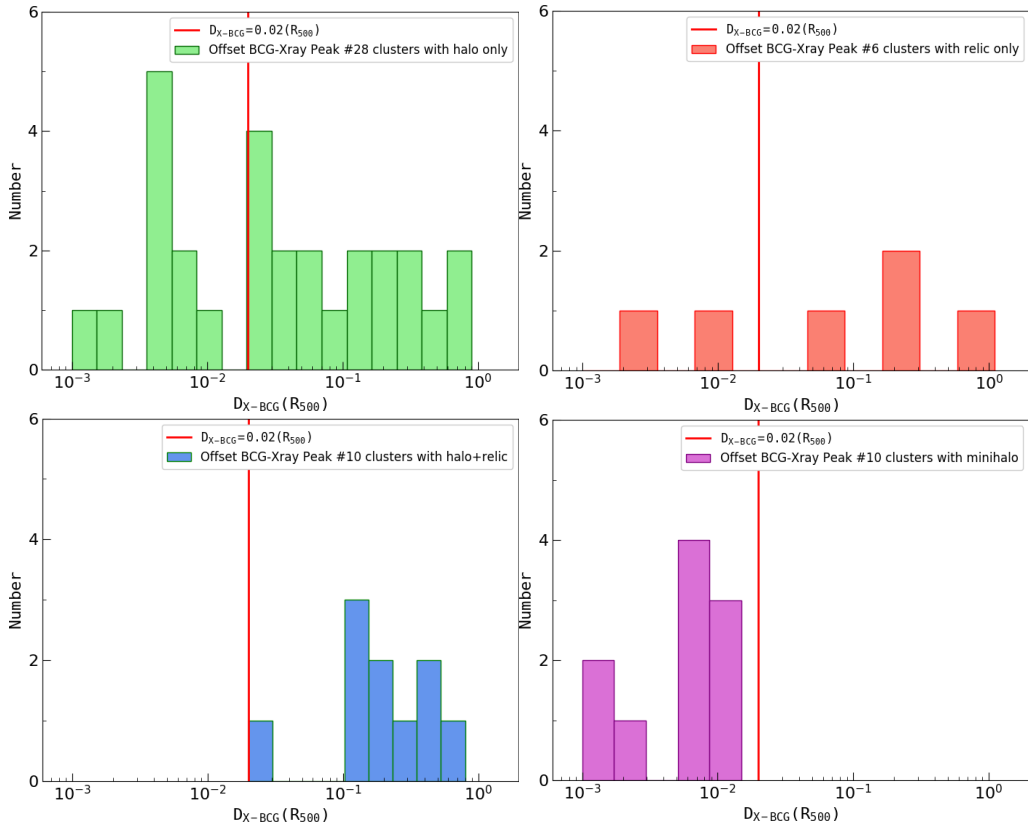


Figure 4.2: Offset distribution of the sample of clusters divided by type of diffuse emission with respect to the threshold relaxed/non relaxed (vertical red line) as in Sanders et al. (2009); Rossetti et al. (2016).

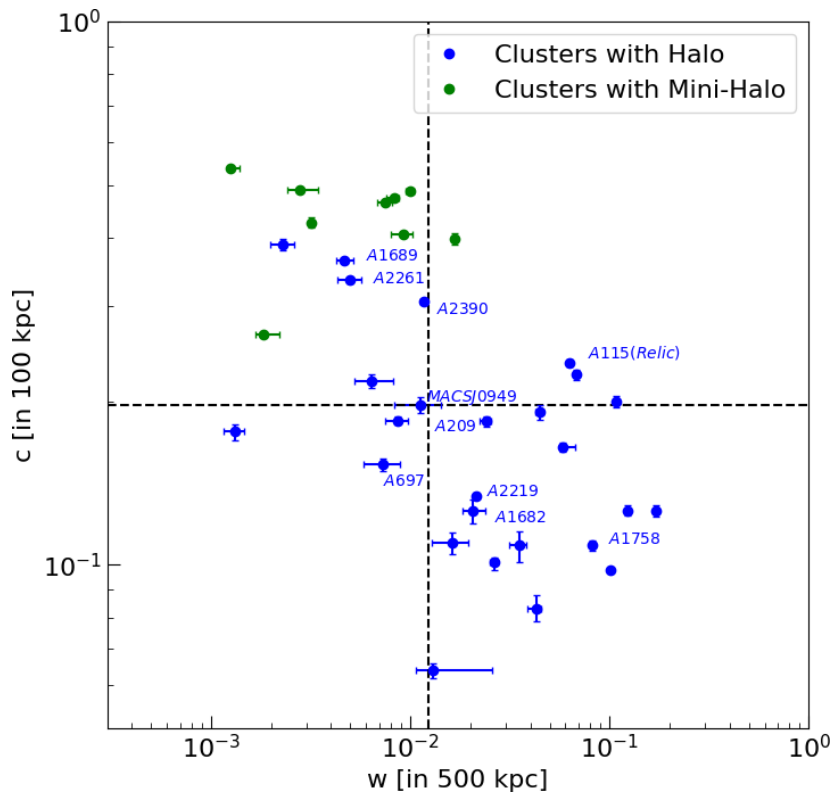
Although the considered cluster sample is not very large, however, from the plots of Fig. 4.2 it is possible to notice a general correspondence between large offsets and the presence of halos and/or relics, usually observed only in unrelaxed systems. On the other hand, all the clusters containing a minihalo show offsets below the threshold of $0.02 R_{500}$ and, as expected, they can be classified as relaxed. The systems with a halo and one or more relics are always disturbed with respect to the D_{X-BCG} offset and confirm their strong merger history. The presence of some outliers can be explained with the intrinsic limitation of the D_{X-BCG} indicator that suffers from projection effects: if a merger is separating the BCG and the X-ray peak along the line of sight, D_{X-BCG} would be underestimated with respect to the true physical offset. Rossetti et al. (2016) estimated the fraction of objects classified as relaxed although they are disturbed of 7.5%. In our sample the fraction of outliers is 22% (12 clusters). For these clusters we will compare in the next section the offset dynamical classification with that obtained from the other morphological indicators .

Table 4.1: D_{X-BCG} offset of a sample of 54 galaxy clusters with diffuse radio emission.

Cluster	z	D_{X-BCG}		Diff. Sou.	Cluster	z	D_{X-BCG}		Diff. Sou.
		kpc	R_{500}				kpc	R_{500}	
A3888	0.151	143.8	0.1137	H	A1351*	0.322	42.4	0.0348	H
A2029*	0.0766	2.3	0.0017	MH	A665*	0.1818	51.4	0.0383	H
A2744*	0.3066	71.9	0.0533	H	A209*	0.206	7.9	0.0060	H
A2204*	0.1514	2.8	0.021	MH	A773*	0.2172	77.5	0.0614	H
A1795	0.0622	14.0	0.0122	MH	MACSJ0717.5+3745*	0.546	401.0	0.3091	H
A2667*	0.2264	2.0	0.0016	MH	A697*	0.282	2.6	0.0018	H
A2345	0.176	204.7	0.1719	R	A520*	0.203	234.7	0.1847	H
A2142	0.0894	32.4	0.0229	H	MACSJ0417.5-1154	0.443	6.3	0.0046	H
A2420	0.1145	1015.8	0.8484	H	MACSJ0949.8+1707	0.3826	7.3	0.0058	H
RXCJ1720.1+2637*	0.1644	9.1	0.0073	MH	A1413*	0.1427	10.3	0.0084	MH
A2034	0.113	185.7	0.1603	H+R	A1443*	0.269	192.6	0.1511	H+R
A2261*	0.224	6.2	0.0048	H	RXCJ1144.6+1945	0.0214	218.0	0.2576	R
RXCJ2243.3-0935	0.447	157.1	0.1208	H+R	A754	0.0542	726.49	0.5558	H+
A1914*	0.1712	242.2	0.1900	H	MACSJ0553.4+3342*	0.430	163.5	0.1280	H
RXCJ1752.0+4440	0.366	341.3	0.2878	H+R	A3411	0.1687	65.4	0.0525	H+R
A2219*	0.228	13.8	0.0095	H	A3376	0.0468	1004.0	1.0987	R
A2390*	0.2329	7.2	0.0052	H	Bullet cluster*	0.2965	127.9	0.3829	H+R
A2319	0.0577	33.1	0.0233	H	A3444*	0.138	13.8	0.0108	MH
A2552*	0.2988	31.6	0.0253	H	A1300*	0.3075	28.7	0.0219	H+R
A2255	0.0809	123.7	0.1038	H+R	PSZ1G286.00+3290	0.39	168.9	0.1142	H+R
CL1821+643*	0.3315	716.9	0.6162	H	El Gordo cluster*	0.87	814.2	0.7747	H+R
A2218*	0.1709	33.9	0.0273	H	A1689*	0.1832	5.4	0.0039	H+R
A1758a*	0.279	1.7	0.0013	H	RXCJ1347.5-1144	0.4516	7.6	0.0058	MH
A2256	0.0581	222.38	0.1950	H+R	A1835*	0.2528	7.1	0.0053	MH
A1682*	0.2259	6.4	0.0053	H	A3667	0.0556	88.9	0.0715	R
A85	0.0555	3.7	0.0032	R	AS0780*	0.2357	15.1	0.0117	MH
A115*	0.1971	9.2	0.0072	R	RXCJ1514.9-1523*	0.2226	444.6	0.3345	H

4.3 D_{X-BCG} vs other morphological estimators

In the previous section we reported that 10 clusters hosting a radio halo and 2 clusters hosting a radio relic are characterized by small offsets ($D_{X-BCG} < 0.02 R_{500}$) and have therefore to be considered as relaxed (Sanderson et al. 2009; Rossetti et al. 2016). Using the morphological parameters reported by Cassano et al. (2010, 2016) and Cuciti et al. (2015) for 32 clusters of our sample (labelled with * in Tab. 4.1), we want to verify if the dynamical state of the outliers is consistent also with their position in the (w, c) , $(P_3/P_0, w)$ and $(P_3/P_0, c)$ planes. It also seemed to us interesting to compare directly D_{X-BCG} with each of the three morphological parameters by plotting the (D_{X-BCG}, c) , $(D_{X-BCG}, P_3/P_0)$ and $(P_3/P_0, w)$ planes and verify in each pair of parameters the possible presence of a correlation. Following Cassano et al. (2010) we report in Fig. 4.3 the distribution of the 32 clusters in the three morphological diagrams, each divided into quadrants by the median value of each parameter. The D_{X-BCG} outlier clusters are labeled with their names.



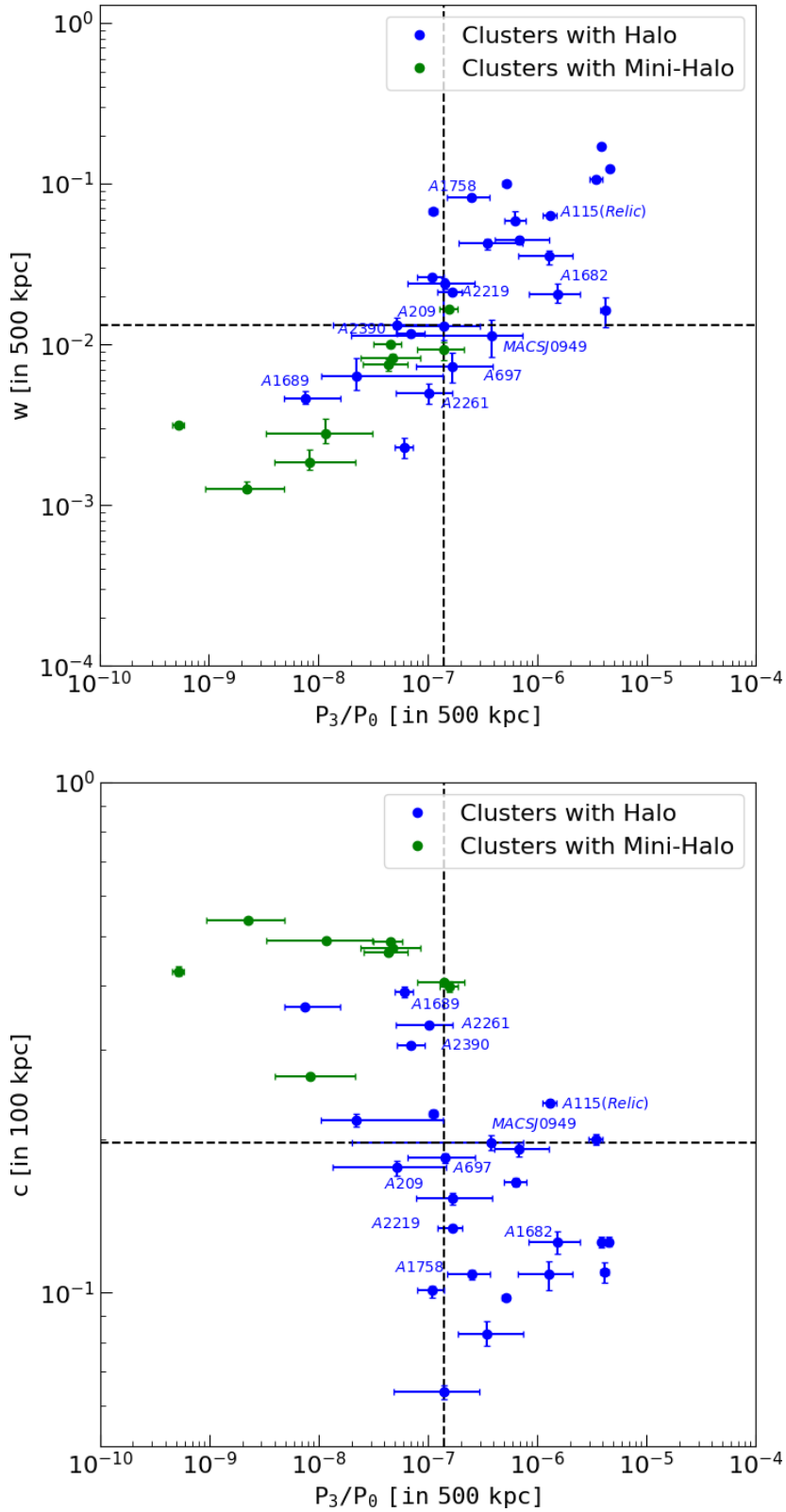


Figure 4.3: – a): concentration parameter c vs. centroid shift w ; b): w vs. the power ratio P_3/P_0 ; c): c vs. P_3/P_0 . Vertical and horizontal dashed lines (medians): $c = 0.197$, $w = 0.0123$, $P_3/P_0 = 1.41 \times 10^{-7}$. Blu and green dots represent clusters with RH and clusters hosting minihalo respectively. Labels are referred to the D_{X-BCG} outliers clusters.

We used the median lines of the diagrams of Fig. 4.3 to separate merging not relaxed clusters ($c < 0.2$, $w > 0.12$ and $P_3/P_0 > 1.2 \times 10^{-7}$) from relaxed clusters ($c > 0.2$, $w < 0.12$ and $P_3/P_0 < 1.2 \times 10^{-7}$). Three outliers: A1689, A2261 and A2390 always fall in the regions of relaxed clusters, while the other D_{X-BCG} outliers are located in the quadrants of disturbed cluster, as expected because of the presence of a hosted halo. Andersson & Madejski (2004) showed that A1689 is undergoing a merger event at very small angle with the line of sight and therefore its morphological parameters are likely biased due to projection effects. More puzzling is the case of A2390 and A2261 where the presence of a cool core was observed in both clusters (Allen 2000; Maughan et al. 2008). More recently, Sommer et al. (2017) performed a radio and X-ray analysis confirming the anomalous presence of giant radio halos in these cool core relaxed clusters. Although some asymmetric features that can indicate past minor mergers are seen in the X-ray brightness images, nevertheless whether such non-disruptive mergers can generate enough turbulent kinetic energy to eventually power particle acceleration, and how long such elevated level of turbulence lasts, remain open questions.

If we exclude the well studied cases seen before, it seems that for most of the outliers of our sample the D_{X-BCG} offset is not able to predict correctly their disturbed dynamical state in agreement with the other morphological estimators. A possible explanation lies in the accuracy with which is possible to estimate the position of the peak of the X-ray emission: it depends on the statistical quality of the observations, on the possible presence of non-detected point sources and on the surface brightness distribution with the possible presence of multiple peaks (Mann & Ebeling 2012; Rossetti et al. 2016). It is thus not easy to estimate the D_{X-BCG} offset uncertainties, to which are added the uncertainties in determining the position of the BCGs, and therefore in some cases, this morphological parameter could not be appropriate as a dynamical indicator.

4.4 Correlations with D_{X-BCG}

As previously introduced, we test here the existence in our sub-sample of 32 clusters (see section 4.3) of a possible correlation between D_{X-BCG} and the other morphological parameters: c , w and P_3/P_0 .

4.4.1 c vs. D_{X-BCG}

In the *left panel* of Fig. 4.4 we report the (D_{X-BCG}, c) plane. The clusters marked with labels are the outliers of par. 4.3. Half of these are located in the relaxed quadrant even though they host a radio halo while the second half are located out of the relaxed not/relaxed regions according to what was previously discussed. We performed a regression analysis based on OLS estimators (Akritas & Bershadsky 1996) assuming a linear fit in the form $\log(c) = A \times \log(D_{X-BCG}) + B$. We found a weak anti-correlation confirmed by a Pearson's parametric coefficient $r = -0.476$ ($p = 0.00384$) and a Spearman non-parametric value $\rho = -0.457$ ($p = 0.00572$). We decided therefore to exclude the three outliers marked with red circles in the *right panel* of Fig. 4.4. We obtained a sharply strongest correlation with $r = -0.751$ ($p = 1.11 \times 10^{-6}$) and $\rho = -0.730$ ($p = 3.20 \times 10^{-6}$) and found the existence of a significant anti-correlation between the two dynamical state indicators in clusters hosting diffuse radio emission. Adopt-

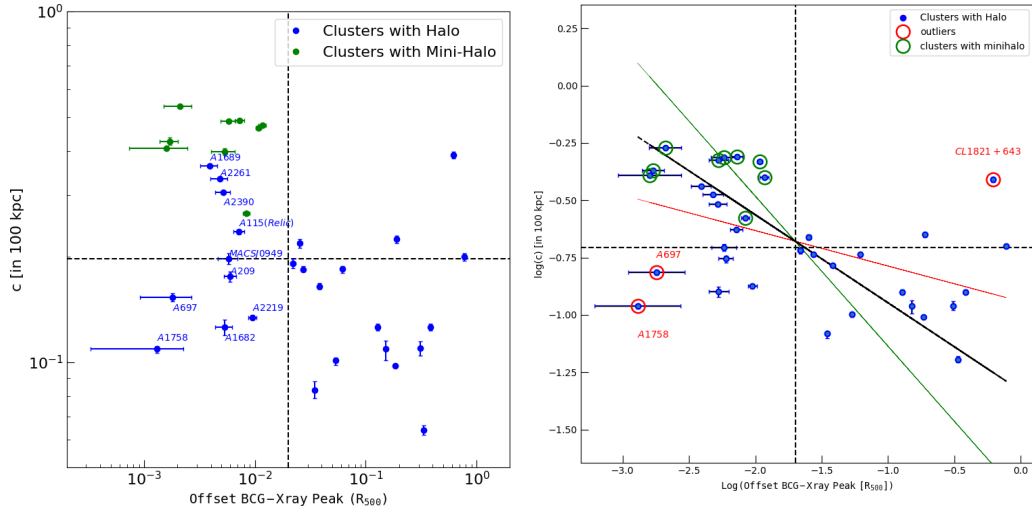


Figure 4.4: *left panel* Distribution of the 32 clusters hosting diffuse emission in the (D_{X-BCG}, c) diagram. Dotted lines are the median values. *right panel* Scaling relation between D_{X-BCG} and c in the log-log plane. Black line is the bisector, red circles are the outliers, green circles are the clusters with a minihalo. Dotted lines are the log of the median values.

ing the OLS(bisector) as the best fit we found $A = (-0.38 \pm 0.04)$ and $B = (-1.33 \pm 0.08)$ which corresponds to $c \propto D_{X-BCG}^{-(0.38 \pm 0.04)}$ dependency. A weaker non parametric anti-correlation between c and D_{X-BCG} offset has been reported also by Rossetti et al. (2017) for a wide sample of galaxy clusters. Comparing these results with ours, we suggest the hypothesis that this anti-correlation becomes stronger in clusters where diffuse radio emis-

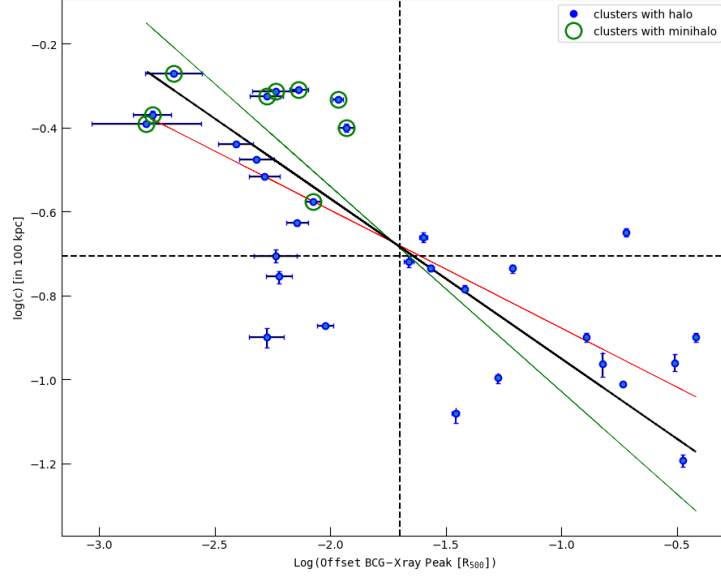


Figure 4.5: Scaling relation between D_{X-BCG} and c in the log-log plane without outliers. The OLS best fitting lines are reported with different colors: OLS(Y/X): red, OLS(X/Y): green, OLS(bisector): black. The bisector line is $\log(c) = (-0.38 \pm 0.04) \times \log(D_{X-BCG}) + (-1.33 \pm 0.08)$. Dotted lines are the log of the median values.

sion is detected. In Fig. 4.5 is reported the OLS(X/Y), OLS(Y/X) and OLS(bisector) regression analysis.

4.4.2 w vs. D_{X-BCG}

The distribution of our cluster sample in the (D_{X-BCG}, w) plane (*left panel* of Fig. 4.6) is similar to that of the (D_{X-BCG}, c) plane. Also in this plot the labeled outliers lie in the relaxed region or out of the relaxed/non relaxed quadrants. Excluding the outliers (marked with red circles in *right panel* of Fig. 4.6), we found a significant correlation also between w and D_{X-BCG} dynamical indicators with $r = 0.707$ ($p = 4.24 \times 10^{-6}$) and $\rho = 0.702$ ($p = 5.26 \times 10^{-6}$). The BCES bisector best fit line resulted $\log(w) = (0.71 \pm 0.07) \times \log(D_{X-BCG}) + (-0.58 \pm 0.15)$ with scaling relation $w \propto D_{X-BCG}^{(0.71 \pm 0.07)}$. This quasilinear dependence confirms that the D_{X-BCG} offset behaves similarly to w in quantifying the evolving morphology of clusters and how far the system is from virial and hydrostatic equilibrium (e.g. Poole et al. 2006).

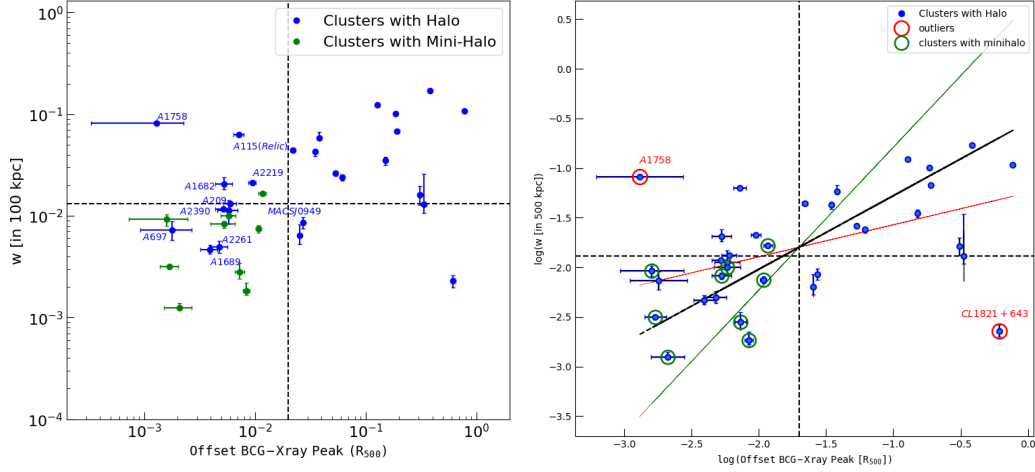


Figure 4.6: *Left panel:* distribution of the 32 clusters hosting diffuse emission in the (D_{X-BCG}, w) diagram. Dotted lines are the median values. *Right panel:* scaling relation between D_{X-BCG} and w in the log-log plane. Black line is the bisector, red circles are the outliers, green circles are the clusters with a minihalo. Dotted lines are the log of the median values.

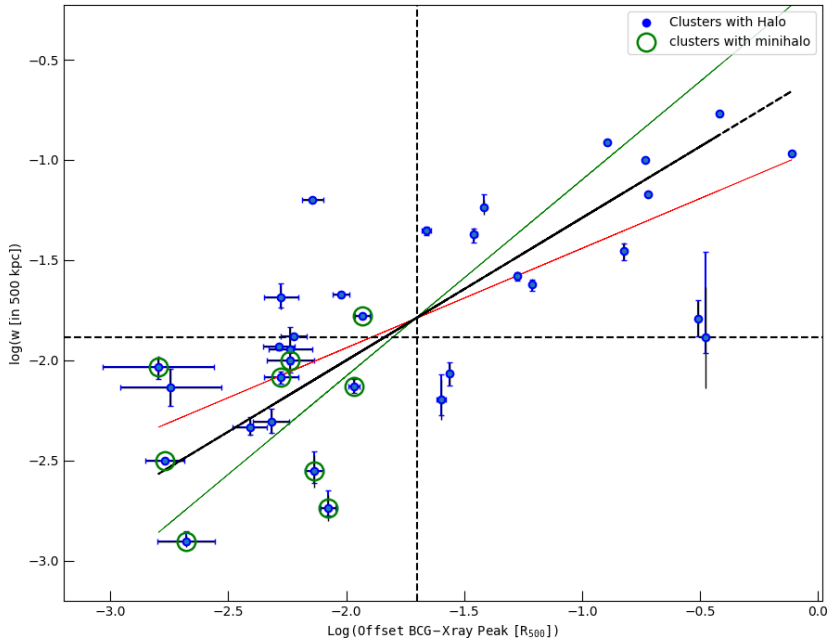


Figure 4.7: Scaling relation between D_{X-BCG} and w in the log-log plane without outliers. The OLS best fitting lines are reported with different colors: OLS(Y/X): red, OLS(X/Y): green, OLS(bisector): black. The bisector line is $\log(c) = (0.71 \pm 0.07) \times \log(D_{X-BCG}) + (-0.58 \pm 0.15)$. Dotted lines are the log of the median values.

4.4.3 P_3/P_0 vs. D_{X-BCG}

The centroid shift and power ratio approaches are both capable of identifying either highly disturbed systems or systems with significant, well-defined substructures (Poole et al. 2006). The amplitude of the power

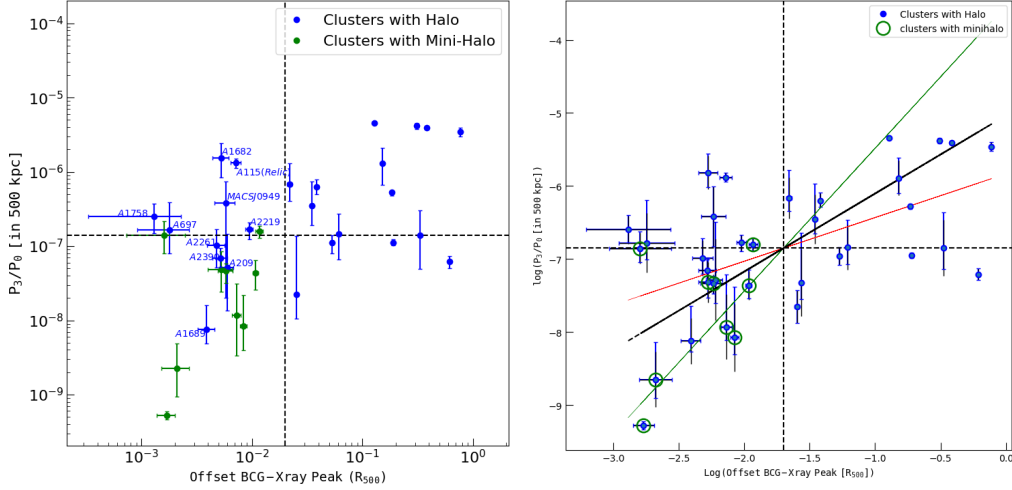


Figure 4.8: *left panel* D_{X-BCG} vs. P_3/P_0 correlation with labeled outliers. *right panel* The OLS best fitting lines are reported with different colors: OLS(Y/X): red, OLS(X/Y): green, OLS(bisector): black. The possible scaling relation line is $\log(P_3/P_0) = (1.07 \pm 0.13) \times \log(D_{X-BCG}) + (-5.03 \pm 0.25)$. Dotted lines are the log of the median values.

ratios is relatively low when the system is not highly perturbed and appears to be highly susceptible to noise in the X-ray images. If we exclude the labeled outliers, the points in the $(P_3/P_0, D_{X-BCG})$ plot appear more dispersed respect to the previous planes (*left panel* Fig. 4.8) and there are not clusters with such anomalous values that they can be excluded. However, the correlation between P_3/P_0 and D_{X-BCG} is not as significant as for the others indicators ($r = 0.537$ and $p = 0.000878$; $\rho = 0.445$; ($p = 0.00793$). The OLS bisector best fit of this weak correlation is $\log(P_3/P_0) = (1.07 \pm 0.13) \times \log(D_{X-BCG}) + (-5.03 \pm 0.25)$ that suggests the possible existence of a linear correlation $P_3/P_0 \propto D_{X-BCG}^{(1.07 \pm 0.13)}$. To exclude possible selection effects, we tested the correlations c vs. D_{X-BCG} and w vs. D_{X-BCG} without the clusters hosting minihalos. We found that the correlations remain significant as shown in tab. 4.2.

Performing the OLS bisector best fits the scaling relations between the

Table 4.2: Output of the correlation tests

Correlation	Pearson r	p	Spearman	p
(D_{X-BCG}, c)	-0.657	8.89×10^{-4}	-0.674	5.86×10^{-4}
(D_{X-BCG}, w)	0.642	7.22×10^{-4}	0.6705	3.37×10^{-4}

two couples of indicators result $c \propto D_{X-BCG}^{-(0.31 \pm 0.03)}$ and $w \propto D_{X-BCG}^{-(0.62 \pm 0.06)}$ respectively. The slopes are slightly lower with respect to the correlations

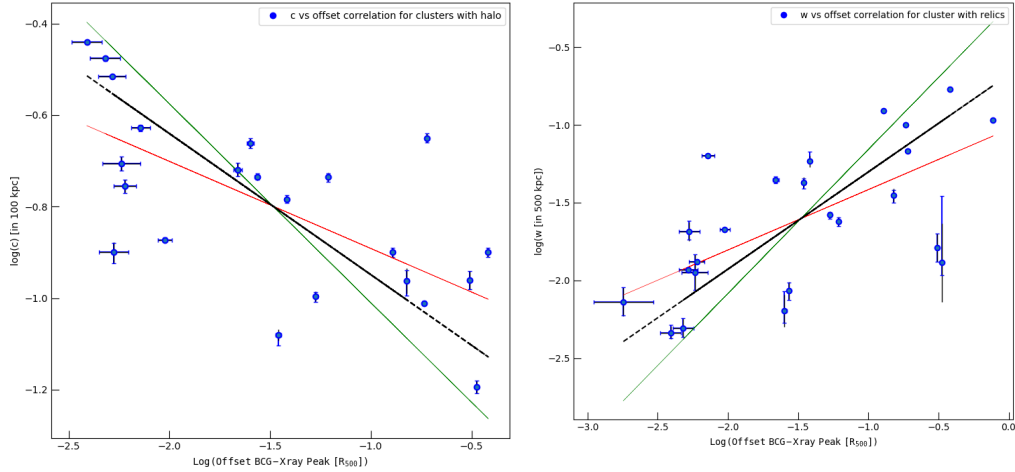


Figure 4.9: *left panel* c vs. D_{X-BCG} correlation. The OLS bisector best fits is $\log(c) = -(0.31 \pm 0.03) \times \log(D_{X-BCG}) + (-1.25 \pm 0.07)$ *right panel* w vs. D_{X-BCG} correlation. The OLS bisector best fits is $\log(w) = (0.62 \pm 0.06) \times \log(D_{X-BCG}) + (-0.68 \pm 0.12)$. Fitting lines are reported with different colors: OLS(Y/X): red, OLS(X/Y): green, OLS(bisector): black.

found including also the clusters with minihalos. In Fig. 4.9 are reported the best fit lines. In this chapter we have used as indicator of the dynamical state of a sample of galaxy clusters with diffuse radio emission, the projected offset between the position of the X-ray peak and the position of the BCG. D_{X-BCG} offset correctly predicted the dynamical state of most of the clusters: disturbed when a radio halo or relic is hosted, relaxed when a minihalo is present. Nevertheless, we found a not negligible number of outliers ($\sim 20\%$) that required a further analysis. We tested the effectiveness of the offset as dynamical indicator for these outliers by comparing it with the morphological indicators c , w and P_3/P_0 . With the exception of A1689, A2261 and A2390 classified as relaxed also by these parameters, all the other clusters resulted classified as not relaxed. The possible explanation of these discrepancy is that D_{X-BCG} offset suffers of projection effects more respect to the other morphological parameters. Another limitation is the estimate of BCG from an heterogeneous set of literature information which may result in an underestimation of the measured offset for some clusters (Rossetti et al. 2017). However, the presence of strong correlations between D_{X-BCG} with c and w confirms this parameter as a powerful indicator of the dynamical state of a cluster together with the other most used morphological tests.

Chapter 5

Topics and aims of the present thesis

5.1 Overview

In the previous chapters we presented an overview of the diffuse radio sources in galaxy clusters reported in the literature up to April 2018. We examined some intrinsic properties of halos, relics and mini-halos and their correlation with the properties of the clusters where they are hosted. Summarizing the main features:

- Radio halos are present in rich clusters, characterized by high mass, high X-ray luminosity, and high gas temperature. The radio power of the halos is strongly correlated with the X-ray luminosity (and thus also the mass) of the host cluster. A similar correlation, even if not so strong, is found for relics and mini-halos.
- Diffuse cluster sources are not present in all galaxy clusters. The occurrence of radio halos and relics has been studied by Giovannini (1999) in the NVSS sample, finding that is higher in cluster showing high X-ray luminosity. Halos are present in $\sim 20 - 30\%$ while relics in $\sim 25\%$ of the clusters with $L_X > 5 \times 10^{44} \text{ erg s}^{-1}$. More recently Cuciti et al. (2015) reported the occurrence of radio halos as a function also of cluster mass in a selected sample finding a drop of the fraction of clusters hosting radio halos for less massive systems.
- A clear dichotomy is observed between disturbed and relaxed clusters: radio halos and relics are exclusively associated with clusters showing signs of recent or ongoing merging and are never found in cool-core

clusters. Mini-halos associated with the cD in cool-core clusters are of very different physical origin and nature.

- The radio properties of halos and relics are closely connected to the intra-cluster medium (ICM), suggesting a causal connection between the hot and the relativistic plasma. Merger events supply energy to radio halos and relics via turbulence and shock re-acceleration mechanisms respectively. Many theoretical papers (e.g. Brunetti & Lazarian 2011a,b, 2016; Brunetti & Jones 2014), as well as numerical simulations (e.g. Vazza et al. 2010, 2011) are in agreement with the observational results outlined above.
- Most of the clusters studied up to now are at redshift < 0.3 , even if in the last decade the number of diffuse radio sources with redshift beyond this value has significantly increased. Nevertheless, the overall average redshift is 0.25 for halos and 0.20 for relics.

5.2 Scarce sampling at $z \geq 0.3$ of known halos and relics

Up to date, the number of halos and relics discovered at $z \geq 0.3$ does not allow a suitable statistics to correlate the non-thermal properties with the evolution of galaxy clusters. These redshift limitations appear clear if we consider the planes ($P_{1.4GHz}$, $L_{X,500}$) reported in the *left panels* of Fig. 5.1 and 5.2, where clusters at high redshift with diffuse emission are highlighted with colored circles. Also the scaling relations at $z > 0.3$ reported in the *right panels* of Fig. 5.1 and 5.2, are affected by a scanty number of points.

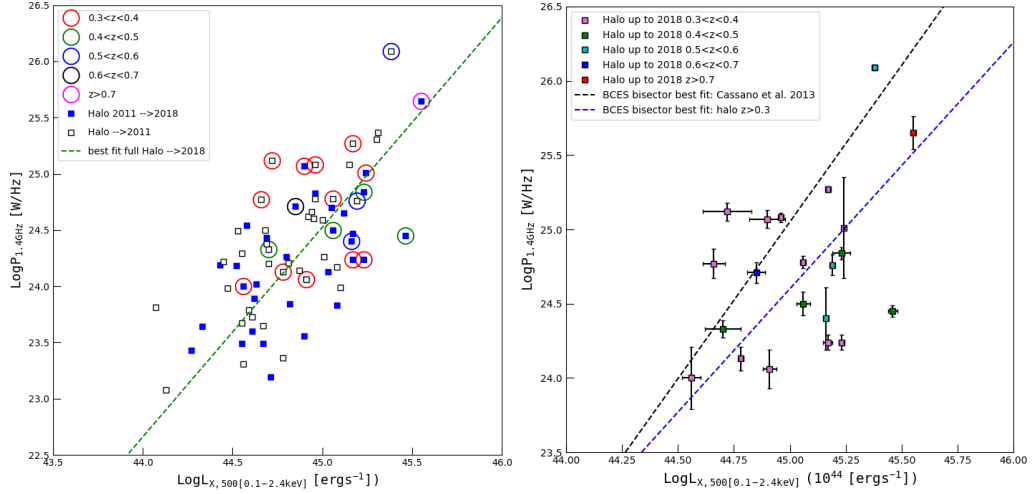


Figure 5.1: *Left panel:* correlation $P_{1.4\text{GHz}} - L_{X,500}$ of the halos known up to 2018. Circled dots are the diffuse sources detected at $z \geq 0.3$. Green dotted line is the best fit line of the whole collection. *Right panel:* distribution of halos with $z > 0.3$ in the $P_{1.4\text{GHz}} - L_{X,500}$ plane and comparison between scaling relations. Black dotted line: literature (e.g. Cassano et al. 2013); blue dotted line: 2018 updated halo collection at $z > 0.3$.

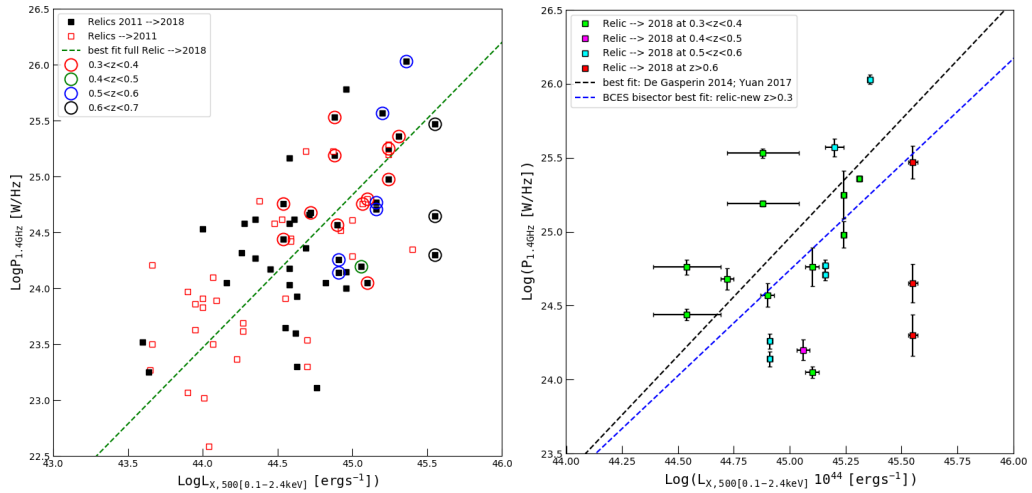


Figure 5.2: *Left panel:* correlation $P_{1.4\text{GHz}} - L_{X,500}$ of the relics known up to 2018. Circled dots are the diffuse sources detected at $z \geq 0.3$. Green dotted line is the best fit line of the whole collection. *Right panel:* distribution of relics with $z > 0.3$ in the $P_{1.4\text{GHz}} - L_{X,500}$ plane and comparison between scaling relations. Black dotted line: literature (e.g. de Gasperin et al. 2014); blue dotted line: 2018 updated relic collection at $z > 0.3$.

5.3 Selection of a high redshift cluster sample

In order to correlate the non-thermal cluster properties with cluster evolution it is necessary to increase the statistics of diffuse radio emission at redshifts beyond the nearby Universe ($z < 0.3$). The detection in these last years of 5 halos and 9 relics in clusters with $z > 0.5$ clearly demonstrates that high redshift non thermal emission is possible. The selection of a sample

including *active* and *quiescent* clusters it would have been ideal to provide the necessary comparison to understand statistical properties. In a sample of the brightest X-ray clusters we expect to find, because of known correlation between radio power and X-ray luminosity, a relatively high number of diffuse radio sources in a limited observing time.

We selected an homogeneous sample of very luminous X-ray clusters detected in the Massive Cluster Survey (MACS) presented by Ebeling et al. (2010), including all MACS with X-ray fluxes in excess of $2 \times 10^{-12} \text{erg s}^{-1} \text{cm}^{-2}$ (0.1–2.4 keV) in the ROSAT Bright Source Catalogue. The redshift range is from 0.3 to 0.5. Moreover we added the complete sample of most distant MACS clusters ($z > 0.5$) presente in Ebeling et al. (2007). Among these clusters we have excluded the few well studied systems most of which are already present in Feretti et al. (2012) (see Chapt. 2) or more recent papers. We asked to observe the 45 remaining targets not yet observed with radio observations deeper and at higher resolution with respect to the NVSS radio data, with the following goals:

- to establish in this new sample the presence or not of diffuse radio emission.
- to compare statistical properties of non thermal emission at high redshift ($z > 0.3$) with known results that we have reported in Chapt. 2 and Chapt. 3. Our purpose is to further extend the correlation with redshift of the properties reported in the present chapter including the new high redshift diffuse radio sources we expected to find in our sample.
- to study the dynamical state of high redshift clusters with or without diffuse emission using the indicators based on the morphology of X-ray images such us *power ratio*, *centroid shift*, *concentration parameter* and the *X-ray peak – BCG offset*.

The description of the observation carried out with the JVLA and the results of our measurements are reported in Chapter 6.

Chapter 6

JVLA radio observations of a homogeneous sample of high redshift MACS clusters

In this chapter we summarize the characteristics and the results of our observational campaign in L-band with the JVLA carried out using C and D configurations between February–May, 2017 (D–array) and May–August, 2017 (C–array).

6.1 The Jansky Very Large Array Radio Telescope

The Very Large Array (VLA) is currently one of the world's premier astronomical radio observatories. It is operated by the National Radio Astronomy Observatory (NRAO), a facility of the National Science Foundation operated under cooperative agreement by Associated Universities, inc. The VLA was built in the 1970s and in 2011, a decade long project had resulted in the VLA expanding its technical capacities by replacing the 1970s era electronic with the state of the art equipment and a new central super-computer with an innovative design. When the upgrade project started, the VLA was called the Expand VLA or EVLA. On March 2012 the array was officially renamed "The Karl Jansky Very Large Array" or more simply JVLA. It consists of 27 radio antennas in a Y–shaped configuration and is located on the Plains of San Augustin fifty miles west of Socorro, New Mexico. Each antenna is 25 meters in diameter and the antenna system can be physically relocated to a number of prepared positions, allowing aperture

synthesis interferometry with up to 351 independent baselines. There are four configurations: A array, with a maximum antenna separation of 36 km; B array with 10 km; C array with 3.6 km and D array with 1 km. The telescopes are switched between these configurations every four months or so. Each of the JVLA's 25-meter parabolic dish antennas use 10 receivers that allow them to operate in ten frequency bands with high sensitivity over a wide range of angular resolution depending on the configuration set as reported in tab. 6.1

Table 6.1: Main JVLA parameters

Band	<i>Array</i> → Frequency	A	B	C	D
		θ_{HPBW} (arcsec)			
Band 4 (405 cm)	74 MHz	24	80	260	850
P Band (90 cm)	350 MHz	5.6	18.5	60	200
L Band (20 cm)	1.5 GHz	1.3	4.3	14	46
S Band (10 cm)	3.0 GHz	0.65	2.1	7.0	23
C Band (5 cm)	6.0 GHz	0.33	1.0	3.5	12
X Band (3 cm)	10.0 GHz	0.20	0.60	2.1	7.2
Ku Band (2 cm)	15.0 GHz	0.13	0.42	1.4	4.6
K Band (1.4 cm)	22.0 GHz	0.089	0.28	0.95	3.1
Ka Band (0.9 cm)	33.0 GHz	0.059	0.19	0.63	2.1
Q Band (0.7 cm)	45.0 GHz	0.043	0.14	0.47	1.5
max baseline (km)→		36.4	11.1	3.4	1.03

6.2 Observing proposal of a high redshift MACS sample of galaxy clusters

As already introduced in the Chapt. 5, to achieve our scientific goal to correlate the non-thermal cluster properties with cluster evolution, we focused our attention on a sample of clusters characterized by both high redshift ($z > 0.3$) and high X-ray luminosity. For these reasons our choice has naturally fallen on the Ebeling Massive Cluster Survey (MACS) (Ebeling et al. 2007, 2010). MACS was launched in 1998 with the goal of compiling the first large, statistical sample of very X-ray luminous clusters at $z > 0.3$. The MACS cluster sample is compiled by applying limits in the X-ray flux and spectral hardness to all sources listed in the RASS (ROSAT All-Sky Survey) Bright Source Catalogue that fall within the part of extragalactic sky that is

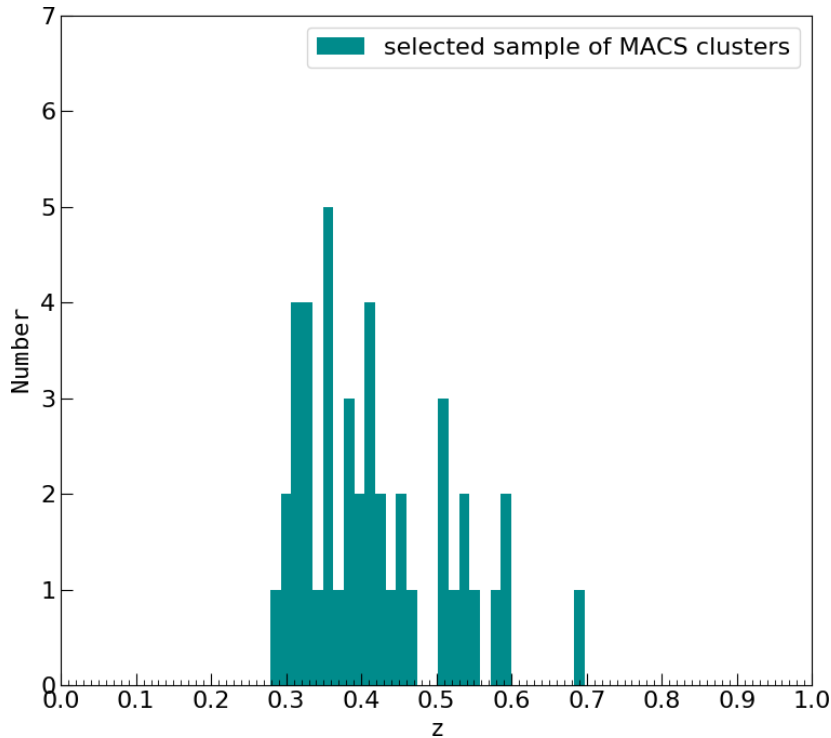


Figure 6.1: Redshift distribution of selected sample of MACS high redshift clusters.

observable from Mauna Kea. Cluster candidates are then targeted in spectroscopic observations and added to the MACS catalogue if their measured redshifts exceeds $z = 0.3$. We considered the catalogue reported in Ebeling et al. (2010) that comprises all MACS clusters with nominal X-ray fluxes in excess of $2 \times 10^{-12} \text{ erg s}^{-1} \text{ cm}^{-2}$ (0.1–2.4 keV) and redshift range from 0.3 to 0.5. Moreover we added the complete sample of most distant MACS clusters ($z > 0.5$) presented in Ebeling et al. (2007), excluding the few well studied systems most of them already present in Feretti et al. (2012) or in more recent papers (see Chapt. 2-3). We asked JVLA to observe 44 target clusters whose redshift distribution and sky projection are reported in the in Fig 6.1 and 6.2. Because of the high redshift we requested C array observations at L band since it has enough short baselines to map diffuse sources. However the possible presence of giant radio halos ($\sim 2 \text{ Mpc}$), radio bridges and peculiar structures strongly suggested us for shorter observations also in D configuration. We asked therefore for 15 minutes/target in D array L band to allow a good uv-coverage in the short baseline region, and a sensitivity near the confusion limit of $\sim 0.09 \text{ mJy/beam}$ (robust weight); 30 minutes/target in C array in L band and a sensitivity of $\sim 0.02 \text{ mJy/beam}$ to map faint structures and to subtract discrete sources. Combined data will produce images with a sensitivity of about $0.1 \mu\text{Jy/arcsec}$. Our proposal

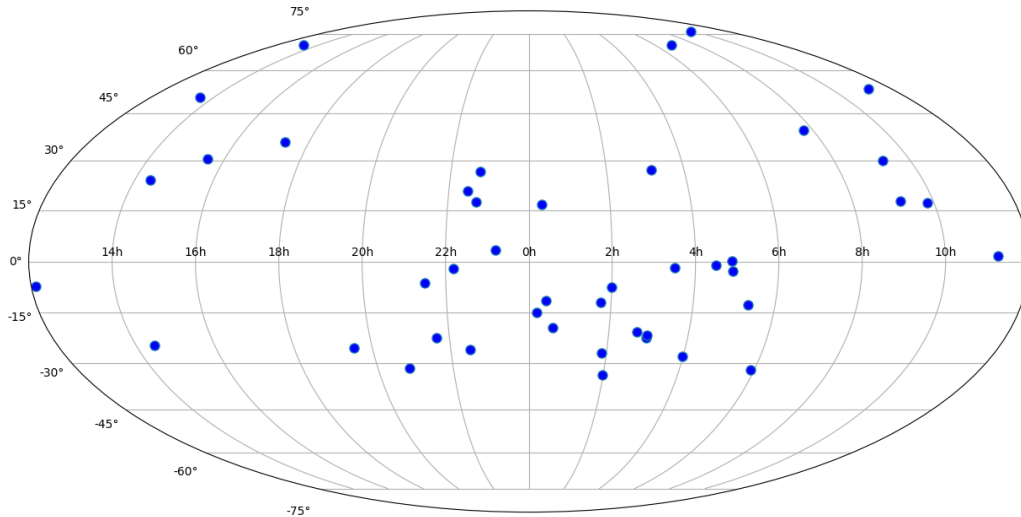


Figure 6.2: Sky distribution of the selected sample of MACS high redshift clusters.

has been accepted with ID: VLA/17A-025.

6.3 Project 17A-025: radio Observations and data reduction

In this section we present the details of the JVLA observations in D and C array carried out in the period February-August, 2017. Due to the large number of observed objects with the aim to reduce the data reduction time the VLA calibration pipeline has been applied on most of the requested clusters. The details of the observations are reported in the following subsections, some details about the flagging and calibration of the data with the VLA Calibration Pipeline are also reported.

6.3.1 D array observations

In tab. 6.2 we report the observed clusters processed with the VLA calibration pipeline and the details of the observations in the D configuration.

Table 6.2: Project 17A-025: details of the JVLA observations in D Array

Cluster	R.A. (J2000)	Decl. (J2000)	z	Obs. frequency ν GHz	Time mm:ss	Observation date
MACSJ0011.7–1523	00 11 42.9	–15 23 22	0.379	1.008/2.032	10:50	03-Apr.-2017
MACSJ0018.5+1626	00 18 33.8	+16 26 16	0.546	1.008/2.032	10:20	20-Feb.-2017
MACSJ0025.4–1222	00 24 29.3	–12 22 37	0.584	1.008/2.032	09:45	03-Apr.-2017
MACSJ0035.4–2015	00 35 26.5	–20 15 48	0.352	1.008/2.032	11:50	03-Apr.-2017
MACSJ0152.5–2852	01 52 34.5	–28 53 36	0.413	1.008/2.032	10:50	08-Apr.-2017

Table 6.2 (*continued*)

Cluster	R.A. (J2000)	Decl. (J2000)	z	Obs. frequency ν GHz	Time mm:ss	Observation date
MACSJ0159.8-0849	01 59 49.4	-08 49 59	0.406	1.008/2.032	09:50	08-Apr.-2017
MACSJ0242.5-2132	02 42 35.9	-21 32 26	0.314	1.008/2.032	12:45	04-Mar.-2017
MACSJ0257.1-2325	02 57 09.1	-23 26 05	0.505	1.008/2.032	10:15	04-Mar.-2017
MACSJ0257.6-2209	02 57 41.1	-22 09 18	0.322	1.008/2.032	09:50	04-Mar.-2017
MACSJ0308.9+2645	03 08 55.8	+26 45 37	0.356	1.008/2.032	10:15	20-Feb.-2017
MACSJ0358.8-2955	03 58 54.5	-29 55 32	0.425	1.008/2.032	09:50	04-Mar.-2017
MACSJ0647.7+7015	06 47 50.4	+70 14 54	0.591	1.008/2.032	11:45	14-Feb.-2017
MACSJ0744.8+3927	07 44 52.4	+30 27 27	0.698	1.008/2.032	09:50	14-Feb.-2017
MACSJ0911.2+1746	09 11 11.2	+17 46 31	0.505	1.008/2.032	12:15	14-Feb.-2017
MACSJ0947.2+7623	09 47 13.0	+76 23 14	0.354	1.008/2.032	09:45	14-Feb.-2017
MACSJ0949.8+1708	09 49 51.7	+17 07 08	0.384	1.008/2.032	09:50	14-Feb.-2017
MACSJ1115.8+0129	11 15 52.0	+01 29 55	0.355	1.008/2.032	09:50	06-May-2017
MACSJ1206.2-0847	12 06 12.2	-08 48 01	0.439	1.008/2.032	09:20	06-May-2017
MACSJ1427.6-2521	14 27 39.4	-25 21 02	0.363	1.008/2.032	09:15	06-May-2017
MACSJ1931.8-2634	19 31 49.6	-26 34 34	0.352	1.008/2.032	14:45	12-Feb.-2017
MACSJ2049.9-3217	20 49 56.2	-32 16 50	0.323	1.008/2.032	10:50	12-Feb.-2017
MACSJ2129.4-0741	21 29 26.2	-07 41 26	0.589	1.008/2.032	10:20	12-Feb.-2017
MACSJ2140.2-2339	21 40 15.2	-23 39 40	0.313	1.008/2.032	10:50	12-Feb.-2017
MACSJ2211.7-0349	22 11 46.0	-03 49 47	0.397	1.008/2.032	09:45	12-Feb.-2017
MACSJ2214.9-1359	22 14 57.4	-14 00 10	0.503	1.008/2.032	10:45	12-Feb.-2017
MACSJ2228.5+2036	22 28 34.0	+20 37 18	0.411	1.008/2.032	12:15	13-Feb.-2017
MACSJ2228.5+2036	22 28 34.0	+20 37 18	0.411	1.008/2.032	14:15	20-Feb.-2017
MACSJ2229.7-2755	22 29 45.2	-27 55 37	0.324	1.008/2.032	09:50	12-Feb.-2017
MACSJ2241.8+1732	22 41 50.6	+17 31 42	0.314	1.008/2.032	09:50	13-Feb.-2017
MACSJ2241.8+1732	22 41 50.6	+17 31 42	0.314	1.008/2.032	10:45	20-Feb.-2017
MACSJ2245.0+2637	22 45 04.6	+26 38 05	0.301	1.008/2.032	09:45	13-Feb.-2017
MACSJ2245.0+2637	22 45 04.6	+26 38 05	0.301	1.008/2.032	10:45	20-Feb.-2017
MACSJ2311.5+0338	23 11 33.1	+03 38 07	0.305	1.008/2.032	10:50	20-Feb.-2017

Three clusters: MACSJ2228.5, MACSJ2241.8 and MACSJ2245.0 have been observed twice on two different days. Their measurement sets have been combined with the CASA task concat.

6.3.2 C array observations

In tab. 6.3 we report the observed sources, processed with the VLA calibration pipeline and the details of the observations in the C configuration.

Among the observed clusters 31 clusters in D array and 36 clusters in C

Table 6.3: Project 17A-025: details of the JVLA observations in C Array

Cluster	R.A. (J2000)	Decl. (J2000)	z	Obs. frequency ν GHz	Time mm:ss	Observation date
MACSJ0011.7-1523 ^d	00 11 42.9	-15 23 22	0.379	1.008/2.032	24:40	17-Jul.-2017
MACSJ0018.5+1626 ^d	00 18 33.8	+16 26 16	0.546	1.008/2.032	23:40	01-Jul.-2017
MACSJ0025.4-1222 ^d	00 24 29.3	-12 22 37	0.584	1.008/2.032	23:40	17-Jul.-2017
MACSJ0035.4-2015 ^d	00 35 26.5	-20 15 48	0.352	1.008/2.032	23:45	17-Jul.-2017
MACSJ0152.5-2852	01 52 34.5	-28 53 36	0.413	1.008/2.032	24:40	09-Jul.-2017
MACSJ0159.0-3412 ^d	01 59 00.3	-34 13 00	0.458	1.008/2.032	23:40	09-Jul.-2017
MACSJ0159.8-0849 ^d	01 59 49.4	-08 49 59	0.406	1.008/2.032	23:40	09-Jul.-2017
MACSJ0242.5-2132 ^d	02 42 35.9	-21 32 26	0.314	1.008/2.032	25:40	06-Jul.-2017
MACSJ0257.1-2325 ^d	02 57 09.1	-23 26 05	0.505	1.008/2.032	24:40	06-Jul.-2017
MACSJ0257.6-2209 ^d	02 57 41.1	-22 09 18	0.322	1.008/2.032	24:45	06-Jul.-2017

Table 5.3 (*continued*)

Cluster	R.A. (J2000)	Decl. (J2000)	z	Obs. frequency ν GHz	Time mm:ss	Observation date
MACSJ0308.9+2645 [‡]	03 08 55.8	+26 45 37	0.356	1.008/2.032	24:10	01-Jul.-2017
MACSJ0329.7-0212	03 29 40.8	-02 11 53	0.450	1.008/2.032	27:40	08-Jul.-2017
MACSJ0358.8-2955 [‡]	03 58 54.5	-29 55 32	0.425	1.008/2.032	24:40	06-Jul.-2017
MACSJ0429.6-0253	04 29 36.0	-02 53 08	0.399	1.008/2.032	24:40	08-Jul.-2017
MACSJ0451.9+0006	04 51 55.0	+00 06 14	0.430	1.008/2.032	24:40	08-Jul.-2017
MACSJ0454.1-0300	04 54 11.1	-03 00 53	0.538	1.008/2.032	24:40	08-Jul.-2017
MACSJ0520.7-1328	05 20 42.0	-13 28 50	0.336	1.008/2.032	23:30	01-Jul.-2017
MACSJ0553.4-3342	05 53 27.1	-33 42 53	0.407	1.008/2.032	24:45	01-Jul.-2017
MACSJ0647.7+7015 [‡]	06 47 50.4	+70 14 54	0.591	1.008/2.032	22:40	24-Jun.-2017
MACSJ0744.8+3927 [‡]	07 44 52.4	+30 27 27	0.698	1.008/2.032	25:10	22-Jul.-2017
MACSJ0911.2+1746 [‡]	09 11 11.2	+17 46 31	0.505	1.008/2.032	24:40	22-Jul.-2017
DLSCJ0916.2+2951	09 16 09.0	+29 52 00	0.520	1.008/2.032	23:40	22-Jul.-2017
MACSJ0947.2+7623 [‡]	09 47 13.0	+76 23 14	0.354	1.008/2.032	21:45	25-Jun.-2017
MACSJ0949.8-1708 [‡]	09 49 51.7	+17 07 08	0.384	1.008/2.032	23:40	22-Jul.-2017
MACSJ1115.2+5320	11 15 14.8	+53 20 13	0.466	1.008/2.032	24:40	28-Aug.-2017
MACSJ1319.9+7003	13 20 08.4	+70 04 37	0.327	1.008/2.032	24:10	28-Aug.-2017
MACSJ1423.8+2404	14 23 47.6	+24 04 40	0.543	1.008/2.032	25:15	17-Jul.-2017
MACSJ1532.8+3201	15 32 53.8	+30 20 58	0.363	1.008/2.032	24:40	17-Jul.-2017
MACSJ1720.2+3536	17 20 16.8	+35 36 26	0.387	1.008/2.032	23:40	17-Jul.-2017
MACSJ1931.8-2634 [‡]	19 31 49.6	-26 34 34	0.352	1.008/2.032	22:40	26-May-2017
MACSJ2049.9-3217 [‡]	20 49 56.2	-32 16 50	0.323	1.008/2.032	21:45	26-May-2017
MACSJ2129.4-0741 [‡]	21 29 26.2	-07 41 26	0.589	1.008/2.032	23:45	24-May-2017
MACSJ2211.7-0349 [‡]	22 11 46.0	-03 49 47	0.397	1.008/2.032	23:10	24-May-2017
MACSJ2228.5+2036 [‡]	22 28 34.0	+20 37 18	0.411	1.008/2.032	25:40	21-May-2017
MACSJ2241.8+1732 [‡]	22 41 50.6	+17 31 42	0.314	1.008/2.032	23:40	21-May-2017
MACSJ2245.0+2637 [‡]	22 45 04.6	+26 38 05	0.301	1.008/2.032	23:40	21-May-2017
MACSJ2311.5+0338 [‡]	23 11 33.1	+03 38 07	0.305	1.008/2.032	23:40	01-Jul.-2017

[‡] cluster observed also in the D array

array have been reduced with the pipeline, 25 clusters have been observed and reduced both in C and D configuration and therefore 42 different clusters have been observed and reduced. For some clusters, we performed calibration and imaging using both CASA and AIPS (Astronomical Image Processing System) to check the VLA pipeline performance and when the pipeline results were not satisfactory.

6.3.3 the VLA calibration pipeline

The VLA calibration pipeline is a NRAO facility tool to perform basic flagging and calibration on VLA data and it consists in a collection of python scripts that use CASA, the Common Astronomy Software Applications package being developed for supporting the data post-processing tasks. VLA pipeline performs the following operations:

- loads the data in a SDM-BDF format to a CASA MeasurementSet (MS), performs a Hanning smoothing extracting info about contents;
- applies online flags and other deterministic flags;

- sets flux calibration models (primary flux calibrators);
- derives pre-determined calibrations (antenna position corrections, gain curves, atmospheric opacity corrections, requantizer gains, etc.);
- iteratively determines initial delay and bandpass calibrations, including flagging of RFI (Radio Frequency Interference) and some automated identification of system problems;
- derives initial gain calibration, and derives the spectral index of the bandpass calibrator;
- derives final delay, bandpass, and gain/phase calibrations, and applies them to the data;
- runs the RFI flagging algorithm on the target data;
- calculates data weights based on the inverse square RMS noise of the MS;

6.3.4 imaging

The imaging of the observed clusters was performed with the Common Astronomy Software Applications package v.5.0 (CASA; McMullin et al. 2007). From the calibrated measurement sets obtained with the pipeline, we extracted the uv data of each cluster using the CASA task `split`. Automatic RFI flagging was applied using the task `flagdata` (mode= `rflag`). We run several rounds of phase-only and a final amplitude and phase self-calibration. Wide band imaging is crucial when dealing with the 1 GHz bandwidth of the JVLA, therefore we used two Taylor terms (`nterms` = 2) to take the frequency dependence of the brightness distribution into consideration. For the self calibration we used a `natural` weighting. For some of the cluster showing diffuse emission, we combined, after a separate self calibration, the C and D array when both available using CASA task `concat`. The error Δ_{S_ν} associated with the measured radio flux is calculated as:

$$\Delta_{S_\nu} = \sqrt{\left(rms \times \sqrt{\frac{A_s}{A_b}} \right)^2 + (\sigma_c \times S_\nu)^2} \quad (6.1)$$

where A_s is the source area (pixels), A_b is the beam area (pixels) and σ_c is the calibration uncertainty, estimated around 5% for the JVLA.

6.4 Data reduction and imaging results I. Detection of diffuse emission: halos and relics

In this section we present the clusters observed in our JVLA campaign where evidences of diffuse emission have been detected. We carried out an analysis of the radio properties also respect to the X-ray and the optical images, extracted from the Chandra Data Archive and from ESO DSS2-red Survey, respectively.

6.4.1 MACSJ0018.5+1626

MACSJ0018.5+1626 is a massive ($M_{500} = 7.78 \pm 1.25 \times 10^{14} M_{\odot}$), X-ray luminous ($L_{X,500} = 1.79 \pm 0.03 \times 10^{45}$ erg/s), hot ($kT = 9.4 \pm 1.3$ keV) cluster situated at $z=0.5456$ (Ebeling et al. 2007; Piffaretti et al. 2011). It is identified with CL 0016+1609 (Ebeling et al. 2007). Our JVLA observations in C and D array detect an extended diffuse radio emission located at the center of the cluster. The C array radio iso-contours at 1.32 GHz overlapped with the optical (DSS2-red) and 0.1–10.0 keV X-ray (CHANDRA) images are reported in Fig. 6.3 and 6.4 respectively. The radio image has an FWHM of 40 arcsec \times 40 arcsec and the total flux density is estimated to be (8.7 ± 0.1) mJy. This flux corresponds to a radio power $P_{1.4GHz} = (11.7 \pm 0.1) \times 10^{24}$ W/Hz, adopting a spectral index $\alpha = 1.3$ for the k -correction (see e.g. Casano et al. 2013). The diffuse emission has an angular extension of about 4.1' (the Largest Linear Size is $LLS \simeq 1.57$ Mpc at the cluster distance). The presence of diffuse radio emission in CL0016+16 first observed by Moffet & Birkinshaw (1989) was confirmed by Giovannini & Feretti (2000) as a giant radio halo. They also noticed the presence of a fainter radio emission west of the halo coincident with a galaxy group visible in the optical image. Our image with a better sensitivity and angular resolution shows a giant diffuse radio halo. The W emission appears connected with the giant halo. We consider all the diffuse emission as a unique source possibly related to the filamentary structure surrounding MACSJ0018.5+1626. Geach et al. (2010) who studied the star formation in this filamentary large-scale structure found in the halo region the presence of an overdensity with probability of galaxies characterized by enhanced star formation. We report in the following table the main characteristics of the radio halo.

Table 6.4: Properties of the extended source in MACSJ0018.5+1626 (CL 0016+26)

Cluster Name	z	M_{500} $10^{14} M_{\odot}$	$L_{X,500}$ 10^{44} erg/s	T_X keV	ν_{obs} GHz	Type	S_{ν} mJy	$P_{1.4}$ 10^{24} W/Hz	LLS (kpc)
MACSJ0018.5	0.546	7.78	17.9	9.4	1.322	H	8.7 ± 0.1	11.7 ± 0.1	1.57

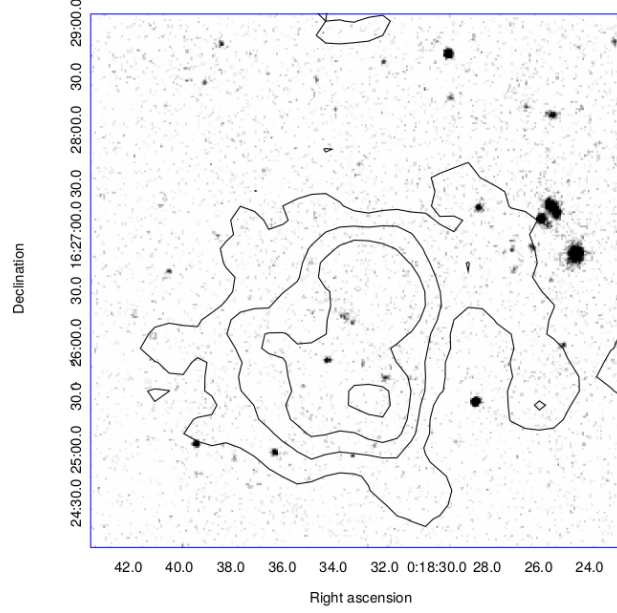


Figure 6.3: MACSJ0018.5+1626 total intensity radio contour at 1.322 GHz with the JVLA in C configuration. The image has a restoring FWHM of $40'' \times 40''$ ($PA = 0^\circ$). Levels at (0.300, 0.500, 0.700, 1, 3, 5, 10, 30, 50, 100, 200) mJy/beam (the rms is 0.05 mJy/beam). The contours of radio intensity are overlaid on the optical image taken from the DDS2 Sky Survey.

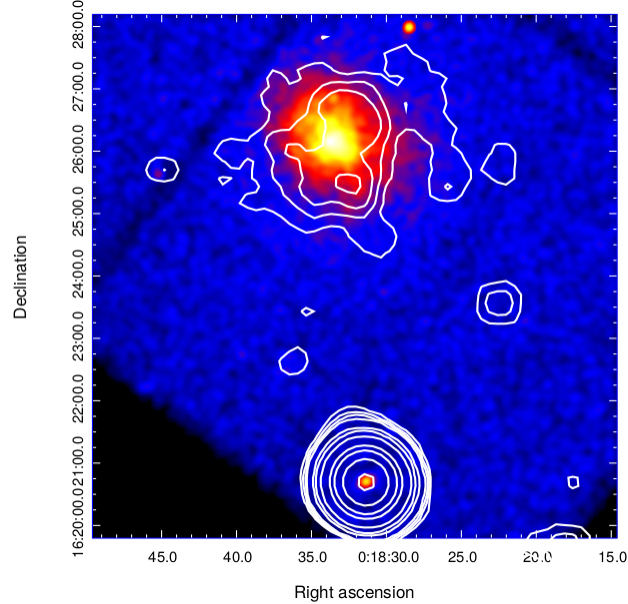


Figure 6.4: MACSJ0018.5+1626 total intensity radio contour (the same of Fig. 6.3) with the JVLA in C configuration overlaid on the CHANDRA X-ray color image.

6.4.2 MACSJ0025.4–1222

MACSJ0025.4–1222 is one of the clusters identified by Ebeling et al. (2007) in the Massive Cluster Survey sample of high X-ray luminosity and high redshift clusters at $z = 0.5843$. The *Chandra* MCXC R_{500} X-ray luminosity in the 0.1–2.4 keV band is $(8.0 \pm 0.2) \times 10^{44}$ erg/s, the temperature $kT = (7.1 \pm 0.7)$ keV and the $M_{500} = (4.64 \pm 0.70) \times 10^{14} M_{\odot}$. Riseley et al. (2017) reported the GMRT observation at 325 MHz of MACSJ0025.4 and the detection of two diffuse sources that appear consistent with a pair of radio relics in the NW and SE position respect to the X-ray center. Our radio images obtained with the C and D array data-set are of not good quality due to RFI presence during the observations. Nevertheless we found two extended radio structures symmetrically located in the same directions respect to the X-ray center as represented in Fig. 6.5 where radio contours are overlaid to the DSS2 optical image. In the right-hand panel a higher resolution image with the C array data-set is reported: three point sources (labeled with 1, 2 and 3) appear clearly distinguishable. The total flux density (primary beam corrected) of the SE source is (37.1 ± 1.9) mJy while the flux density of the NW source is (1.2 ± 0.1) mJy. Point sources have fluxes: 1 (7.4 ± 0.4) mJy, 2 (3.5 ± 0.2) mJy and 3 (24.5 ± 1.2) mJy respectively. By subtracting the flux density of these embedded discrete sources a flux density of (1.7 ± 0.1) appears to be associated with the SE low brightness diffuse emission. More uncertain is the question about the NW source: no any point source seems to be associated and its position appears displaced of about $1'$ respect to the NW relic location detected by Riseley et al. (2017). Even if the flux densities of the detection at 325 MHz and 1400 MHz are comparable (adopting a spectral index $\alpha = 1.1$) we cannot argue no conclusion or hypothesis because of the not good quality of our radio data. In tab. 6.5 are summarized the main characteristics of the diffuse emission measured in our observation and reported by Riseley et al. (2017). In Fig. 6.6 the radio image of the cluster is superimposed to the *Chandra* X-ray image.

Table 6.5: Properties of the extended sources of MACSJ0025.4–1222

Cluster Name	z	M_{500} $10^{14} M_{\odot}$	$L_{X,500}$ 10^{44} erg/s	T_X keV	ν_{obs} GHz	Type	S_{ν} mJy	$P_{1.4}$ 10^{24} W/Hz	LLS (kpc)
MACSJ0025-SE	0.5483	4.64	8.0	7.1	1.423	R (c)	1.7 ± 0.1	1.76 ± 0.20	601
					0.325	R	8.88 ± 1.01		640
MACSJ0025-NW					1.423	R (c)	1.2 ± 0.1	1.29 ± 0.14	250
					0.325	R	6.54 ± 0.73		577

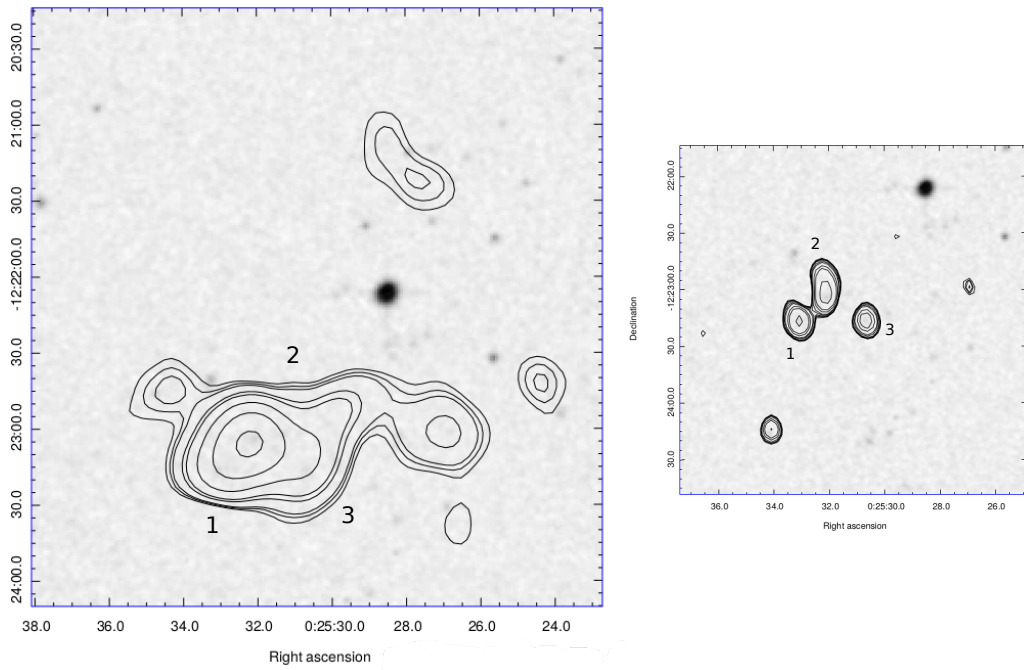


Figure 6.5: *Left panel:* MACSJ0025.4–1222 total intensity radio contour at 1.42 GHz with the JVLA overlaid to the DSS2 optical image. The FWHM (restoring beam) of the radio image is $21'' \times 21''$ (PA= 0.0°). Contour levels are at $(3, 5, 6, 14, 18, 36, \dots) \times \sigma$ with rms noise $\sigma = 0.13$ mJy/beam. *Right panel:* C array high resolution map of MACSJ0025.4–1222. The beam is $12.21'' \times 9.23''$ (PA= 2.82°). The point sources are labelled with 1, 2, 3.

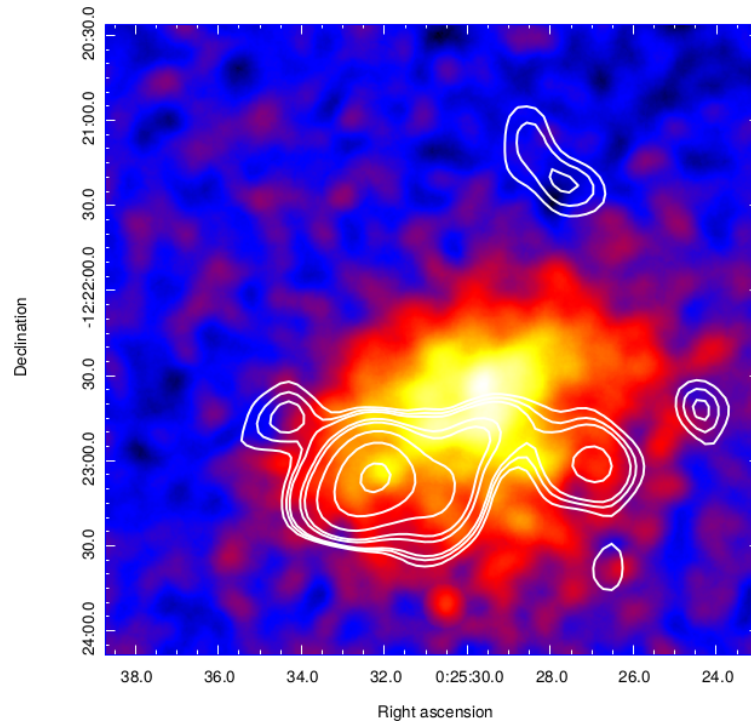


Figure 6.6: MACSJ0025.4–1222 total intensity radio contour at 1.42 GHz (the same of Fig. 6.5, *left panel*) overlaid on the CHANDRA X-ray color image.

6.4.3 MACSJ0152.5–2852

This massive cluster ($M_{500} = 7.90 \times 10^{14} M_{\odot}$) is reported in the MCXC meta-catalog with an X-ray luminosity in the 0.1–2.4 keV band $L_{X,500} = (8.6 \pm 0.5) \times 10^{44}$ erg/s and a temperature $kT = (4.7 \pm 0.5)$ keV at redshift $z = 0.413$ (Ebeling et al. 2010; Piffaretti et al. 2011). Ebeling et al. (2010) assigned to this cluster a morphological class 2 with a good optical/X-ray alignment and concentric contours. This class is intermediate between 1 (apparently relaxed) and 4 (extremely disturbed). The optical image does not show a dominant galaxy. No radio observations are reported in the literature. We have combined the C and D array data-sets obtaining the image of fig. 6.7 where the radio contours are overlaid to the optical image. We found in the central region of MACSJ0152.5 the presence of a low-surface brightness diffuse emission, with a discrete source embedded. The radio morphology of this diffuse emission is quite regular with a round shape and the center slightly shifted respect to the X-ray center (see Fig. 6.8) and a LAS of about $1.9'$, corresponding to a projected largest linear size (LLS) of ~ 620 kpc at the cluster distance. We classify this source as a candidate radio halo. To separate the diffuse emission from the discrete sources, we produced an image at higher resolution reported in the right panel of Fig. 6.7 using the C array data-set. The discrete sources are labeled with A, B and C: only source A is embedded within the diffuse emission while source B appear only marginally embedded. A total flux density of (2.65 ± 0.13) mJy is calculated from the C+D datasets, by integrating the total intensity surface brightness in the region of the diffuse emission down to the 3σ level. By subtracting the flux density of the two embedded discrete sources A (0.19 ± 0.01) mJy and B (0.12 ± 0.01) mJy as calculated from the C configuration dataset, we find a diffuse source with a flux density of (2.34 ± 0.15) mJy. This flux density corresponds to a radio power of $P_{1.4GHz} = (1.58 \pm 0.10) \times 10^{24}$ W/Hz assuming a spectral index $\alpha = 1.3$ for the k -correction. In table 6.6 we summarize the properties of the extended source.

Table 6.6: Properties of the extended source of MACSJ0152.5–2852

Cluster Name	z	M_{500} $10^{14} M_{\odot}$	$L_{X,500}$ 10^{44} erg/s	T_X keV	ν_{obs} GHz	Type	S_{ν} mJy	$P_{1.4}$ 10^{24} W/Hz	LLS (kpc)
MACSJ0152.5	0.413	7.90	8.6	7.4	1.5	H (c)	2.34 ± 0.15	1.58 ± 0.10	620

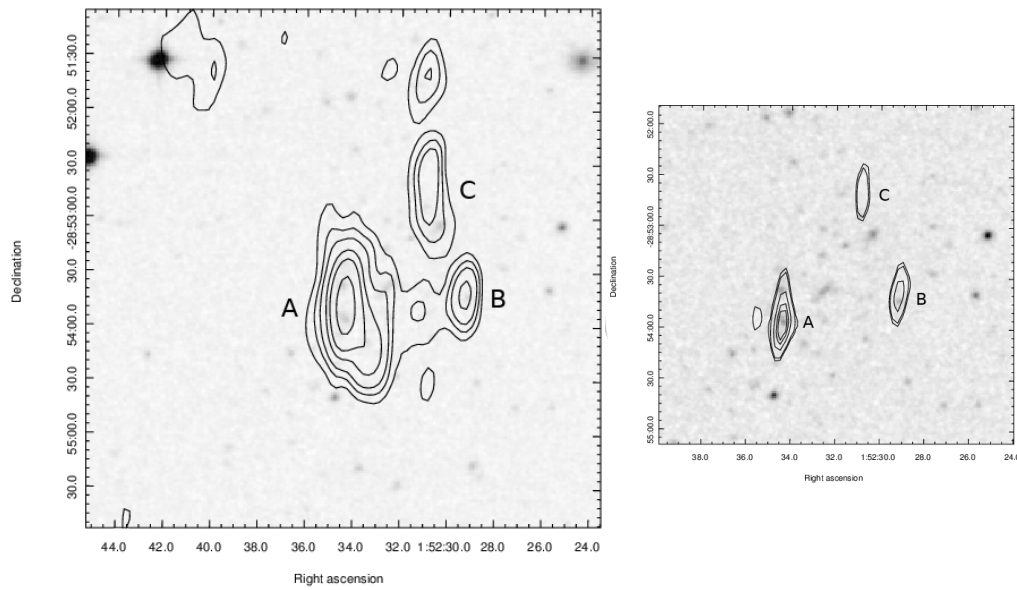


Figure 6.7: *Left panel:* total intensity C+D array radio contours of MACSJ0152.5–2852 at 1.52 GHz. The image has an FWHM of $36.19'' \times 15.25''$ (PA = -6.41°). Contour levels are at $(3, 6, 9, 12, 24, 48, \dots) \times \sigma$ with rms noise $\sigma = 0.034$ mJy/beam. *Right panel:* JVLA C array contours using only the longest baselines. The beam is $26.33'' \times 6.66''$ (PA = -5.45°). All radio images are superimposed on the optical DDS image. Point sources are labeled with A, B, C.

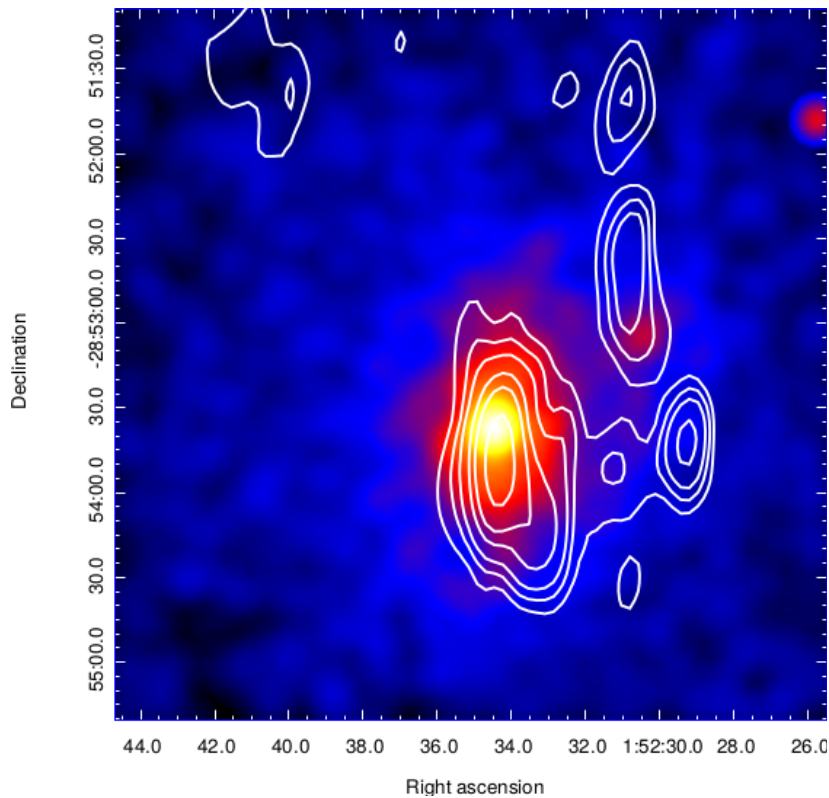


Figure 6.8: MACSJ0152.5–2852 C+D total intensity radio contour (the same of Fig. 6.7, *left panel*) overlaid on the CHANDRA X-ray color image.

6.4.4 MACSJ0257.6–2209

MACSJ0257.6–2209, also known as A402, has been classified by Ebeling et al. (2010) in the morphological class 2 (good optical/X-ray alignment, concentric contours) and therefore it is characterized by a moderately disturbed dynamical state. At redshift $z = 0.322$ its X-ray luminosity is $L_{X,500} = (7.0 \pm 0.4) \times 10^{44}$ erg/s, the mass is $M_{500} = 5.88 \times 10^{14} M_{\odot}$ and (7.0 ± 0.9) keV the temperature. The C and D array measurement sets have been combined and the resulting images are reported in Fig. 6.9. With a restoring beam of $37'' \times 37''$ (PA= 0°) and contour levels $(3, 6, 9, 12, \dots) \times \sigma$ ($\sigma = 0.048$ mJy/beam) the image on the *left panel* shows a complex radio emission where almost 5 discrete sources appear connected. The total flux density of this radio structure at 1.5 GHz is (43.47 ± 2.17) mJy. In the *right panel* is reported the image obtained with the C array using the longest baselines (uv -range $> 7k\lambda$) to discriminate the point sources from the diffuse emission. It is possible to recognize the 5 discrete sources labelled from A to E. Their respective flux densities are: A (2.50 ± 0.13) mJy, B (1.46 ± 0.07) mJy, C (0.14 ± 0.01) mJy, D (0.16 ± 0.01) mJy, and E formed by 3 different sources (17.27 ± 0.88) mJy. By subtracting the flux densities of these point sources from the total flux density of the complex structure we found (21.94 ± 3.27) mJy corresponding to a radio power at 1.4 GHz $(5.48 \pm 0.82) \times 10^{24}$ W/Hz adopting a spectral index $\alpha = 1.3$ for the k -correction. From the radio image overlaid to the X-ray *Chandra* image (see Fig. 6.10) the diffuse emission appears centered to the X-ray center surrounding towards the East-West direction the discrete radio sources. We classify the central part of diffuse emission as a candidate radio halo. Because of the great difficulty to properly subtract the point sources from the complex structure it is not easy to estimate the LAS of the diffuse emission. We report in the following table the main characteristics of the extended source of the cluster.

Table 6.7: Properties of the extended source of MACSJ0257.6–2209

Cluster Name	z	M_{500} $10^{14} M_{\odot}$	$L_{X,500}$ 10^{44} erg/s	T_X keV	ν_{obs} GHz	Type	S_{ν} mJy	$P_{1.4}$ 10^{24} W/Hz	LLS (kpc)
MACSJ257.6	0.322	5.88	7.0	7.0	1.487	H (c)	21.94 ± 3.27	5.48 ± 0.82	300

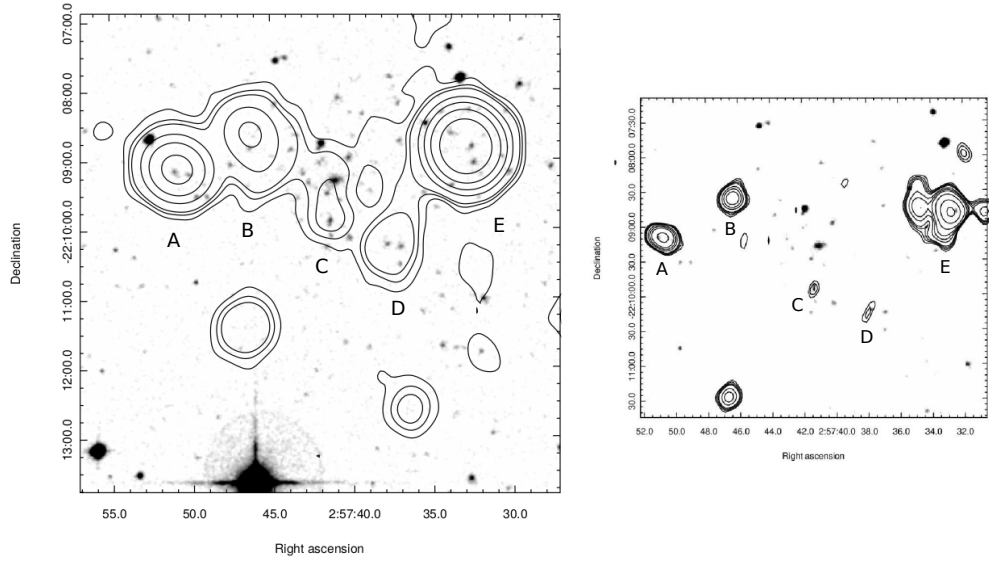


Figure 6.9: *Left panel:* MACSJ0257.6–2209 total intensity radio contour at 1.5 GHz with the JVLA in C+D configuration overlaid to the DSS2 optical image. The FWHM (restoring beam) of the radio image is $37'' \times 37''$ (PA= 0°). Contour levels are at (3, 6, 9, 12, ...) $\times \sigma$ with rms noise $\sigma = 0.048$ mJy/beam. *Right panel:* C array image of MACSJ0744.9+3927 compact sources obtained with a uv -range > 8 k λ . The restoring beam is $20'' \times 20''$ (PA= 48.7°). Point sources are labelled with A, B, C, D, and E.

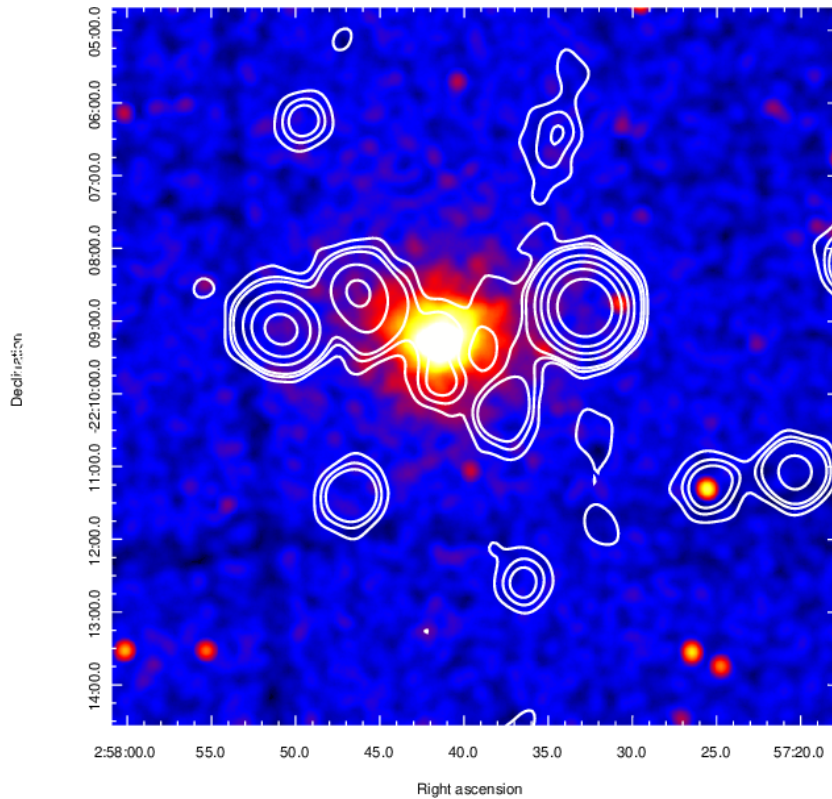


Figure 6.10: MACSJ025.4–1222 total intensity radio contour at 1.5 GHz with the JVLA in C+D configuration overlaid on the CHANDRA X-ray color image.

6.4.5 MACSJ0308.9+2645

It is a massive ($M_{500} = 10.75 \times 10^{14} M_{\odot}$), hot with $kT = (10.5 \pm 1.1)$ keV and X-ray luminous ($L_{X,500} = (17.9 \pm 0.9) \times 10^{44}$) cluster at $z = 0.356$. Ebeling et al. (2010) classified MACSJ0308.9 as extremely disturbed and assigned to it the morphological class 4 (poor optical/X-ray alignment, multiple peaks, no cD galaxy). Parekh et al. (2017) performed an X-ray morphological analysis of this cluster using *Chandra* images. They found in the temperature map the presence of two nearby cool regions at the cluster center considering them as a part of merging clusters. They also detected with the GMRT at 610 MHz diffuse radio emission located between these two cool regions in the north-south direction roughly perpendicular to the merger axis joining the cool regions. They considered this diffuse emission as a candidate radio halo (Parekh et al. 2017). Our radio images, obtained combining the C and D array data-sets, show a very complex radio morphology with four point sources embedded by a diffuse radio emission. Because of the great difficulty to properly subtract the point sources from the diffuse emission, we produced radio images from the C-array data-set using the longest baselines. These images, superimposed to the DSS2 survey optical image of the cluster are reported in Fig. 6.11. The integrated flux of this complex system of sources (Fig. 6.11 *left*) within 3σ contour level is (39.2 ± 1.9) mJy. The flux density of the halo, obtained by subtracting the flux densities of the point sources A (8.78 ± 0.44) mJy, B (18.39 ± 0.92) mJy, C (1.95 ± 0.10) mJy and D (0.38 ± 0.02) mJy, is (9.70 ± 3.38) mJy. This value is comparable with the flux obtained at 610 MHz by Parekh et al. (2017) if extrapolated to 1.4 GHz adopting a spectral index $\alpha_{0.610GHz}^{1.4GHz} = 1.3$. The integrated spectral index of the radio halo, calculated using the observed flux values, results $\alpha_{0.610GHz}^{1.4GHz} = (1.36 \pm 0.42)$. The corresponding radio power at 1.4 GHz is $P_{1.4GHz} = 4.64 \times 10^{24}$ W/Hz. The radio halo of our images has a LAS of about $2.6'$ corresponding to a projected size LLS ~ 750 kpc at the cluster distance and it is extended in the sud-north and west-est directions. In tab. 6.8 we summarize the properties of the diffuse emission detected with the JVLA and the GMRT.

Table 6.8: Properties of the extended source of MACSJ0308.9+2645

Cluster Name	z	M_{500} $10^{14} M_{\odot}$	$L_{X,500}$ 10^{44} erg/s	T_X keV	ν_{obs} GHz	Type	S_{ν} mJy	$P_{1.4}$ 10^{24} W/Hz	LLS (kpc)
MACSJ0308.9	0.356	10.75	8.6	7.4	1.5	H	9.7 ± 3.4	4.65	750
					0.610	H (c)	30.0 ± 4.1	2.09	850

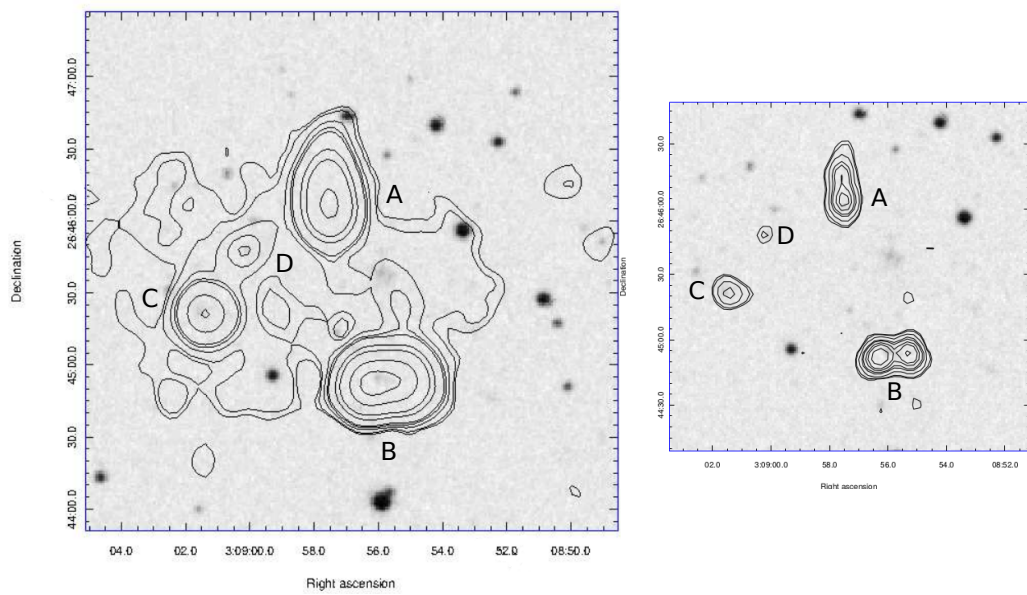


Figure 6.11: *Left panel:* MACSJ0308.5+2645 total intensity radio contour at 1.5 GHz with the JVLA in C+D configuration overlaid to the DSS2 optical image. The FWHM of the radio image is $16.20'' \times 14.61''$ (PA = -6.09°). Contour levels are at (3, 6, 9, 12, 24, 48, ...) $\times \sigma$ with rms noise $\sigma = 0.034$ mJy/beam. *Right panel:* C array high resolution map of MACSJ0308.5+2645. The beam is $8.74'' \times 7.71''$ (PA = -0.40°). The point sources are labeled with A, B, C and D.

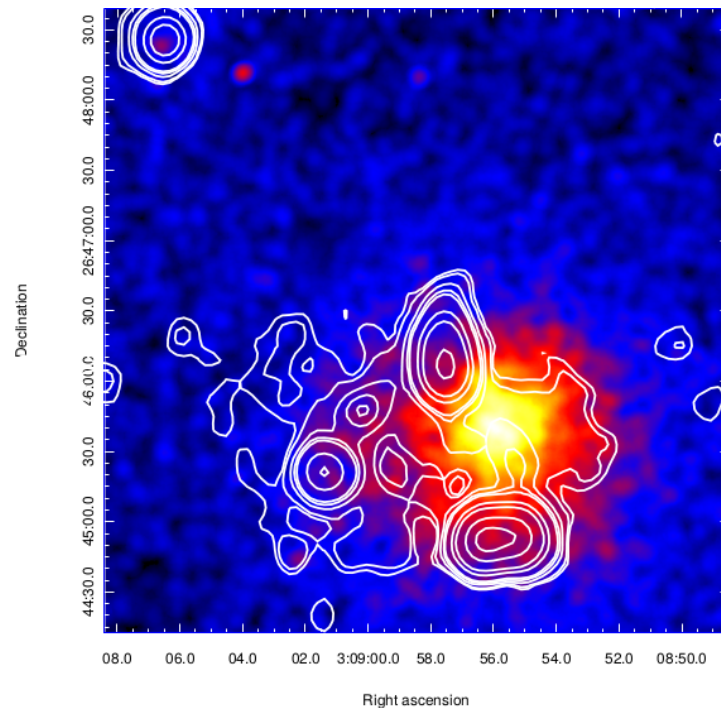


Figure 6.12: MACSJ0308.9+2645 total intensity radio contour at 1.5 GHz with the JVLA in C+D configuration overlaid on the CHANDRA X-ray color image.

6.4.6 MACSJ0451.9+0006

In the MCXC catalog this cluster is reported with a mass $M_{500} = 4.10 \times 10^{14} M_{\odot}$ and a X-ray luminosity $L_{500} = 6.75 \times 10^{44}$ erg/s. Morandi et al. (2015) from the *Chandra* archive reported a cluster temperature $kT = (7.66 \pm 1.04)$ keV with a centroid shift $\omega = (2.01 \pm 0.73)$ typical of a dynamically disturbed cluster. No radio studies of MACSJ0451.9+0006 are reported in the literature. The VLA L-band B array data set (project AE0147) contained in the NRAO Science data archive has been very useful to discriminate the point radio sources. In our project 17A-025 only the C array has been reduced with the VLA calibration pipeline and from this data we obtained the radio image contour reported in the *left panel* of Fig. 6.13. The FWHM is $24.30'' \times 15.02''$ (PA=0°) radio contours at 1.5 GHz are drawn at $(3, 4.5, 6.5, 15, 24, \dots) \times \sigma$ with $\sigma = 0.029$ mJy. A diffuse arc-like structure connects the 2 point-like radio sources labeled with A and B, where B is the source located in the X-ray center of the cluster. The flux density is (2.65 ± 0.13) mJy. From the morphology and the position of the arc respect to the cluster center ($\sim 0.7'$ corresponding to ~ 250 kpc at the cluster redshift, taking account for possible projection effects) we classify this source a candidate radio relic. The flux densities of the point sources A and B obtained from the VLA B array image are (0.61 ± 0.03) mJy and (0.52 ± 0.03) mJy respectively (*right panel* of Fig. 6.13). By subtracting the flux density of the arc-like structure from the fluxes of A and B we obtain for the radio relic a flux of (1.52 ± 0.19) mJy corresponding to a radio power $P_{1.4} = (1.13 \pm 0.14) \times 10^{24}$ W/Hz; the LAS is $\sim 1.7'$ corresponding to a LLS ~ 600 kpc at the cluster distance. We collect the properties of MACSJ0451.9+0006 in the following table.

Table 6.9: Properties of the extended source of MACSJ0451.9+0006

Cluster Name	z	M_{500} $10^{14} M_{\odot}$	$L_{X,500}$ 10^{44} erg/s	T_X keV	ν_{obs} GHz	Type	S_{ν} mJy	$P_{1.4}$ 10^{24} W/Hz	LLS (kpc)
MACSJ0451.9	0.430	4.10	6.75	7.66	1.520	R (c)	1.52 ± 0.19	1.13 ± 0.14	600

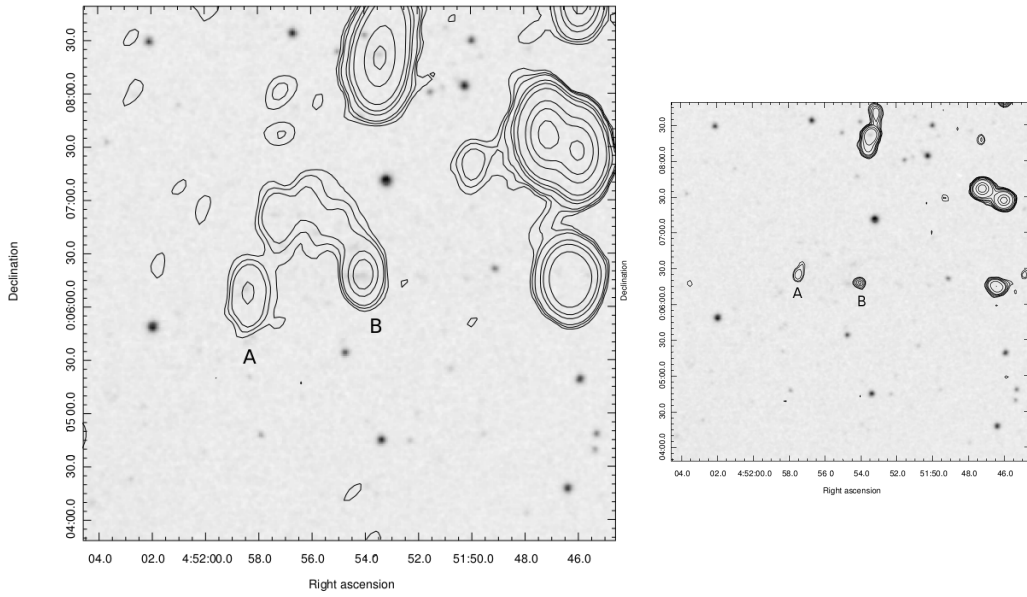


Figure 6.13: *Left panel:* MACSJ0451.9+0006 total intensity radio contour at 1.520 GHz with the JVLA in C configuration overlaid to the DSS2 optical image. The FWHM of the radio image $24.30'' \times 15.02''$ (PA=0°). Contour levels are at $(3, 4.5, 6.5, 15, 24, \dots) \times \sigma$ with $\sigma = 0.029$ mJy/beam. *Right panel:* B array map of MACSJ0451.9+0006 at 1.425 GHz. The beam is $7.0'' \times 7.0''$ (PA= 0°) with rms 0.02 mJy. The point sources are labelled with A and B.

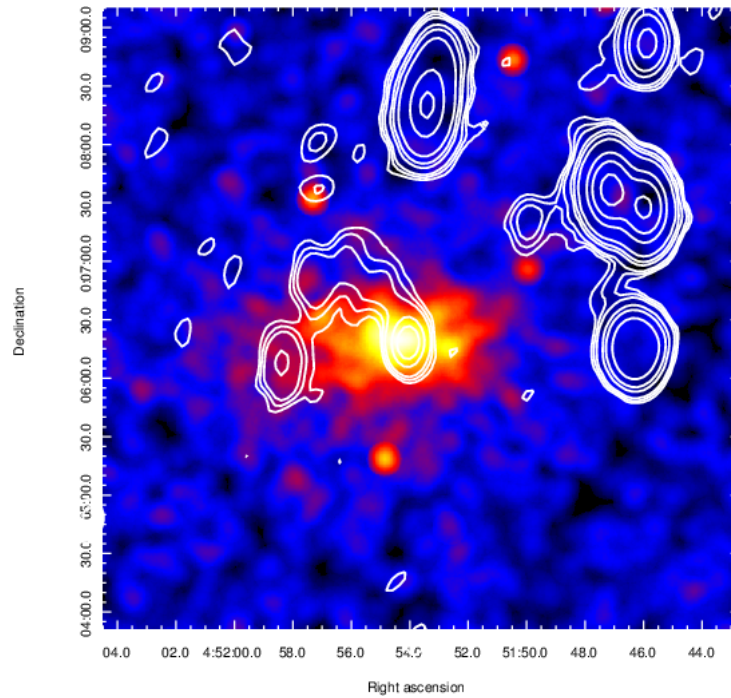


Figure 6.14: MACSJ0451.9+0006 total intensity radio contour at 1.5 GHz (the same of Fig. 6.13 *left panel*) overlaid on the CHANDRA X-ray image.

6.4.7 MACSJ0454.1–0300

MACSJ0454.1–0300 reported in Ebeling et al. (2007) where are listed a subset of 12 galaxy clusters detected at $z > 0.5$ has the following main characteristics: $M_{500} = (7.13 \pm 2.8) \times 10^{14} M_{\odot}$, $L_{500} = (15.4 \pm 0.6) \times 10^{44}$ and $kT = 7.5 \pm 1.0$ keV at redshift $z = 0.5377$. A morphological code 2 (good optical/X-ray alignment, concentric contours) classifies the dynamical state of this cluster as intermediate between apparently relaxed and extremely disturbed. No detection of diffuse radio emission is reported in the literature. Also for this cluster it is available only the C array. In the low-resolution image of Fig. 6.15 (*left panel*) with a restoring beam $33'' \times 33''$ (PA=0°) we found a diffuse emission embedding two discrete sources symmetrically located in the East-West direction respect to the X-ray center of the cluster. The flux density of the whole radio structure at 1.520 GHz is (3.59 ± 0.18) mJy. Performing a high resolution image of the cluster (w -range > 7 k λ) with a FWHM (restoring beam) of $11'' \times 11''$ (PA=0°) we estimated the flux density of the point sources labelled with 1 and 2 and found (1.07 ± 0.05) mJy for the source 1 and (1.60 ± 0.08) mJy for source 2. The radio contours are reported in the *right panel* of Fig. 6.15. Using the CASA task `uvsub` we performed the subtraction of the point sources and the resulting image of the radio contours shows the presence of a residual diffuse emission located just between the two subtracted sources (1 and 2). The restoring beam of the image is 30 arcsec \times 30 arcsec (PA=0°) and the flux density of the diffuse source is (1.04 ± 0.05) mJy, value in agreement with the flux density calculated as the difference between the central whole radio emission and the point sources. The radio power at 1.4 GHz results $P_{1.4} = (1.35 \pm 0.06) \times 10^{24}$ W/Hz adopting a spectral index $\alpha = 1.3$. The LAS estimated with a gaussian fit is $\sim 0.9'$ corresponding to a LLS of ~ 350 kpc at the cluster distance. If we consider the shape of the diffuse emission we classify the detected diffuse emission as a candidate radio halo, however its position displaced of about $20''$ (127 kpc) from the X-ray center would not exclude the possibility to consider this diffuse emission as a candidate radio relic. The following table reports the main characteristics of the extended source of MACSJ0454.1–0300.

Table 6.10: Properties of the extended source of MACSJ0454.1–0300

Cluster Name	z	M_{500} $10^{14} M_{\odot}$	$L_{X,500}$ 10^{44} erg/s	T_X keV	ν_{obs} GHz	Type	S_{ν} mJy	$P_{1.4}$ 10^{24} W/Hz	LLS (kpc)
MACSJ0454.1	0.538	7.13	15.4	7.5	1.520	H (c)	1.04 ± 0.05	1.35 ± 0.06	350

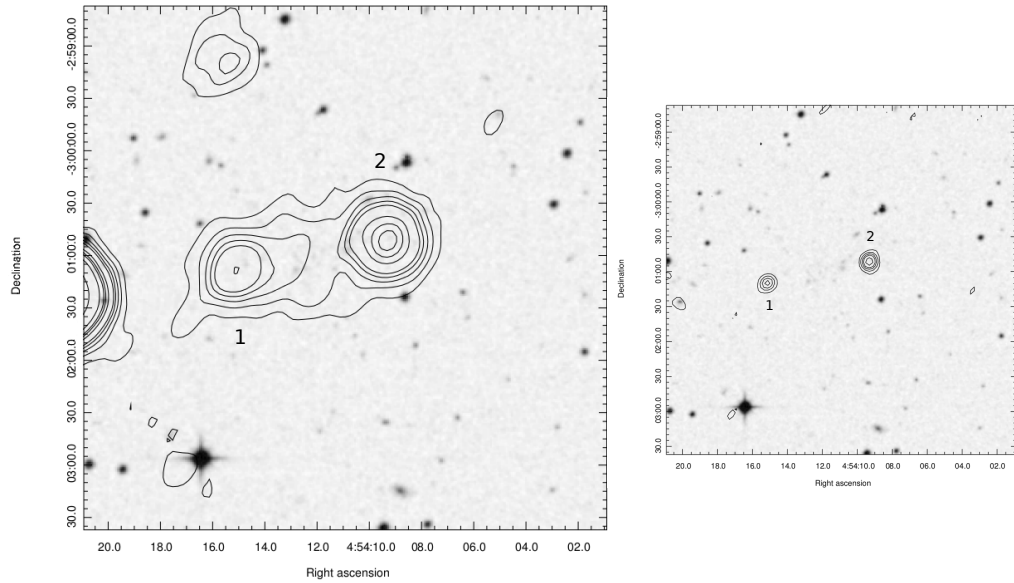


Figure 6.15: *Left panel:* MACSJ0454.1–0300 total intensity radio contour at 1.5 GHz with the JVLA in C configuration overlaid to the DSS2 optical image. The FWHM of the radio image $33'' \times 33''$ (PA= 0°). Contour levels are at $(3, 6, 9, \dots) \times \sigma$ with $\sigma = 0.043$ mJy/beam, the rms noise is 0.035 mJy/beam. *Right panel:* high resolution C array map of MACSJ0454.1–0300 at 1.520 GHz. The beam is $11.0'' \times 11.0''$ (PA= 0°) with rms 0.06 mJy/beam. The point sources are labelled with 1 and 2.

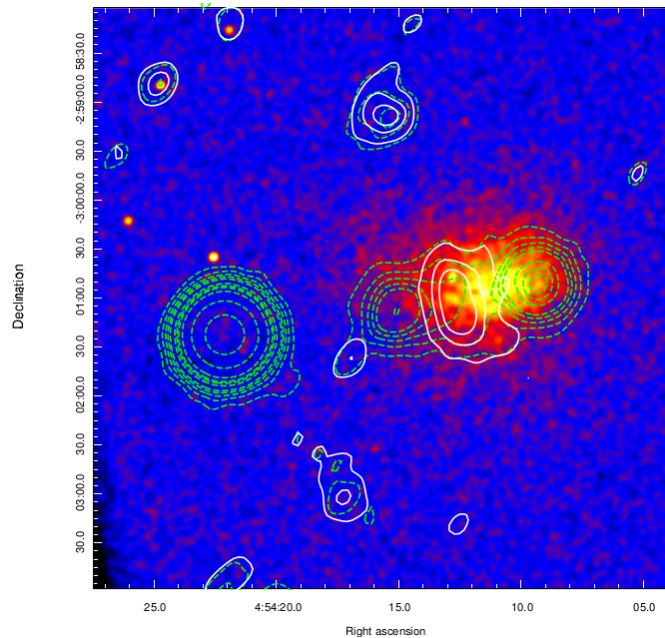


Figure 6.16: MACSJ0454.1–0300 total intensity radio contours at 1.520 GHz after subtraction of discrete sources. The image has an FWHM of $30.0'' \times 30.0''$ (PA= 0°). The contour levels are at $(3, 6, 8, 12, \dots) \times \sigma$ with $\sigma = 0.048$ mJy/beam. The rms noise is 0.035 mJy/beam. Green dotted lines indicate the positions of the subtracted discrete sources. The contours of radio intensity are overlaid on the CHANDRA X-ray image.

6.4.8 MACSJ0520.7–1328

MACSJ0520.7–1328 is located at $z = 0.336$ and has an X-ray luminosity of $L_{X,500} = (7.8 \pm 0.4) \times 10^{44}$ erg/s. It is classified as a relatively relaxed system on the basis of its morphological properties i.e. good optical/X-ray alignment and quite concentric X-ray surface brightness contours (morphological class 2 by Ebeling et al. (2010)). The estimated mass from SZ measures is $M_{500} \sim 6.30 \times 10^{14} M_{\odot}$ (Planck Collaboration et al. 2014). Macario et al. (2014) observed this cluster with GMRT at 323 MHz as a part of a large observational program with the aim to search for diffuse radio emission in a sample of galaxy clusters selected from MACS (X-ray) and the XMM-Planck (X-ray/SZ) catalogs in the redshift range 0.3-0.45 (Macario et al. 2014). They found that the radio map of the central field of MACSJ0520 is dominated by the very bright and slightly extended emission of the BCG and detected also a diffuse non thermal emission associated to the IGM and intracluster medium around a newly detected cluster. The *Chandra* X-ray analysis carried out by Macario et al. (2014) detected beyond the X-ray emission associated with the galaxy cluster MACSJ0520 a SE diffuse X-ray source, the 1WG AJ0521, coincident with the newly detected diffuse radio source. 1WG AJ0521 has been classified as a galaxy cluster with a probably disturbed dynamical state at the same distance of MACSJ0520. According to our new image, the diffuse emission is D1 (see Fig. 6.17), peripheral to the new cluster. The classification of the diffuse radio emission appears debated: a radio relic associated to 1WG AJ0521 possibly interacting with MACSJ0520, a possible radio halo embedding the discrete sources S1 and S2. Our radio images do not confirm the diffuse sources D2, D3 and D4 reported by Macario et al. (2014). Our radio observation in L-band is shown in Fig. 6.17 superimposed to the DSS2 (red) optical image. We found an elongated diffuse radio emission at ~ 2.4 kpc in the SE direction from the central BCG corresponding to the diffuse source labeled with D1 in Macario et al. (2014). The flux density is (1.49 ± 0.08) mJy and the radio power at 1.4 GHz of $(7.50 \pm 0.40) \times 10^{23}$ W/Hz adopting a spectral index $\alpha = 1.2$. The LAS is ~ 3.7 arcmin corresponding to a LLS ~ 1.1 Mpc at the cluster distance. If we compare the radio and morphological properties of these diffuse radio source with the scale relations for radio relics (see Capt. 2, 3) they are in good agreement with the correlation $P_{1.4}$ vs $L_{X,500}$ and $P_{1.4}$ vs LLS and therefore we classify it as a radio relic. Nevertheless its origin is uncertain: it is difficult to relate it to the cluster MACSJ0520 which

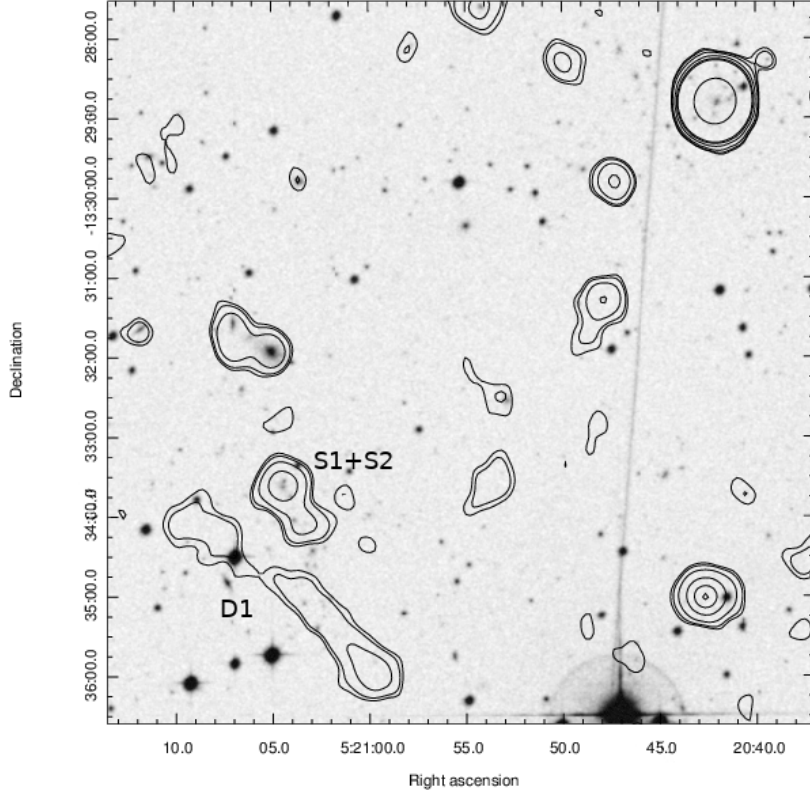


Figure 6.17: 1.586 GHz low resolution image of MACSJ0520 and 1WGAJ0521. The FWHM (restoring beam) is $24'' \times 24''$. Contours level are at $(3,6,9,12,24,48) \times \sigma$ with rms noise $\sigma = 0.023$ mJy/beam. Radio contours are overlaid on the DSS2 optical red image.

seems a relaxed system while relics are generally found to be associated to merging clusters but also to the new cluster 1WGAJ0521. In this last case the emission would be associated with the passage of a shock that may have accelerate particles from ICM or revived fossil plasma from a previous activity of a radio loud AGN. Nevertheless, the diffuse emission is located closer to the cluster center with respect to what is typically observed. We report in tab. 6.11 the main properties of MACSJ0520 and those reported in the literature.

Table 6.11: Properties of the extended source of MACSJ0520.7

Cluster Name	z	M_{500} $10^{14} M_{\odot}$	$L_{X,500}$ 10^{44} erg/s	T_X keV	ν_{obs} GHz	Type	S_{ν} mJy	$P_{1.4}$ 10^{24} W/Hz	LLS (kpc)
MACSJ0520.7	0.336	6.30	7.8	6.5					
1WGAJ0521.0	0.34	2.5		3.6					
17A-025					1.586	R	1.49 ± 0.08	0.75 ± 0.06	1.1
Macario 2014					0.323	H/R	61.2 ± 5.7		0.8

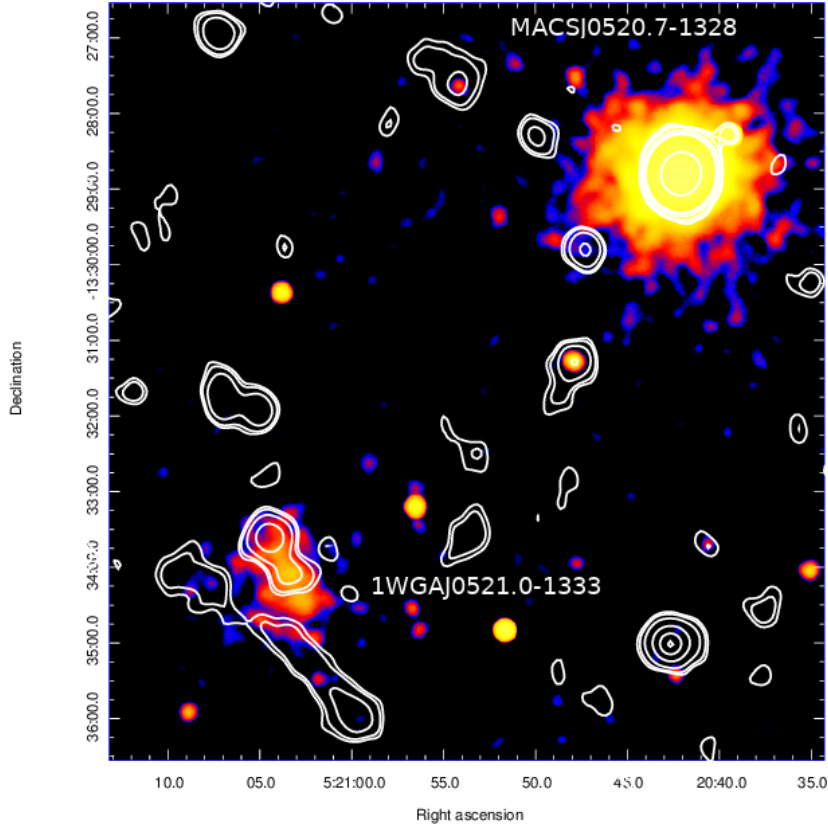


Figure 6.18: Smoothed *Chandra* X-ray image with overlaid the 1.586 GHz JVLA low resolution contours (same as in Fig. 6.17).

6.4.9 MACSJ0553.4–3342

From both optical and X-ray images MACSJ0553.4–3342 appears as a disturbed cluster at $z = 0.430$ (Ebeling et al. 2010; Mann & Ebeling 2012). Mann & Ebeling (2012) reported the presence of an undergoing binary head-on merger with two X-ray peaks clearly visible in the *Chandra* images: these peaks are the cores of the two merging clusters. From the analysis on the X-ray data the merger axis lies approximately in the plane of the sky (Mann & Ebeling 2012). This kind of merger in clusters with mass of $\sim 10^{15} M_{\odot}$ it is expected to produce Mpc-sized shocks in the ICM, moreover the geometry of the merger should give the best orientation to detect the emission of a radio relic within the radio and X-ray fields of view (Vazza et al. 2012). Bonafede et al. (2012) with the GMRT at 323 MHz detected in this cluster a wide radio source classified as a giant radio halo but with no evidence of radio relic, giving as possible explanations the position of the wave front still along the merging axis close to the cluster’s cores and/or the low contrast of the relic against the halo emission.

More recently Botteon et al. (2018) confirmed the presence of a disconti-

nity classifying it as a cold front and also of a shock heated region to the E of the cold front (see Fig. 6.19). He also reported the detection of a second cold front at the W side of the merging axis. Our radio images obtained with the C array confirm the detection of the halo: the radio image in the *left panel* of Fig. 6.19 has a FWHM (restoring beam) of $14 \text{ arcsec} \times 14 \text{ arcsec}$ (PA=0°), rms noise $\sigma = 0.018 \text{ mJ/beam}$. The high resolution image (uv -range $> 7k\lambda$) of the *right panel* shows the embedded point sources labeled with A and B. The total flux density of the radio halo including the source B is $(12.96 \pm 0.65) \text{ mJy}$. The image obtained after the subtraction of the point sources is reported in Fig. 6.20: the radio halo has a flux density of $(8.09 \pm 0.40) \text{ mJy}$ corresponding to a radio power at 1.4 GHz of $P_{1.4} = (6.23 \pm 0.51) \times 10^{24} \text{ W/Hz}$ adopting the spectral index $\alpha_{0.323}^{1.4GHz} = (1.39 \pm 0.09)$ calculated using the halo flux at 323 MHz reported in Bonafede et al. (2012); the LAS is $\sim 3 \text{ arcmin}$ (LLS $\sim 1.010 \text{ Mpc}$). In the radio image of Fig. 6.19 at the W of the radio halo is present a N-S elongated (LLS of $\sim 600 \text{ kpc}$) diffuse radio structure with no point sources in correspondence, well separated from the halo and apparently not correlated with it. Its origin is quite puzzling: it could be classified as a radio relic even if there are no shock regions in the W part of the cluster. Nevertheless, it is fully contained in the W cold front region (Fig. 6.19) and maybe related to the physical processes occurring in cold front regions, even though a straightforward relation is not easy to find. The flux density is $(1.06 \pm 0.05) \text{ mJy}$ and the radio power at 1.4 GHz of $P_{1.4} = (7.67 \pm 0.36) \times 10^{23} \text{ W/Hz}$, adopting a spectral index $\alpha = 1.3$. In correspondence of the E shock region (red line in Fig. 6.21) there are no evidences of diffuse radio emission. In tab. 6.12 we summarize the observational properties of the cluster.

Table 6.12: Properties of the extended sources of MACSJ0553.4–3342

Cluster Name	z	M_{500} $10^{14} M_{\odot}$	$L_{X,500}$ 10^{44} erg/s	T_X keV	ν_{obs} GHz	Type	S_{ν} mJy	$P_{1.4}$ 10^{24} W/Hz	LLS (kpc)
MACSJ0553.4	0.430	9.39	17.0	13.1	1.520	H	8.09 ± 0.40	6.39 ± 0.51	1.010
					0.323	H	62 ± 5		1.300
					1.520	U	1.06 ± 0.05	0.77 ± 0.04	0.600

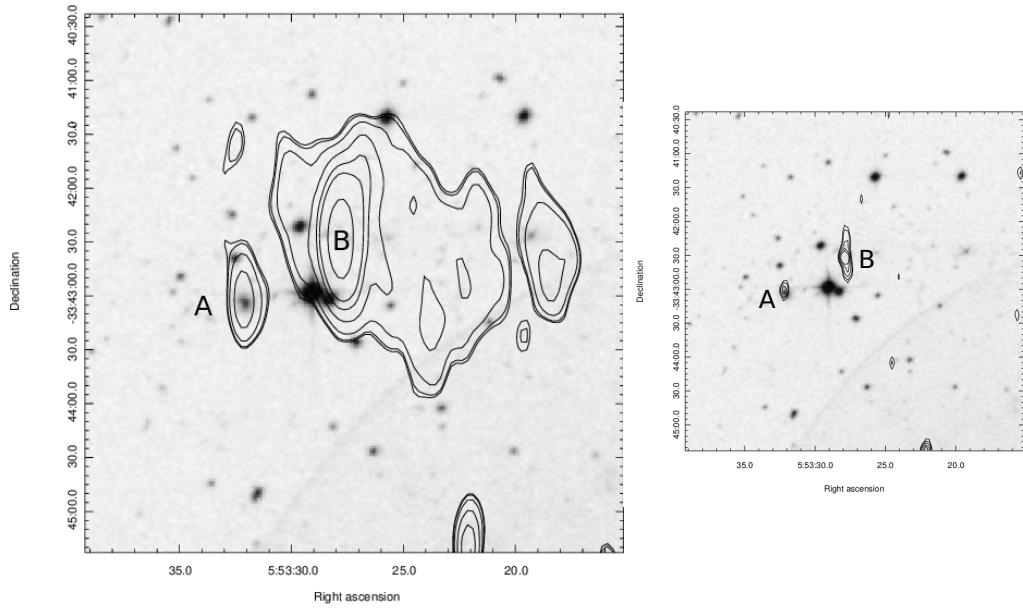


Figure 6.19: *Left panel:* MACSJ0553.4–3342 total intensity radio contour at 1.520 GHz with the JVLA in C configuration overlaid to the DSS2 optical image. The FWHM of the radio image $14'' \times 14''$ ($PA=0^\circ$). Contour levels are at $(3, 3.8, 5, 9, 12, \dots) \times \sigma$ with rms noise $\sigma = 0.02$ mJy/beam. *Right panel* high resolution C array map of MACSJ0553.4–3342 at 1.520 GHz. The restoring beam is $9.0'' \times 7.0''$ ($PA= 0^\circ$) with rms 0.05 mJy/beam. The point sources are labelled with A and B.

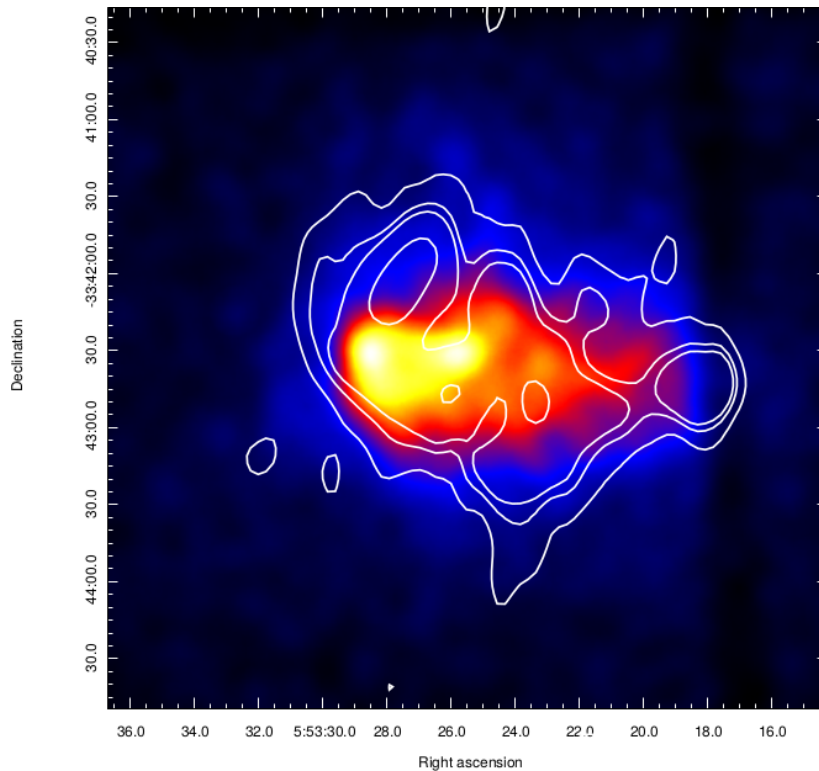


Figure 6.20: MACSJ0553.4–3342 total intensity radio contours at 1.520 GHz after subtraction of discrete sources. The image has an FWHM of $23.0'' \times 21.0''$ ($PA=0.6^\circ$). The contour levels are at $(3, 5, 6, 10, 15, 24) \times \sigma$ with rms noise $\sigma = 0.035$ mJy/beam.

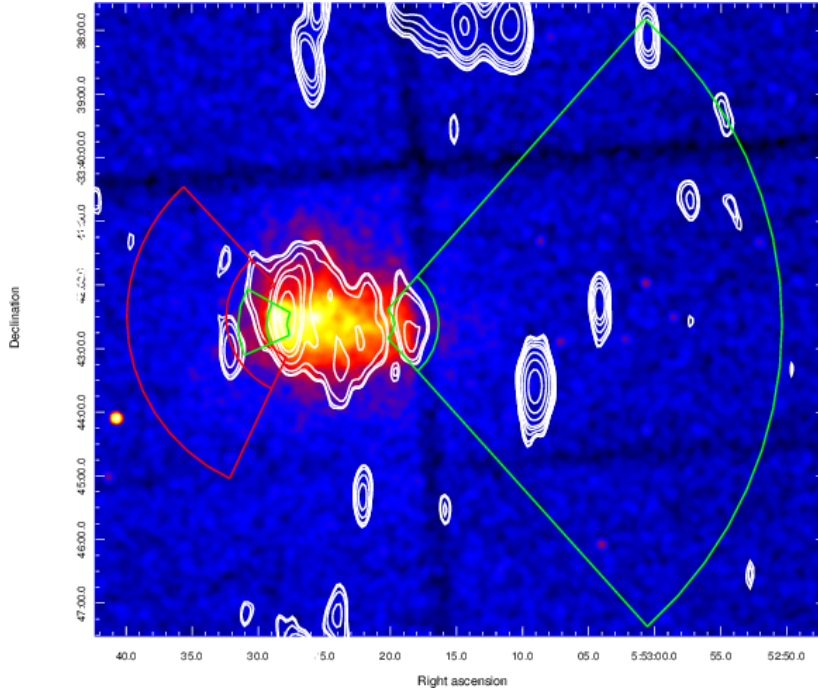


Figure 6.21: MACSJ0553.4–3342 total intensity radio contour at 1.520 GHz with the JVLA in C configuration overlaid to *Chandra* image and to the regions reported in Botteon et al. (2018) where cold fronts are marked in green, shocks are marked in white (courtesy of A. Botteon).

6.4.10 MACSJ0744.9+3927

MACSJ0744.9+3927 is the most distant cluster of the Ebeling MACS survey (Ebeling et al. 2007, 2010) with $z = 0.6976$. Its mass is $M_{500} = (11.8 \pm 2.8) \times 10^{14} M_{\odot}$ (Serenio & Ettori 2015), $L_{500} = (22.9 \pm 0.6) \times 10^{44}$ is the *Chandra* X-ray luminosity and 8.1 ± 0.6 keV is the cluster temperature (Ebeling et al. 2010). Korngut et al. (2011), using Sunyaev-Zel’dovich and X-ray observations revealed an intracluster shock just outside the center of the cluster related to a merger activity, albeit not a major one (green contours Fig. 6.22). More recently, to search for diffuse radio emission associated with the merger Wilber et al. (2018) carried out LOFAR radio observations at 120–165 MHz reporting the detection of a previously undetected AGN emission (red contours Fig. 6.22) but without clear presence of cluster scale diffuse emission in the form of radio relic nor radio halo. The diffuse emission they detected after the subtraction of the compact source (white contours Fig. 6.22) is mostly caused by the active galaxies whose lobes extend to ~ 570 kpc eclipsing the possibly radio halo. Nevertheless they determined upper limits for a possibly radio halo and relic: for the potential radio relic they estimated a flux density at 143 MHz inside a pie cut region of

(2.05 ± 0.21) mJy corresponding to a radio power $P_{143} = (4.90 \pm 0.49) \times 10^{24}$ W/Hz, while for the radio halo they found an upper limit at 143 MHz $S_{143} = 19.9$ mJy and an extrapolated power at 1.4 GHz $P_{1.4} = 2.61 \times 10^{24}$ W/Hz.

Our low resolution radio images reported in the *left-panel* of Fig. 6.23

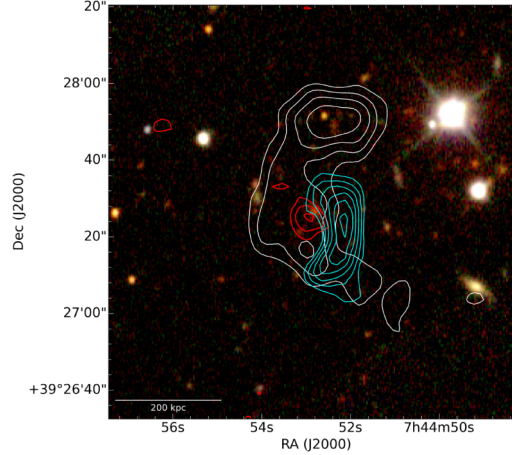


Figure 6.22: Wilber et al. 2018: MACSJ0744.9+3927 SDSS image with radio emission overlaid. LOFAR compact emission is shown by red contours (beam $8.6'' \times 6.5''$). LOFAR diffuse emission after compact source subtraction is shown in white contours (beam $14'' \times 12''$). Cyan contours are from the SZ MUSTANG map from Korngut et al. 2011.

(restoring beam of $40 \text{ arcsec} \times 40 \text{ arcsec}$) obtained combining the C and D array show a large radio structure surrounding the central BCG with a LAS of about $1.62'$ corresponding to a LLS ~ 700 kpc at the cluster distance; the flux density is (1.30 ± 0.07) mJy. In order to discriminate the radio emission of the central compact source from the possibly presence of diffuse emission we produced high resolution images with a uv -range $> 7 \text{ k}\lambda$ reported in the *right-panel* of Fig.6.23: we found that the central source has flux density of (0.42 ± 0.06) mJy. We estimated for difference that the flux density of the candidate diffuse source is (0.88 ± 0.13) mJy at 1.52 GHz corresponding at 1.4 GHz to 1.00 mJy and to a radio power $P_{1.4}$ of $(2.52 \pm 0.03) \times 10^{24}$ W/Hz assuming a spectral index $\alpha = 1.3$, value comparable with the predicted value by Wilber et al. (2018) and slightly underluminous respect to the correlations $P_{1.4}$ vs $L_{X,500}$ and $P_{1.4}$ vs LLS (see Chapt. 3). The morphology, the extension beyond the ~ 570 kpc lobes of the central active galaxy and the flux of the candidate diffuse radio emission in MACSJ0744.9+3927 suggest us that it could be the missed radio halo searched but not found by the above mentioned authors.

Table 6.13: Properties of the extended source of MACSJ0744.9+3927

Cluster Name	z	M_{500} $10^{14} M_{\odot}$	$L_{X,500}$ 10^{44} erg/s	T_X keV	ν_{obs} GHz	Type	S_{ν} mJy	$P_{1.4}$ 10^{24} W/Hz	LLS (kpc)
MACSJ0744	0.6976	11.8	22.9	8.1	1.520	H (c)	0.88 ± 0.13	2.52 ± 0.03	700
					0.143	H (c)	<19.9 UL		<570

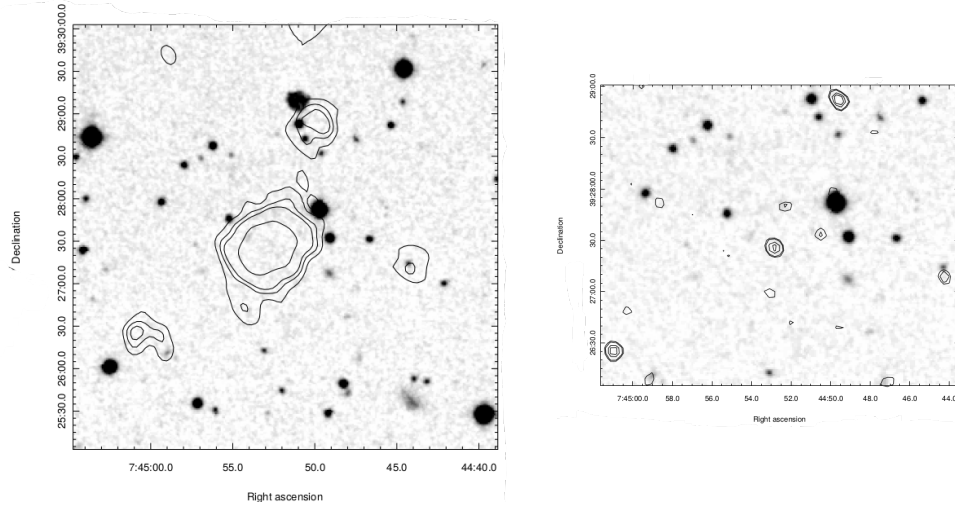


Figure 6.23: *Left panel:* MACSJ0744.9+3927 total intensity radio contour at 1.520 GHz with the JVLA in C+D configuration overlaid to the DSS2 optical image. The FWHM (restoring beam) of the radio image is $40'' \times 40''$ (PA = 0°). Contour levels are at $(2, 2.8, 3.5, 6) \times \sigma$ with rms noise $\sigma = 0.01$ mJy/beam. *Right panel:* C array high resolution map of MACSJ0744.9+3927. The beam is $9.82'' \times 7.70''$ (PA = 48.7°).

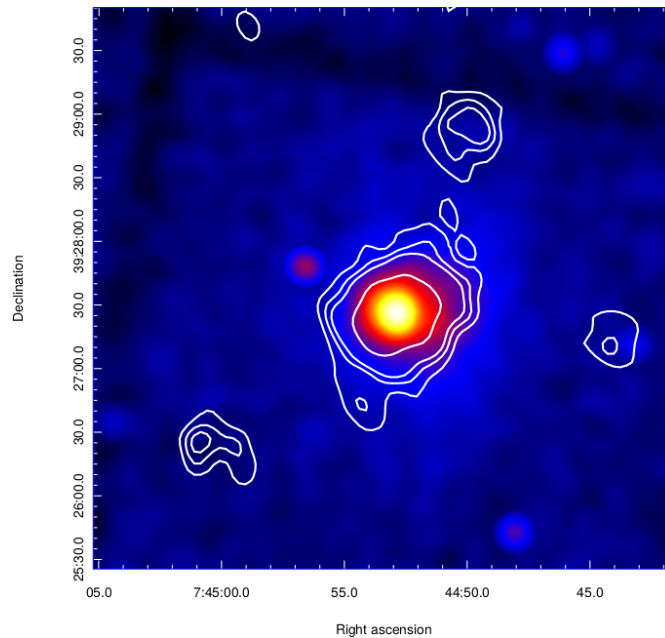


Figure 6.24: MACSJ0744.9+3927 total intensity radio contour at 1.520 GHz with the JVLA in C+D configuration overlaid on the CHANDRA X-ray color image.

6.4.11 MACSJ2211.7–0349

MACSJ2211.7–0349 is one of the X-ray brightest cluster of the Ebeling MACS survey with $L_{X,500} = (2.40 \pm 1.2) \times 10^{45}$ erg/s. The R_{500} mass is $M_{500} = (18.1 \pm 2.5) \times 10^{14} M_{\odot}$, $kT = (14.0 \pm 2.7)$ keV is the temperature at redshift $z = 0.3970$. Ebeling et al. (2010) assigned to this cluster the morphological class 2 intermediate between apparently relaxed and extremely disturbed clusters while Sayers et al. (2013), studying the SZ effect with the Caltech Bolocam photometer of a sample of massive cluster, classified MACSJ2211.7–0349 as a cool core cluster. In the literature are not reported detection of diffuse radio emission. Processing the data from the VLA calibration pipeline the D array appeared severely corrupted by RFI and it was not possible to obtain images of acceptable quality. In the C array images (*left panel* Fig. 6.25) we detected in the central region of the cluster a low-surface brightness diffuse emission with almost three discrete sources embedded. Performing a higher resolution imaging (uv -range > 8 k λ) these three sources appear well separated while the diffuse emission is no longer visible (*right panel* Fig. 6.25). We attempted the subtraction of the discrete sources with the CASA task `uvsub` and the resulting image confirms the presence of a low surface brightness diffuse radio emission which we classify as a radio halo. The flux density associated to the halo is (2.87 ± 0.14) mJy which corresponds to a radio power $P_{1.4GHz} = (1.76 \pm 0.09) \times 10^{24}$ W Hz $^{-1}$. The overall diffuse emission has an angular extension of about 2' (the Largest Linear Size is $LLS \simeq 620$ kpc at the cluster distance). The contours of the radio intensity of the halo overlaid on the *Chandra* smoothed X-ray image are reported in Fig. 6.26. In the following table (Tab. 6.14) we summarize the main properties of the detected diffuse emission.

Table 6.14: Properties of the extended source of MACSJ2211.7–0349

Cluster Name	z	M_{500} $10^{14} M_{\odot}$	$L_{X,500}$ 10^{44} erg/s	T_X keV	ν_{obs} GHz	Type	S_{ν} mJy	$P_{1.4}$ 10^{24} W/Hz	LLS (kpc)
MACSJ2211.7	0.397	18.1	24.0	14.0	1.520	H	2.87 ± 0.14	1.76 ± 0.09	620

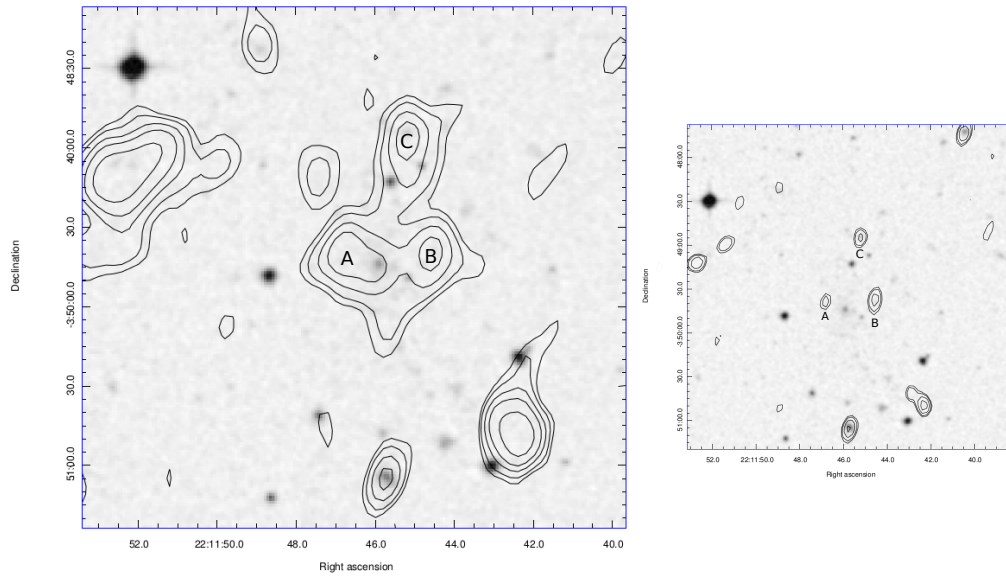


Figure 6.25: *Left panel:* MACSJ2211.7–0349 total intensity radio contour at 1.520 GHz with the JVLA in C configuration overlaid to the DSS2 optical image. The FWHM of the radio image is $20'' \times 13''$ ($PA = -14^\circ$). Contour levels are at $(3, 6, 9, 12, \dots) \times \sigma$ with rms noise $\sigma = 0.04$ mJy/beam. *Right panel:* C array high resolution map of MACSJ0744.9+3927. The beam is $9.3'' \times 8.1''$ ($PA = -21^\circ$). Point sources are labelled with A, B, and C.

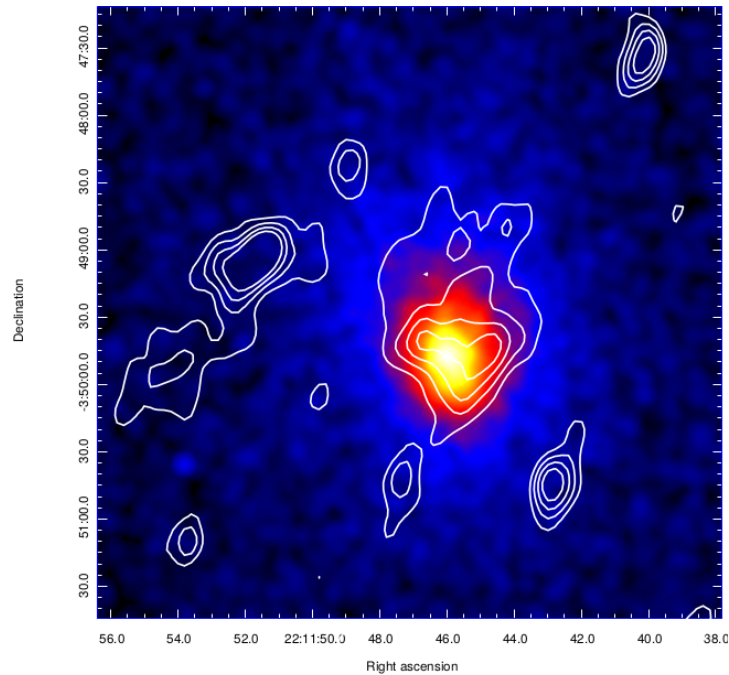


Figure 6.26: MACSJ2211.7–0349 total intensity radio contour at 1.520 GHz with the JVLA in C configuration after subtraction of discrete sources. The image has a FWHM of $21'' \times 13''$. The contour levels are at $(3, 5, 7, 9, 12, 24) \times \sigma$ with $\sigma = 0.029$ mJy/beam. Radio image is overlaid on the CHANDRA X-ray color image.

6.4.12 MACSJ2228.5+2036

MACSJ2228.5+2036 is a massive ($M_{500} = 8.26 \times 10^{14} M_{\odot}$) and hot ($kT=8.16$ keV) galaxy cluster at redshift $z = 0.411$. The meta-catalog of X-ray detected clusters of galaxies (MCXC) reports an X-ray luminosity in the (0.1–2.4) keV band $L_{500} = 1.93 \times 10^{45}$ erg/s (Piffaretti et al. 2011). The cluster is disturbed in its X-ray morphology: Ebeling et al. (2010) assigned to this cluster a morphological class 4 with a poor optical/X-ray alignment, multiplepeaks, no cD galaxy and classified it as extremely disturbed.

Venturi et al. (2008) first observed the cluster using GMRT as a part of GMRT radio halo survey but with no detection of any diffuse radio emission. Parekh et al. (2017) report upper limits at 610 MHz measuring the rms in the central region of this cluster but without reveal the presence of diffuse emission.

The radio contours at 1.5 GHz obtained with the JVLA in C+D configuration is shown in the *left panel* of fig. 6.27 overlaid with the DSS2 optical image. We detect a diffuse low surface brightness radio emission which we classify as a radio halo, surrounding three discrete sources labeled with A, B and C. The flux density of this structure is (18.70 ± 0.94) mJy. Performing an high resolution radio image using the C array with the longest baselines (*right panel* of Fig. 6.27), we found for the point sources the following flux densities: A (1.00 ± 0.05) mJy, B (1.39 ± 0.06) mJy and C (1.35 ± 0.07) mJy. By subtracting these fluxes from the flux of the extended source we found for the diffuse radio halo a flux of (14.96 ± 1.12) mJy, which corresponds to a radio power of $P_{1.4GHz} = (9.98 \pm 0.75) \times 10^{24}$ W Hz $^{-1}$, assuming a spectral index $\alpha = 1.3$ for the k -correction. The radio contour with point sources subtracted overlaid on the CHANDRA X-ray in the 0.1–2.4 keV band is shown in fig. 6.28. The radio halo has an angular extension (LAS) of about $200''$ which corresponds to a LLS ~ 1.092 Mpc at the cluster distance. In table 6.15 we summarize the properties of the extended source.

Table 6.15: Properties of the extended source of MACSJ2228.5+2036

Cluster Name	z	M_{500} $10^{14} M_{\odot}$	$L_{X,500}$ 10^{44} erg/s	T_X keV	ν_{obs} GHz	Type	S_{ν} mJy	$P_{1.4}$ 10^{24} W/Hz	LLS (kpc)
MACSJ2228.5	0.411	8.26	19.3	7.4	1.5	H	14.96 ± 1.12	9.98 ± 0.75	1.092

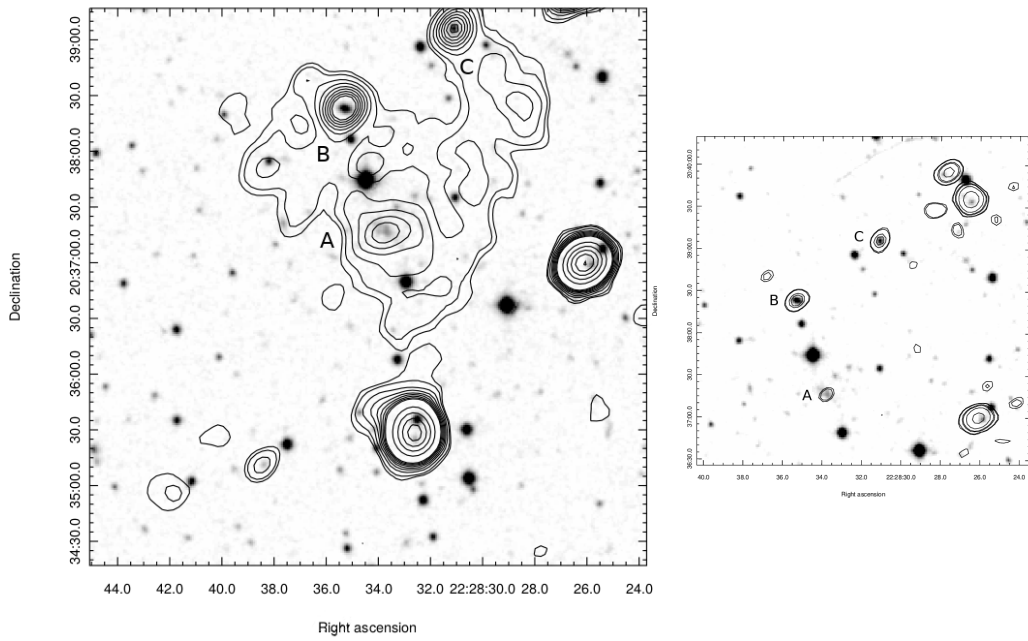


Figure 6.27: *Left panel:* MACSJ2228.5+2036: JVLA radio contours at 1.5 GHz with point sources subtracted overlaid on the CHANDRA color image. The white contour levels are $(3, 6, 9, 12, 24, 48, \dots) \times \sigma$ with rms noise $\sigma = 0.031$ mJy/beam. *Right panel:* C array high resolution map. The beam is $11.7'' \times 9.0''$ (PA = -43°). The rms noise $\sigma = 0.060$ mJy/beam. Point sources are labelled with A, B, and C.

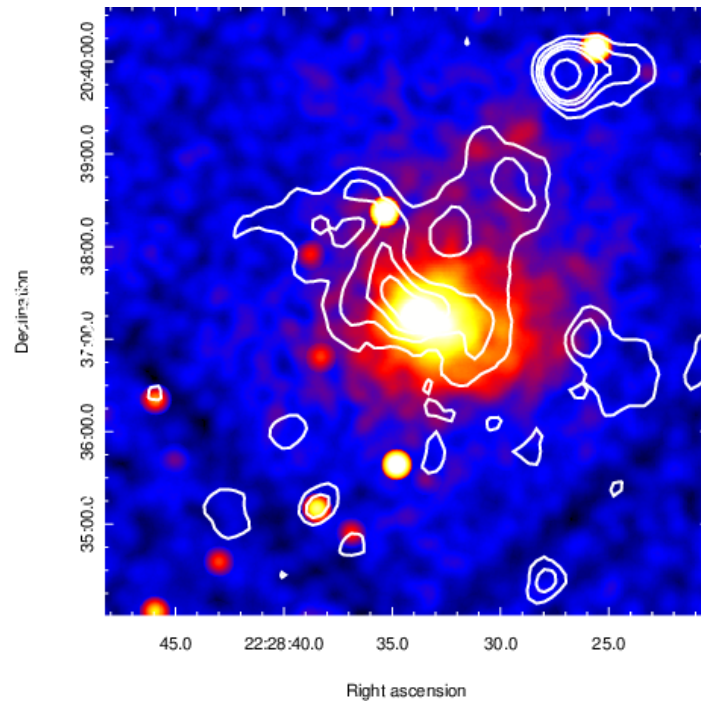


Figure 6.28: MACSJ2228.5+2036: JVLA radio contours at 1.5 GHz with point sources subtracted overlaid on the CHANDRA color image. The white contour levels are $(3, 6, 9, 12, 24, 48, \dots) \times \sigma$ with rms noise $\sigma = 0.031$ mJy/beam.

6.5 Data reduction and imaging results II. Detection of diffuse emission: mini halos.

6.5.1 MACSJ0159.8–0849

At $z = 0.405$ this relatively high redshift cluster shows a regular X-ray morphology with the surface brightness profile peaked at the BCG and gas temperature declining toward the center as typically observed in other cool-core clusters (Cavagnolo et al. 2009; Giacintucci et al. 2014). MACSJ0159.8 has a $M_{500} = 9.15 \pm 0.94 \times 10^{14} M_{\odot}$, temperature $kT = (9.4 \pm 0.7)$ keV and $L_{X,500} = (14.4 \pm 0.6) \times 10^{44}$ erg/s. Giacintucci et al. (2014) analyzed this cluster using the VLA archival observations (L-band in B configuration and X-band in A configuration) reporting the discovery of a candidate mini halo. The radio image obtained from our observation with the L-band C configuration is reported in Fig. 6.29, overlaid on the optical image taken from SLOAN Digital Sky Survey (red). This radio image has an FWHM beam of $19.2'' \times 12.6''$ (PA= 0.20°) with radio contours drawn at $(3, 6, 12, \dots) \times \sigma$ with rms= $\sigma = 0.048$ mJy/beam. In agreement with Giacintucci et al. (2014) we also detected the point source at the BCG, a second point source to the NE (possible member galaxy) and a diffuse radio emission around the central source. We measured the total flux density of these sources and found (37.5 ± 1.9) mJy. To estimate the contribute of the diffuse emission we subtracted the flux density of the point sources reported by Giacintucci et al. (2014) obtained with the VLA in L-band B configuration. The resulting flux density is (2.1 ± 0.1) mJy corresponding to a radio power $P_{1.4} = (1.22 \pm 0.06) \times 10^{24}$ W/Hz adopting a spectral index $\alpha = -1$: these values are in good agreement with those reported by the previous authors and confirm also in L-band C configuration the detection of the mini-halo reported in the literature. In the following table are summarized the properties of MACSJ0159.8 and mini-halo. In Fig. 6.30 radio contours (the same of Fig. 6.29) are overlaid to the Chandra X-ray image.

Table 6.16: Properties of the extended source of MACSJ0159.8–0849

Cluster Name	z	M_{500} $10^{14} M_{\odot}$	$L_{X,500}$ 10^{44} erg/s	T_X keV	ν_{obs} GHz	Type	S_{ν} mJy	$P_{1.4}$ 10^{24} W/Hz	LLS (kpc)
MACSJ0159.8	0.404	9.15	14.4	9.4	1.519 (C)	MH (c)	2.1 ± 0.1	1.22 ± 0.10	
Giacintucci 2014					1.400 (B)	MH (c)	2.4 ± 0.2	1.40 ± 0.14	90

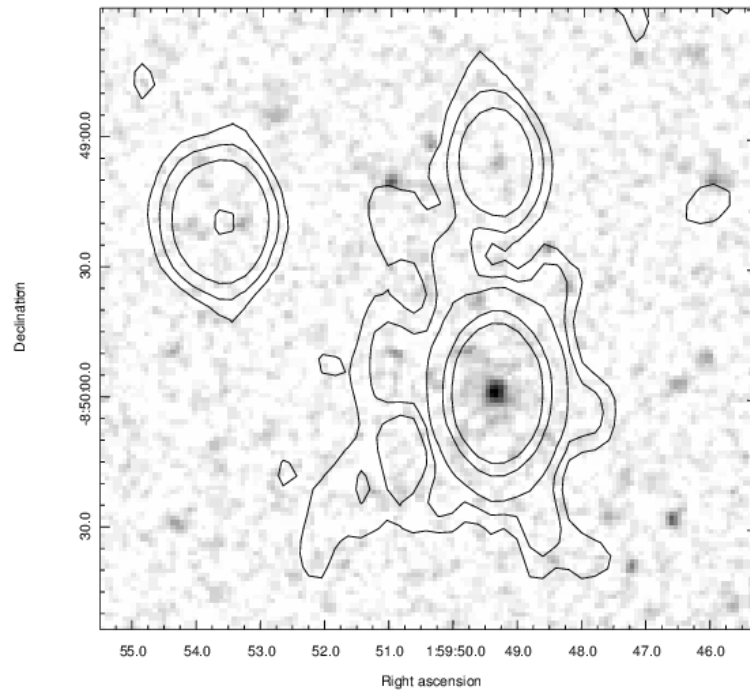


Figure 6.29: MACSJ0159.8–0849 total intensity radio contour at 1.519 GHz with the JVLA in C configuration overlaid on the DSS2 optical image. The FWHM is $19.23'' \times 12.59''$ (PA= 0.20°). The rms noise is $1\sigma = 0.048$ mJy/beam and contours are: (3, 6, 12, 48, 96) $\times \sigma$.

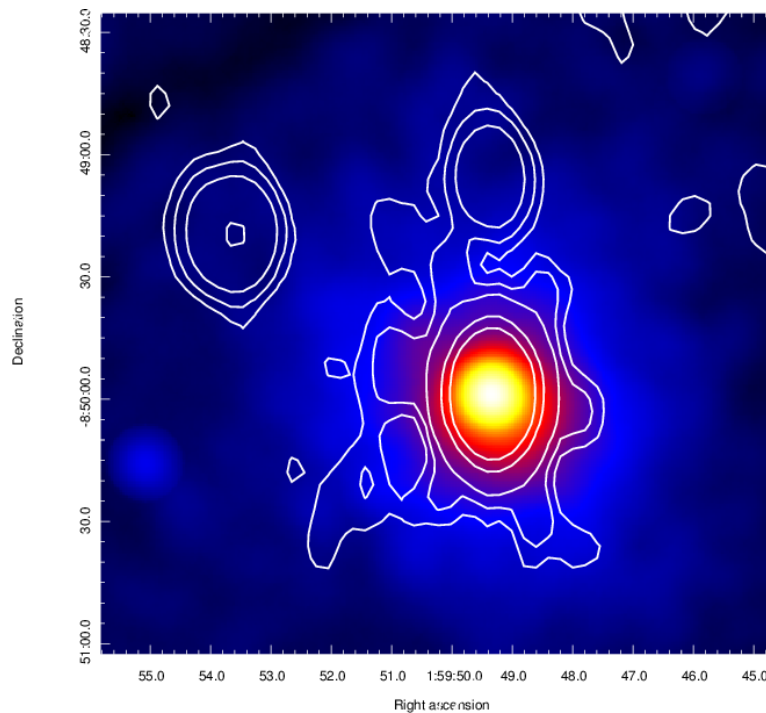


Figure 6.30: ACSJ0159.8–0849 total intensity radio contour (the same of Fig. 6.29) overlaid on the CHANDRA X-ray color image.

6.5.2 MACSJ0947.2+7623 (RBS0797)

MACSJ0947 also known as RBS0797 is a cooling flow cluster at $z = 0.354$ well studied by several authors (e.g. Gitti et al. 2006; Cavagnolo et al. 2008; Doria et al. 2012). Multifrequency observations showed the presence in the center of the cluster of a complex radio emission and a supermassive binary black holes (SMBBHs) system (Gitti et al. 2013). In particular it was found the presence of extended diffuse radio emission on a scale of hundreds of kpc, roughly comparable to the size of the cooling region, characterized by amorphous morphology and steep spectra and classified as a mini-halo (Gitti et al. 2006; Doria et al. 2012). Combining the C and D array datasets of our JVLA observations we obtained the radio image reported in Fig. 6.31 (*left panel*). The image has a FWHM of $23.8'' \times 17.51''$ (PA = -33.2°), radio contours are at $(3, 4, 6, 9, 12, \dots) \times \sigma$ with $\sigma = \text{rms} = 0.038$ mJy/beam. The total flux of the central region is (20.8 ± 1.0) mJy, comparable with the flux of (24.0 ± 0.3) mJy obtained by Doria et al. (2012) combining A, B and C array VLA archive data. Measuring the flux of the point sources of the high resolution image reported in the *right panel* of Fig. 6.31, we found a flux of (12.4 ± 0.6) mJy. The flux of the diffuse emission estimated for difference from the previous two fluxes results (8.4 ± 1.6) mJy corresponding to a radio power of $P_{1.4} = (3.62 \pm 0.70) \times 10^{24}$ W/Hz. Our results are in agreement with the data reported in literature (Gitti et al. 2006; Doria et al. 2012; Giacintucci et al. 2014) and do not add new significant features. In Tab. 6.17 we report the main properties of MACSJ0947 and of the hosted extended radio source.

Table 6.17: Properties of MACSJ0947.2+7623 (RBS0797)

Cluster Name	z	M_{500} $10^{14} M_\odot$	$L_{X,500}$ 10^{44} erg/s	T_X keV	ν_{obs} GHz	Type	S_ν mJy	$P_{1.4}$ 10^{24} W/Hz	LLS (kpc)
RBS0797	0.354	6.27	20.0	6.73	1.455	MH	8.4 ± 1.6	3.62 ± 0.70	180

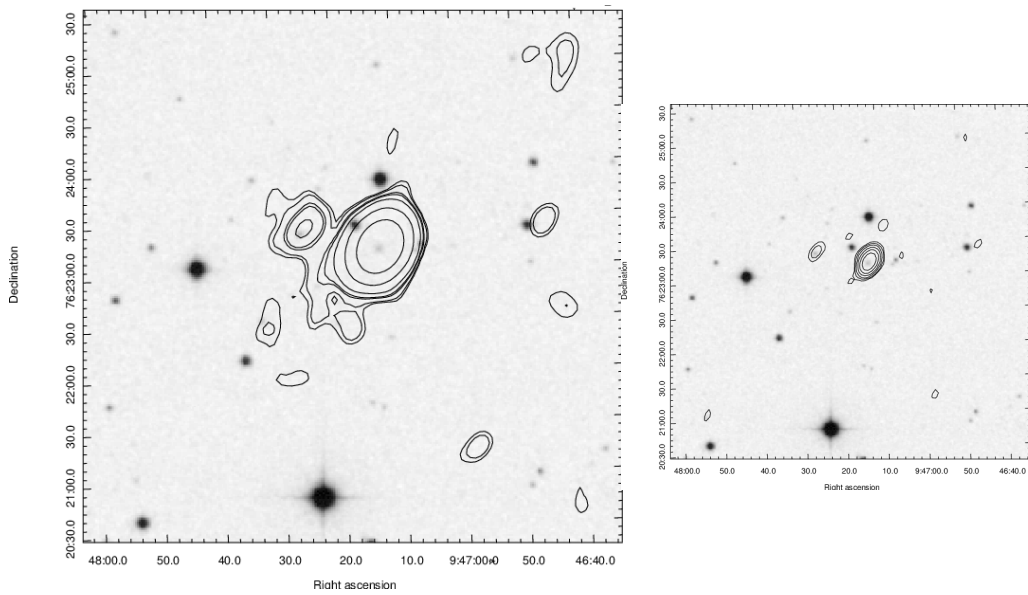


Figure 6.31: *Left panel:* RBS0797 total intensity radio contour at 1.455 GHz with the JVLA in C+D configuration overlaid to the DSS2 optical image. The FWHM of the radio image is $23.78'' \times 17.51''$ (PA = -33.2°). Contour levels are at $(3, 4, 6, 9, 12, \dots) \times \sigma$ with rms noise $\sigma = 0.038$ mJy/beam. *Right panel:* C array high resolution map of RBS0797 (uv -range 7 – 22 k λ). The beam is $14.6'' \times 8.64''$ (PA = -29.8°).

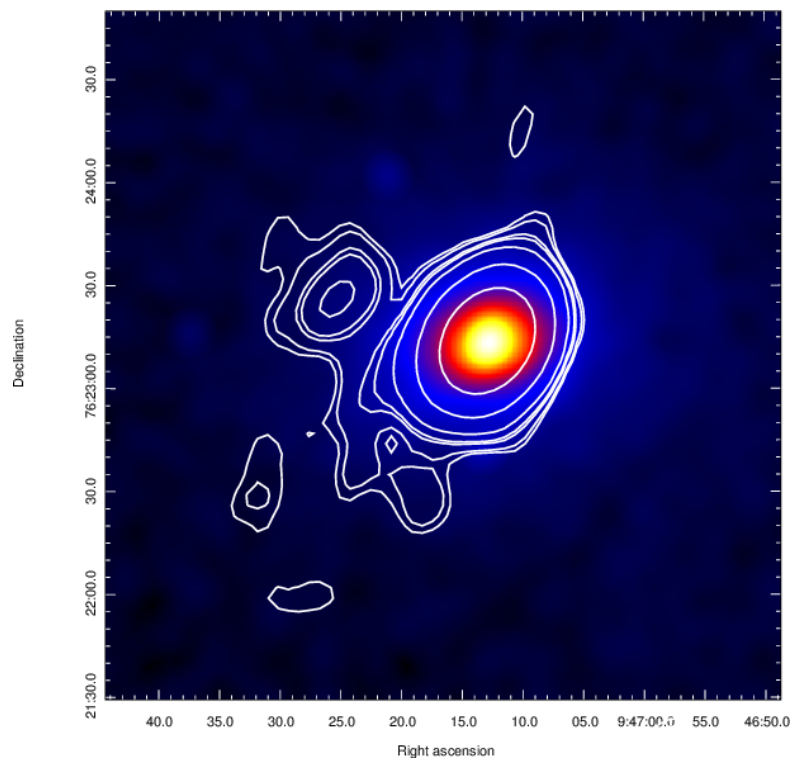


Figure 6.32: RBS0797 total intensity radio contour (same as in Fig. 6.25) at 1.455 GHz with the JVLA in C+D configuration overlaid on the CHANDRA X-ray color image.

6.5.3 MACSJ1532.8+3021

MACSJ1532.8 is a galaxy cluster well studied in all the wavelengths (e.g. Hlavacek-Larrondo et al. 2013a) with $M_{500} = (9.5 \pm 1.7) \times 10^{14} M_{\odot}$, temperature $kT = (6.8 \pm 1.0)$ keV and $L_{X,500} = (14.7 \pm 0.1) \times 10^{44}$ erg/s at $z = 0.362$. Chandra and XMM-Newton observations revealed the presence of a steeply rising X-ray surface brightness profile, drop in temperature near the center and short radiative cooling time, typical of a cool core relaxed cluster. The VLA observations in L-band A and B configuration analyzed in Hlavacek-Larrondo et al. (2013a) and Giacintucci et al. (2014) reveal a prominent minihalo in the cluster core with a radius of ~ 100 kpc. Our L-band radio image obtained from the C array data is reported in Fig. 6.33 (*left panel*). The unresolved central radio source has a flux density of (20.1 ± 1.0) mJy and radius of ~ 90 kpc. By subtracting the flux of the central BCG obtained from the VLA L-band A+B array archival observations as reported in Giacintucci et al. (2014), it results in flux density related to the extended radio emission of (4.4 ± 0.3) mJy corresponding to a radio power of $P_{1.4} = (1.96 \pm 0.13) \times 10^{24}$ W/Hz, sharply underluminous if compared with the values reported in the literature for the minihalo, probably due to a flux leakage related to a too short observation time. In tab. 6.18 we summarize the main characteristics of the cluster. In *right panel* of Fig. 6.33 radio contours are overlaid to *Chandra* X-ray image.

Table 6.18: Properties of the extended source of MACSJ1532.9+3021

Cluster Name	z	M_{500} $10^{14} M_{\odot}$	$L_{X,500}$ 10^{44} erg/s	T_X keV	ν_{obs} GHz	Type	S_{ν} mJy	$P_{1.4}$ 10^{24} W/Hz	LLS (kpc)
MACSJ1532	0.362	9.5	14.7	6.8	1.520 (C)	MH	4.4 ± 0.3	1.96 ± 0.13	90
Giac. 2014					1.4 (A+B)	MH	7.5 ± 0.4	3.35 ± 0.17	100

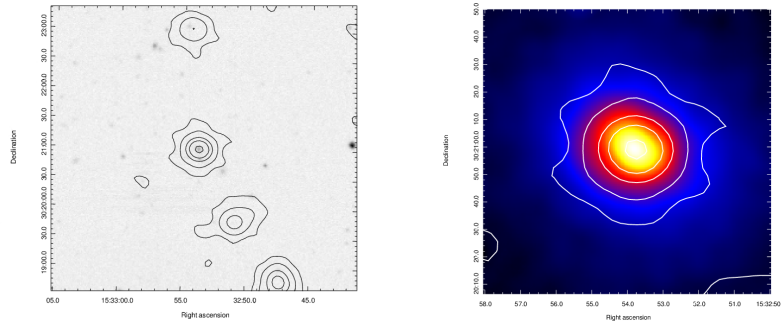


Figure 6.33: *Left panel:* MACSJ1532.9 total intensity radio contour at 1.52 GHz with the JVLA in C configuration overlaid on the DSS2 optical image. The FWHM is $17.35'' \times 15.01''$ (PA=84.6°). The rms noise is $1\sigma = 0.038$ mJy/beam and contours are: $(3, 24, 96, \dots) \times \sigma$. *Right panel:* radio contours overlaid to the *Chandra* X-ray image.

6.5.4 MACSJ1931.8–2634

MACSJ1931.8 is a massive ($M_{500} = (5.9 \pm 0.8) \times 10^{14} M_{\odot}$) relaxed cluster at $z = 0.352$ with temperature $kT = (6.9 \pm 0.7)$ keV and X-ray luminosity $L_{X,500} = (19.6 \pm 1.0) \times 10^{44}$ erg/s. Giacintucci et al. (2014) using the VLA data archive observations found in MACSJ1931.8 a diffuse radio emission embedding the central compact source coincident with the BCG and a second compact source at $\sim 3''$ from the latter. In the image of our L-band C array observation the radio emission of these two sources is not resolved (label A of Fig. 6.34) and results partially overlapped to the emission of the south point source (label B of Fig. 6.34) also detected in Giacintucci et al. (2014) with the GMRT at 150 MHz. The flux density of A+B is (191 ± 10) mJy while the flux of A roughly estimated is $\sim (65 \pm 3)$ mJy. These values are comparable with the total flux measured by Giacintucci et al. (2014) in the low resolution L-band B array image. By subtracting the fluxes of the two compact sources obtained with the L-band A array also reported in Giacintucci et al. (2014) the flux of the outer diffuse emission results (50 ± 4) mJy corresponding to a radio power of $P_{1.4} = (20.9 \pm 1.7) \times 10^{24}$ W/Hz. In Tab. 6.19 are summarized the properties of MACSJ1931.8 and in Fig. 6.35 radio contours (the same of Fig. 6.34) are overlaid to the *Chandra* X-ray image.

Table 6.19: Properties of the extended source of MACSJ1938.8–2634

Cluster Name	z	M_{500} $10^{14} M_{\odot}$	$L_{X,500}$ 10^{44} erg/s	T_X keV	ν_{obs} GHz	Type	S_{ν} mJy	$P_{1.4}$ 10^{24} W/Hz	LLS (kpc)
MACSJ1938	0.352	5.9	19.6	6.9	1.520	MH	50 ± 3	20.9 ± 1.7	118

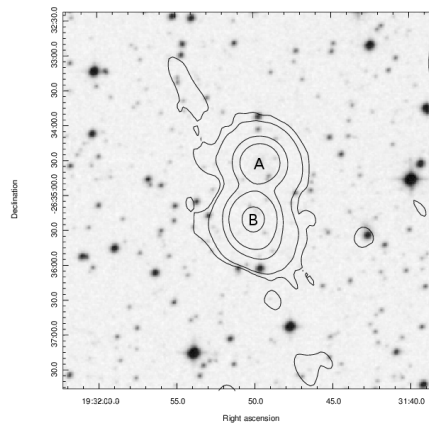


Figure 6.34: MACSJ1938.8 total intensity radio contour at 1.52 GHz with the JVLA in C configuration overlaid on the DSS2 optical image. The restored FWHM is $25'' \times 25''$ (PA=0°). The rms noise is $1\sigma = 0.072$ mJy/beam and contours are: $(3, 9, 12, \dots) \times \sigma$.

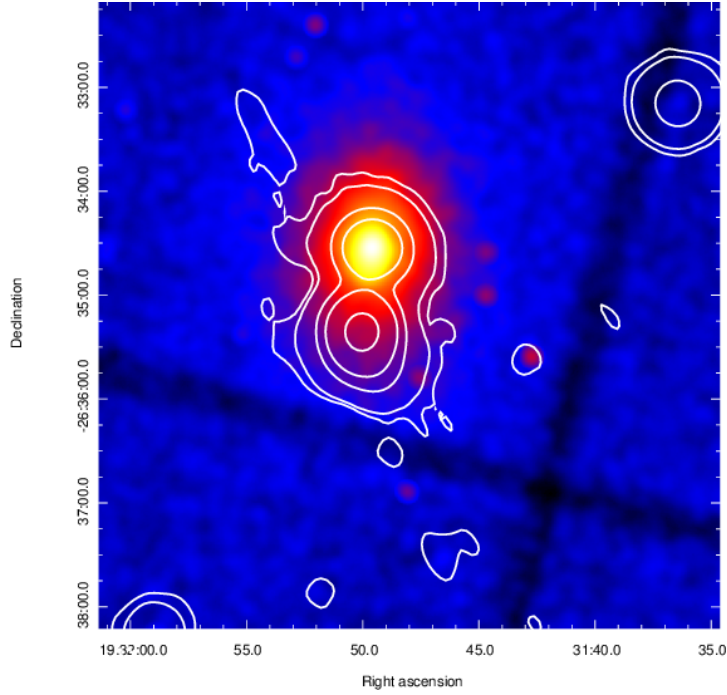


Figure 6.35: MACSJ1938.8 total intensity radio contour at 1.52 GHz with the JVLA in C configuration overlaid overlaid to the *Chandra* X-ray image.

MACSJ0329.6–0211 ($z = 0.450$)

Giacintucci et al. (2014) using a VLA archive observation in L-band B array, reported the discovery of a candidate minihalo in this distant and relaxed cool core cluster (Cavagnolo et al. 2009). We detected in our radio images at the centre of the cluster a bright source extended ~ 160 kpc with a flux density of (7.8 ± 0.4) mJy. By subtracting the flux density of the central point source reported by the previous authors we obtained a flux of (4.0 ± 0.6) mJy for the surrounding extended emission, comparable with the value reported in the literature. The corresponding radio power results $P_{1.4} = 3.0 \times 10^{24}$ W/Hz adopting a spectral index $\alpha = -1$. In Fig. 6.36 we report radio contours overlaid to the DSS2-red optical image (*left panel*) and the *Chandra* X-ray image (*right panel*). In Tab. 6.20 we summarize the properties of MACSJ0329.6 and of the hosted diffuse radio emission.

Table 6.20: Properties of the extended source of MACSJ0329.6–0211

Cluster Name	z	M_{500} $10^{14} M_{\odot}$	$L_{X,500}$ 10^{44} erg/s	T_X keV	ν_{obs} GHz	Type	S_{ν} mJy	$P_{1.4}$ 10^{24} W/Hz	LLS (kpc)
MACSJ0329 Giac. 2014	0.450	4.46	13.6	6.44	1.520 1.4	MH (c) MH (c)	4.0 ± 0.6 3.8 ± 0.4	3.0 ± 0.5 2.84 ± 0.30	160 ~ 100

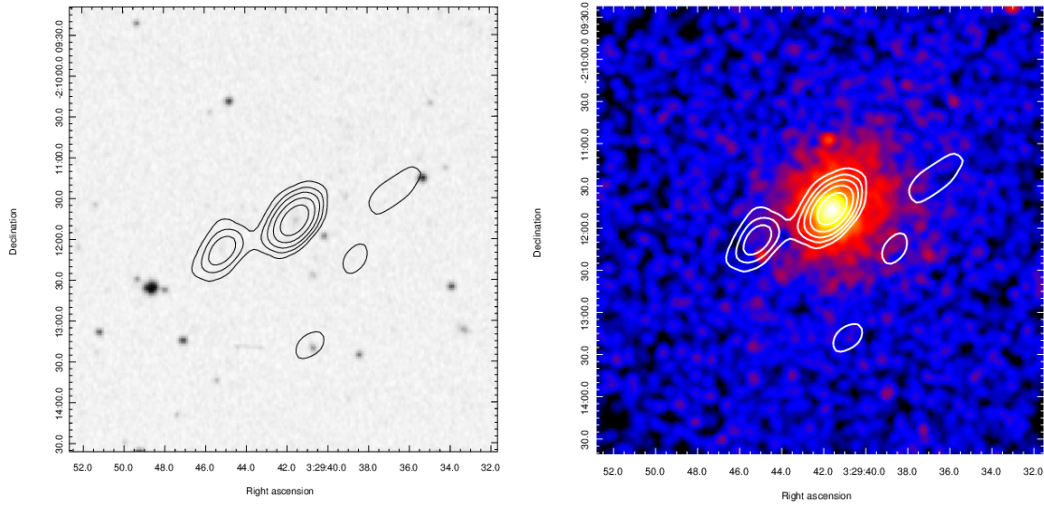


Figure 6.36: *left panel* MACSJ0329.6 total intensity radio contour at 1.52 GHz with the JVLA in C configuration overlaid on the DSS2 optical image. The FWHM is $26.4'' \times 15.6''$ ($PA = -38^\circ$). The rms noise is $1\sigma = 0.05$ mJy/beam and contours are: (3, 6, 9, 12, ...) $\times \sigma$. *Right panel* the same contours overlaid with *Chandra* X-ray image.

Our observation in the C array confirms the detection of a candidate minihalo first detected with the JVLA at higher resolution.

Chapter 7

Clusters without detection of diffuse sources and clusters with uncertain diffuse emission

Among the 42 clusters observed in our campaign with the JVLA, in 25 clusters we did not detect diffuse radio sources or the detection of extended sources was too uncertain to be classified as a radio halo, a radio relic or a mini-halo. In this chapter, we present the individual clusters, their properties and the properties of the radio sources that we have found.

7.1 Notes on individual clusters without diffuse sources

In this section 7.1. we report the individual clusters in which our observations have not detected diffuse radio emission and in section 7.1.2 their radio contours overlaid to the DSS2 optical image (*left panel*) and *Chandra* X-ray image (*right panel*).

7.1.1 Clusters without diffuse emission

MACSJ0011.7–1523 ($z = 0.379$)

This cluster has been classified as relaxed (e.g. Ebeling et al. 2010; Mantz et al. 2015). At the center of the cluster we detected a not resolved radio source with a flux density of ~ 20 mJy. No high resolution radio observations in L-band are reported in the literature and it was therefore not possi-

ble to estimate by difference the possibly presence of diffuse radio emission. Radio contours of the images (C array) reported in sect. 7.1.2 are drawn at (3, 6, 9, 12, 24, ...) $\times \sigma$ with rms noise $\sigma = 0.04$ mJy/beam. FWHM: 26.2" \times 14.5" (PA= 11.0°).

MACSJ0035.4–2015 ($z = 0.352$)

Ebeling et al. 2010 assigned to this cluster a morphological class 3 classifying it as a not relaxed cluster. In the literature no radio observations are reported. Both in the C and D array images there is no evidence of diffuse radio emission. Radio contours (C array) in sect. 6.1.2 are drawn at (3, 6, 9, 12, 24, ...) $\times \sigma$ with rms noise $\sigma = 0.18$ mJy/beam. Restoring FWHM: 45" \times 45" (PA= 0°).

MACSJ0159.0–3412 ($z = 0.458$)

This extremely disturbed cluster (Mann & Ebeling 2012) is poorly studied in the literature. In our C and D array images there is no diffuse emission. The discrete radio sources near the center of the cluster have optical counterparts in the DSS2 (red) image. Radio contours (C array) of sect. 7.1.2 are drawn at (3, 6, 9, 12, 24, ...) $\times \sigma$ with rms noise $\sigma = 0.05$ mJy/beam. Restoring FWHM: 26" \times 26" (PA= 0°).

MACSJ0242.5–2132 ($z = 0.314$)

Mann & Ebeling (2012) assigned to MACSJ0242.5 a morphological class 1 and classified it as a relaxed cluster. In our C and D array radio images at the center of the cluster is present a not resolved bright radio source with flux density (1143 ± 57) mJy and extended $\sim 0.5'$ (~ 150 kpc; C array). Hlavacek-Larrondo et al. (2013b) analyzed in a sample of clusters the AGN properties in brightest cluster galaxies (BCGs) reporting for the central source of this relaxed cluster a flux density at 1.4 GHz of (1255 ± 73) mJy. Because of the lower value obtained with our observations we can not deduce in MACSJ0242.5 the presence of diffuse radio emission.

Radio contours (C array) of sect. 7.1.2 are drawn at (3, 6, 9, 12, 24, ...) $\times \sigma$ with rms noise $\sigma = 0.18$ mJy/beam. FWHM: 33.1" \times 14.3" (PA= -29.1°).

MACSJ0429.6–0253 ($z = 0.399$)

The radio image we have obtained with the C array of this relaxed cluster (Ebeling et al. 2010) shows the presence at the centre of a ~ 145 kpc strong radio source not resolved. The flux density is (132.1 ± 6.6) mJy. Hlavacek-Larrondo et al. (2013b) reported for the central BCG of MACSJ0429.6 a radio flux at 1.4 GHz of (138.8 ± 8.1) mJy. Comparing these two fluxes, it would not seem to be present diffuse radio emission.

Radio contours (C array) of sect. 7.1.2 are drawn at $(3, 6, 9, 12, 24, \dots) \times \sigma$ with rms noise $\sigma = 0.07$ mJy/beam. FWHM: $27.0'' \times 13.9''$ (PA = -40.3°).

MACSJ0911.2+1746 ($z = 0.505$)

This extremely disturbed high redshift galaxy cluster in the FIRST and in the NVSS radio images does not show point sources at the centre. Our C, D and C+D array radio maps confirm the absence of discrete and diffuse radio sources in the central region of this cluster. Radio contours (C+D arrays) of sect. 7.1.2 are drawn at $(3, 6, 9, 12, 24, \dots) \times \sigma$ with rms noise $\sigma = 0.055$ mJy/beam. FWHM: $27.7'' \times 24.6''$ (PA = -63.7°).

MACSJ1115.2+5320 ($z = 0.466$)

Mann & Ebeling (2012) 2012 measured the projected offset of the brightest cluster galaxy from the peak of the X-ray emission assigning to this cluster a morphological class 1 and classifying it as relaxed. In our radio images there are no discrete and/or diffuse sources at the centre. Radio contours (C array) of sect. 7.1.2 are drawn at $(3, 6, 9, 12, 24, \dots) \times \sigma$ with rms noise $\sigma = 0.048$ mJy/beam. FWHM: $19.0'' \times 11.7''$ (PA = 28.0°).

MACSJ1115.8+0129 ($z = 0.352$)

This cluster has only been observed in D array. The FIRST radio image shows the presence of a point radio source in the centre of the cluster that has been classified as relaxed by Ebeling et al. (2010).

MACSJ1319.9+7003 ($z = 0.327$)

Classified as moderately disturbed this cluster, also known as Abell 1722, has been observed in radio band with the GMRT at 610 MHz by Kale et al. (2015b) but without the detection of diffuse radio emission. In our

C array radio map two point sources are shown at the peripheral of the X-ray emission but without diffuse emission. Radio contours (C array) of sect. 6.1.2 are drawn at (3, 6, 9, 12, 24, ...) $\times \sigma$ with rms noise $\sigma = 0.065$ mJy/beam. Restoring FWHM: $22'' \times 18''$ (PA = 0°).

MACSJ1720.2+3536 ($z = 0.387$)

With morphological class 1 this cluster is classified as relaxed. The C array radio images of our dataset show a central strong point-like radio source. The flux density is (17.2 ± 0.9) mJy. Deriving the flux density at 1.4 GHz from the NVSS survey, Hlavacek-Larrondo et al. (2013b) reported for the central BCG of this cluster a value of (16.8 ± 1.0) mJy comparable with our JVLA measure. There is no evidence of diffuse radio emission. Radio contours (C array) of sect. 7.1.2 are drawn at (3, 6, 9, 12, 24, ...) $\times \sigma$ with rms noise $\sigma = 0.059$ mJy/beam. FWHM: $15.7'' \times 15.6''$ (PA = -51.2°).

MACSJ2049.9–3217 ($z = 0.323$)

In this disturbed cluster (morphological class 3; Ebeling et al. (2010)) there are no radio data reported in the literature. The radio images from our JVLA observations show some discrete radio sources near the centre of the cluster but without evidences of diffuse radio emission. Radio contours (C array) of sect. 7.1.2 are drawn at (3, 6, 9, 12, 24, ...) $\times \sigma$ with rms noise $\sigma = 0.09$ mJy/beam. FWHM: $40.9'' \times 14.3''$ (PA = 14.2°).

MACSJ2214.9–1359 ($z = 0.5027$)

In our D array radio image of this moderately disturbed cluster we have not detected point sources or diffuse radio emission in the centre. Radio contours (D array) of sect. 7.1.2 are drawn at (3, 6, 9, 12, 24, ...) $\times \sigma$ with rms noise $\sigma = 0.06$ mJy/beam. Restoring FWHM: $20'' \times 20''$ (PA = 0°).

MACSJ2229.7–2755 ($z = 0.324$)

This cluster is classified as relaxed. There are not radio observations reported in the literature. Radio images in the D array show a bright central radio source extended ~ 180 kpc with flux density of (4.3 ± 0.2) mJy. From the observations in D array alone we can not suggest presence of diffuse radio emission. Radio contours (C array) of sect. 7.1.2 are drawn at (3,

6, 9, 12, 24, ...) $\times \sigma$ with rms noise $\sigma = 0.2$ mJy/beam. Restoring FWHM: $40'' \times 40''$ (PA= 0°).

MACSJ2241.8+1732 ($z = 0.314$)

The C and D array images of our dataset show a point source also detected in the NVSS near the centre but without diffuse emission. No radio data are available in the literature. This cluster is also known as Abell 2742. Radio contours (C array) of sect. 7.1.2 are drawn at (3, 6, 9, 12, 24, ...) $\times \sigma$ with rms noise $\sigma = 0.05$ mJy/beam. FWHM: $19.2'' \times 16.0''$ (PA= -55.8°).

MACSJ2245.0+2637 ($z = 0.314$)

Classified as relaxed by Ebeling et al. (2010), the C and D array images of this cluster show the presence of a central radio source with a flux density of (4.6 ± 0.2) mJy. Giacintucci et al. (2017) investigating the occurrence of minihalos, reported for MACSJ2245.0 no detection of diffuse radio emission. High resolution L band observations, not reported in the literature, are needed to verify by difference the possible presence of a residual diffuse emission.

Radio contours (C array) of sect. 7.1.2 are drawn at (3, 6, 9, 12, 24, ...) $\times \sigma$ with rms noise $\sigma = 0.09$ mJy/beam. FWHM: $17.2'' \times 16.0''$ (PA= -56.3°).

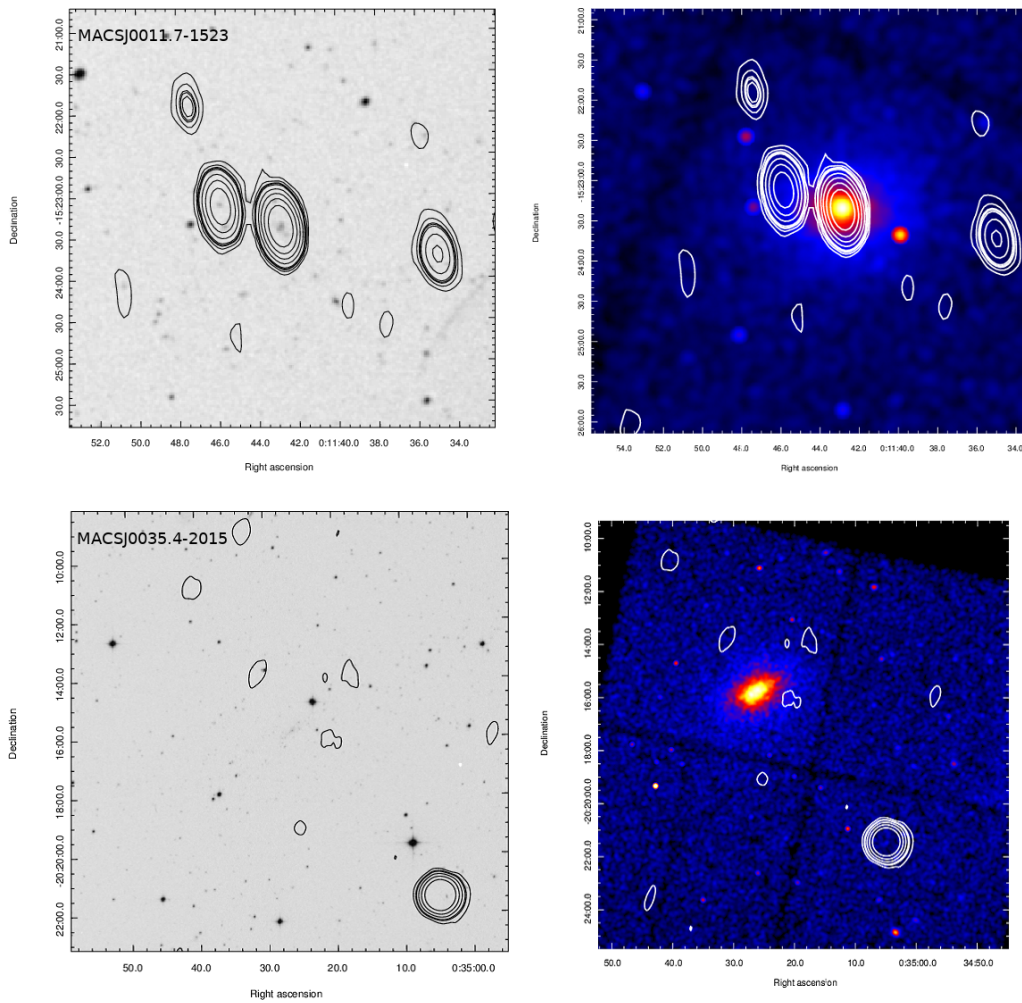
MACSJ2311.5+0338 ($z = 0.305$)

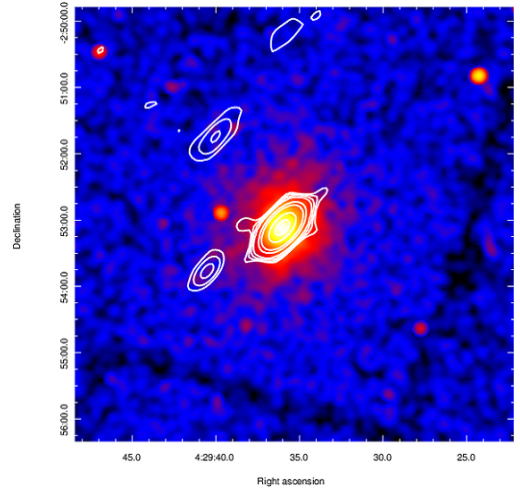
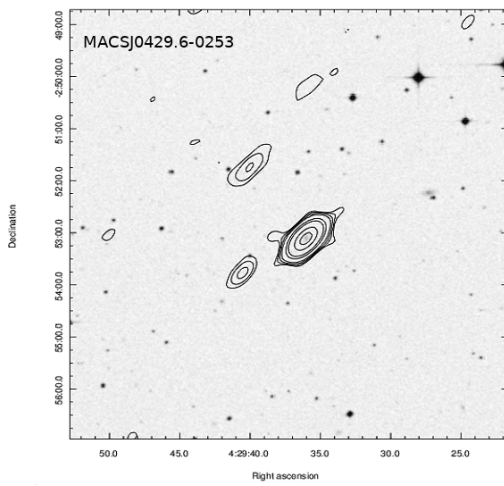
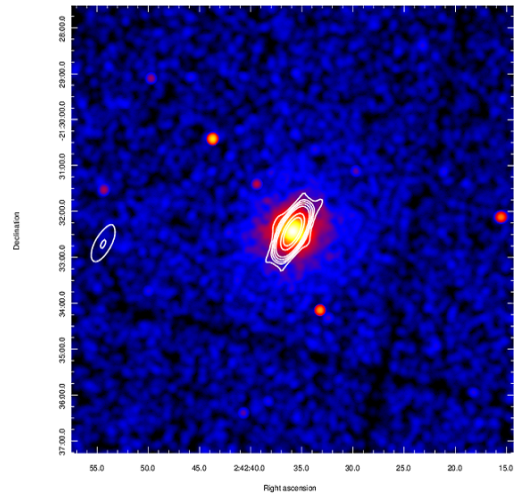
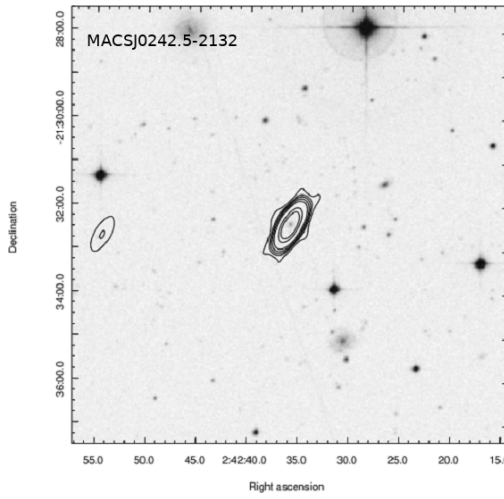
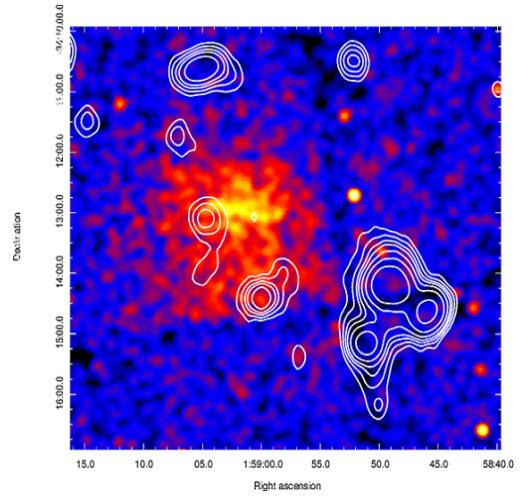
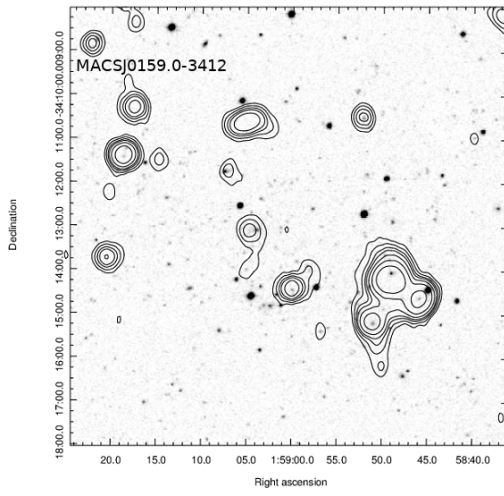
In this disturbed cluster (morphological code 3; Ebeling et al. (2010)) we detected in the C+D array image two sources one of them located at the centre, not present in the NVSS and FIRST radio images. The density flux of this structure is (0.92 ± 0.05) mJy. In the C array high resolution image (uv -range 7–22 $k\lambda$) the central radio emission is resolved in two point radio sources, labeled with A and B, with density flux of (0.69 ± 0.06) and (0.28 ± 0.05) respectively. Since there is no significant difference between the C+D and high resolution C emissions, we conclude that there is not detection of diffuse radio emission in MACSJ2231.5.

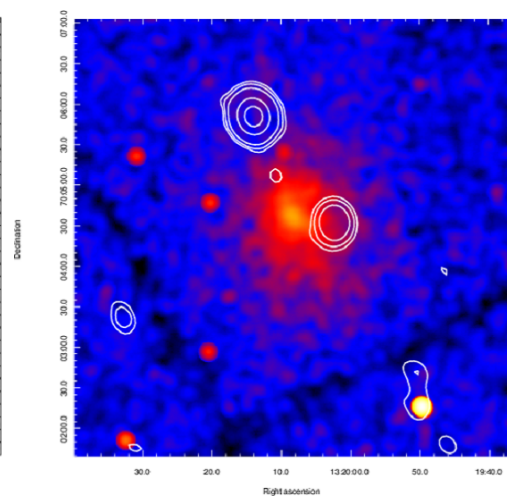
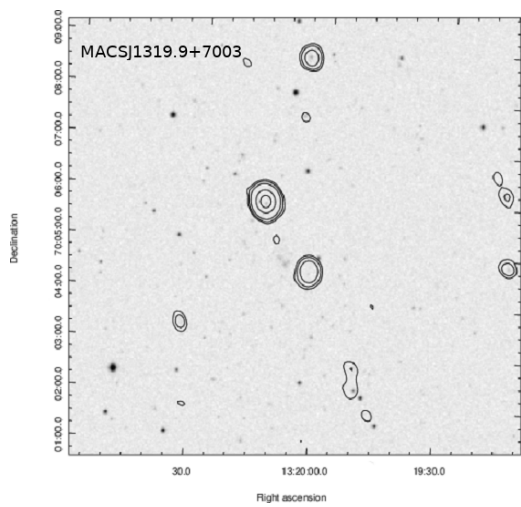
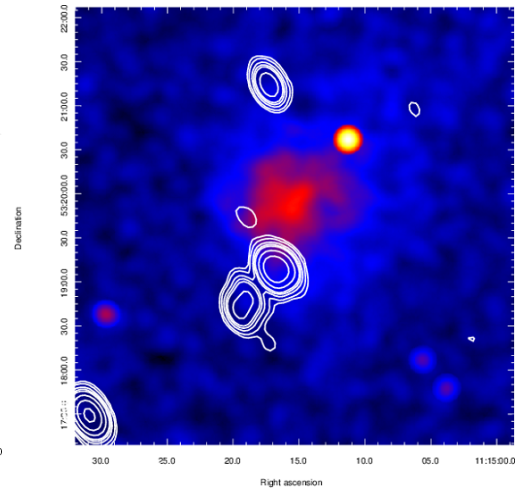
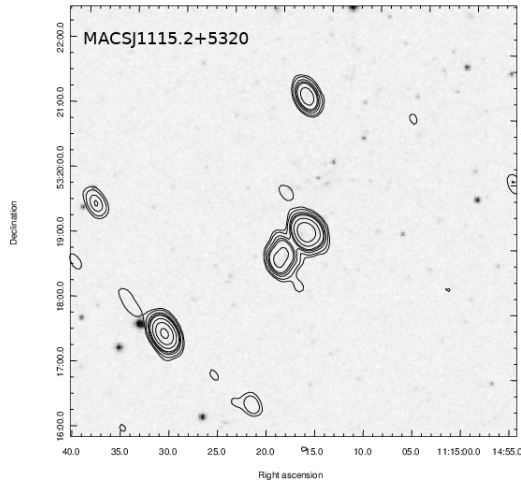
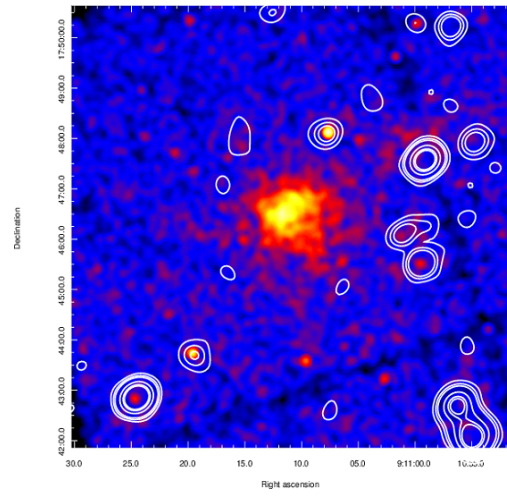
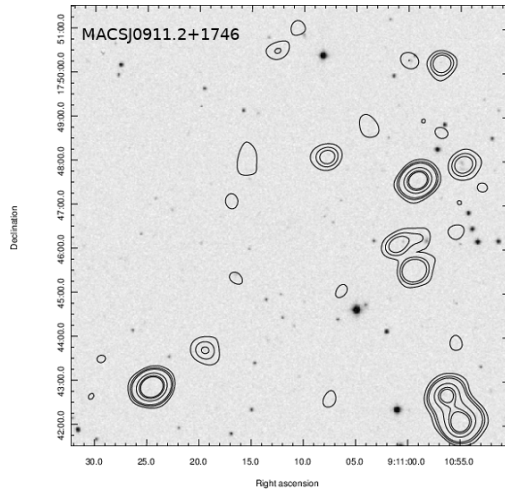
Radio contours (C+D array) of sect. 7.1.2 are drawn at (3, 6, 9, 12, 24, ...) $\times \sigma$ with rms noise $\sigma = 0.04$ mJy/beam. FWHM: $25.2'' \times 18.2''$ (PA= 37.3°).

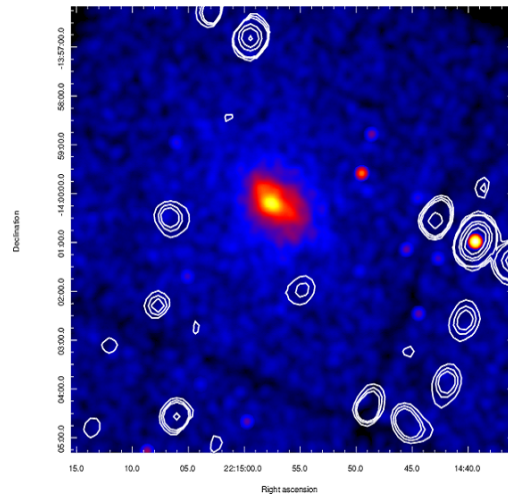
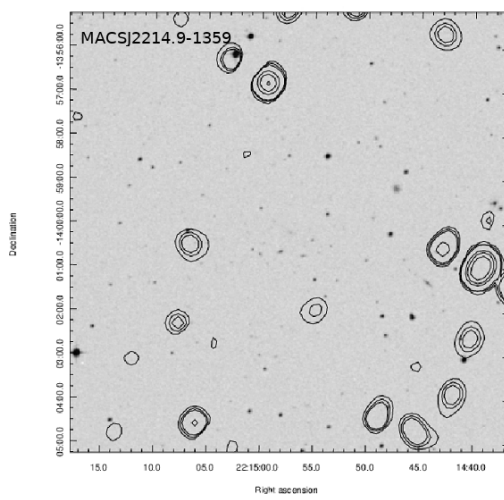
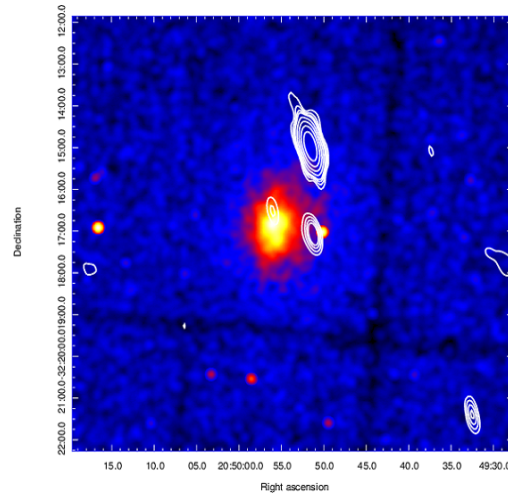
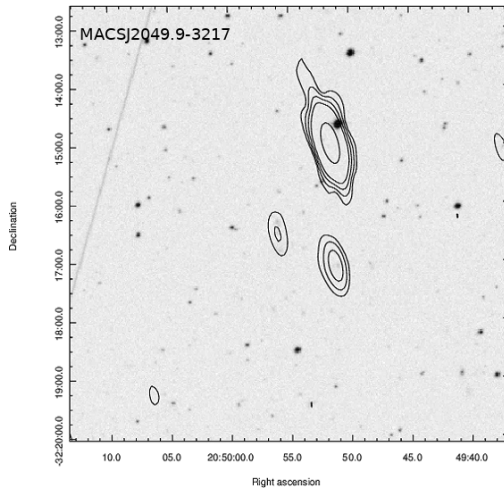
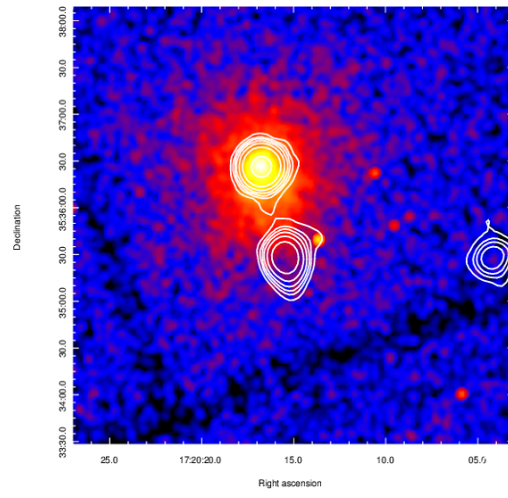
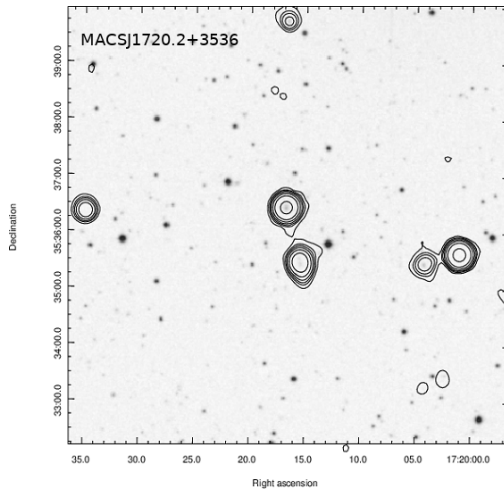
7.1.2 Plots of clusters without diffuse radio emission

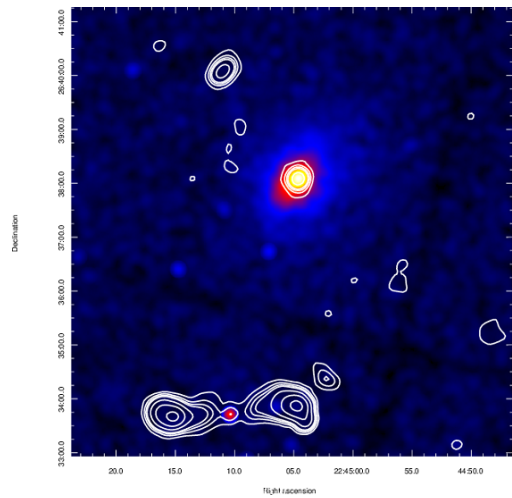
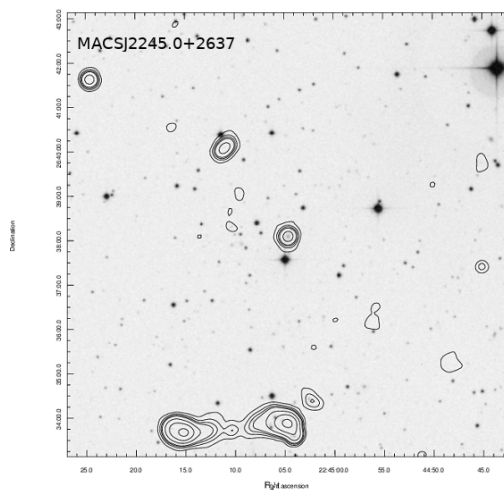
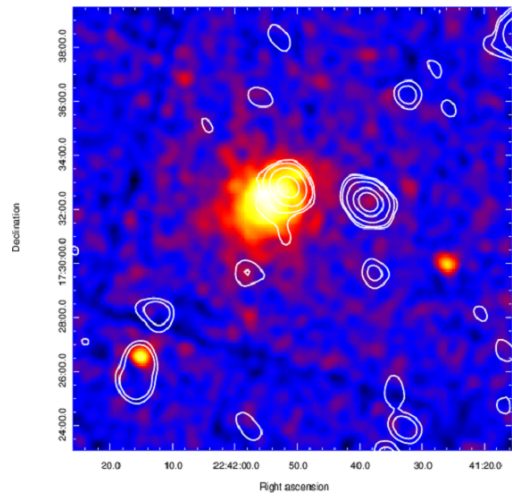
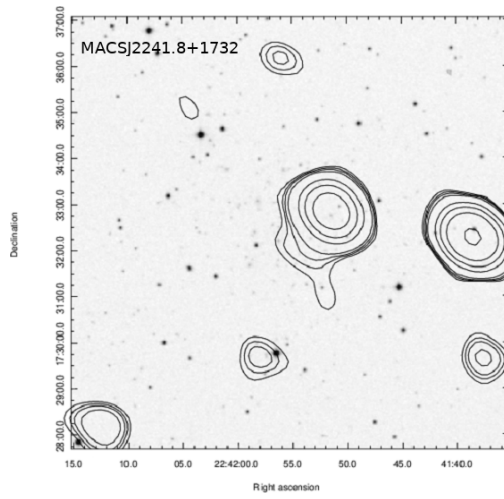
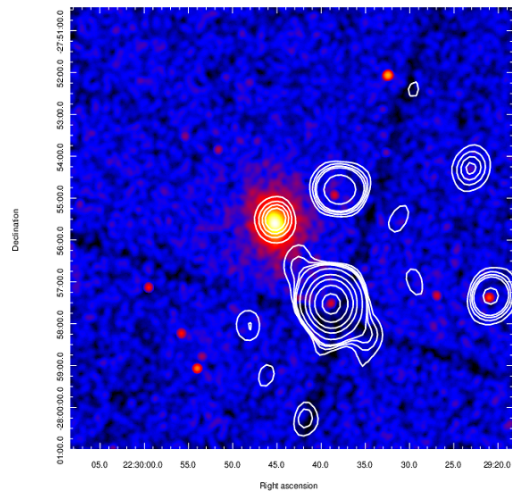
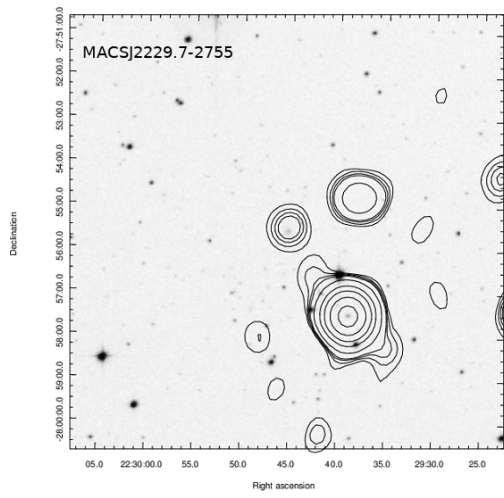
We report in this subsection the radio contours overlaid to DSS2-red optical images (*left panels*) and the same contour overlaid to the *Chandra* X-ray images for the above listed clusters without detection in our JVLA observational campaign of diffuse radio emission.











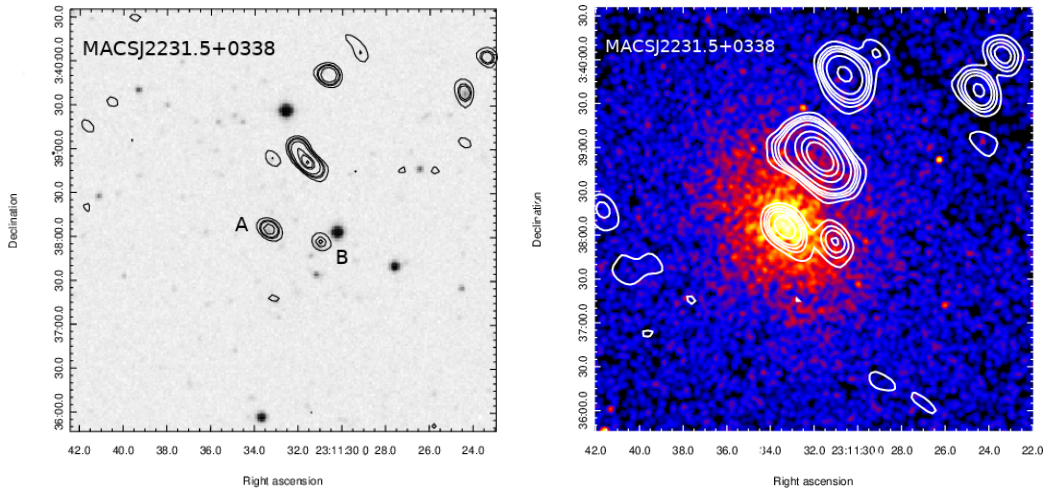


Figure 7.1: (*left panel*) Clusters without detection of diffuse radio emission: radio contours overlaid to DSS2-red optical images. (*right panel*) Radio contours of the same clusters without detection of diffuse radio emission: radio contours overlaid to *Chandra* X-ray color images

7.2 Notes on individual clusters with uncertain diffuse sources

In this section we list the clusters in which the detection of diffusion emissions was uncertain and would require further investigation to be clarified.

MACSJ0257.1–2325 ($z = 0.504$)

High redshift cluster included by Ebeling et al. 2010 in the subset of the 12 most distant galaxy clusters detected at $z > 0.5$ and classified as moderately disturbed (morphological class 2). No radio observations are reported in literature. In the radio images obtained combining the C and D arrays, we detected a ~ 180 kpc extended radio source centered on the X-ray emission with a flux density of (3.68 ± 0.18) mJy. The flux density measured in the high resolution C array images (uv -range = $7 - 22k\lambda$) is (3.20 ± 0.11) mJy. In the D array this source is not resolved from the other radio sources located near the centre. Subtracting the C array flux from the C+D array flux, we obtain a residual value of (0.48 ± 0.29) mJy corresponding to a radio power of $P_{1.4} = (7.06 \pm 0.43) \times 10^{23}$ W/Hz adopting a spectral index $\alpha = -1$. This slight excess flux it is probably related to the presence of diffuse radio emission, but its classification (halo or minihalo) is uncertain and needs of further investigation.

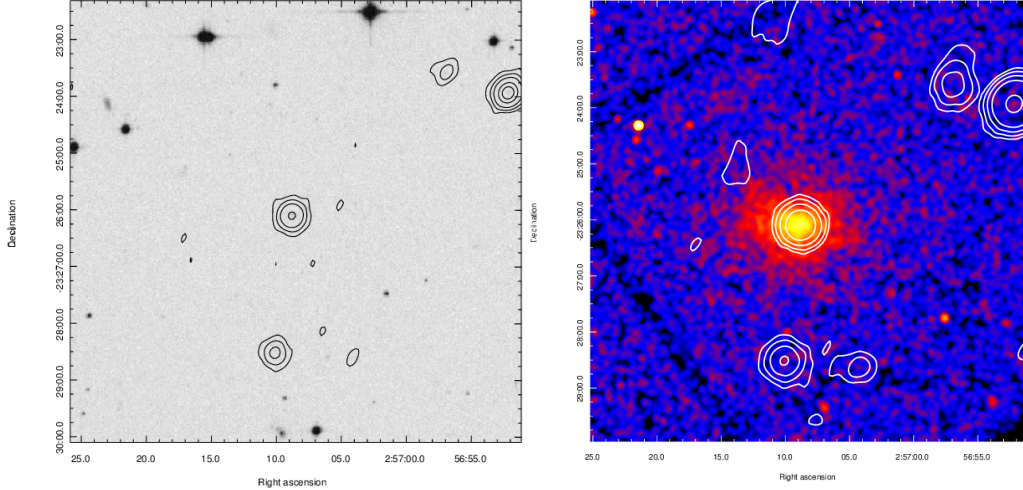


Figure 7.2: *left panel* MACSJ0257.1: C array radio image ((uv) -range 7–22 $k\lambda$) overlaid on the DSS2-red image. FWHM (restoring beam): $20'' \times 20''$ (PA= 0°) with rms noise is $1\sigma = 0.04$ mJy/beam and contours $(3, 6, 9, \dots) \times \sigma$. *Right panel* C+D array radio contours overlaid with *Chandra* X-ray image. FWHM (restoring beam): $30'' \times 30''$ (PA= 0°) with rms noise is $1\sigma = 0.05$ mJy/beam and contours $(3, 6, 9, \dots) \times \sigma$.

MACSJ0358.8-2955 ($z = 0.425$)

MACSJ0358.8 is a massive and hot cluster with a disturbed X-ray morphology. Parek et al. (2016) observed this cluster with the GMRT at 610 MHz but without the discovery of any diffuse radio emission. In the C+D array we detected a complex radio emission at the centre of the cluster with embedded a point source and extended ~ 800 kpc. The flux density of this radio structure is (13.1 ± 0.7) mJy. In the C array high resolution map the radio structure is resolved in three point sources labeled with A, B and C. Their fluxes are: A+B (4.2 ± 0.2) mJy and C (1.8 ± 0.1) mJy. If we subtract the fluxes of these point sources from the flux of the complex source detected in the C+D array, we found a residual flux of (7.1 ± 1.0) mJy corresponding to a radio power of $P_{1.4} = (6.5 \pm 0.9) \times 10^{24}$ W/Hz adopting a spectra index $\alpha = -1$. We hypothesize the presence of diffuse radio emission with the morphology of a radio halo, but the difficulty of properly subtracting the point sources makes our classification uncertain. In Fig. 7.3 we report the C array high resolution radio contours overlaid to the DSS2-red optical image and the C+D arrays radio contours overlaid to the *Chandra* X-ray image.

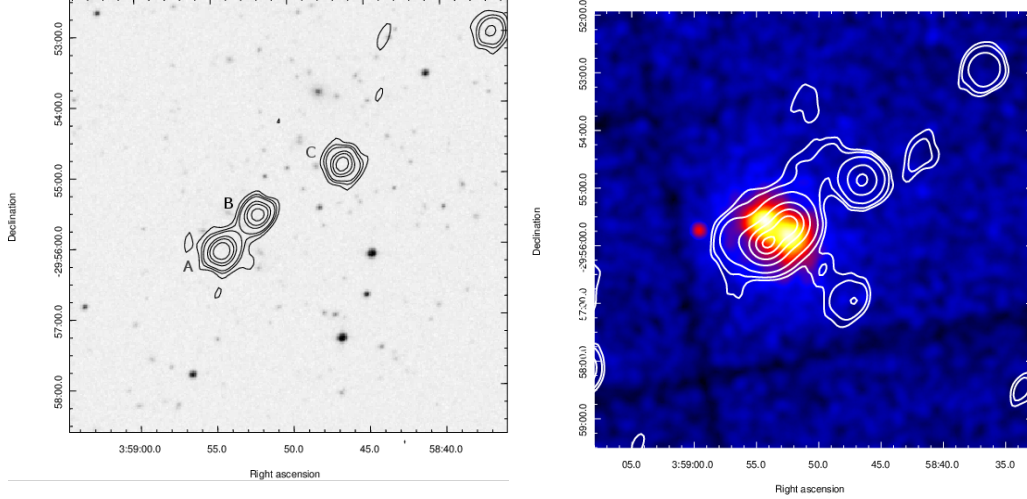


Figure 7.3: *left panel* MACSJ0358.8 radio contours at 1.52 GHz with the JVLA in C configuration (uv-range 7-22 k λ) overlaid on the DSS2 optical image. The FWHM (restoring beam) is $20.0'' \times 20.0''$ (PA = 0°). The rms noise is $1\sigma = 0.045$ mJy/beam and contours are: (3, 6, 9, 12, ...) $\times \sigma$. *Right panel* radio contours at 1.52 GHz in C+D configuration overlaid with *Chandra* X-ray image. The FWHM (restoring beam) is $30'' \times 30''$ (PA = 0°). The rms noise is $1\sigma = 0.04$ mJy/beam and contours are: (3, 6, 9, 12, ...) $\times \sigma$.

MACSJ0647.7+7015 ($z = 0.591$)

Classified as moderately disturbed (morphological class 2), in the literature are not reported radio observations of this high redshift cluster. In the D array maps of our dataset, as in the NVSS image, there are not discrete or diffuse radio sources at the centre of the cluster. In the C and C+D array images we detected a ~ 250 kpc diffuse central emission with flux density of (1.1 ± 0.1) corresponding to a radio power of $P_{1.4} = (2.3 \pm 0.2) \times 10^{24}$ W/Hz adopting a spectral index $\alpha = -1$. The morphology and the radio properties of this source suggest that it could be a possible radio halo, even if this classification appears somewhat uncertain. In the SE side, located at a distance of ~ 530 kpc from the central emission, it is also present an elongated diffuse radio structure with a LAS of $\sim 0.7'$ (~ 300 kpc at the cluster distance) and a radio flux of ~ 1.0 mJy. Its morphology and location suggest the possibility of a candidate radio relic, but further investigations are needed to hypotize MACSJ0647 as a system where a radio halo and a radio relic are both present. In Fig. 7.4 we report the C+D radio contours overlaid to DSS2 optical and *Chandra* X-ray images.

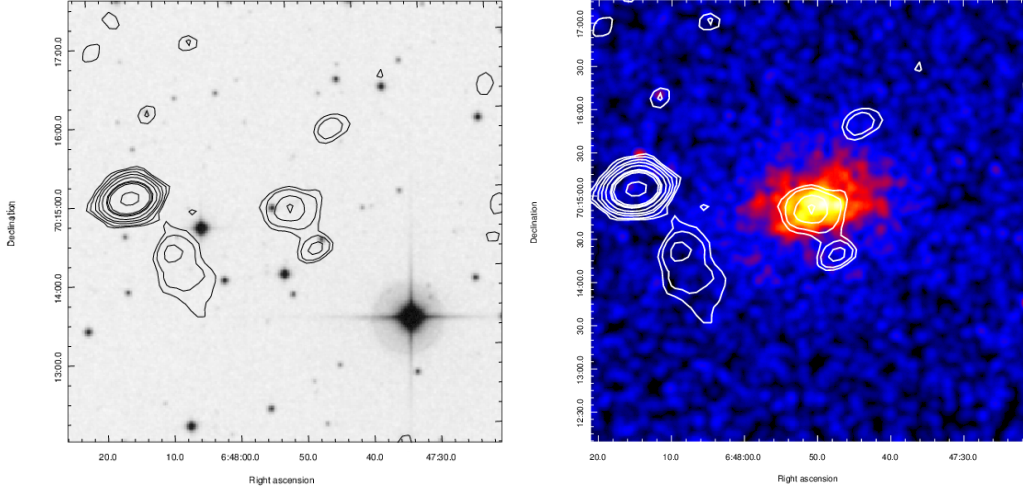


Figure 7.4: *left panel* MACSJ0647.7 radio contours at 1.52 GHz with the JVLA in C+D configuration overlaid on the DSS2 optical image. The FWHM is $27.1'' \times 19.2''$ (PA = -74°). The rms noise is $1\sigma = 0.05$ mJy/beam and contours are: (3, 6, 9, 12, ...) $\times \sigma$. *Right panel* the same contours overlaid with *Chandra* X-ray image.

MACSJ0949.8+1708 ($z = 0.384$)

MACSJ00949.8 is an X-ray luminous cluster classified by Ebeling et al. (2010) with a morphological code 2 as moderately disturbed with no pronounced cool core but with a good optical–X-ray alignment and concentric X-ray contours. This cluster have been observed by Venturi et al. (2008) and Bonafede et al. (2015) with the GMRT at 616 MHz and 323 MHz: they detected a diffuse radio emission classified as candidate radio halo. Combining the C and D array the resulting radio image shows an extended emission embedding some point sources. The density flux of this radio structure is (3.15 ± 0.16) mJy. In the C array image the embedded sources are well resolved (labeled with A, B, C, and D). They have an overall flux density of (1.97 ± 0.10) mJy. We estimate by difference a residual flux density of (1.18 ± 0.26) mJy probably associated to the diffuse emission of the halo reported by the previous authors, even if lower than the flux they measured at 323 MHz of (21.0 ± 2.2) which corresponds at 1.42 GHz of (3.06 ± 0.3) mJy. For this reason we consider our detection uncertain. In Fig. 7.5 we report the C array radio image overlaid to the DSS2-red optical image (*left panel*) and the C+D radio image overlaid to the *Chandra* X-ray image (*right panel*).

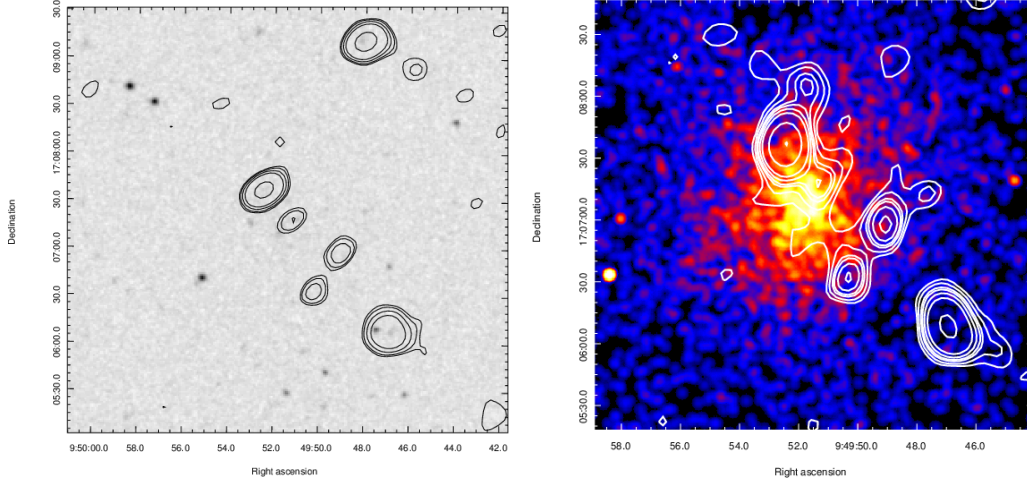


Figure 7.5: *left panel* MACSJ0949.8 radio contours at 1.46 GHz with the JVLA in C configuration overlaid on the DSS2 optical image. The FWHM is $20.4'' \times 14.2$ (PA = -55°). The rms noise is $1\sigma = 0.045$ mJy/beam and contours are: (3, 6, 9, 12, ...) $\times \sigma$. *Right panel* radio contours at 1.42 GHz in C+D configuration overlaid with *Chandra* X-ray image. The FWHM is $20.9'' \times 15.4$ (PA = 0°). The rms noise is $1\sigma = 0.03$ mJy/beam and contours are: (3, 6, 9, 12, ...) $\times \sigma$.

MACSJ1423.8+2404 ($z = 0.543$)

Classified as relaxed, this high redshift cluster shows in our radio images at the centre a ~ 160 kpc extended not resolved radio source with flux density of (6.6 ± 0.3) mJy. Hlavacek-Larrondo et al. (2013) derived the radio flux of the central BCG of MACSJ1423.8 from the 1.4 GHz VLA Faint Images of the radio Sky at Twenty-cm (FIRST) survey (Becker, White & Helfand 1994) reporting a value of (5.2 ± 0.4) mJy. The flux excess of (1.4 ± 0.7) mJy we have found, corresponding to a radio power $P_{1.4} = (2.5 \pm 1.3) \times 10^{24}$ W/Hz, could be associate to a candidate diffuse radio emission, but data are too uncertain and require of further radio observations to be correctly interpreted.

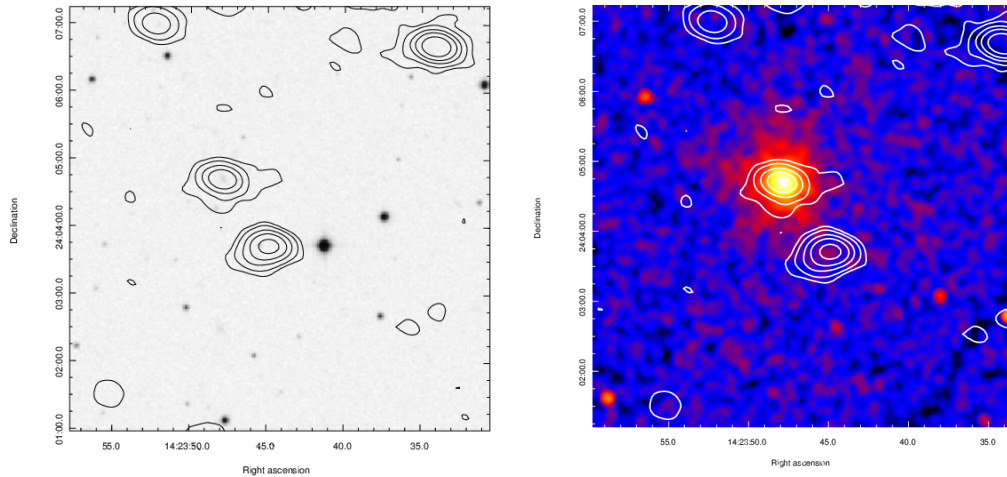


Figure 7.6: *left panel* MACSJ1423.8 radio contours at 1.52 GHz with the JVLA in C configuration overlaid on the DSS2 optical image. The FWHM is $24.9'' \times 16.8''$ (PA= 82°). The rms noise is $1\sigma = 0.05$ mJy/beam and contours are: (3, 6, 9, 12, ...) $\times \sigma$. *Right panel* the same contours overlaid with *Chandra* X-ray image.

MACSJ2129.4–0741 ($z = 0.589$)

About this dynamically disturbed cluster, the literature does not report studies in the radio band. The D array data of our observation have been severely corrupted by the transit of the sun and have not been used to produce radio maps. The C array radio images show a weak central radio source not detected in the NVSS nor in the FIRST surveys. It is ~ 110 kpc extended and has a flux density of ~ 0.5 mJy corresponding to a radio power of $P_{1.4} \sim 1.1 \times 10^{24}$ W/Hz. Its location is slightly shifted respect to the X-ray centre and it seems to have no optical counterpart. However, the classification of this source as a diffuse radio emission is sharply uncertain, as well as the two elongated radio structures located in the NE and SW sides respect to the central one. Fig. 7.7 shows radio contours overlaid on the DSS2-red optical and *Chandra* X-ray images.

h

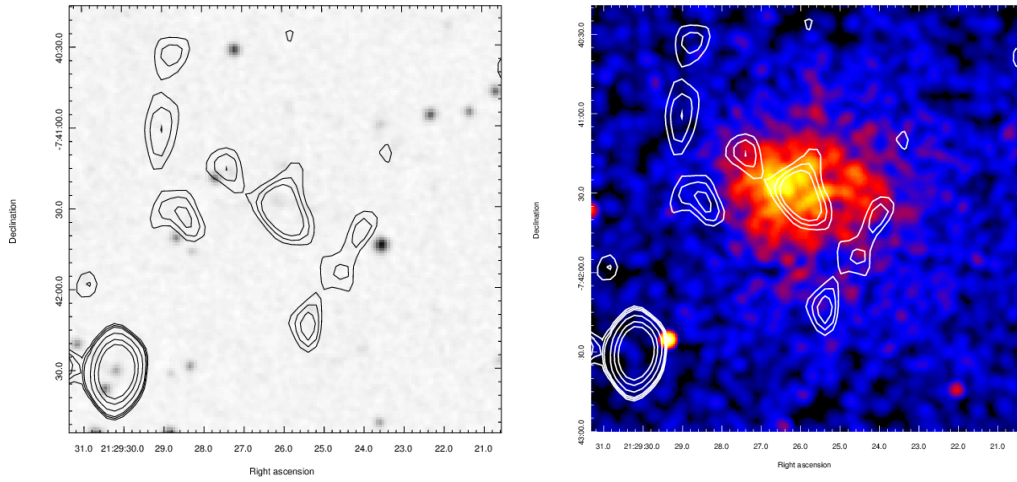


Figure 7.7: *left panel* MACSJ2129.4 radio contours at 1.49 GHz with the JVLA in C configuration overlaid on the DSS2 optical image. The FWHM is $22.2'' \times 14.2''$ (PA = -7.1°). The rms noise is $1\sigma = 0.029$ mJy/beam and contours are: (3, 3.5, 4, 6, 9, ...) $\times \sigma$. *Right panel* the same contours overlaid with *Chandra* X-ray image.

Chapter 8

Summary and conclusions

The aim of this thesis was mainly to investigate the evolution history of non-thermal properties in galaxy clusters, actually limited to low redshifts ($z < 0.3$). At this purpose we attempted to increase the number of known diffuse radio sources detected at $z \geq 0.3$ through new interferometric radio observations. We selected as suitable target an homogeneous sample of 44 high massive and X-ray luminous galaxy clusters extracted from the Ebeling Massive Cluster Survey (MACS). We discovered 8 new diffuse objects classified as 6 radio halos and 2 radio relics and confirmed the detection of other 10 diffuse sources most of them observed at different wavelengths. We studied and compared their radio properties and the properties of the hosting clusters with respect to up to date collections of diffuse radio sources detected at $z > 0.3$ and $z \leq 0.3$. We performed also a preliminary study of the dynamical state of a selected sample of clusters with diffuse radio emission using c , w , P_3/P_0 and the D_{X-BCG} offset as morphological indicators. We found interesting correlations between the offset BCG/X-ray peak, the concentration parameter c and the centroid shift w that could be adopted as a proxy to study the dynamical state evolution of clusters hosting diffuse emission. We are waiting for the offsets of the whole MACS collection to become available in the literature to conclude our study.

In the following we present our main results, conclusions and future perspectives.

8.1 Results of the Project 17A-025 radio observations

As discussed in Chap. 6, the number of the observed and reduced clusters was 42. In the following table we summarize the main properties of these clusters and the results (detection/non detection and kind of detection) of our radio observations.

Table 8.1: Observational results in Prj VLA/17A-025

Cluster Name	z	$L_{X,500}$ 10^{44} erg/s	ν_{obs} GHz	Array of images	Detected source/s	S_ν mJy	$P_{1.4}$ 10^{24} W/Hz	LLS (kpc)
MACSJ0011.7	0.379	8.9	1.52	C	CeSou	~ 20	-	-
MACSJ0018.5	0.546	17.9	1.32	C	H	8.7	11.7	1570
MACSJ0025.4	0.584	8.0	1.42	C	2R	1.7,1.2	-	601,250
MACSJ0035.4	0.352	11.9	1.52	C	no det.	-	-	-
MACSJ0152.5	0.413	8.6	1.52	C,D	H	2.34	1.58	620
MACSJ0159.0	0.458	8.5	1.52	C	no det.	-	-	-
MACSJ0159.8	0.406	14.4	1.52	C	MH	2.1	1.22	-
MACSJ0242.5	0.314	13.2	1.68	C	CeSou	1144	-	-
MACSJ0257.1	0.505	12.5	1.68	C,C+D	H/MH (u)	0.48	0.71	180
MACSJ0257.6	0.322	7.0	1.52	C,C+D	H	21.9	5.48	300
MACSJ0308.9	0.356	17.9	1.52	C+D	H	9.7	4.65	750
MACSJ0329.7	0.450	13.6	1.52	C	MH	4.0	3.0	160
MACSJ0358.8	0.425	18.9	1.52	C,C+D	H (u)	7.1	6.5	~ 800
MACSJ0429.6	0.399	10.5	1.52	C	CeSou	132	-	-
MACSJ0451.9	0.430	6.75	1.52	C	R	1.52	1.13	600
MACSJ0454.1	0.538	15.4	1.52	C	H	1.04	1.35	350
MACSJ0520.7	0.336	7.8	1.59	C	R	1.49	0.75	1100
MACSJ0553.4	0.407	17.0	1.52	C	H,R(u)	8.1,1.1	6.4,0.8	1000,600
MACSJ0647.7	0.591	13.1	1.52	C+D	H(u),R(u)	1.1,~ 1.0	2.3, -	250,300
MACSJ0744.8	0.698	22.9	1.52	C+D	H	0.88	2.52	700
MACSJ0911.2	0.505	7.13	1.46	C+D	no det.	-	-	-
MACSJ0947.2	0.354	20.0	1.46	C+D	MH	8.4	3.62	180
MACSJ0949.8	0.384	14.7	1.46	C,C+D	H(u)	1.18	-	-
MACSJ1115.2	0.466	9.6	1.74	C	No det.	-	-	-
MACSJ1115.8	0.355	14.5	1.43		CeSou	9.89	-	-
MACSJ1206.2	0.439	17.6	1.40		CeSou	170	-	-
MACSJ1319.9	0.327	4.2	1.65	C	No det.	-	-	-
MACSJ1423.8	0.543	13.1	1.52	C	(u)	1.4	2.5	~ 160
MACSJ1427.6	0.363	4.1	1.40		CeSou	3.02	-	-
MACSJ1532.8	0.363	14.7	1.52	C	MH	4.4	1.96	90
MACSJ1720.2	0.387	10.2	1.52	C	CeSou	17.2	-	-
MACSJ1931.8	0.352	19.6	1.52	C	MH	50.0	20.9	-
MACSJ2049.9	0.323	6.1	1.52	C	No det.	-	-	-
MACSJ2129.4	0.589	12.0	1.49	C	(u)	0.5	1.1	~ 110
MACSJ2140.2	0.313	11.1	1.40		CeSou	3.6	-	-
MACSJ2211.7	0.397	24.0	1.52	C	H	2.87	1.76	620
MACSJ2214.9	0.503	12.9	1.42	D	No det.	-	-	-
MACSJ2228.5	0.411	19.3	1.52	C,C+D	H	14.96	9.98	1092
MACSJ2229.7	0.324	10.0	1.52	D	CeSou	4.3	-	-
MACSJ2241.8	0.314	5.6	1.52	C	No det.	-	-	-
MACSJ2245.0	0.301	7.6	1.52	C	CeSou	4.6	-	-
MACSJ2311.5	0.305	12.9	1.52	C+D	CeSou	0.69	-	-

CeSou=Central Source

8.2 Discovery of new diffuse emission at $z \geq 0.3$

In our L-band radio observations with the JVLA, we detected diffuse radio emission in 18 clusters corresponding to $\sim 43\%$ of the sample. This percentage is in good agreement with the value of 27-44% of clusters hosting diffuse emission with $L_x > 5 \cdot 10^{44}$ erg/s, reported in the literature. This trend seems to be confirmed also at high redshift. Among 18 we detected 8 new diffuse sources: 6 classified as radio halos and 2 as radio relics. Their main properties are summarized in Tab. 8.2.

Table 8.2: Diffuse sources detected in Prj VLA/17A-025

Cluster Name	z	M_{500} $10^{14} M_{\odot}$	$L_{X,500}$ 10^{44} erg/s	T_X keV	ν_{obs} GHz	Type	S_{ν} mJy	$P_{1.4}$ 10^{24} W/Hz	LLS (kpc)
MACSJ0152.5	0.413	7.90	8.6	7.4	1.5	H	2.34±0.15	1.58±0.10	620
MACSJ257.6	0.322	5.88	7.0	7.0	1.487	H	21.94±3.27	5.48±0.82	300
MACSJ0451.9	0.430	4.10	6.75	7.66	1.520	R	1.52±0.19	1.13±0.14	600
MACSJ0454.1	0.538	7.13	15.4	7.5	1.520	H	1.04±0.05	1.35±0.06	350
MACSJ0553.4	0.430	9.39	17.0	13.1	1.520	R	1.06±0.05	0.77±0.04	600
MACSJ0744	0.698	11.8	22.9	8.1	1.520	H	0.88±0.13	2.52±0.02	700
MACSJ2211.7	0.397	18.1	24.0	14.0	1.520	H	2.87±0.14	1.76±0.09	620
MACSJ2228.5	0.411	8.26	19.3	7.4	1.5	H	14.96±1.12	9.98±0.75	1092

We confirmed in 10 clusters the presence of diffuse radio emission: 6 already detected at 1.4 GHz (MACSJ0018.5, MACSJ0159.8, MACSJ0329.6, MACSJ0947.2, MACSJ1532.8, MACSJ1931.8), and 4 detected at different wavelengths (323 MHz: MACSJ0025.4, 610 MHz: MACSJ0308.9, 323 MHz: MACSJ0520.7, 323 MHz: MACSJ0553.4). In 6 clusters (MACSJ0257.1, MACSJ0358.8, MACSJ0647.7, MACSJ0949.8, MACSJ1423.8, MACSJ2129.4) we found good traces of diffuse emission but they require further investigations to be properly classified. Finally, 19 clusters did not show any evidence of the presence of diffuse radio emission.

The discovery of the new radio sources implies a growth in the number of known radio halos and relics at $z > 0.3$ of about 21% for halos and about 9% for relics. These percentages will be higher if the uncertain sources should be confirmed by other observations. We report in Fig. 8.1 the results of our observational campaign (*Left panel*) and its contribute to the known population of diffuse radio sources (*Right panel*).

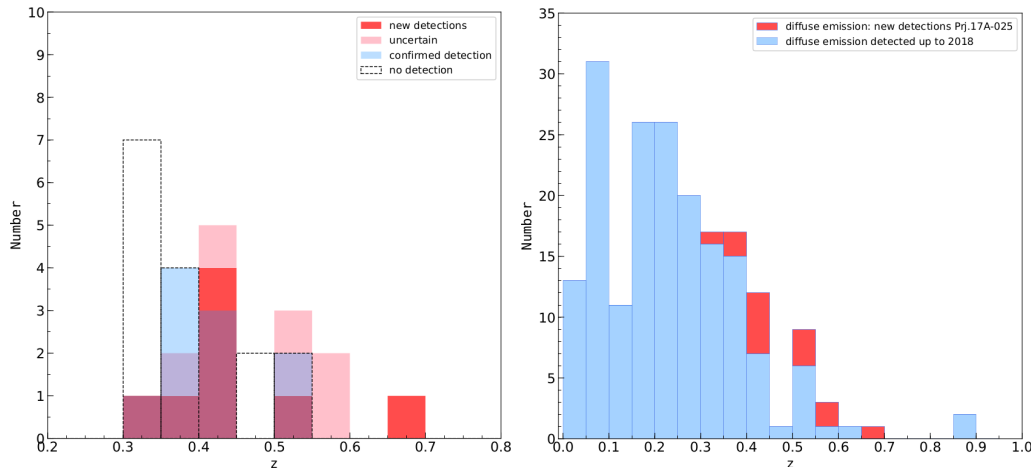


Figure 8.1: *Left panel:* redshift distribution and type of sources detected in Prj. 17A-025 *Right panel:* contribute of our JVLA observational campaign to the known population of diffuse emission.

8.3 Statistical analysis

The properties of non-thermal diffuse emission are strictly connected to the properties of the hosting clusters (e.g. mass and X-ray luminosity). This connection is confirmed by the existence of a scaling relation between radio power of halos, relics and minihalos and the X-ray luminosity of the related cluster. The correlation $P_{1.4GHz}$ vs $L_{X,500}$ as well the correlation radio power vs projected size (LLS) represent good tools to study the redshift evolution of non-thermal emission. We performed a statistical analysis of these correlations on the following collections:

- halos, relics and minihalos detected up to 2011 (Chap. II);
- halos, relics and minihalos discovered between 2011 and 2018 (Chap. III);
- the whole radio diffuse objects collection up to 2018;
- halos and relics at $z < 0.3$;
- halos and relics at $z \geq 0.3$.

In order to homogenize the data collections extracted from the literature we have rescaled radio powers and X-ray luminosities to the same cosmology ($H_0 = 70 \text{ km s}^{-1} \text{ Mpc}^{-1}$, $\Omega_m = 0.3$, $\Omega_\Lambda = 0.7$) and considered the disposable X-ray luminosity in the 0.1–2.4 keV band within R_{500} . When not available we used $\alpha = 1.3$ for halos and $\alpha = 1.2$ for relics as spectral indices for the k -corrections.

8.4 Redshift evolution of radio halos

In Fig. 8.2 we report the distribution in the plane ($P_{1.4GHz}$, $L_{X,500}$) of a 2018 updated collection of radio halos and the new radio halos discovered in our observational campaign.

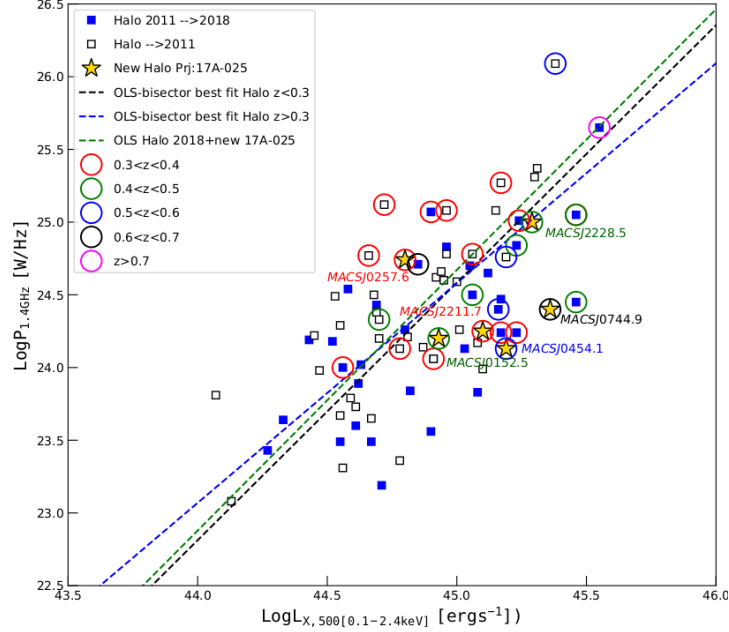


Figure 8.2: Distribution in the ($P_{1.4GHz}$, $L_{X,500}$) plane of the 2018 updated halo collection. Circled dots are the halos detected in clusters with $z \geq 0.3$. Labeled circled stars are the new halos detected in proj. VLA/17A-025. Colored dotted lines are the following OLS-bisector best fits:

black ($z < 0.3$): $\log P_{1.4GHz} = (1.77 \pm 0.17) \log L_{X,500} + (-55.11 \pm 7.58)$ ($r = 0.628$, $p = 1.06 \times 10^{-6}$);
 blue ($z \geq 0.3$): $\log P_{1.4GHz} = (1.51 \pm 0.36) \log L_{X,500} + (-43.43 \pm 16.42)$ ($r = 0.325$, $p = 0.0977$);
 green (2018+new): $\log P_{1.4GHz} = (1.79 \pm 0.16) \log L_{X,500} + (-56.10 \pm 7.28)$ ($r = 0.629$, $p = 8.97 \times 10^{-10}$).

We distinguished with circled dots the halos detected in clusters at $z \geq 0.3$ and with circled stars the six new halos. The distribution seems not affected by selection effects (Malmquist bias): we observe at the highest values of $P_{1.4GHz}$ and $L_{X,500}$, both halos detected at $z < 0.3$ and halos detected at $z \geq 0.3$. Moreover, the most luminous halos are included in the redshift range $0.3 < z < 0.4$. Excluding a few exceptions, we found that the halos at high redshifts ($z \geq 0.3$) also have the highest radio and X-ray brightness even if the most luminous are not the most distant. Nevertheless, it is difficult to confirm this general trend due to the still scanty number of known high redshift halos. Excluding MACSJ2228.5, the 6 new halos appear slightly underluminous in the radio band (see Fig. 8.3 *Upper panel*). The scaling relations we obtained performing an OLS-bisector best fit regression are also reported in Fig. 8.2. The best fit lines of the 2018 full halo collection (including the 6 new halos) and the collection of halos with

$z < 0.3$ are in agreement with $P_{1.4GHz} \propto L_{X,500}^{1.8}$. The correlation in the halo collection with $z \geq 0.3$ resulted only marginal (Pearson correlation parameter $r = 0.325$ with $p_0 = 0.0977$) due to the large dispersion and inhomogeneities of the radio data (see Fig. 8.3 *bottom panel*). For this data we found a lower slope of the fit line with $P_{1.4GHz} \propto L_{X,500}^{1.5}$.

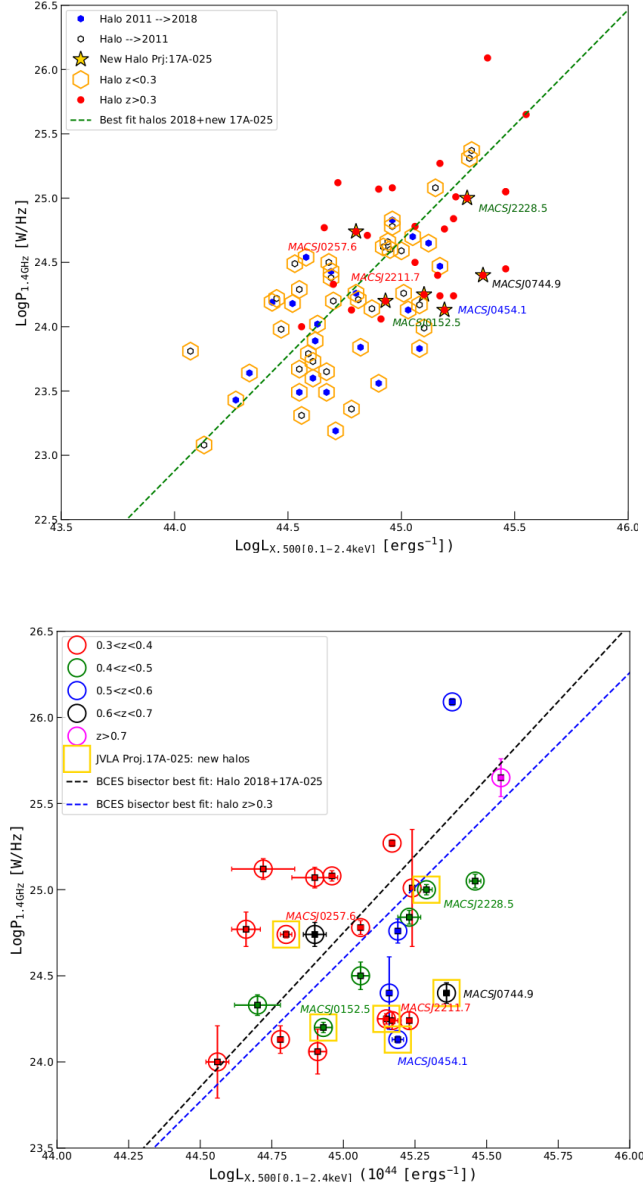


Figure 8.3: *Upper panel:* Distribution of halos at $z < 0.3$ and halos at $z \geq 0.3$. Green dotted line is the OLS-bisector best fits : $\log P_{1.4GHz} = (1.79 \pm 0.16) \log L_{X,500} + (-56.10 \pm 7.28)$ ($r = 0.629$, $p = 8.97 \times 10^{-10}$). *Bottom panel:* distribution of radio halos with $z \geq 0.3$ in the $(P_{1.4GHz}, L_{X,500})$ plane. Dotted lines are the OLS-bisector best fits of: halos with $z \geq 0.3$ (blue line) and 2018 halo collection including VLA17A–025 new halos (black line).

If we consider the correlations reported in the literature, the scaling relations of the halo collection in Feretti et al. (2012) and (e.g. Cassano et al. 2013) are steeper respect to the 2018 whole collection. They found $P_{1.4GHz} \propto L_{X,500}^{2.3}$ and $P_{1.4GHz} \propto L_{X,500}^{2.1}$ respectively. In Fig. 8.4 is reported the distribution of the 2018 full collection of radio halos in the $(P_{1.4GHz}, LLS)$ plane. The different colors of the circles are referred to different redshift ranges. Also for this correlation there are no evidences of selection effects (Malmquist bias). We can notice that the most distant clusters are relatively small, trend that seems to be confirmed also in the new halos. We hypothesize that this evidence is in some way related to the evolution of radio halos, allowing the possibility that their size grows with the time. Anyway, the new halos (gold stars) follow the correlation with the exception of MACSJ257.6 which appears the smallest respect to its radio power. For the $z \geq 0.3$ halo collection (including the new halos), the correlation $P_{1.4GHz}$ vs LLS resulted "robust" (Pearson correlation parameter $r = 0.576$ with $p = 5.67 \times 10^{-4}$), steeper than the $z < 0.3$ collection and in agreement with the 2018 updated collection.

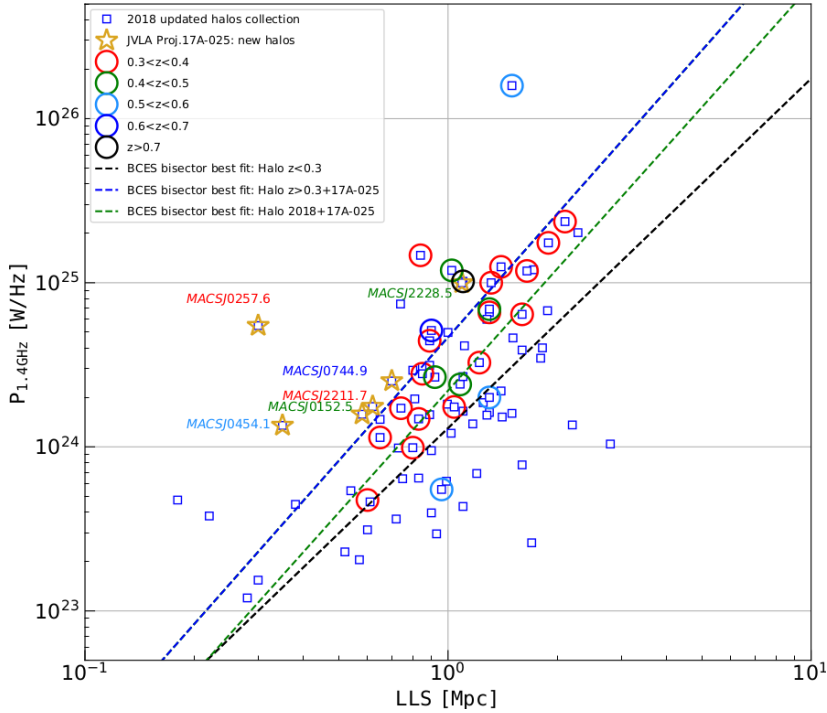


Figure 8.4: Distribution of the 2018 full collection of radio halos in the $(P_{1.4GHz}, LLS)$ plane. The different colors of circles are referred to the different redshift ranges. Labelled gold stars are the new halos discovered in this thesis. Dotted lines are the OLS bisector best fit lines:

- black ($z < 0.3$): $\log P_{1.4GHz} = (2.14 \pm 0.24) \log LLS + (17.75 \pm 0.70)$ ($r = 0.606$, $p = 1.50 \times 10^{-6}$);
- blue ($z \geq 0.3$) + new): $\log P_{1.4GHz} = (2.50 \pm 0.55) \log LLS + (17.16 \pm 1.67)$ ($r = 0.576$, $p = 5.67 \times 10^{-4}$);
- green (2018 + new): $\log P_{1.4GHz} = (2.47 \pm 0.24) \log LLS + (16.93 \pm 10.73)$ ($r = 0.638$, $p = 5.6 \times 10^{-10}$).

8.5 Redshift evolution of radio relics

The distribution of radio relics in the $(P_{1.4GHz}, L_{X,500})$ plane reported in Fig. 8.5, shows clearly that the farthest objects are the most radio and X-ray luminous. We suggest the possibility that this evidence is affected by a selection bias (Malmquist).

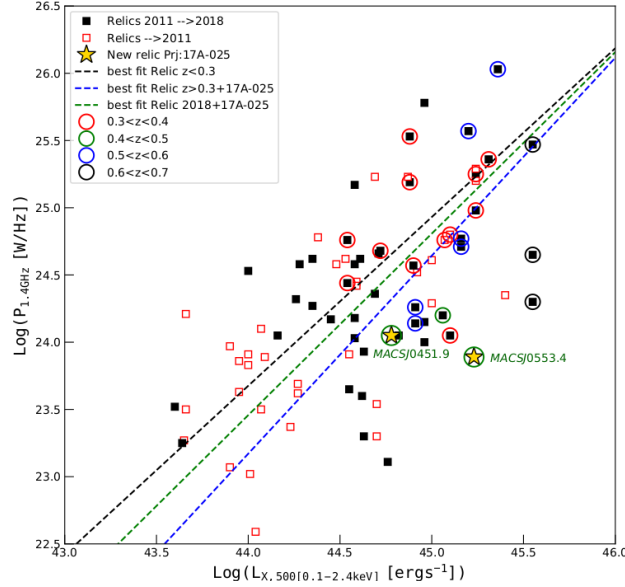


Figure 8.5: Distribution in the $(P_{1.4GHz}, L_{X,500})$ plane of the 2018 updated relic collection. Circled dots are the relics detected in clusters with $z \geq 0.3$. Labeled circled stars are the new relics detected in proj. VLA/17A-025. Colored dotted lines are the following OLS-bisector best fits:

black ($z < 0.3$): $\log P_{1.4GHz} = (1.25 \pm 0.16) \log L_{X,500} + (-31.55 \pm 6.96)$ ($r = 0.517$, $p = 3.31 \times 10^{-5}$);
 blue ($z \geq 0.3$): $\log P_{1.4GHz} = (1.47 \pm 0.35) \log L_{X,500} + (-41.61 \pm 15.95)$ ($r = 0.272$, $p = 0.21$);
 green (2018+new): $\log P_{1.4GHz} = (1.35 \pm 0.11) \log L_{X,500} + (-35.94 \pm 4.74)$ ($r = 0.612$, $p = 1.01 \times 10^{-9}$).

If we report as in Fig. 8.6 the radio power distributions of relics detected

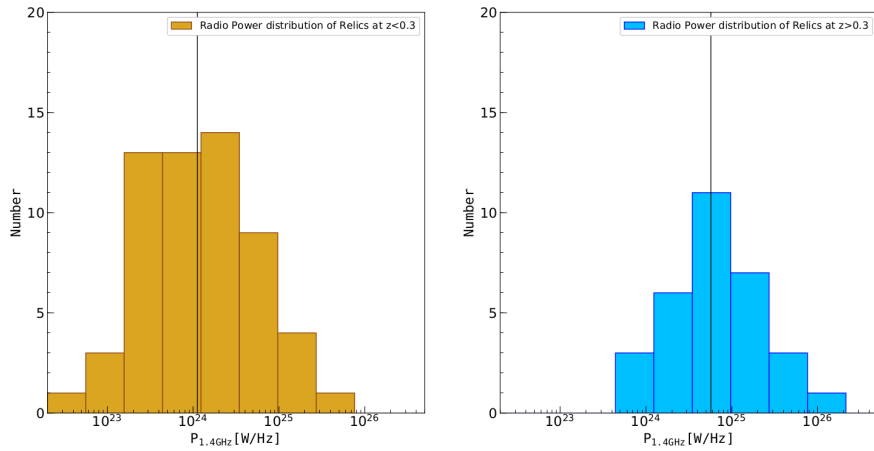


Figure 8.6: *Left panel:* radio power distribution of relics with $z < 0.3$. Vertical black line is the median value 1.12×10^{24} W/Hz. *Right panel:* radio power distribution of relics with $z \geq 0.3$. Vertical black line is the median value 5.71×10^{24} W/Hz

at $z < 0.3$ and $z \geq 0.3$ and calculate the median value of each distribution we confirm that relics with the highest redshifts are distributed around the highest values of radio power. In the literature the correlation $P_{1.4GHz}$ vs $L_{X,500}$ results only marginal, nevertheless the scaling relation seems not change significantly with the redshift. We found $P_{1.4GHz} \propto L_{X,500}^{\sim 1.3}$ for the $z < 0.3$ relic collection, $P_{1.4GHz} \propto L_{X,500}^{\sim 1.5}$ for the $z \geq 0.3$ relic collection (including the new relics detected in this thesis) and $P_{1.4GHz} \propto L_{X,500}^{\sim 1.4}$ for the 2018 updated relic collection (including the new relics). Best fit lines are shown in Fig. 8.5.

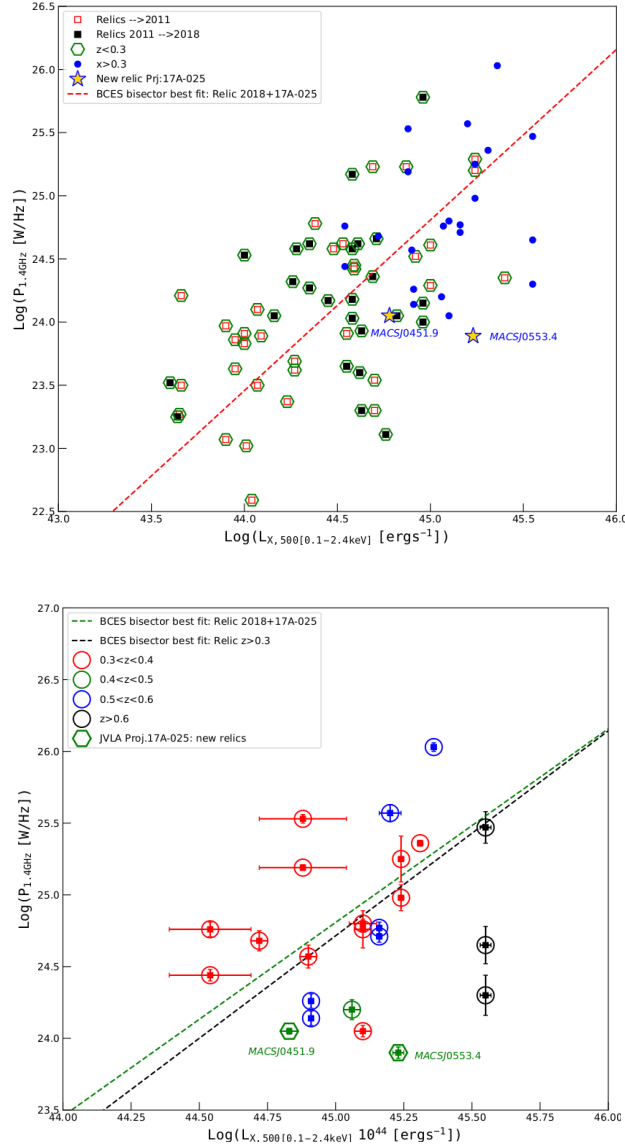


Figure 8.7: *Upper panel:* Green colored dotted line is the OLS-bisector best fit: (2018+new) $\log P_{1.4GHz} = (1.35 \pm 0.11) \log L_{X,500} + (-35.94 \pm 4.74)$ ($r = 0.612$, $p = 1.017 \times 10^{-9}$). *Bottom panel:* distribution of radio relics with $z \geq 0.3$ in the $(P_{1.4GHz}, L_{X,500})$ plane. Dotted lines are the OLS-bisector best fits of: relics with $z \geq 0.3$ (blue line) and 2018 relic collection including VLA/17A-025 new relics (black line).

The best fit correlation of the 2018 updated relic collection with included the new relics also results in good agreement with the correlation reported by Feretti et al. (2012). The scaling relation of both collections is $P_{1.4GHz} \propto L_{X,500}^{\sim 1.35}$. The most recent correlation proposed by Yuan is instead steeper resulting $P_{1.4GHz} \propto L_{X,500}^{\sim 1.60}$. The scaling relation of the relics with $z \geq 0.3$ (*bottom panel* of Fig. 8.7) appears steeper than the 2018 updated collection but data are sharply dispersed and the correlation weakly significant. The scaling relation between the radio power and the linear largest size (LLS) of the relic collections with different redshift ranges is characterized by very little differences among relics detected at $z < 0.3$ and relics detected at $z \geq 0.3$ as shown in Fig. 8.8. Nevertheless, in the $z \geq 0.3$ collections resulted a weak correlation.

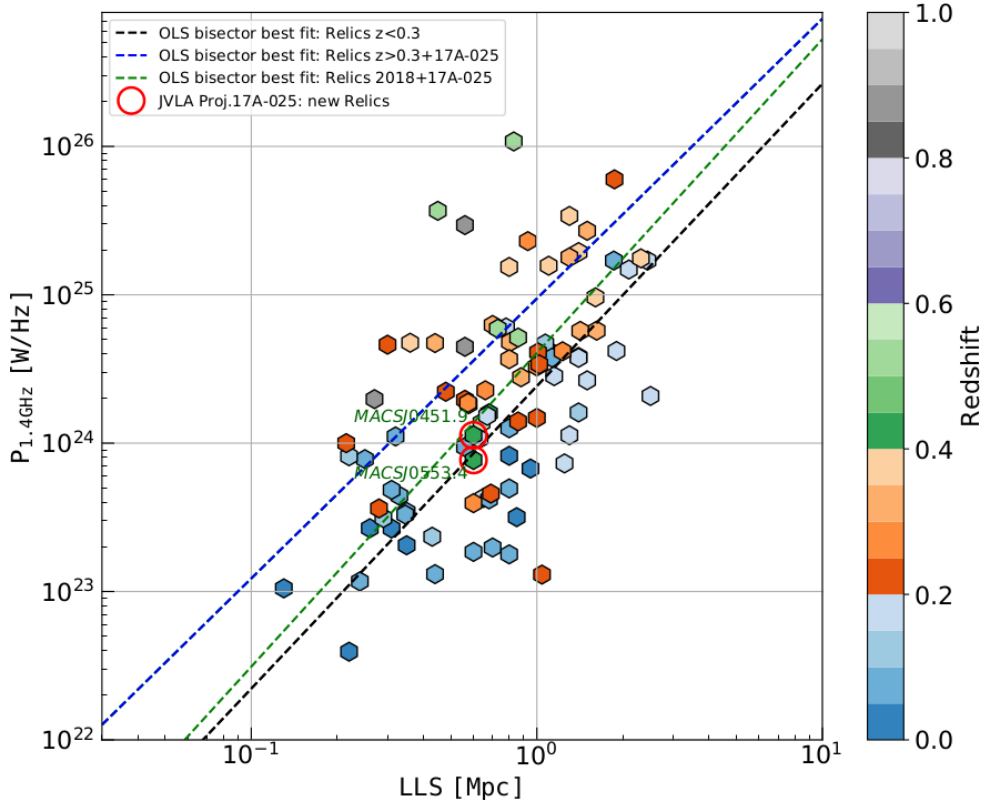


Figure 8.8: Distribution of the 2018 full collection of radio relics in the ($P_{1.4GHz}$, LLS) plane. The different colors of the dots are referred to the different redshift values reported in the colorbar scale. Labelled dots with red circles are the new relics discovered in this thesis. Dotted lines are the OLS bisector best fit lines:
- black ($z < 0.3$): $\log P_{1.4GHz} = (2.04 \pm 0.184) \log LLS + (18.27 \pm 0.52)$ ($r = 0.663$, $p = 3.33 \times 10^{-9}$);
- blue ($z \geq 0.3 + new$): $\log P_{1.4GHz} = (1.89 \pm 0.33) \log LLS + (19.32 \pm 0.98)$ ($r = 0.372$, $p = 0.0392$);
- green (2018+new): $\log P_{1.4GHz} = (2.10 \pm 0.21) \log LLS + (18.26 \pm 0.60)$ ($r = 0.580$, $p = 9.07 \times 10^{-10}$).

Also for this scaling relation we test the possible presence of selection effects, even if from the plot they do not seem to be present. The histograms with the size distribution of relics at $z < 0.3$ and $z \geq 0.3$ are reported in Fig.

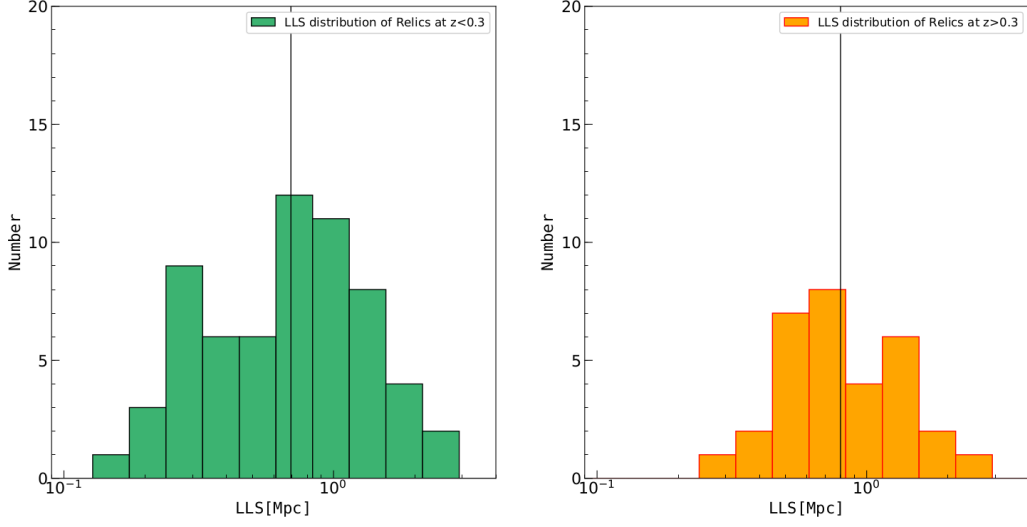


Figure 8.9: *Left panel:* size (LLS) distribution of relics with $z < 0.3$. Vertical black line is the median value 0.69 Mpc. *Right panel:* size distribution of relics with $z \geq 0.3$. Vertical black line is the median value 0.80 Mpc.

8.9. The median value of these two distribution do not show significant differences and therefore we can exclude the presence of the Malmquist effect. In general, excluding some outliers, the relics with the higher redshift are also the most extendend and radio luminous. The new relics, detected in this thesis, appear under-luminous for their size and they need to be better investigate.

8.6 Redshift evolution of radio minihalos

The little number of minihalos known today makes very difficult the study of the redshift evolution of these kind of objects. The correlation $P_{1.4GHz}$ vs $L_{X,500}$ results significant with scaling relation $P_{1.4GHz} \propto L_{X,500}^{\sim 2.2}$. In the plot of Fig. 8.10 (*left panel*) 7 minihalos are reported with $z \geq 0.3$ and have the highest values of radio and X-ray luminosity. Nevertheless from this scanty number of sources it is not possible to understand if this effect is real or related to a selection bias. The correlation of the radio power with the R_{MH} is weakly significant as well the attempt to extrapolate a trend of the points ($P_{1.4GHz}$, $L_{X,500}$) with the redshift (*right panel* of Fig. 8.10).

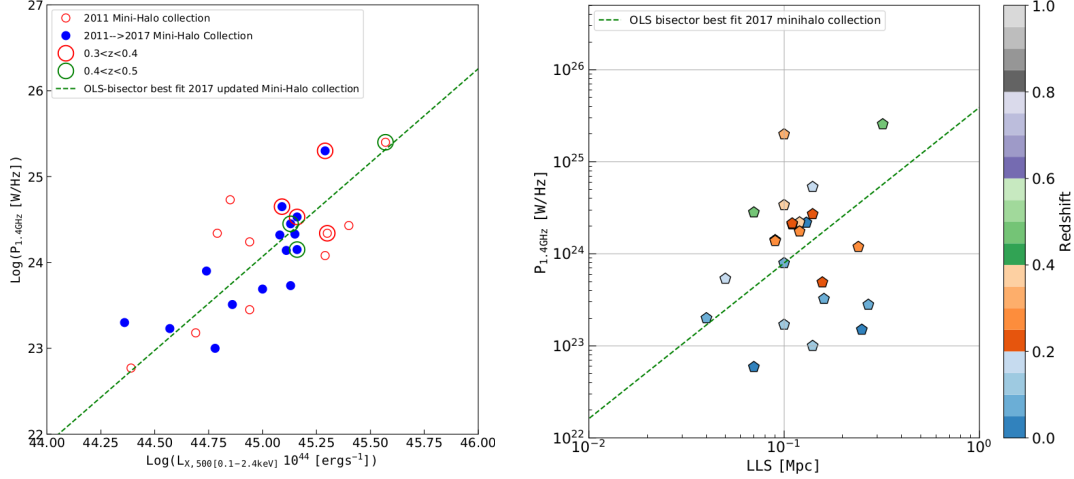


Figure 8.10: *Left panel:* Distribution in the $(P_{1.4\text{GHz}}, L_{X,500})$ plane of the 2017 updated minihalo collection. Circled dots are the minihalos detected in clusters with $z \geq 0.3$. Green dotted line is the OLS-bisector best fit:

$$\log P_{1.4\text{GHz}} = (2.19 \pm 0.24) \log L_{X,500} + (-74.33 \pm 10.80) \quad (r = 0.770, p = 6.77 \times 10^{-6});$$

Right panel: distribution of radio minihalos in the $(P_{1.4\text{GHz}}, L_{MH})$ plane. Green dotted line is the OLS-bisector best fit:

$$\log P_{1.4\text{GHz}} = (1.69 \pm 0.76) \log L_{MH} + (20.52 \pm 1.55) \quad (r = 0.212, p = 0308).$$

8.7 Dynamical state indicators and redshift

In the previous sections we discussed the evolution history of non-thermal emission using as proxies the correlations $P_{1.4\text{GHz}}$ vs $L_{X,500}$ and $P_{1.4\text{GHz}}$ vs LLS. From our analysis arises that to extrapolate a "robust" correlation of these properties with the redshift it is necessary to consider also the redshift dependence of the cluster dynamical state. At this purpose the scaling relation discussed in Chap. 4 could be very useful. In particular when considered in clusters hosting diffuse radio emission the offset between the BCG and the X-ray peak seems to be a simple and reliable tool to associate the dynamical state of the cluster to the redshift. Because of the unavailability of the offset data for most of the clusters with diffuse emission at $z \geq 0.3$ this study could not be done in this thesis.

8.8 Future perspectives

The work in this thesis has tried to take a look at the properties of non-thermal emission in high redshift galaxy clusters. The temporal evolution of the scale relations discussed in the previous sections needs of further observations to be confirmed. The still scanty number of sources discovered at $z \geq 0.3$ causes the correlation $(P_{1.4\text{GHz}}, L_{X,500})$ and $(P_{1.4\text{GHz}}, \text{LLS})$ to be

only marginal. Moreover, many diffuse emission at high redshift are classified as candidates or uncertain and must to be confirmed. The D_{BCG-X} offset can also be improved with more precise optical and X-ray measurements of the positions of the X-peak and the BCG. The next generation of radio interferometers with more sensitive facilities (e.g. ngVLA, uGMRT, LOFAR and SKA) will allow to increase the number of diffuse radio objects and will make the statistics more meaningful. The expected growth of the number of non-thermal radio sources will lead to a better comprehension of their origin, properties and connection with the related clusters.

Bibliography

- Akritas, M. G. & Bershad, M. A. 1996, *Astrophysical Journal*, 470, 706
- Aleksić, J., Antonelli, L. A., Antoranz, P., et al. 2010, *Astrophysical Journal*, 710, 634
- Allen, S. 2000, in *Large Scale Structure in the X-ray Universe*, ed. M. Plionis & I. Georgantopoulos, 69
- Allen, S. W., Ettori, S., & Fabian, A. C. 2001, *Monthly Notices of the RAS*, 324, 877
- Allen, S. W., Schmidt, R. W., & Fabian, A. C. 2002, *Monthly Notices of the RAS*, 335, 256
- Andersson, K. E. & Madejski, G. M. 2004, *Astrophysical Journal*, 607, 190
- Bacchi, M., Feretti, L., Giovannini, G., & Govoni, F. 2003, *Astronomy and Astrophysics*, 400, 465
- Bagchi, J., Durret, F., Neto, G. B. L., & Paul, S. 2006, *Science*, 314, 791
- Bagchi, J., Sirothia, S. K., Werner, N., et al. 2011, *Astrophysical Journal Letters*, 736, L8
- Bahcall, N. A. & Lubin, L. M. 1994, *Astrophysical Journal*, 426, 513
- Berezinsky, V. S., Blasi, P., & Ptuskin, V. S. 1997, *Astrophysical Journal*, 487, 529
- Blasi, P. & Colafrancesco, S. 1999, *Astroparticle Physics*, 12, 169
- Böhringer, H., Pratt, G. W., Arnaud, M., et al. 2010, *Astronomy and Astrophysics*, 514, A32
- Bonafede, A., Brüggén, M., van Weeren, R., et al. 2012, *Monthly Notices of the RAS*, 426, 40

- Bonafede, A., Cassano, R., Brüggén, M., et al. 2017, *Monthly Notices of the RAS*, 470, 3465
- Bonafede, A., Feretti, L., Giovannini, G., et al. 2009a, *Astronomy and Astrophysics*, 503, 707
- Bonafede, A., Giovannini, G., Feretti, L., Govoni, F., & Murgia, M. 2009b, *Astronomy and Astrophysics*, 494, 429
- Bonafede, A., Giovannini, G., Feretti, L., Govoni, F., & Murgia, M. 2009c, *Astronomy and Astrophysics*, 494, 429
- Bonafede, A., Intema, H., Brüggén, M., et al. 2015, *Monthly Notices of the RAS*, 454, 3391
- Bonafede, A., Intema, H. T., Brüggén, M., et al. 2014a, *Astrophysical Journal*, 785, 1
- Bonafede, A., Intema, H. T., Brüggén, M., et al. 2014b, *Monthly Notices of the RAS*, 444, L44
- Botteon, A., Gastaldello, F., & Brunetti, G. 2018, *Monthly Notices of the RAS*, 476, 5591
- Brough, S., Collins, C. A., Burke, D. J., Lynam, P. D., & Mann, R. G. 2005, *Monthly Notices of the RAS*, 364, 1354
- Brough, S., Couch, W. J., Collins, C. A., et al. 2008, *Monthly Notices of the RAS*, 385, L103
- Brown, S., Duesterhoeft, J., & Rudnick, L. 2011a, *Astrophysical Journal, Letters*, 727, L25
- Brown, S., Emerick, A., Rudnick, L., & Brunetti, G. 2011b, *Astrophysical Journal, Letters*, 740, L28
- Brunetti, G. 2009, *Astronomy and Astrophysics*, 508, 599
- Brunetti, G. & Blasi, P. 2005, *Monthly Notices of the RAS*, 363, 1173
- Brunetti, G., Blasi, P., Cassano, R., & Gabici, S. 2004, in *COSPAR Meeting, Vol. 35, 35th COSPAR Scientific Assembly*, ed. J.-P. Paillé, 929
- Brunetti, G., Cassano, R., Dolag, K., & Setti, G. 2009, *Astronomy and Astrophysics*, 507, 661

- Brunetti, G. & Jones, T. W. 2014, *International Journal of Modern Physics D*, 23, 1430007
- Brunetti, G. & Lazarian, A. 2007, *Monthly Notices of the RAS*, 378, 245
- Brunetti, G. & Lazarian, A. 2011a, *Monthly Notices of the RAS*, 410, 127
- Brunetti, G. & Lazarian, A. 2011b, *Monthly Notices of the RAS*, 412, 817
- Brunetti, G. & Lazarian, A. 2016, *Monthly Notices of the RAS*, 458, 2584
- Buote, D. A. 2001, *Astrophysical Journal, Letters*, 553, L15
- Buote, D. A. & Tsai, J. C. 1995, *Astrophysical Journal*, 452, 522
- Cantwell, T. M., Scaife, A. M. M., Oozeer, N., Wen, Z. L., & Han, J. L. 2016, *Monthly Notices of the RAS*, 458, 1803
- Cassano, R. 2009, in *Astronomical Society of the Pacific Conference Series*, Vol. 407, *The Low-Frequency Radio Universe*, ed. D. J. Saikia, D. A. Green, Y. Gupta, & T. Venturi, 223
- Cassano, R., Brunetti, G., Giocoli, C., & Etori, S. 2016, *Astronomy and Astrophysics*, 593, A81
- Cassano, R., Brunetti, G., Setti, G., Govoni, F., & Dolag, K. 2007, *Monthly Notices of the RAS*, 378, 1565
- Cassano, R., Brunetti, G., & Venturi, T. 2011, *Journal of Astrophysics and Astronomy*, 32, 519
- Cassano, R., Etori, S., Brunetti, G., et al. 2013, *Astrophysical Journal*, 777, 141
- Cassano, R., Etori, S., Giacintucci, S., et al. 2010, *Astrophysical Journal, Letters*, 721, L82
- Cassano, R., Gitti, M., & Brunetti, G. 2008, *Astronomy and Astrophysics*, 486, L31
- Cavagnolo, K. W., Donahue, M., Voit, G. M., & Sun, M. 2008, *Astrophysical Journal, Letters*, 683, L107
- Cavagnolo, K. W., Donahue, M., Voit, G. M., & Sun, M. 2009, *Astrophysical Journal, Supplement*, 182, 12

- Churazov, E., Forman, W., Jones, C., Sunyaev, R., & Böhringer, H. 2004, *Monthly Notices of the RAS*, 347, 29
- Clarke, T. E. 2004, *Journal of Korean Astronomical Society*, 37, 337
- Clarke, T. E. & Ensslin, T. 2006a, *Astronomische Nachrichten*, 327, 553
- Clarke, T. E. & Ensslin, T. A. 2006b, *Astronomical Journal*, 131, 2900
- Clarke, T. E., Kronberg, P. P., & Böhringer, H. 2001, *Astrophysical Journal, Letters*, 547, L111
- Cohen, A. S. & Clarke, T. E. 2011, *Astronomical Journal*, 141, 149
- Condon, J. J. 1999, *Proceedings of the National Academy of Science*, 96, 4756
- Cuciti, V., Brunetti, G., van Weeren, R., et al. 2018, *Astronomy and Astrophysics*, 609, A61
- Cuciti, V., Cassano, R., Brunetti, G., et al. 2015, *Astronomy and Astrophysics*, 580, A97
- de Gasperin, F., Intema, H. T., Ridl, J., et al. 2017, *Astronomy and Astrophysics*, 597, A15
- de Gasperin, F., Intema, H. T., van Weeren, R. J., et al. 2015, *Monthly Notices of the RAS*, 453, 3483
- de Gasperin, F., van Weeren, R. J., Brüggén, M., et al. 2014, *Monthly Notices of the RAS*, 444, 3130
- Dennison, B. 1980, *Astrophysical Journal, Letters*, 239, L93
- Doria, A., Gitti, M., Ettori, S., et al. 2012, *Astrophysical Journal*, 753, 47
- Ebeling, H., Barrett, E., Donovan, D., et al. 2007, *Astrophysical Journal, Letters*, 661, L33
- Ebeling, H., Edge, A. C., Mantz, A., et al. 2010, *Monthly Notices of the RAS*, 407, 83
- Edge, A. C. 1991, *Monthly Notices of the RAS*, 250, 103
- Edge, A. C. & Stewart, G. C. 1991, *Monthly Notices of the RAS*, 252, 414

- Enßlin, T., Pfrommer, C., Miniati, F., & Subramanian, K. 2011, *Astronomy and Astrophysics*, 527, A99
- Ensslin, T. A., Biermann, P. L., Klein, U., & Kohle, S. 1998, *Astronomy and Astrophysics*, 332, 395
- Ensslin, T. A., Biermann, P. L., Kronberg, P. P., & Wu, X.-P. 1997, *Astrophysical Journal*, 477, 560
- Enßlin, T. A. & Gopal-Krishna. 2001a, in *Astronomical Society of the Pacific Conference Series*, Vol. 250, *Particles and Fields in Radio Galaxies Conference*, ed. R. A. Laing & K. M. Blundell, 454
- Enßlin, T. A. & Gopal-Krishna. 2001b, *Astronomy and Astrophysics*, 366, 26
- Farnsworth, D., Rudnick, L., Brown, S., & Brunetti, G. 2013, *Astrophysical Journal*, 779, 189
- Feretti, L. 2003, in *Texas in Tuscany. XXI Symposium on Relativistic Astrophysics*, ed. R. Bandiera, R. Maiolino, & F. Mannucci, 209–220
- Feretti, L., Bacchi, M., Slee, O. B., et al. 2006, *Monthly Notices of the RAS*, 368, 544
- Feretti, L., Fusco-Femiano, R., Giovannini, G., & Govoni, F. 2001, *Astronomy and Astrophysics*, 373, 106
- Feretti, L., Giovannini, G., & Böhringer, H. 1997, *New Astronomy Journal*, 2, 501
- Feretti, L., Giovannini, G., Govoni, F., & Murgia, M. 2011, in *IAU Symposium*, Vol. 274, *Advances in Plasma Astrophysics*, ed. A. Bonanno, E. de Gouveia Dal Pino, & A. G. Kosovichev, 340–347
- Feretti, L., Giovannini, G., Govoni, F., & Murgia, M. 2012, *Astronomy and Astrophysics Reviews*, 20, 54
- Feretti, L., Schuecker, P., Böhringer, H., Govoni, F., & Giovannini, G. 2005, *Astronomy and Astrophysics*, 444, 157
- Ferrari, C., Govoni, F., Schindler, S., Bykov, A. M., & Rephaeli, Y. 2008, *Social Science Research, Journal*, 134, 93

- Fujita, Y. & Ohira, Y. 2013, *Monthly Notices of the RAS*, 428, 599
- Gavazzi, G. & Trinchieri, G. 1983, *Astrophysical Journal*, 270, 410
- Geach, J. E., Cimatti, A., Percival, W., et al. 2010, *Monthly Notices of the RAS*, 402, 1330
- Ghizzardi, S., Rossetti, M., & Molendi, S. 2010, *Astronomy and Astrophysics*, 516, A32
- Giacintucci, S., Dallacasa, D., Venturi, T., et al. 2011a, *Astronomy and Astrophysics*, 534, A57
- Giacintucci, S., Kale, R., Wik, D. R., Venturi, T., & Markevitch, M. 2013, *Astrophysical Journal*, 766, 18
- Giacintucci, S., Markevitch, M., Brunetti, G., Cassano, R., & Venturi, T. 2011b, *Astronomy and Astrophysics*, 525, L10
- Giacintucci, S., Markevitch, M., Cassano, R., et al. 2017, *Astrophysical Journal*, 841, 71
- Giacintucci, S., Markevitch, M., Venturi, T., et al. 2014, *Astrophysical Journal*, 781, 9
- Giacintucci, S., Venturi, T., Brunetti, G., et al. 2009, *Astronomy and Astrophysics*, 505, 45
- Giacintucci, S., Venturi, T., Macario, G., et al. 2008, *Astronomy and Astrophysics*, 486, 347
- Giovannini, G. 1999, in *Diffuse Thermal and Relativistic Plasma in Galaxy Clusters*, ed. H. Boehringer, L. Feretti, & P. Schuecker, 13
- Giovannini, G., Bonafede, A., Feretti, L., et al. 2009, *Astronomy and Astrophysics*, 507, 1257
- Giovannini, G. & Feretti, L. 2000, *New Astronomy Journal*, 5, 335
- Giovannini, G., Feretti, L., Girardi, M., et al. 2011, *Astronomy and Astrophysics*, 530, L5
- Giovannini, G., Feretti, L., & Stanghellini, C. 1991, *Astronomy and Astrophysics*, 252, 528

- Girardi, M. & Biviano, A. 2002, in *Astrophysics and Space Science Library*, Vol. 272, *Merging Processes in Galaxy Clusters*, ed. L. Feretti, I. M. Gioia, & G. Giovannini, 39–77
- Gitti, M., Brunetti, G., & Setti, G. 2002, *Astronomy and Astrophysics*, 386, 456
- Gitti, M., Brunetti, G., Setti, G., & Feretti, L. 2004, in *The Riddle of Cooling Flows in Galaxies and Clusters of galaxies*, ed. T. Reiprich, J. Kempner, & N. Soker
- Gitti, M., Feretti, L., & Schindler, S. 2006, *Astronomy and Astrophysics*, 448, 853
- Gitti, M., Ferrari, C., Domainko, W., Feretti, L., & Schindler, S. 2007, *Astronomy and Astrophysics*, 470, L25
- Gitti, M., Giroletti, M., Giovannini, G., Feretti, L., & Liuzzo, E. 2013, *Astronomy and Astrophysics*, 557, L14
- Govoni, F., Feretti, L., Giovannini, G., et al. 2001a, *Astronomy and Astrophysics*, 376, 803
- Govoni, F., Ferrari, C., Feretti, L., et al. 2012, *Astronomy and Astrophysics*, 545, A74
- Govoni, F., Murgia, M., Feretti, L., et al. 2005, *Astronomy and Astrophysics*, 430, L5
- Govoni, F., Murgia, M., Giovannini, G., Vacca, V., & Bonafede, A. 2011, *Astronomy and Astrophysics*, 529, A69
- Govoni, F., Murgia, M., Markevitch, M., et al. 2009, *Astronomy and Astrophysics*, 499, 371
- Govoni, F., Taylor, G. B., Dallacasa, D., Feretti, L., & Giovannini, G. 2001b, *Astronomy and Astrophysics*, 379, 807
- Henry, J. P. & Henriksen, M. J. 1986, *Astrophysical Journal*, 301, 689
- Hlavacek-Larrondo, J., Allen, S. W., Taylor, G. B., et al. 2013a, *Astrophysical Journal*, 777, 163
- Hlavacek-Larrondo, J., Fabian, A. C., Edge, A. C., et al. 2013b, *Monthly Notices of the RAS*, 431, 1638

- Hoang, D. N., Shimwell, T. W., Stroe, A., et al. 2017a, *Monthly Notices of the RAS*, 471, 1107
- Hoang, D. N., Shimwell, T. W., Stroe, A., et al. 2017b, *Monthly Notices of the RAS*, 471, 1107
- Hudson, D. S., Mittal, R., Reiprich, T. H., et al. 2010, *Astronomy and Astrophysics*, 513, A37
- Ikebe, Y., Reiprich, T. H., Böhringer, H., Tanaka, Y., & Kitayama, T. 2002, *Astronomy and Astrophysics*, 383, 773
- Jeltema, T. E., Canizares, C. R., Bautz, M. W., & Buote, D. A. 2005, *Astrophysical Journal*, 624, 606
- Johnston-Hollitt, M. & Ekers, R. D. 2004, *ArXiv Astrophysics e-prints*
- Kale, R., Venturi, T., Cassano, R., et al. 2015a, *Astronomy and Astrophysics*, 581, A23
- Kale, R., Venturi, T., Giacintucci, S., et al. 2015b, *Astronomy and Astrophysics*, 579, A92
- Kale, R., Wik, D. R., Giacintucci, S., et al. 2017, *Monthly Notices of the RAS*, 472, 940
- Katayama, H., Hayashida, K., Takahara, F., & Fujita, Y. 2003, *Astrophysical Journal*, 585, 687
- Kempner, J. C. & Sarazin, C. L. 2001a, *Astrophysical Journal*, 548, 639
- Kempner, J. C. & Sarazin, C. L. 2001b, *Astrophysical Journal*, 548, 639
- Keshet, U. & Loeb, A. 2010, *Astrophysical Journal*, 722, 737
- Kim, K.-T. 1990, *Nuovo Cimento B Serie*, 105, 845
- Knowles, K., Intema, H. T., Baker, A. J., et al. 2016, *Monthly Notices of the RAS*, 459, 4240
- Komissarov, S. S. & Gubanov, A. G. 1994, *Astronomy and Astrophysics*, 285, 27
- Korngut, P. M., Dicker, S. R., Reese, E. D., et al. 2011, *Astrophysical Journal*, 734, 10

- Liang, H. 2000, ArXiv Astrophysics e-prints
- Lindner, R. R., Baker, A. J., Hughes, J. P., et al. 2014, *Astrophysical Journal*, 786, 49
- Longair, M. S. 1981, *High energy astrophysics*
- Macario, G., Intema, H. T., Ferrari, C., et al. 2014, *Astronomy and Astrophysics*, 565, A13
- Malmquist, K. G. 1922, *Meddelanden fran Lunds Astronomiska Observatorium Serie I*, 100, 1
- Mann, A. W. & Ebeling, H. 2012, *Monthly Notices of the RAS*, 420, 2120
- Mantz, A., Allen, S. W., Rapetti, D., Ebeling, H., & Drlica-Wagner, A. 2010, in *Bulletin of the American Astronomical Society*, Vol. 42, American Astronomical Society Meeting Abstracts #215, 391
- Mantz, A. B., Allen, S. W., Morris, R. G., et al. 2015, *Monthly Notices of the RAS*, 449, 199
- Mao, M. Y., Sharp, R., Saikia, D. J., et al. 2010, *Monthly Notices of the RAS*, 406, 2578
- Markevitch, M. & Vikhlinin, A. 2007, *Physics Reports*, 443, 1
- Markevitch, M., Vikhlinin, A., & Mazzotta, P. 2001, *Astrophysical Journal Letters*, 562, L153
- Martinez Aviles, G., Ferrari, C., Johnston-Hollitt, M., et al. 2016, *Astronomy and Astrophysics*, 595, A116
- Maughan, B. J., Jones, C., Forman, W., & Van Speybroeck, L. 2008, *Astrophysical Journal Supplement*, 174, 117
- Mazzotta, P., Edge, A. C., & Markevitch, M. 2003, *Astrophysical Journal*, 596, 190
- Mazzotta, P., Markevitch, M., Vikhlinin, A., et al. 2001, *Astrophysical Journal*, 555, 205
- Middelberg, E. & Bach, U. 2008, *Reports on Progress in Physics*, 71, 066901
- Moffet, A. T. & Birkinshaw, M. 1989, *Astronomical Journal*, 98, 1148

- Mohr, J. J., Mathiesen, B., & Evrard, A. E. 1999, *Astrophysical Journal*, 517, 627
- Morandi, A., Sun, M., Forman, W., & Jones, C. 2015, in *IAU General Assembly*, Vol. 29, 2244785
- Murgia, M., Govoni, F., Feretti, L., & Giovannini, G. 2010, *Astronomy and Astrophysics*, 509, A86
- Murgia, M., Govoni, F., Markevitch, M., et al. 2009, *Astronomy and Astrophysics*, 499, 679
- Nuza, S. E., Gelszinnis, J., Hoeft, M., & Yepes, G. 2017, *Monthly Notices of the RAS*, 470, 240
- Ogrean, G. A., van Weeren, R. J., Jones, C., et al. 2015, *Astrophysical Journal*, 812, 153
- Pandey-Pommier, M., Richard, J., Combes, F., et al. 2016, in *SF2A-2016: Proceedings of the Annual meeting of the French Society of Astronomy and Astrophysics*, ed. C. Reyl e, J. Richard, L. Cambr esy, M. Deleuil, E. P econtal, L. Tresse, & I. Vauglin, 367–372
- Parekh, V., Dwarakanath, K. S., Kale, R., & Intema, H. 2017, *Monthly Notices of the RAS*, 464, 2752
- Patel, P., Maddox, S., Pearce, F. R., Arag on-Salamanca, A., & Conway, E. 2006, *Monthly Notices of the RAS*, 370, 851
- Petrosian, V. 2001, *Astrophysical Journal*, 557, 560
- Pfrommer, C. & En lin, T. A. 2004, *Astronomy and Astrophysics*, 413, 17
- Piffaretti, R., Arnaud, M., Pratt, G. W., Pointecouteau, E., & Melin, J.-B. 2011, *Astronomy and Astrophysics*, 534, A109
- Pizzo, R. F., de Bruyn, A. G., Bernardi, G., & Brentjens, M. A. 2011, *Mem. Societa Astronomica Italiana*, 82, 565
- Planck Collaboration, Ade, P. A. R., Aghanim, N., et al. 2014, *Astronomy and Astrophysics*, 571, A29
- Planck Collaboration, Ade, P. A. R., Aghanim, N., et al. 2015, *Astronomy and Astrophysics*, 581, A14

- Planck Collaboration, Ade, P. A. R., Aghanim, N., et al. 2011, *VizieR Online Data Catalog*, 8088
- Poole, G. B., Fardal, M. A., Babul, A., et al. 2006, *Monthly Notices of the RAS*, 373, 881
- Randall, S. W., Clarke, T. E., Nulsen, P. E. J., et al. 2010, *Astrophysical Journal*, 722, 825
- Randall, S. W., Clarke, T. E., van Weeren, R. J., et al. 2016, *Astrophysical Journal*, 823, 94
- Reid, A. D., Hunstead, R. W., Lemonon, L., & Pierre, M. M. 1999, *Monthly Notices of the RAS*, 302, 571
- Reimer, O., Pohl, M., Sreekumar, P., & Mattox, J. R. 2003, *Astrophysical Journal*, 588, 155
- Riseley, C. J., Scaife, A. M. M., Wise, M. W., & Clarke, A. O. 2017, *Astronomy and Astrophysics*, 597, A96
- Rossetti, M., Eckert, D., Cavalleri, B. M., et al. 2011, *Astronomy and Astrophysics*, 532, A123
- Rossetti, M., Gastaldello, F., Eckert, D., et al. 2017, *Monthly Notices of the RAS*, 468, 1917
- Rossetti, M., Gastaldello, F., Ferioli, G., et al. 2016, *Monthly Notices of the RAS*, 457, 4515
- Rottgering, H. J. A., Wieringa, M. H., Hunstead, R. W., & Ekers, R. D. 1997, *Monthly Notices of the RAS*, 290, 577
- Sanderson, A. J. R., Edge, A. C., & Smith, G. P. 2009, *Monthly Notices of the RAS*, 398, 1698
- Santos, J. S., Rosati, P., Tozzi, P., et al. 2008, *Astronomy and Astrophysics*, 483, 35
- Sarazin, C. L. 2002, in *Astrophysics and Space Science Library*, Vol. 272, *Merging Processes in Galaxy Clusters*, ed. L. Feretti, I. M. Gioia, & G. Giovannini, 1–38
- Sayers, J., Czakon, N. G., Mantz, A., et al. 2013, *Astrophysical Journal*, 768, 177

- Sereno, M. & Etori, S. 2015, *Monthly Notices of the RAS*, 450, 3633
- Shakouri, S., Johnston-Hollitt, M., & Dehghan, S. 2016, *Monthly Notices of the RAS*, 458, 3083
- Shimwell, T. W., Markevitch, M., Brown, S., et al. 2015, *Monthly Notices of the RAS*, 449, 1486
- Shimwell, T. W., Rottgering, H. J. A., Best, P. N., et al. 2017, *VizieR Online Data Catalog*, 359
- Sifón, C., Menanteau, F., Hughes, J. P., Carrasco, M., & Barrientos, L. F. 2014, *Astronomy and Astrophysics*, 562, A43
- Sijbring, L. G. 1993, A radio continuum and HI line study of the perseus cluster
- Skibba, R. A. & Macciò, A. V. 2011, *Monthly Notices of the RAS*, 416, 2388
- Slee, O. B., Roy, A. L., Murgia, M., Andernach, H., & Ehle, M. 2001, *Astronomical Journal*, 122, 1172
- Sommer, M. W., Basu, K., Intema, H., et al. 2017, *Monthly Notices of the RAS*, 466, 996
- Subrahmanyan, R., Beasley, A. J., Goss, W. M., Golap, K., & Hunstead, R. W. 2003, *Astronomical Journal*, 125, 1095
- Taylor, G. B., Fabian, A. C., & Allen, S. W. 2002, *Monthly Notices of the RAS*, 334, 769
- Vacca, V., Govoni, F., Murgia, M., et al. 2011, *Astronomy and Astrophysics*, 535, A82
- van den Bosch, F. C., Weinmann, S. M., Yang, X., et al. 2005, *Monthly Notices of the RAS*, 361, 1203
- van Haarlem, M. P., Wise, M. W., Gunst, A. W., et al. 2013, *Astronomy and Astrophysics*, 556, A2
- van Weeren, R. J., Brügger, M., Röttgering, H. J. A., et al. 2011a, *Astronomy and Astrophysics*, 533, A35
- van Weeren, R. J., Fogarty, K., Jones, C., et al. 2013, *Astrophysical Journal*, 769, 101

- van Weeren, R. J., Hoeft, M., Röttgering, H. J. A., et al. 2011b, *Astronomy and Astrophysics*, 528, A38
- van Weeren, R. J., Intema, H. T., Lal, D. V., et al. 2014a, *Astrophysical Journal, Letters*, 786, L17
- van Weeren, R. J., Intema, H. T., Lal, D. V., et al. 2014b, *Astrophysical Journal, Letters*, 781, L32
- van Weeren, R. J., Intema, H. T., Röttgering, H. J. A., Brügger, M., & Hoeft, M. 2011c, *Mem. Societa Astronomica Italiana*, 82, 569
- Van Weeren, R. J., Jones, C., Forman, W. R., et al. 2014, in *American Astronomical Society Meeting Abstracts*, Vol. 223, *American Astronomical Society Meeting Abstracts #223*, 431.03
- van Weeren, R. J., Röttgering, H. J. A., & Brügger, M. 2011d, *Astronomy and Astrophysics*, 527, A114
- van Weeren, R. J., Röttgering, H. J. A., Brügger, M., & Cohen, A. 2009a, *Astronomy and Astrophysics*, 508, 75
- van Weeren, R. J., Röttgering, H. J. A., Brügger, M., & Cohen, A. 2009b, *Astronomy and Astrophysics*, 505, 991
- van Weeren, R. J., Röttgering, H. J. A., Brügger, M., & Hoeft, M. 2010a, *Science*, 330, 347
- van Weeren, R. J., Röttgering, H. J. A., Brügger, M., & Hoeft, M. 2010b, *Science*, 330, 347
- van Weeren, R. J., Röttgering, H. J. A., Intema, H. T., et al. 2012, *Astronomy and Astrophysics*, 546, A124
- Vazza, F., Brügger, M., van Weeren, R., et al. 2012, *Monthly Notices of the RAS*, 421, 1868
- Vazza, F., Brunetti, G., & Gheller, C. 2009, *Monthly Notices of the RAS*, 395, 1333
- Vazza, F., Brunetti, G., Gheller, C., & Brunino, R. 2010, *New Astronomy Journal*, 15, 695
- Vazza, F., Dolag, K., Ryu, D., et al. 2011, *Monthly Notices of the RAS*, 418, 960

- Ventimiglia, D. A., Voit, G. M., Donahue, M., & Ameglio, S. 2008, *Astrophysical Journal*, 685, 118
- Venturi, T. 2011, *Mem. Societa Astronomica Italiana*, 82, 499
- Venturi, T., Bardelli, S., Dallacasa, D., et al. 2003, *Astronomy and Astrophysics*, 402, 913
- Venturi, T., Giacintucci, S., Brunetti, G., et al. 2007, *Astronomy and Astrophysics*, 463, 937
- Venturi, T., Giacintucci, S., & Dallacasa, D. 2011, *Journal of Astrophysics and Astronomy*, 32, 501
- Venturi, T., Giacintucci, S., Dallacasa, D., et al. 2008, *Astronomy and Astrophysics*, 484, 327
- Venturi, T., Giacintucci, S., Dallacasa, D., et al. 2013, *Astronomy and Astrophysics*, 551, A24
- Vikhlinin, A., Kravtsov, A., Forman, W., et al. 2006, *Astrophysical Journal*, 640, 691
- Völk, H. J., Aharonian, F. A., & Breitschwerdt, D. 1996, in *TeV Gamma-ray Astrophysics. Theory and Observations*, ed. H. J. Voelk & F. A. Aharonian, 279–297
- Völk, H. J. & Atoyan, A. M. 2000, *Astrophysical Journal*, 541, 88
- Werner, N., Durret, F., Ohashi, T., Schindler, S., & Wiersma, R. P. C. 2008, *Social Science Research, Journal*, 134, 337
- Wilber, A., Brüggén, M., Bonafede, A., et al. 2018, *Monthly Notices of the RAS*, 476, 3415
- Wong, K.-W., Sarazin, C. L., Blanton, E. L., & Reiprich, T. H. 2008, *Astrophysical Journal*, 682, 155
- Xue, Y.-J. & Wu, X.-P. 2000, *Monthly Notices of the RAS*, 318, 715
- Yuan, Z. S., Han, J. L., & Wen, Z. L. 2015, *Astrophysical Journal*, 813, 77